Data fusion to determine North American sources and sinks of carbon dioxide at high spatial and temporal resolution from 2004 to 2008

Co-Principal Investigators: A. Scott Denning, Colorado State University
Kenneth J. Davis, Klaus Keller, Natasha R. Miles and Scott J. Richardson, The Pennsylvania State University

1. Introduction

There is strong evidence that North America terrestrial ecosystems are currently a substantial sink of carbon dioxide. The magnitude of the sink has a large range of uncertainty, we have a limited understanding of how it has varied over time, and the processes responsible for this sink are not entirely clear. Our limited understanding is linked to methodological limits, as well as limited continental data. Quantifying spatial patterns and temporal variability of carbon dioxide sources and sinks at continental to regional scales remains a challenging problem.

In response to this challenge a rapid expansion of the N. American carbon cycle observational network is underway. This expansion includes a network (AmeriFlux) of continuous, eddy-covariance based CO_2 flux measurements and a network of continuous, continental CO_2 mixing ratio observations of comparable precision and accuracy to the marine flask network. Inverse studies of the N. American carbon budget have only begun to utilize these emerging data sources directly (i.e. tower fluxes and continuous continental mixing ratio observations), and how to best utilize these data together is a topic of great uncertainty and intensive research. This is the focus area of our research. We are conducting a program of research that will turn the emerging wealth of data in N. America to our advantage. This will be accomplished by a continued collaboration between research groups at the forefronts of terrestrial boundary layer CO_2 flux and mixing ratio observations, and high resolution, land-atmosphere carbon cycle modeling. This collaboration has resulted in substantial progress towards fusion of flux and mixing ratio observations in a coupled land-atmosphere data assimilation framework. This project will further develop methods for fusion of CO_2 flux and mixing ratio observations via inverse modeling incorporating the N. American CO_2 mixing ratio observational network, forwards modeling built upon the N. American flux network, and cross-evaluation of these two approaches. We have published analyses of the mechanisms controlling interannual variability of carbon fluxes over North America (Baker et al, 2010), and a separate estimate of photosynthesis and respiration derived from data fusion for North America in 2004 (Schuh et al, 2010). Further, we will apply the methods already developed via this collaborative effort to examine interannual variability of N. American carbon fluxes from 2004 to 2008.

Hypotheses:

1) Flux and mixing ratio observations can be merged into a consistent analysis at synoptic, seasonal, and interannual time scales;

2) The N. American CO_2 budget will be well constrained by our data analysis system;

3) The 2004-2008 record of N. American net annual terrestrial CO_2 fluxes will show a persistent net sink of carbon of location and magnitude consistent with previous estimates based on ecological inventory methods, and;

4) The same flux record will yield detectable, spatially-resolved, climate-driven interannual variability.

Expected products include:

1) a growing database of flux-tower based, continuous CO_2 mixing ratio observations suitable for application to continental inversions;

2) a comprehensive analysis system for estimation of monthly CO_2 exchange across N. America at high spatial resolution;

3) significant reduction in the uncertainty in the annual net N. American CO_2 flux and its interannual variations, and;

4) spatially and temporally resolved terrestrial CO_2 fluxes and uncertainty estimates for 2004 through 2008 encompassing all of N. America.

Ultimately, our results will support the development of dynamic predictions of the future carbon cycle by providing a regionally and temporally resolved multi-year record of whole continent terrestrial carbon fluxes needed to evaluate continental-scale models.

2. Research highlights.

As part of the North American Carbon Program, we worked with our colleagues at the Pennsylvania State University to build a network of highly-calibrated observations of CO2 mixing ratio over North America from 2007 through 2009. We also developed and tested innovative data fusion methods to combine these data with a variety of remote sensing and in-situ data products to obtain highly-resolved maps of CO2 sources and sinks over North America.

The project has been a resounding success. Besides pioneering the field and modeling methodology, we published a detailed analysis of the treatment of spatial errors in atmospheric inversions of CO2 (Schuh et al, 2009); the first continental-scale maps of the terrestrial carbon budget using mesoscale transport models (Schuh et al, 2010); an analysis of the processes that control regional variations and interannual variations in carbon fluxes over North America (Baker et al, 2010); an analysis of the effect of crops on atmospheric CO2 in the USA (Corbin et al, 2010); a method for treatment of continuous continental CO2 data in global inversions (Butler et al, 2010); systematic error analysis for high-resolution inversions (Lauvaux et al, 2012a,b); and three years' worth of measurements of fine-scale variations of CO2 over the US Midwest (Miles et al, 2012).

Arguably the most important result of the project has been the unprecedented quantitative evaluation of regional inverse modeling using atmospheric CO2 measurements compared to some of the most detailed and spatially resolved carbon flux inventory data ever collected (Schuh et al, 2012). This last paper (in the final stages of review for Global

Change Biology) shows that three different inverse models applied over three very different spatial domains (global, continental, and regional) are all able to recover annual carbon budgets over the midcontinent region within the uncertainty of the bottom-up inventory. No previous study has ever been able to evaluate the accuracy of annual flux estimates before. We have also documented the effects of transport errors, changes in prior flux estimates, resolution, treatment of lateral boundary inflows, and measurement density so that future studies can better merge top-down and bottom up constraints on carbon fluxes with more confidence.

This study has paved the way for future studies of regional carbon balance using continuous in-situ measurements and high-resolution transport models, which is very exciting now that observing networks supported by both NOAA and EarthNetworks are maturing. The future of data fusion for carbon cycle science is bright.

3. Research products.

Information concerning instrumentation and sites collecting data can be found at http://www.amerifluxco2.psu.edu and http://ring2.psu.edu.

Results of our regional inversion were submitted to the North American Carbon Program regional interim synthesis activity for inclusion in that comparison project.

4. Peer-reviewed publications, conference proceedings and presentations.

4.a) Peer-reviewed publications:

Schuh, A. E., A. S. Denning, K. D. Corbin, I. T. Baker, M. Uliasz, N. Parazoo, A. E. Andrews, and D. E. J. Worthy, 2010. A regional high-resolution carbon flux inversion of North America for 2004. *Biogeosciences*, **7**, 1625–1644.

Baker, I.T., A. S. Denning, R. Stockli, 2010. North American gross primary productivity: Regional characterization and interannual variability. *Tellus*. **62B**, 533–549. DOI: 10.1111/j.1600-0889.2010.00492.x

Butler, M. P., K. J. Davis, A. S. Denning, and S. R. Kawa, 2010. Using continental observations in global atmospheric inversions of CO_2: 1. North American carbon sources and sinks. *Tellus*. **62B**, 550-572. DOI: 10.1111/j.1600-0889.2010.00501.x

Schuh, A. E., A. S. Denning, M. Uliasz, K. D. Corbin, 2009. Seeing the Forest through the Trees: Recovering large scale carbon flux biases in the midst of small scale variability. *Jour. Geophys. Res*., doi:10.1029/2008JG000842.

Corbin, K.D., A.S. Denning, E.Y. Lokupitya, A.E. Schuh, N.L. Miles, K.J. Davis, S. Richardson, I.T. Baker, 2010: Assessing the impact of crops on regional CO2 fluxes and atmospheric concentrations. Tellus. 62B, 521–532. DOI: 10.1111/j.1600-0889.2010.00485.x.

Lauvaux, T., A. E. Schuh, M. Uliasz, S. Richardson, N. Miles, A. E. Andrews, C. Sweeney, L. I. Diaz, D. Martins, P. B. Shepson, and K. J. Davis, 2012. Constraining the CO2 budget of the corn belt: exploring uncertainties from the assumptions in a mesoscale inverse system. *Atmos. Chem. Phys*., **12**, 337–354, 2012. doi:10.5194/acp-12-337-2012.

Lauvaux, T., A. E. Schuh, M. Bocquet, L. Wu, S. Richardson, N. Miles, and K. J. Davis, 2012. Network design for mesoscale inversions of CO2 sources and sinks. Tellus, B 2012, 64, 17980, doi:10.3402/tellusb.v64i0.17980.

Miles, N. L., S. J. Richardson, K. J. Davis, T. Lauvaux, A. E. Andrews, T. O. West, V. Bandaru, and E. R. Crosson, 2012. Large amplitude spatial and temporal gradients in atmospheric boundary layer CO2 mole fractions detected with a tower-based network in the U.S. upper Midwest. Jour. Geophys. Res. 117, G01019, doi:10.1029/2011JG001781.

Schuh, A. E., T. Lauvaux, T. West, A. S. Denning, D. Cooley, K. J. Davis, M. Uliasz, N. Miles, S. Richardson, A. Andrews, and S. Ogle, 2012. Evaluating atmospheric CO2 inversions at multiple scales over a highly-inventoried agricultural landscape. Submitted to *Global Change Biol*.

4.b) Reports to agencies:

4.c) Conference proceedings:

Denning, A. S., K. D. Corbin, I. T. Baker, E. Lokupitiya, E. McGrath-Spangler, R. Stockli, A. Schuh, K. R. Gurney, N. Parazoo, D. Zupanski, M. Uliasz, N. Miles, K. Davis, and S. Richardson. The North American Carbon Cycle as Seen In Models and Observations. Presented at the American Geophysical Union Fall 2008 Meeting, San Francisco CA, USA.

Denning, A. S., N. Parazoo, A. Schuh, and M. Uliasz. Gulf Coast Atmospheric Inflow: A Key Element of the North American CO2 Budget. Presented at the American Geophysical Union Fall 2008 Meeting, San Francisco CA, USA.

A. S Denning, N. Cavallaro, C. Ste-Marie, A. Muhlia-Melo. CarboNA: International studies of the North American carbon cycle. Invited Presentation at the American Geophysical Union Spring 2009 Meeting, Toronto, Canada.

A.E. Schuh, A. S. Denning, S.M. Ogle, K. Corbin, M. Uliasz, K.J. Davis, T. Lauvaux, N. Miles, A.E. Andrews, G. Petron, D.N. Huntzinger. 2009. Atmospheric CO2 inversions of the mid-continental intensive (MCI) region. Invited Presentation at the American Geophysical Union Fall 2009 Meeting, San Francisco CA, USA.

F.J. Breidt, D.S. Cooley, Q. Thurier, Y. Wang, A.E. Schuh, A. S. Denning, K.J. Davis, T.O. West, S.M. Ogle, 2009. Reconciliation of carbon dioxide flux estimates from atmospheric inversions and inventories in the mid-continent intensive. Presented at the American Geophysical Union Fall 2009 Meeting, San Francisco CA, USA.

I.T. Baker, A. S. Denning, and R. Stockli, 2009. B51D-0332. North American gross primary productivity: regional characterization and interannual variability. Presented at the American Geophysical Union Fall 2009 Meeting, San Francisco CA, USA.

Davis, K. J., A. E. Andrews, M. Cambaliza, A. S. Denning, K. R. Gurney, T. Lauvaux, N. L. Miles, S. M. Ogle, A. Possolo, S. Richardson, A. E. Schuh, P. B. Shepson, C. Sweeney, J. C. Turnbull, T. O. West, and J. R. Whetstone, 2010. Greenhouse gas emissions derived from regional measurement networks and atmospheric inversions: results from the MCI and INFLUX experiments. GC41G-07. Presented at the American Geophysical Union Fall 2010 Meeting, San Francisco CA, USA.

Uliasz, M., A. E. Schuh, and A. S. Denning, 2010. Regional modeling support for planning airborne campaigns to observe CO2 and other trace gases. A51C-0128. Presented at the American Geophysical Union Fall 2010 Meeting, San Francisco CA, USA.

Schuh, A. E., S. M. Ogle, K. J. Davis, A. S. Denning, T. Lauvaux, N. L. Miles, S. Richardson, A. R. Jacobson, A. E. Andrews, M. Uliasz, L. I. Diaz Isaac, T. O. West, and D. S. Cooley, 2010. Top-down bottom-up comparison of the Mid-Continental Intensive (MCI) region (INVITED). B51L-05. Presented at the American Geophysical Union Fall 2010 Meeting, San Francisco CA, USA.

Lokupitiya, E. L. and A. S. Denning, 2010. Observed and modeled carbon and energy fluxes for agricultural sites under the North American Carbon Program site-level interim synthesis. B51L-06. Presented at the American Geophysical Union Fall 2010 Meeting, San Francisco CA, USA.

Denning, A. S., N. Parazoo, R. S. Lokupitiya, and D. F. Baker, 2010. A comprehensive carbon

dioxide analysis system for estimating CO2 emissions. Presented at the American Geophysical Union Fall 2010 Meeting, San Francisco CA, USA.

Katherine D. Haynes; Ian T. Baker; A Scott Denning; Reto Stockli; Erandathie Y. Lokupitiya , 2011. Impacts of Prognostic Phenology and Agriculture on the Seasonal Cycle of Carbon Fluxes. B23A-0383. Presented at the American Geophysical Union Fall 2011 Meeting, San Francisco CA, USA.

Ian Shiach; Ian T. Baker; A Scott Denning , 2011. Evaluating the Response of the Terrestrial Biosphere to Significant Drought, B23C-0425. Presented at the American Geophysical Union Fall 2011 Meeting, San Francisco CA, USA.

4.d) Other Presentations:

Schuh, A., A.S. Denning, M. Uliasz, N.R. Miles, K.J. Davis, and S.J. Richardson, Regional-scale atmospheric measurements of CO2 sources and sinks. Plenary talk, Air and Waste Management Association First International Greenhouse Gas Measurement Symposium, 23-25 March, 2009, San Francisco, CA.

Participation in the 2nd North American Carbon Program All-Investigators Meeting. 17-20 February, 2009, San Diego, CA, including a project-related presentations:

Co-convener of session on Integrated Studies of Regional Carbon Exchange at the Fall Meeting of the American Geophysical Union, December, 2008, San Francisco, CA.

5. Student degrees supported.

Ph.D. dissertation:

Schuh, Andrew. Primary support from this project.

Butler, Martha.

6. Final Technical Report

6.1 Observations

This project builds upon the NOAA Global Monitoring Division (GMD) network of flask measurements (e.g. Conway *et al.,* 1994), aircraft profiles and tall towers (e.g. Bakwin *et al.,* 1998), and enhances this network with high-quality CO_2 mixing ratio measurements on 13 AmeriFlux towers, 5 of whose CO_2 instrumentation are maintained via this project, and all of whose mixing ratio data are being combined to make a uniform data product via this project. We will also work with 3 Fluxnet Canada sites with similar data. Note that most flux towers do not maintain CO_2 measurements of sufficient absolute accuracy or long-term precision to be useful in atmospheric inversion studies. These data will be further complemented by a mountaintop network in the Rockies (Fig. 1).

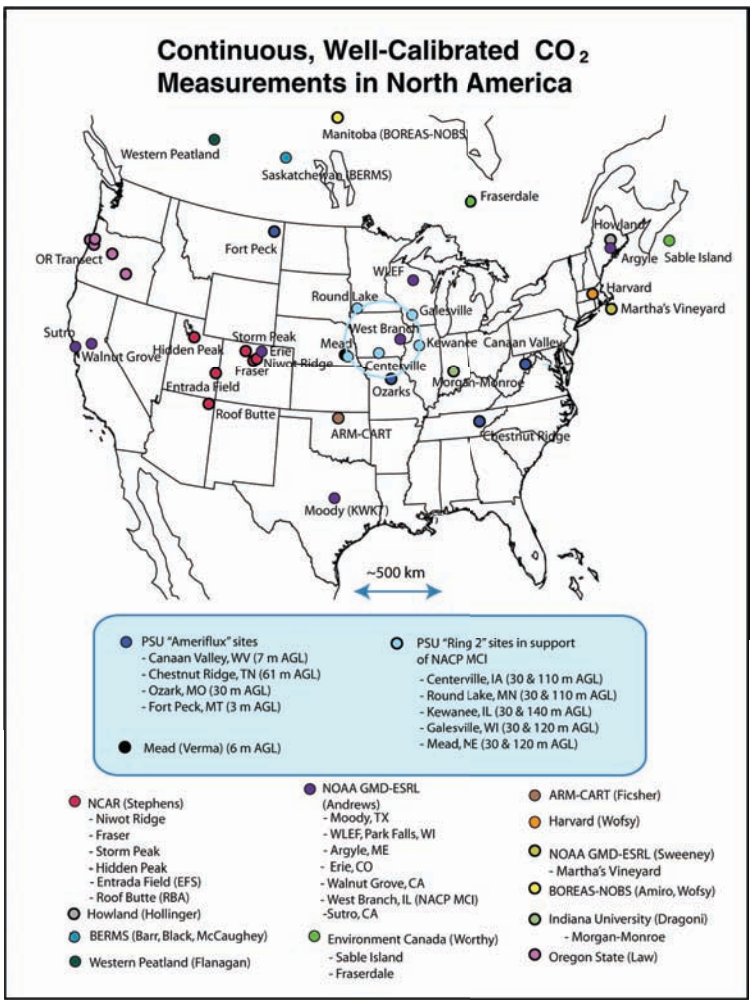

The surface layer mixing ratios measured at these towers, when subsampled for midday conditions, are very similar to the mixing ratio of the mixed layer (e.g. Yi *et al.,* 2004). Butler *et al.,* (in preparation) shows that further, the small difference between the surface layer mixing ratio and the mid-convective boundary layer (CBL) can be estimated from micrometeorological scaling arguments that have been fitted to the CO_2 flux and mixing ratio measurements from the 447 m tall WLEF tower. The average bias for hourly data is less than 0.2 ppm in summer, less than 0.1 ppm in spring and fall, and less than 0.5 ppm in winter (when mixing is the weakest). The average annual bias for houly data is less than 0.05 ppm. Data from the surface layer, subsampled for midday conditions, contain abundant large-scale synoptic and seasonal structure (e.g. Bakwin *et al.,* 2004; Hurwitz *et al.*, 2004).

The data from the network are available at http://ring2.psu.edu and http://amerifluxco2.psu.edu, as described in the annual progress report of our co-Investigators at Penn State.

6.2 Assimilation of CO2 Mixing Ratio data into Models

A fundamental assumption in the two-step assimilation procedure we propose is that high-frequency variations in NEE are driven by radiation and weather and can be successfully modeled by the flux-tower-optimized SiB-CASA. This allows us to accumulate mixing ratio data over a longer period of time to estimate spatial variations in state variables (e.g., carbon stocks) that control the lower frequency source-sink dynamics. We use the model and environmental data to account for spatial and high-frequency time variations of photosynthesis and respiration by assuming that they are driven by well-understood and easily modeled processes (vegetation distribution, radiation, temperature, soil moisture), then solve for unknown multiplicative biases in each component flux after smoothing in space and time. This is accomplished by convolving the influence functions generated from LPDM with gridded photosynthesis (gross primary production, GPP) and ecosystem respiration (RESP) at each time step in SiB-CASA. The net ecosystem exchange (NEE) is composed of these two component fluxes:

$$NEE(x,y,t) = RESP(x,y,t) - GPP(x,y,t) \quad \text{(eq 1)}$$

where x and y represent grid coordinates and t represents time. Sub-hourly variations in the simulated component fluxes in time are primarily controlled by the weather (especially changes in radiation due to clouds and the diurnal cycle of solar forcing), whereas seasonal changes are derived from phenological calculations parameterized from satellite imagery. Fine-scale variations in space are driven by variations in vegetation cover, soil texture, and soil moisture. To estimate regional fluxes from atmospheric mixing ratios, we assume that the model of the component fluxes is biased, and that the biases are smoother in time and space than the fluxes themselves:

$$NEE(x,y,t) = (1+\beta_{RESP}(x,y))RESP(x,y,t) - (1+\beta_{GPP}(x,y))GPP(x,y,t) \quad \text{(eq 2)}$$

A persistent bias in photosynthesis might result from underestimation of leaf area, available nitrogen, or soil moisture, whereas a persistent bias in respiration might result from overestimation of soil carbon or coarse woody debris. In any case, it is reasonable that such biases vary much more slowly than the fluxes. We generate surface flux influence functions by integrating the backward-in-time particle trajectories from LPDM. Using these, we can represent the mixing ratio observed at a given station k at time m as

$$C_{k,m} = \sum_{i,j,n} \left(\left((1+\beta_{R,i,j}) RESP_{i,j,n} - (1+\beta_{A,i,j}) GPP_{i,j,n} \right) C^*_{k,m,i,j,n} \right) \Delta t_f \Delta x \Delta y + C_{BKGD,k,m} \quad \text{(eq 3)}$$

where i and j are grid indices in the zonal and meridional directions, n is the time at which GPP and Respiration occurred (not usually the time at which the resulting change in mixing ratio was measured!). Fossil fuel combustion is specified according to an hourly analysis on a 32-km grid being developed in collaboration with K. Gurney and tested at CSU. The influence function $C^*_{k,m,i,j,n}$ is then the discrete form of the partial derivative of the observed mixing ratio with respect to the NEE at grid cell (i,j) at time step n. The length scales Δx and Δy are the sizes of the grid cells in the zonal and meridional direction, and Δt_f is the time step over which the fluxes are applied. The term $C_{BKGD,k,m}$ represents the contribution of "background" CO_2 flowing into the model domain from the larger scales (estimated from the global PCTM analyses). With a little algebra and a healthy dose of computer time, we obtain a simpler representation more practical suitable for optimization:

$$C_{obs} = \sum_{cell=1}^{nCell} (1+\beta_{RESP,cell}) C^*_{RESP,obs,cell} + \sum_{cell=1}^{nCell} (1+\beta_{GPP,cell}) C^*_{GPP,obs,cell} + C_{BKGD,obs} \quad \text{(eq 4)}$$

where *obs* is an observation number (combines indices *k* and *m*), and *cell* is a grid cell number (combines indices *i* and *j*). The influence functions have been convolved with the GPP and RESP terms from the forward model and integrated over the time period over which the bias terms are assumed to apply:

$$\begin{aligned} C^*_{RESP,obs,cell} &= \Delta t_f \Delta x \Delta y \sum_n RESP_{cell,n} C^*_{obs,cell,n} \\ C^*_{GPP,obs,cell} &= -\Delta t_f \Delta x \Delta y \sum_n GPP_{cell,n} C^*_{obs,cell,n} \end{aligned} \quad \text{(eq 5)}$$

Equation 4 is a linear system which can be written simply as

$$\vec{y} = h\vec{x} \quad \text{(eq 6)}$$

where $\vec{y}$ is the vector of observations C_{obs} and $\vec{x}$ is the vector of unknown bias terms $\beta_{\text{GPP,cell}}$ and $\beta_{\text{Resp,cell}}$. The Jacobian matrix *h* contains the influence functions $C^*_{GPP,obs,cell}$ and $C^*_{RESP,obs,cell}$. The rows of *h* correspond to each observation, and each column corresponds to an unknown bias term β_{RESP} or β_{GPP} at a given grid cell over the 10-day integration period. In practice, we treat the background mixing ratio by prescribing lateral inflow from the global PCTM. We treat errors in this boundary condition additively by augmenting the vector of unknowns $\vec{x}$ with lateral boundary concentrations and "transporting" them to the receptor by augmenting matrix *h* with additional influence functions for these fluxes.

We minimize a cost function that penalizes model-data mismatch and is regularized by imposing a weak prior constraint:

$$J = (\vec{y} - h\vec{x})^T r^{-1} (\vec{y} - h\vec{x}) + (\vec{x} - \vec{x}_p)^T p^{-1} (\vec{x} - \vec{x}_p)$$

where *r* is the observation error covariance, and *p* is the prior error covariance of the unknown β's.

6.3 Detailed Results

Please see the attached articles, which report the detailed technical results of the research.

JOURNAL OF GEOPHYSICAL RESEARCH, VOL. 114, G03007, doi:10.1029/2008JG000842, 2009

Seeing the forest through the trees: Recovering large-scale carbon flux biases in the midst of small-scale variability

A. E. Schuh,[1] A. S. Denning,[1] M. Uliasz,[1] and K. D. Corbin[1]

Received 8 August 2008; revised 31 March 2009; accepted 5 May 2009; published 15 August 2009.

[1] This paper investigates the effect of fine-scale spatial variability in carbon fluxes upon regional carbon flux inversion estimates in North America using simulated data from 1 May through 31 August 2004 and a hypothetical sparse network of eight towers in North America. A suite of random smooth regional carbon flux patterns are created and then obscured with random fine-scale spatial flux ''noise'' to mimic the effect of fine-scale heterogeneity in carbon fluxes found in nature. Five hundred and forty grid-scale atmospheric inversions are run using the synthetic data. We find that, regardless of the particular fine spatial scale carbon fluxes used (noise), the inversions can improve a priori carbon flux estimates significantly by capturing the large-scale regional flux patterns. We also find significant improvement in the root-mean-square error of the model are possible across a wide range of spatial decorrelation length scales. Errors associated with the inversion decrease as estimates are sought for larger and larger areas. Results show dramatic differences between postaggregated fine-scale inversion results and preaggregated coarse-scale inversion results confirming recent warnings about the ''preaggregation'' of inversion regions.

Citation: Schuh, A. E., A. S. Denning, M. Uliasz, and K. D. Corbin (2009), Seeing the forest through the trees: Recovering large-scale carbon flux biases in the midst of small-scale variability, *J. Geophys. Res.*, *114*, G03007, doi:10.1029/2008JG000842.

1. Introduction

[2] During the last decade, Bayesian-based atmospheric inversion techniques have emerged as a viable tool to investigate the spatiotemporal pattern of terrestrial carbon fluxes [*Enting et al.* 1994; *Fan et al.*, 1998; *Gurney et al.*, 2002; *Rodenbeck et al.*, 2003; *Baker et al.*, 2006; *Peters et al.*, 2007]. Research has largely been focused on continental-sized regions of the earth, using coupled general circulation models (GCM). Lately, researchers have begun applying these techniques to regional flux domains with increasingly finer resolution inversion domains [*Gerbig et al.*, 2003; *Carouge et al.*, 2008a, 2008b; *Lauvaux et al.*, 2008].

[3] In general, regional scale inversions focusing on temporal biases that are of a seasonal length, or longer, are possible because biosphere models have become adept at capturing the majority of carbon exchange that occurs on diurnal and seasonal time scales. The effects of the temperature, available soil water, and sunlight have been modeled extensively and predictions have become reasonably accurate over a variety of conditions and scales [*Baker et al.*, 2003, *Hanan et al.*, 2005; *Vidale and Stockli*, 2005]. However, the necessary components to model longer-term processes such as nitrogen deposition, land management, and other biogeochemical dynamics are often missing from these advanced biophysical models and thus lead to errors in the model. These effects may be unrecognizable at the diurnal scale but may dominate over longer temporal scales. Thus, researchers can begin to estimate these unknown processes by effectively removing the high-frequency diurnal signals at fine scales and estimating the residuals over longer time and space scales.

[4] The biggest hurdle to these inversions is insufficient carbon dioxide concentration data to constrain the flux inversion problem. Therefore, various additional constraints must be added. Two major methodologies have been employed to deal with this problem. The first of these two methods, which was employed in many inversion papers [*Enting et al.*, 1994; *Fan et al.*, 1998; *Gurney et al.*, 2002; *Peters et al.*, 2007] involved the preaggregation of large flux regions, generally according to prior guesses of flux patterns based upon global spatial net primary production (NPP) estimates. Largely in response to criticisms of this method [*Kaminski et al.*, 2001; *Engelen et al.*, 2002], geostatistical techniques were employed [*Michalak et al.*, 2004] to constrain the inversion problem. *Michalak et al.* [2004] used maximum likelihood techniques to estimate spatial covariance parameters (of the carbon flux error component) and then applied the resulting smooth covariance matrices to the differences between the underlying fluxes and the a priori fluxes. As a consequence of these additional constraints, inversion resolutions could be used that were much closer to that of the underlying forward transport and carbon flux models. *Zupanski et al.* [2007] used techniques similar to *Michalak et al.* [2004], with the exception that they used a maximum likelihood ensemble filter (MLEF) to track the covariance structure dynamically

[1]Graduate Degree Program in Ecology, Department of Atmospheric Science, Colorado State University, Fort Collins, Colorado, USA.

0148-0227/09/2008JG000842$09.00

instead of using more traditional geostatistical point-based estimates of spatial covariance parameters. *Peylin et al.* [2005] explored the effect of two different error correlation length-scale assumptions when estimating daily fluxes over a large portion of Europe. *Carouge et al.* [2008a, 2008b] used a 10-tower network in Europe in 2001, combined with synthetic data, to explore the sensitivity of inversion-based net ecosystem CO_2 exchange (NEE) estimates to various parameters of the inversion including temporal and spatial correlation.

[5] It seems reasonable to hypothesize that large-scale spatial patterns may exist in the errors for many models. For example, assume that one is modeling a large continental region such as North America. If the underlying flux model consistently underpredicts gross primary productivity (GPP) for forested regions and overpredicts for grassland regions over a given time interval such as a day or a year, then a map of the errors will likely show small positive errors in GPP over the grasslands and larger negative errors over the forested regions. Since grasslands and forested regions tend to exist in ''clumps'' on larger scales, this has the effect of inducing a spatially correlated structure to the errors. However, large-scale biases need not exist simply as a function of vegetation type. Persistent long-term droughts might affect large spatially connected regions of the continent over several different vegetation types. Fertilization effects from nitrogen deposition might also impact NEE over broad regions containing many vegetation types. It is difficult to exactly predict the structure in any of these cases, but it is reasonable to believe that correlations might exist on the order of several hundred kilometers or more. It is important to realize that this does not imply that the structure will be simple to recover. For instance, along ecotones such as the transition from the western to eastern slope of the Rocky Mountains and into the Great Plains of the central United States, one might not expect errors in fluxes to be strongly correlated. It is also reasonable to assume that the covariance function may not simply be a function of distance and may involve some kind of structuring around covariates such as biome classification.

[6] Small-scale spatial variability has been a recurrent theme of eddy flux measurements. For instance, data from the Chequamegon Ecosystem Atmospheric Study (http://cheas.psu.edu) showed significant variability in annual NEE between mature hardwood forests and old growth hardwood forests [*Desai et al.*, 2005]. Disturbance histories and the associated age structure has also been shown to be important to carbon dynamics in ponderosa pines of the Western United States [*Thornton et al.*, 2002; *Law et al.*, 2003]. Important factors explored in these papers, such as stand age and land management, are generally only coarsely modeled, or not modeled at all in larger-scale inversion studies. Of course the sampling footprints of the towers that generate these estimates of variability are generally on the order of a square kilometer or two and thus aggregated flux results at, for instance, 1600 km^2 (40 km by 40 km) might be expected to show less variability than that because of the averaging effect of aggregation. Regional inversions provide corrections to a priori NEE estimates and these corrections exhibit features on much larger scales than 40 km [*Gerbig et al.*, 2003; *Peylin et al.*, 2005]. The effect this has on fluxes is to introduce a layer of ''noise'' relative to potentially larger spatial scale error signals, such as continental scale sinks or large-scale agricultural expansion.

[7] Suppose that the flux model providing the prior estimates underpredicts GPP, on average, for a large forested area of North America. It is reasonable that this bias would vary spatially over this area on fine scales as a function of local land management practices, natural fire regimes, climate, and anthropogenic fertilization effects. These types of effects have different magnitudes and can be persistent at different temporal scales. Small-scale spatial variability has not typically been included as part of the prior error covariance structure [*Michalak et al.*, 2004; *Peylin et al.*, 2005; *Peters et al.*, 2005, 2007; *Zupanski et al.*, 2007], where it would be represented by a independent variance component that is typically termed the ''nugget'' in geostatistical literature [*Cressie*, 1993]. In general, it is unclear how the existence and/or exclusion of this error term in the inversion will affect inversion results.

[8] For instance, assume one is tasked with building and maintaining several towers to collect CO_2 observations which will be used to provide regional scale NEE estimates for a reasonably large managed forest region of North America (the Pacific Northwest United States for instance). Upon getting into the field, the researcher sees that the land is a patchwork of old growth, new growth, and recently clear-cut forest areas, essentially a myriad of fine scale ecosystems. Where might one locate their tower? If one puts their tower in a clear-cut location, will it ''bias'' his observations? Or what aboutputting it in an old growth stand surrounded by very vigorous young tree stands? Will the location have an effect and what will it be? These are obviously very important questions considering the work and cost involved in obtaining carbon dioxide measurements. We certainly know that the precise location of an eddy covariance tower has a huge effect upon the NEE measurements and any inferences that a researcher might want to make from them. The question is then: is the precise location important for a tower providing CO_2 observations to an atmospheric inversion?

[9] In this paper we investigate the effect of fine-scale spatial variability upon large spatial scale improvements in estimated NEE and use synthetic data and experiments to show that regional inversions are robust to fine-scale spatially independent variance in the flux errors. These inversions are performed in a manner in which assumptions need not be made about a fixed ''pattern'' of fluxes across large regions. In particular, we vary both the level of small-scale-independent variance (noise) as well as the decorrelation length scale of the spatially correlated portion of the bias which has a covarying effect upon the success of the inversion. A hypothetical sparse network of 8 towers in North America is used and the effects of varying these two quantities are tested using simulated fluxes and corresponding simulated measurements from a biosphere-meteorological model.

2. Methods

2.1. Model

[10] The Simple Biosphere model (SiB) is based on a land-surface parameterization scheme originally used to compute biophysical exchanges in climate models [*Sellers*

et al., 1986], but later adapted to include ecosystem metabolism [*Sellers et al.*, 1996; *Denning et al.*, 1996]. The parameterization of photosynthetic carbon assimilation is based on enzyme kinetics originally developed by *Farquhar et al.* [1980], and is linked to stomatal conductance and hence to the surface energy budget and atmosphere [*Collatz et al.*, 1991, 1992; *Sellers et al.*, 1996; *Randall et al.*, 1996]. The model has been updated to include prognostic calculation of temperature, moisture, and trace gases in the canopy air space, and the model has been evaluated against eddy covariance measurements at a number of sites [*Baker et al.*, 2003; *Hanan et al.*, 2005; *Vidale and Stockli*, 2005]. SiB has been coupled to the Regional Atmospheric Modeling System (RAMS) and used to study PBL-scale interactions among carbon fluxes, turbulence, and CO_2 mixing ratio [*Denning et al.*, 2003] and regional scale controls on CO_2 variations [*Nicholls et al.*, 2004; *Wang et al.*, 2006]. Other recent improvements include biogeochemical fractionation and recycling of stable carbon isotopes [*Suits et al.*, 2005], improved treatment of soil hydrology and thermodynamics, and the introduction of a multilayer snow model based on the Community Land Model [*Dai et al.*, 2003]. This latest version of SiB is termed SiB3.

[11] In SiB3, the net ecosystem exchange (NEE) is composed of two component fluxes, gross primary productivity (GPP) and ecosystem respiration (RESP), which includes autotrophic and heterotrophic respiration terms where x and y represent grid coordinates and t represents time

$$\mathrm{NEE}(x,y,t) = \mathrm{RESP}(x,y,t) - \mathrm{GPP}(x,y,t). \quad (1)$$

[12] High-frequency time variations of photosynthesis and respiration are assumed to be well understood and easily modeled processes, i.e., because of changes in radiation, temperature, soil moisture, etc. Long-term, more persistent biases are estimated (equation (2)) by solving for unknown multiplicative biases in each component flux after smoothing in space and time. This is accomplished by convolving the observation-specific "influence" functions generated from a Lagrangian particle dispersion model, LPDM [*Uliasz and Pielke*, 1991; *Zupanski et al.*, 2007; *Lauvaux et al.*, 2008], with GPP and RESP at each time step in SiB-RAMS. Figure 1 shows examples of daily mean influence functions for the WLEF tower for ecosystem respiration. One can see that the influence function is weaker for Figure 1 (top), 10 May, mainly because of faster transport from the northwest as well as weaker carbon fluxes due to late spring/early summer conditions in the northern regions of North America.

[13] To summarize, we estimate regional fluxes from atmospheric mixing ratios by assuming that the model of the component fluxes is biased, and that the biases are smoother in time and space than the fluxes themselves:

$$\begin{aligned}\mathrm{NEE}(x,y,t) = {} & (1+\beta_{\mathrm{RESP}}(x,y))\mathrm{RESP}(x,y,t) \\ & - (1+\beta_{\mathrm{GPP}}(x,y))\mathrm{GPP}(x,y,t). \end{aligned} \quad (2)$$

The model domain, shown in Figure 1, consists of most of the United States as well as a large portion of Canada and the northern portions of Mexico. SiB3-RAMS was run on a single 150 × 90 grid of 40 km cells. RAMS meteorology was nudged with NCEP ETA 40 km analysis data throughout the domain using the 4DDA scheme to produce more reliable wind fields. The fine-scale RAMS output was then to used to drive the backward in time LPDM model. SiB3 was run with 8-day fractional photosynthetically available radiation (FPAR) and leaf area index (LAI) fields derived from the MODIS MOD15 product. This was provided from the Numerical Terradynamics Simulation Group at the University of Montana who generated it for use in constructing the official MOD17 GPP product [*Mu et al.*, 2007]. The focus of this study was on the regional domain and therefore boundary inflow of CO_2 was not optimized or investigated. Given the simulated nature of the experiments, no actual estimate of inflow was needed. An inversion of North America using real data could follow a nested coarse-inversion concept, similar to that presented by *Peylin et al.* [2005].

2.2. Synthetic Data

[14] CO_2 mixing ratio observations are simulated hourly at eight measuring sites (WLEF, Harvard Forest, ARM, BERMS, Fraserdale, Western Peatland, WKWT, and Argyle (ME), see Figure 2 for locations) over a 113-day period. These were produced by first running SiB for the period and domain of interest to serve as our a priori biosphere flux model. Then we convolved simulated flux bias fields for GPP and RESP, shown as coefficients to RESP and GPP in equation (2), with LPDM derived influence functions representing contributions to an observation from upwind flux areas. *Gerbig et al.* [2003] found mean standard deviations on the order of 0.6 to 1 ppm when viewing morning and afternoon vertical profiles of CO_2. Afternoon hourly average observations, at 1200, 1400, 1600, and 1800 LT, are used to lessen the impact of low-quality modeling of transport during times of extremely stable and stratified nocturnal atmospheric conditions near the ground. In total, there are 3616 synthetic observations covering the period 1 May to 20 August 2004. An independent mean zero 2 ppm standard deviation Gaussian error term is added to the CO_2 observations to provide a crude estimate of transport errors.

[15] In summary, we used a continental scale model run of SiB, based upon a 113-day period in the summer of 2004, to provide realistic GPP and respiration fluxes. We also used a model run of RAMS during the same period to provide transport fields. We then assume 'truth' is actually represented by these biosphere fluxes multiplied by some synthetic, simulated, bias fields (as shown in Figure 2). We then simulated what the carbon dioxide concentrations would be at the observing towers give these biases. Finally, we performed the inversion to see how well we can estimate the biases from the carbon dioxide concentration observations.

2.3. Inversion Procedure

[16] Standard multivariate normal assumptions are made and data are assimilated using a Bayesian synthesis inversion, or equivalently, a single standard Kalman filter updating step. The resolution of the inversion domain (36 × 60, 100 km grid spacing) and the number of measurements (3616) were selected such that the needed matrix inversions

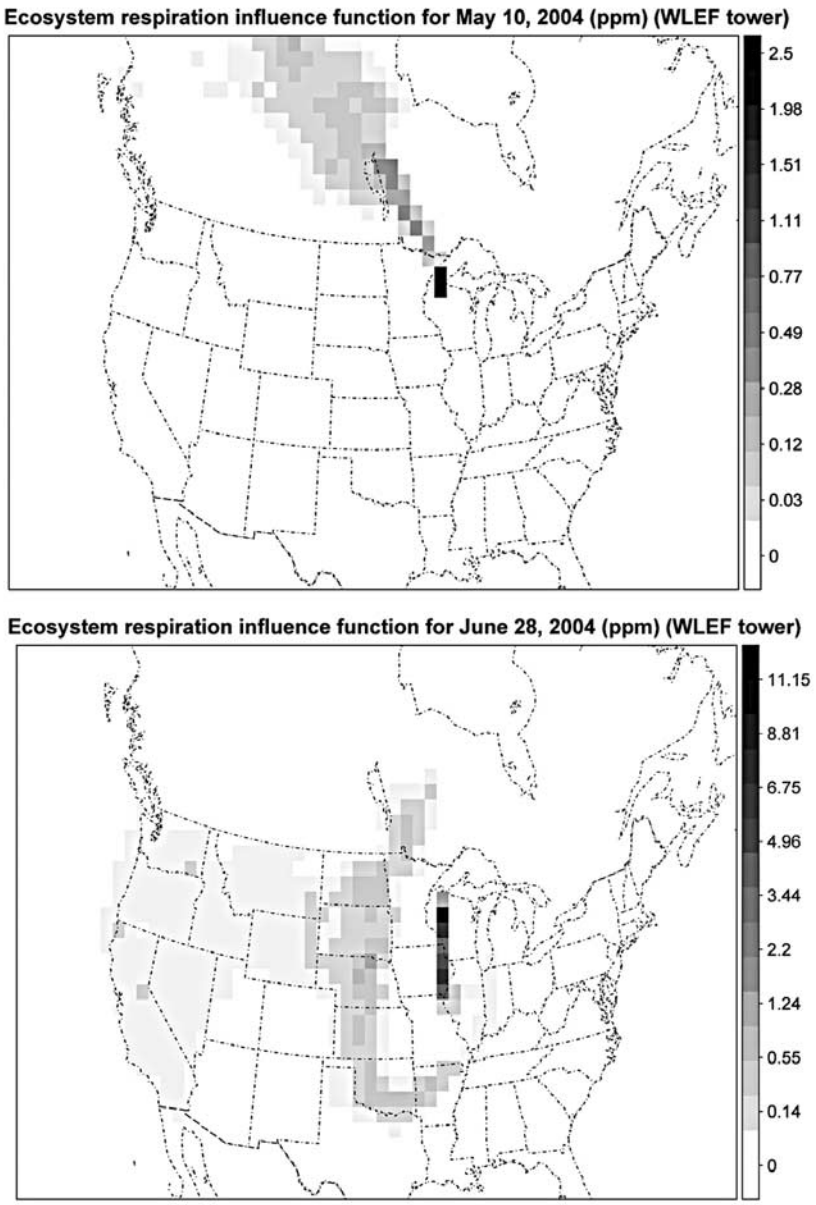

Figure 1. (top) An influence function for the modeled upwind respiration contributions to the WLEF tower for the mean of observations recorded at 1200, 1400, 1600, and 1800 LT on 20 May 2004. For example, if a cell value is 0.29 ppm then it contributed 0.29 ppm to the mean afternoon observation (estimated by the four hourly observations above) at the WLEF tower for that day. (bottom) A similarly derived respiration influence function for 28 June 2004.

could be calculated relatively quickly and without the aid of additional covariance subsampling procedures such as the Ensemble Kalman Filter methods [*Evensen*, 1994; *Zupanski et al.*, 2007] employ. While sufficient for theoretical exercises, it is noted that additional measurements and increased inversion domain resolution would require more involved subsampling procedures such as those used in the ensemble methods as well as a filter mechanism to propagate information forward. In particular, for a length n CO_2 measurement vector $\boldsymbol{y}$, length m CO_2 flux bias vector $\boldsymbol{\beta}$, $n \times n$ observation error covariance matrix $\boldsymbol{\Sigma}$, $n \times m$ Jacobian transport matrix $\boldsymbol{G}$, length m prior flux estimate $\boldsymbol{\beta_0}$, and mxm model prior mismatch covariance matrix $\boldsymbol{\Sigma_0}$, the Bayesian statistical assumptions are ($N(\mu, \Sigma)$ represents a multivariate Gaussian/Normal distribution with mean vector μ and covariance matrix Σ)

$$y|\beta, \Sigma \sim N(G\beta, \Sigma)\beta \sim N(\beta_0, \Sigma_0). \quad (3)$$

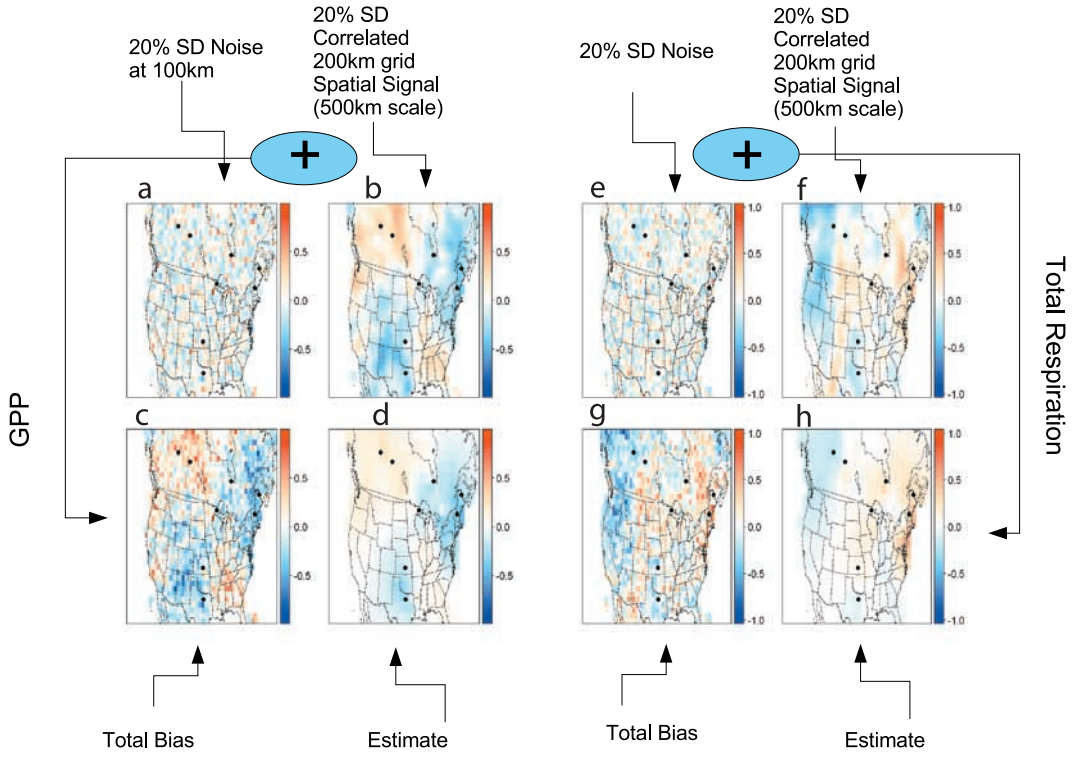

Figure 2. Example correction of (a–d) GPP and (e–h) total respiration signal. (a and e) Small spatial scale bias applied over model domain, (b and f) large-scale bias over model domain which we would like to recover, (c and g) total signal (sum of small and large), and (d and h) posterior estimate of mean bias. The eight CO_2 observing towers are shown as black dots on the images. Since biases are plotted as deviations from the prior (as in equation (2)), the mean a priori fluxes can be visualized as solid white plots with all grid cells equal to zero.

The posterior distribution of the flux vector can be solved for analytically and is

$$p(\beta|y,\Sigma) \propto \frac{1}{2}\left[(G\beta-y)^T\Sigma^{-1}(G\beta-y)+(\beta-\beta_0)^T\Sigma_0^{-1}(\beta-\beta_0)\right] \sim N\left(\left(\Sigma_0^{-1}+G^T\Sigma^{-1}G\right)^{-1}\left(\Sigma_0^{-1}\beta_0+G^T\Sigma^{-1}y\right),\left(\left(\Sigma_0^{-1}+G^T\Sigma^{-1}G\right)\right)^{-1}\right). \quad (4)$$

With a little bit of algebra, one can rewrite the mean/expectation of the posterior distribution of the mean, giving the familiar Kalman filter updating equation

$$E\left[\beta_{\text{posterior}}\right] = \beta_0 + \left(G^T\Sigma^{-1}G+\Sigma_0^{-1}\right)G^T\Sigma^{-1}(y-G\beta_0). \quad (5)$$

With respect to constraining the problem with spatially correlated errors, the covariance matrix Σ_0 is portioned into RESP and GPP components, $\Sigma_{\text{RESP,prior}}$ and $\Sigma_{\text{GPP,prior}}$, and will take on the following form:

$$\sum\nolimits_0 = \begin{bmatrix} \sum_{\text{RESP,prior}} & 0 \\ 0 & \sum_{\text{GPP,prior}} \end{bmatrix}. \quad (6)$$

For the case of correlated errors in the prior flux, the respiration and GPP covariance matrices are each formed from the exponential covariance function, where $\boldsymbol{t_{i,j}}$ is the distance between points $\boldsymbol{x_i}$ and $\boldsymbol{x_j}$

$$\text{Cov}\left(\beta_i,\beta_j\right) = \begin{cases} \sigma_0^2(1-\alpha_0)\exp\left(\frac{-t_{i,j}}{h_0}\right), i \neq j \\ \alpha_0\sigma_0^2, i=j. \end{cases} \quad (7)$$

The h_0 parameter is the range, or decorrelation length-scale parameter, giving the distance at which the covariance between two points is equal to σ_0^2 $(1 - \alpha_0)e^{-1}$. The σ^2 parameter is the scalar variance parameter and determines the variance of the marginal distribution of the particular flux component. The parameter α_0 controls what percentage of the covariance can be attributed to spatial covariance, as opposed to spatially independent errors.

[17] Given a posterior mean NEE $\boldsymbol{x_{\text{posterior}}}$ of length n, a posterior mean NEE variance estimate $\Sigma_{\text{posterior}}$ of dimension $n \times n$, and a scalar vector $\boldsymbol{b}$ of length n that maps higher-resolution fluxes to coarser resolution fluxes, the following result from multivariate Gaussian statistics

Table 1. Summary Statistics[a]

Flux-Based Statistics	200 km	400 km	600 km	1200 km	Domain
Prior mean RMSE (g/m^2)	45.3	38.4	35.3	26.8	2.6
Posterior mean RMSE (g/m^2)	28.2	20.5	16.4	8.0	1.7
Improvement over prior[b] (%)	39.2	49.1	56	72.3	57.1
Improvement in mean SD for grid cell mean over prior[c] (%)	32.5	40	45.8	59.1	77.9

[a]For example, inversion shown in Figure 1. This result is based upon a simulated observation error and thus changes slightly with different realizations.
[b]Presented in Figure 4 for multiple inversion study.
[c]Crude measure of tightening of posterior.

[*Johnson and Wichern*, 1988] can be employed to compare mean NEE at larger postaggregated scales

$$\overline{\mathrm{NEE}}_b = b' x_{\mathrm{posterior}} \sim N\left(b' x_{\mathrm{posterior}}, b' \sum\nolimits_{\mathrm{posterior}} b\right). \quad (8)$$

The scalar vector b can be chosen as a sequence of 1/k's and 0s where one is estimating the mean of a block of k cells together. In essence, this is mapping the higher-resolution posterior mean fluxes to coarser resolution mean fluxes. Given that we are considering NEE as the sum of GPP and RESP, the above result can first be employed to sum GPP and RESP correctly and then employed again to aggregate up resulting NEE. In this example, our finest resolution was 100 km, a grid of 60 by 36. Values of k were chosen to be 4, 9, 16, 36,144, and 2160, which represent aggregations to 400 km, 900 km, 1600 km, 3600 km, 14,400 km, and the entire domain. In order to compare to the prior, this calculation was performed on both the distribution of the mean of the posterior fluxes as well as the assumed distribution of the mean of the prior fluxes.

2.4. Experiments

[18] In order to test the sensitivity of the inversion to fine-scale spatial noise, we introduce a set of Monte Carlo inversion experiments. Recall that the principle motivation of this paper is to investigate the recovery, or estimation, of large-scale flux patterns through a "veil" of small-scale spatial noise. Given the difficulty in estimating decorrelation length scale from the data and the uncertainty surrounding the effect of one's choice of prior decorrelation scale length for the flux errors, we choose to include it in the sensitivity tests. In traditional Bayesian statistics, one is working with 'fixed' observations and so one typically perturbs a priori distributions to test the sensitivity of the estimation procedures to them. We take a different approach

- *Loop over (100 km, 500 km, 1000 km, 2000 km) spatial decorrelation length scale*
  - *Loop over (1%, 5%, 10%, 20%, 40%) standard deviation of Gaussian fine scale flux bias*
    - *Loop over 1,…,18 (18 random samples)*
      1. *generate random "observation" error vector (2 ppm standard deviation.) at 100 km*
      2. *generate random large scale spatial patterns for GPP/RESP flux bias using spatial decorrelaton length scale selected in first loop and 20% standard deviation multiplier*
      3. *generate random small scale spatial pattern for flux bias based upon standard deviation selected in second loop*
      4. *create synthetic data by combining transport and fluxes (at 100 km) and adding "observation" error vector*
      5. *run inversion at 100 km with a priori decorrelation length scale set to 500 km and a priori scalar standard deviation set to 20%*
      6. *statistically aggregate up results to 100 km, 200 km, 300 km, 400 km, 600 km, 1200 km, 1800 km, entire domain*
      7. *compare results from (6) with 'truth' given by (2) + (3) using RMSE of NEE estimate (RESP-GPP)*

Figure 3. A summary of the algorithm used to generate postaggregated experiments in section 3.

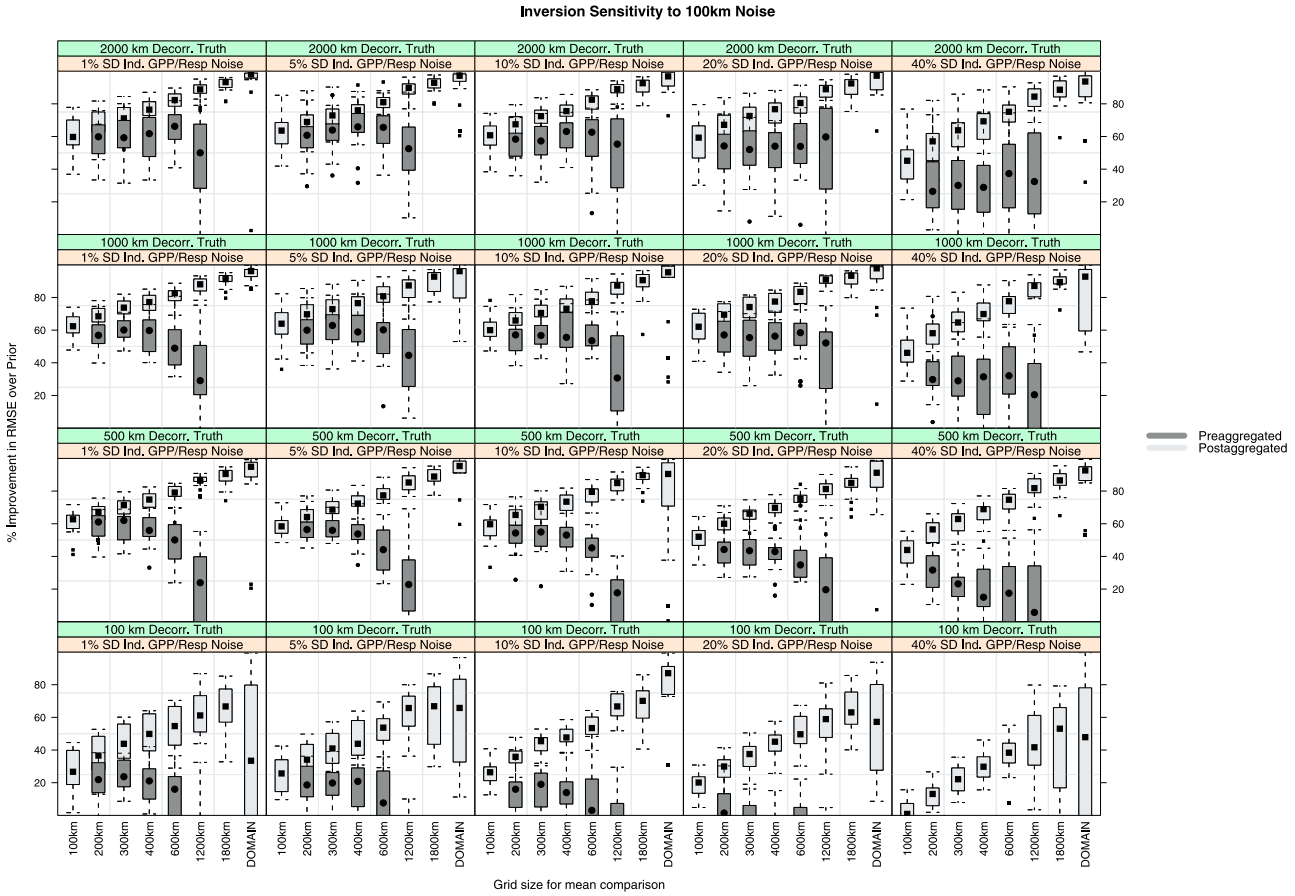

Figure 4. The improvement of posterior with respect to prior for preaggregated (dark gray) and postaggregated (light gray) inversion grid, factored over noise level and decorrelation length scale of true pattern used. Preaggregated (dark gray) inversions are only performed for grid sizes between 200 and 1200 km. An individual box plot shows the median (square for postagg and circle for preagg), the interquartile range (25th to 75th quantile) as the solid gray (light or dark) box, and whiskers indicating the most extreme data point which is no more than 1.5 times the interquartile range from the box (an ad hoc indicator of outliers).

in this paper because of the fact that our observations/data are changing with different simulations. We choose reasonably broad a priori specifications that should apply across many different models and then test how well the estimation procedure can reproduce a variety of simulated 'true' flux situations, each with a corresponding set of simulated CO_2 observations from the eight towers. Recall from section 2 that the forward model of both fluxes (SiB3) and transport (RAMS) operate on a 40 km grid and is then postaggregated to a 100 km grid for computational reasons.

[19] A key component of atmospheric CO_2 inversions is the specification of a priori error bounds for the different fluxes. An intercomparison of atmospheric CO_2 inversion models (Transcom3 [*Gurney et al.*, 2002]) provided source/sink estimates on the order of a few tenths of a Pg of carbon per inversion region per year. When compared to the actual net photosynthesis or ground respiration fluxes for this region, this results in uncertainties on the order of 10–30% in either direction, on a cumulative basis. We chose to represent ensembles of potential 'true' flux scenarios with mean zero, spatially correlated, 20% marginal standard deviation, Gaussian-based biases for individual 100 km grid cell GPP and respiration. These biases also seem to be a reasonably conservative a priori specification for the scalar multiplier on the spatial portion of the prior Gaussian covariance. In other words, we do not expect GPP and RESP biases to be outside of ±40% of the a priori estimates. Simulated flux bias realizations (examples shown in Figures 2b and 2f) are drawn from this range and we assume this is known to set the a priori covariance matrix. Small-scale spatial noise of the same order also seems reasonable, and in combination with the spatial component generates a suitably wide range of potential biases, on the order of 40% standard deviation for the individual 100 km grid cells for which they are applied.

[20] Decorrelation length scales are investigated at levels of 100 km, 500 km, 1000 km, and 2000 km. Small-scale Gaussian flux noise will be allowed to vary between standard deviation levels of 1%, 5%, 10%, 20%, and 40% of the a priori fluxes. The a priori scalar standard deviation on the spatial covariance term is set to 20% and the prior inversion decorrelation length scale will be set to 500 km, a

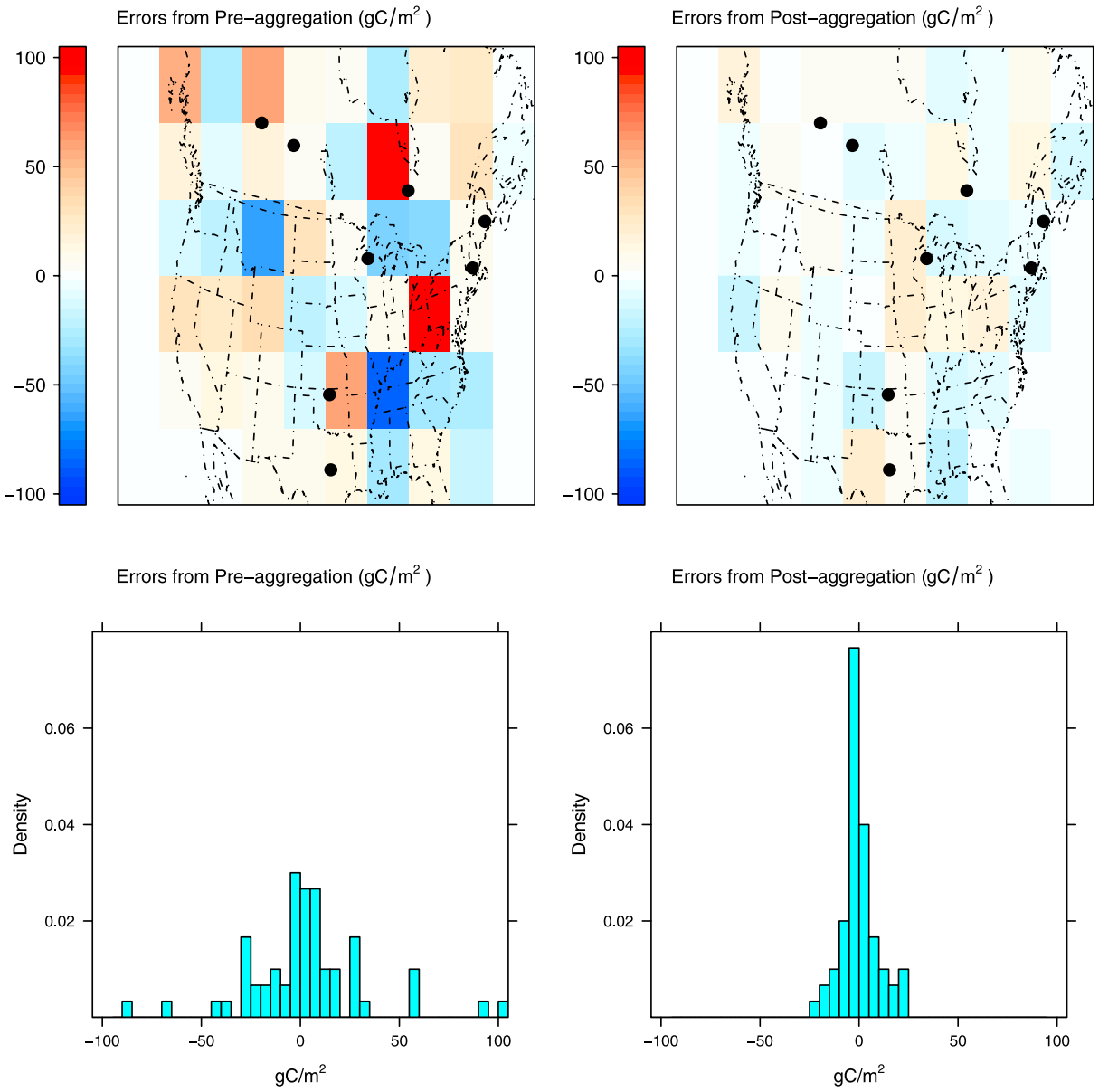

Figure 5. A comparison of errors from preaggregation versus postaggregation. Underlying spatial pattern comes from Figure 2. Preaggregation is a result of summing carbon fluxes on 1200 by 1200 km grid and running inversion on that grid. Postaggregation is a result of summing carbon fluxes on a 100 by 100 km grid and running the inversion on that grid and then summing up fluxes to a 1200 by 1200 km grid. Distinctly better results for postaggregation of fine-scale (100 km grid) inversion shown.

reasonably conservative prior compromise between similar parameters used in some recent papers [*Michalak et al.*, 2004; *Peylin et al.*, 2005]. For each combination of these two levels, 18 realizations of each scenario were run using randomly generated pseudo data corresponding to the levels used. Each realization introduces random "observation" error (mostly transport error) and random flux bias spatial patterns, both large and small scale. Since the temporally varying sampling pattern of the 8 towers is stationary, we must ensure that many different potential flux patterns are realized by the experiments so that the results are not dependent upon the sampling footprint of the towers.

[21] A specific example is presented to show the methodology of one realization. Figure 2 shows the spatial noise pattern, the longer-scale spatially correlated signal, as well as the summed bias and the inversion estimate for both GPP and respiration fluxes. This particular example employed a noise level of 20%, equivalent to the scalar variability of the spatially correlated signal. The spatial decorrelation length scale used to create the correlated flux errors was 500 km, equal to that used as the a priori estimate. Table 1 shows summary statistics for the mean flux estimates of upscaled, increasingly coarse, gridded flux regions for this example. These statistics will be used as the measure of fit for inversions based upon the complete set of levels mentioned above. In section 3 we present inversion results across a variety of 'noise' levels and decorrelation length scales. A

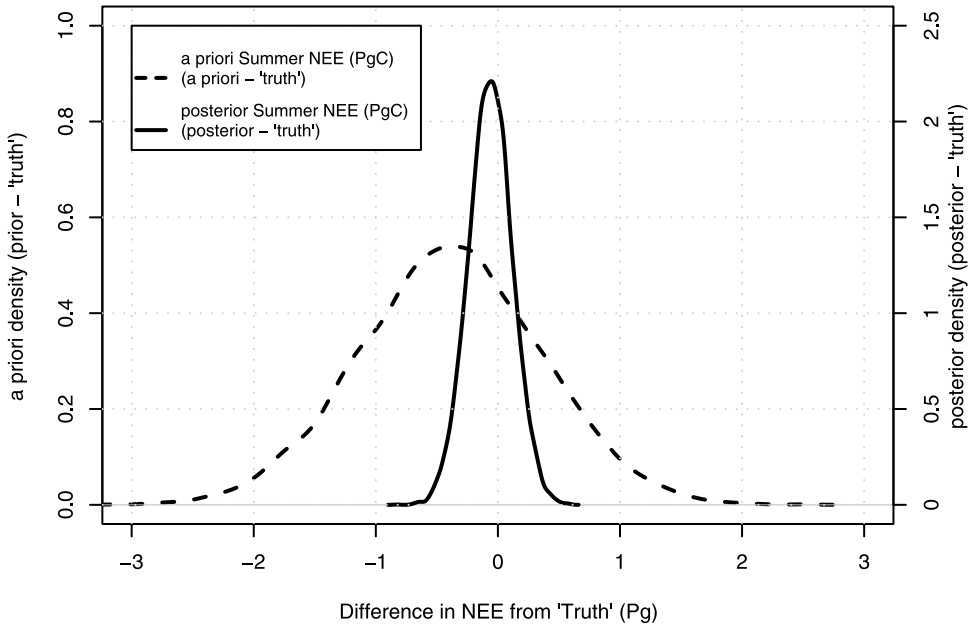

Figure 6. Prior and posterior cumulative NEE over period of 11 May to 31 August 2004, for example, shown in Figure 2 and Table 1.

summary of this procedure, for postaggregated experiments, is shown in Figure 3.

3. Results and Discussion

[22] Results from the sample realization, shown in Figure 2, indicate that the posterior improves fluxes considerably over the a priori estimates. Improvement in the spatial average RMSE over the prior fluxes is from 40% to 90% depending upon the postaggregation level. For example, Table 1 shows that when the inversion is run on a 100 km by 100 km grid and the results are postaggregated to 1200 km by 1200 km grid, the average root mean squared error (RMSE) over all of the 1200 km by 1200 km grid cells is reduced from 26.8 g/m^2 to 8.0 g/m^2. This is promising, considering that the level of small-scale noise (20% at 100 km) is equivalent to that of the spatially correlated portion of the flux errors (20%) for this example.

[23] Figure 4 shows these results over the entire range of small-scale variability and decorrelation length-scale parameters given in the algorithm above. The aggregated results, based upon 100 km resolution inversions, are shown in light gray. Variability within each panel of the image is due to the fact that the underlying bias field is not known and therefore has to be sampled over the set of all possible bias fields. The improvement in the spatial average RMSE over the prior is generally in the range of 20% to 90% over all combinations. The results show that the inversion is robust to small-scale spatial noise over a wide range of noise levels and decorrelation length scales. Although it may seem at first glance that these results contradict findings of others, such as *Peylin et al.* [2005] who found that changing a priori covariance assumptions impacts the strength and location of corrections, spatially, it must be understood that these results are presented as large-scale spatial averages. The degree and location of correction is likely to change with varying a priori spatial assumptions on the errors but as one postaggregates results to larger scales, corrections are more robust. This is likely a result of varying a priori spatial assumptions driving correlated posterior flux estimates.

[24] The power of higher-resolution inversions versus lower-resolution "preaggregated" inversions is shown in Figure 4 as well. Inversions performed on the grid cell size shown in the *x* axis are shown in dark gray. For instance, at the point in an individual panel at which the *x* axis indicates 600 km, the light gray results give aggregated results based upon 100 km inversions while the dark gray results give results based upon 600 km inversions. The difference is clearly most sensitive to the spatial correlation length scale of the bias pattern while much less sensitive to the layer of noise added to the flux biases. This is as one would expect: very smooth bias fields require less precise spatial estimates of the biases while less smooth bias fields require more precise spatial estimates.

[25] Preaggregated and postaggregated inversion results both provide significant NEE corrections but postaggregated results provide larger improvements in estimation than preaggregated results. This is investigated by plotting an example based upon the spatial patterns shown in Figure 2. First, an inversion is run at a 100 km resolution and the results are statistically combined to 1200 km resolution. Then the various carbon fluxes are summed up across a 100 km grid to a 1200 km grid and the inversion is run at the 1200 km grid resolution. The results are shown in Figure 5. It is clear that postaggregation is preferable [*Kaminski et al.*, 2001; *Engelen et al.*, 2002]. If one reviews the differences in the estimates, it becomes clear that they often do not appear in the grid cell that contains the CO2 observing tower, or necessarily in completely unconstrained grid cells. The largest errors appear to coincide with locations where steep sampling gradients (i.e., the upwind sampling crossing primarily a corner of the grid cell) intersect with fairly significant and heterogeneous fluxes at the 100 km scale, the scale of the fine-scale inversion. This manifests itself as

a type of "halo" effect around the combined sampling footprint of the towers.

[26] Figure 6 shows the "contraction" of the cumulative NEE integrated over the entire domain from the a priori cumulative flux to the posterior cumulative flux, centered around the assumed true cumulative NEE. The a priori NEE is the same for all the inversions while the posterior NEE distribution is based upon the example inversion given previously in Figure 2. The posterior cumulative flux estimates are much closer to the truth, displaying significantly less variability. Furthermore, the a priori spatially integrated cumulative fluxes appear to show a reasonable range of possible deviations, ±3PgC per year, from the a priori assumed mean zero annual NEE balance of SiB3, representing the potential to encompass many realistic source/sink scenarios.

4. Conclusions

[27] The results of this paper show that NEE predictions can be significantly improved when large-scale spatial bias patterns exist in the GPP and RESP estimates. Predictions are improved across a range of possible spatial decorrelation length scales. Furthermore, and most importantly, these relatively large-scale postaggregated fluxes are robust to significant small-scale spatial noise that may exist in the flux biases at resolutions that are commonly used for regional inversion studies.

[28] One might have predicted that the inversion would be influenced heavily by small-scale variability in a few grid cells surrounding the towers where the CO_2 observations were made. However, even when only 33% of the overall variability is on the larger scales, improvements of greater than 40% (RMSE) can be made. Furthermore, the estimates get more accurate as the region of interest gets larger. In general, this is not true of eddy-covariance-based flux tower measurements which often capture the effect of a small flux footprint (a few km). These measurements may not be very representative of surrounding fluxes, even those in close proximity to the tower and shows the value of collecting and analyzing CO_2 mixing ratio measurements.

[29] The results also show the continued importance of running inversions at the finest scale available and this confirms the analysis made by [*Kaminski et al.*, 2001]. Preaggregated and postaggregated inversion styles both show robustness to small-scale spatial variability in the flux biases. However, it is clear that preaggregation severely diminishes the quality of the corrections to NEE. In particular, there should be a focus on improving the accuracy of inversions in areas with steep sampling gradients and heterogeneous fluxes.

[30] There are several components of a standard regional inversion which are not addressed in this paper because of the nature of the hypothesis and result. For example, the choice of temporal averaging time for observations is not necessarily needed for this paper but needs investigation in an applied regional inversion. Boundary inflow of CO2 also plays a critical role in regional inversions but is not needed for this paper. These will be investigated and included in an upcoming paper which focuses upon GPP/RESP/NEE prediction in 2004 for North America.

[31] **Acknowledgments.** This research was funded by NOAA contract NA17RJ1228 and by Department of Energy grant DE-FG02-02ER63474. We wish to thank the North American Carbon Program and the Office of Science as well as the Numerical Terradynamics Simulation Group (NTSG) at University of Montana for providing the FPAR/LAI data that was used in this paper. I would like to thank the other authors as well as my Ph.D. committee members whose comments strengthened the paper, i.e., Scott Denning, Niall Hanan, Stephen Ogle, and Jennifer Hoeting, all of Colorado State University. Although not directly used in this paper, we thank the following tower PIs whose work and data provided motivation for this paper, WLEF (Arlyn Andrews, NOAA GMD), ARM at Great Plains (Sebastien Biraud), LBNL at Harvard Forest (William Munger, Harvard University, Argyle), ME (Arlyn Andrews, NOAA GMD), WKWT at Moody, Texas (Arlyn Andrews, NOAA GMD), Fraserdale (Douglas Worthy, MSC), Western Peatland (Larry Flanagan, University of Lethbridge), and BERMS at Candle Lake (Douglas Worthy, MSC). Additionally, I would like to thank the reviewers for many helpful comments and useful suggestions for improving this manuscript.

References

Baker, D. F., S. C. Doney, and D. S. Schimel (2006), Variational data assimilation for atmospheric CO_2, *Tellus B*, *58*, 359–365.

Baker, I., A. S. Denning, N. Hanan, L. Prihodko, M. Uliasz, P. Vidale, K. Davis, and P. Bakwin (2003), Simulated and observed fluxes of sensible and latent heat and CO_2 at the WLEF-TW tower using Sib 2.5, *Global Change Biol.*, *9*, 1262–1277, doi:10.1046/j.1365-2486.2003.00671.x.

Carouge, C., P. Bousquet, P. Peylin, P. J. Rayner, and P. Ciais (2008a), What can we learn from European continuous atmospheric CO_2 measurements to quantify regional fluxes—Part 1: Potential of the network, *Atmos. Chem. Phys. Discuss.*, *8*, 18,591–18,620.

Carouge, C., P. Peylin, P. J. Rayner, P. Bousquet, F. Chevallier, and P. Ciais (2008b), What can we learn from European continuous atmospheric CO_2 measurements to quantify regional fluxes—Part 2: Sensitivity of flux accuracy to inverse setup, *Atmos. Chem. Phys. Discuss.*, *8*, 18,621–18,649.

Collatz, G. J., J. T. Ball, C. Grivet, and J. A. Berry (1991), Physiological and environmental regulation of stomatal conductance, photosynthesis, and transpiration: A model that includes a laminar boundary layer, *Agric. For. Meteorol.*, *54*, 107–136, doi:10.1016/0168-1923(91)90002-8.

Collatz, G. J., M. Ribas-Carbo, and J. A. Berry (1992), Coupled photosythesis-stomatal conductance model for leaves of C4 plants, *Aust. J. Plant Physiol.*, *19*, 519–538.

Cressie, N. (1993), *Statistics for Spatial Data*, Wiley, New York.

Dai, Y., et al. (2003), The common land model (CLM), *Bull. Am. Meteorol. Soc.*, *84*, 1013–1023, doi:10.1175/BAMS-84-8-1013.

Denning, A. S., J. G. Collatz, C. Zhang, D. A. Randall, J. A. Berry, P. J. Sellers, G. D. Colello, and D. A. Dazlich (1996), Simulations of terrestrial carbon metabolism and atmospheric CO_2 in a general circulation model. Part 1: Surface carbon fluxes, *Tellus B*, *48*, 521–542.

Denning, A. S., M. Nicholls, L. Prihodko, I. Baker, P. Vidale, K. Davis, and P. Bakwin (2003), Simulated variations in atmospheric CO_2 over a Wisconsin forest using a couple ecosystem-atmosphere model, *Global Change Biol.*, *9*, 1241–1250, doi:10.1046/j.1365-2486.2003.00613.x.

Desai, A. R., P. V. Bolstad, B. D. Cook, K. J. Davis, and E. V. Carey (2005), Comparing net ecosystem exchange of carbon dioxide between an old-growth and mature forest in the upper Midwest, USA, *Agric. For. Meteorol.*, *128*, 33–55, doi:10.1016/j.agrformet.2004.09.005.

Engelen, R. J., A. S. Denning, and K. R. Gurney (2002), On error estimation in atmospheric CO_2 inversions, *J. Geophys. Res.*, *107*(D22), 4635, doi:10.1029/2002JD002195.

Enting, I., C. Trudinger, and R. Francey (1994), A synthesis inversion of the concentration and d13C of atmospheric CO_2, *Tellus B*, *47*, 35–52.

Evensen, G. (1994), Sequential data assimilation with a nonlinear quasi-geostrophic model using Monte Carlo methods to forecast error statistics, *J. Geophys. Res.*, *99*, 143–162.

Fan, S., M. Gloor, J. Mahlman, S. Pacala, J. Sarmiento, T. Takahashi, and P. Tans (1998), A large terrestrial carbon sink in North America implied by atmospheric and oceanic carbon dioxide data and models, *Science*, *282*, 442–446.

Farquhar, G. D., S. V. Caemmerer, and J. A. Berry (1980), A biochemical model of photosynthetic CO_2 fixation in the leaves of C3 species, *Planta*, *149*, 78–90, doi:10.1007/BF00386231.

Gerbig, C., J. C. Lin, S. C. Wofsy, A. E. Andrews, B. C. Daube, K. J. Davis, and C. A. Grainger (2003), Toward constraining regional-scale fluxes of CO_2 with atmospheric observations over a continent: 2. Analysis of COBRA data using a receptor-oriented framework, *J. Geophys. Res.*, *108*(D24), 4757, doi:10.1029/2003JD003770.

Gurney, K. R., et al. (2002), Towards robust regional estimates of CO_2 sources and sinks using atmospheric transport models, *Nature*, *415*, 626–630, doi:10.1038/415626a.

Hanan, N. P., J. A. Berry, S. B. Verma, E. A. Walter-Shea, A. E. Suyker, G. G. Burba, and A. S. Denning (2005), Testing a model of CO_2, water and energy exhcnage in Great Plains tallgrass prairie and wheat ecosystems, *Agric. For. Meteorol.*, *131*, 162–179.

Johnson, R. A., and D. W. Wichern (1988), *Applied Multivariate Statistical Analysis*, Prentice Hall, Englewood Cliffs, N. J.

Kaminski, T., P. J. Rayner, M. Heimann, and I. G. Enting (2001), On aggregation errors in atmospheric transport inversions, *J. Geophys. Res.*, *106*, 4703–4715, doi:10.1029/2000JD900581.

Lauvaux, T., M. Uliasz, C. Sarrat, F. Chevallier, P. Bousquet, C. Lac, K. J. Davis, P. Ciais, A. S. Denning, and P. J. Rayner (2008), Mesoscale inversion: First results from the CERES campaign with synthetic data, *Atmos. Chem. Phys.*, *8*, 3459–3471.

Law, B. E., O. J. Sun, J. Campbell, S. V. Tuyl, and P. E. Thornton (2003), Changes in carbon storage and fluxes in a chronosequence of ponderosa pine, *Global Change Biol.*, *9*, 510–524, doi:10.1046/j.1365-2486.2003.00624.x.

Michalak, A. M., L. Bruhwiler, and P. P. Tans (2004), A geostatistical approach to surface flux estimation of atmospheric trace gases, *J. Geophys. Res.*, *109*, D14109, doi:10.1029/2003JD004422.

Mu, Q., F. A. Heinsch, M. Zhao, and S. W. Running (2007), Development of a global evapotranspiration algorithm based on MODIS and global meteorology data, *Remote Sens. Environ.*, *111*, 519–536, doi:10.1016/j.rse.2007.04.015.

Nicholls, M. E., A. S. Denning, L. Prihodko, P. Vidale, K. Davis, and P. Bakwin (2004), A multiple-scale simulation of variations in atmospheric carbon dioxide using a coupled biosphere-atmospheric model, *J. Geophys. Res.*, *109*, D18117, doi:10.1029/2003JD004482.

Peters, W., J. B. Miller, J. Whitaker, A. S. Denning, A. Hirsch, M. C. Krol, D. Zupanski, L. Bruhwiler, and P. P. Tans (2005), An ensemble data assimilation system to estimate CO_2 surface fluxes from atmospheric trace gas observations, *J. Geophys. Res.*, *110*, D24304, doi:10.1029/2005JD006157.

Peters, W., et al. (2007), An atmospheric perspective on North American carbon dioxide exchange: Carbon Tracker, *Proc. Natl. Acad. Sci. U. S. A.*, *104*, 18,925–18,930, doi:10.1073/pnas.0708986104.

Peylin, P., et al. (2005), Daily CO_2 flux estimates over Europe from continuous atmospheric measurements: Part 1, Inverse methodology, *Atmos. Chem. Phys.*, *5*, 3173–3186.

Randall, D. A., et al. (1996), A revised land-surface parameterization (SiB2) for atmospheric GCMs. Part 3: The greening of the CSU General Circulation Model, *J. Clim.*, *9*, 738–763, doi:10.1175/1520-0442(1996)009<0738:ARLSPF>2.0.CO;2.

Rodenbeck, C., S. Houweling, M. Gloor, and M. Heimann (2003), CO_2 flux history 1982–2001 inferred from atmospheric data using a global inversion of atmospheric transport, *Atmos. Chem. Phys.*, *3*, 1919–1964.

Sellers, P. J., Y. Mintz, Y. C. Sud, and A. Dalcher (1986), A simple biosphere model (SiB) for use within general circulation models, *J. Atmos. Sci.*, *43*, 505–531, doi:10.1175/1520-0469(1986)043<0505:ASBMFU>2.0.CO;2.

Sellers, P. J., D. A. Randall, G. J. Collatz, J. A. Berry, C. B. Field, D. A. Dazlich, C. Zhang, G. D. Collelo, and L. Bounoua (1996), A revised land surface parameterization (SiB2) for atmospheric GCMs. Part I: Model formulation, *J. Clim.*, *9*, 676–705, doi:10.1175/1520-0442(1996)009<0676:ARLSPF>2.0.CO;2.

Suits, N. S., A. S. Denning, J. A. Berry, C. J. Still, J. Kaduk, J. B. Miller, and I. T. Baker (2005), Simulation of carbon isotope discrimination of the terrestrial biosphere, *Global Biogeochem. Cycles*, *19*, GB1017, doi:10.1029/2003GB002141.

Thornton, P. E., et al. (2002), Modeling and measuring the effects of disturbance history and climate on carbon and water budgets in evergreen needleleaf forests, *Agric. For. Meteorol.*, *113*, 185–222, doi:10.1016/S0168-1923(02)00108-9.

Uliasz, M., and R. A. Pielke (1991), Application of the receptor oriented approach in mesoscale dispersion modeling, in *Air Pollution Modeling and its Applications VIII*, edited by H. Van Dop and D. G. Steyn, pp. 399–408, Plenum, New York.

Vidale, P. L., and R. Stockli (2005), Prognostic canopy air space solutions for land surface exchanges, *Theor. Appl. Climatol.*, *80*, 245–257, doi:10.1007/s00704-004-0103-2.

Wang, J. W., A. S. Denning, L. Lu, I. T. Baker, and K. D. Corbin (2006), Observations and simulations of synoptic, regional, and local variations in atmospheric CO_2, *J. Geophys. Res.*, *112*, D04108, doi:10.1029/2006JD007410.

Zupanski, D., A. S. Denning, M. Uliasz, M. Zupanski, A. E. Schuh, P. J. Rayner, W. Peters, and K. D. Corbin (2007), Carbon flux bias estimation employing Maximum Likelihood Ensemble Filter (MLEF), *J. Geophys. Res.*, *112*, D17107, doi:10.1029/2006JD008371.

K. D. Corbin, A. S. Denning, A. E. Schuh, and M. Uliasz, Graduate Degree Program in Ecology, Department of Atmospheric Science, Colorado State University, 1371 Campus Delivery, Fort Collins, CO 80523-1371, USA. (aschuh@atmos.colostate.edu)

Biogeosciences, 7, 1625–1644, 2010
www.biogeosciences.net/7/1625/2010/
doi:10.5194/bg-7-1625-2010

Biogeosciences

A regional high-resolution carbon flux inversion of North America for 2004

A. E. Schuh[1], A. S. Denning[1], K. D. Corbin[1,*], I. T. Baker[1], M. Uliasz[1], N. Parazoo[1], A. E. Andrews[2], and D. E. J. Worthy[3]

[1]Colorado State University, Fort Collins, Colorado, USA
[2]National Oceanic and Atmospheric Administration Earth System Research Laboratory, 325 Broadway R/GMD1, Boulder, CO 80305, USA
[3]Environment Canada, 4905 Dufferin Street, Toronto, Ontario, Canada
[*]now at: CSIRO Marine and Atmospheric Research Aspendale, VIC, Aspendale, Australia

Received: 9 July 2009 – Published in Biogeosciences Discuss.: 2 November 2009
Revised: 21 April 2010 – Accepted: 23 April 2010 – Published: 20 May 2010

Abstract. Resolving the discrepancies between NEE estimates based upon (1) ground studies and (2) atmospheric inversion results, demands increasingly sophisticated techniques. In this paper we present a high-resolution inversion based upon a regional meteorology model (RAMS) and an underlying biosphere (SiB3) model, both running on an identical 40 km grid over most of North America. Current operational systems like CarbonTracker as well as many previous global inversions including the Transcom suite of inversions have utilized inversion regions formed by collapsing biome-similar grid cells into larger aggregated regions. An extreme example of this might be where corrections to NEE imposed on forested regions on the east coast of the United States might be the same as that imposed on forests on the west coast of the United States while, in reality, there likely exist subtle differences in the two areas, both natural and anthropogenic. Our current inversion framework utilizes a combination of previously employed inversion techniques while allowing carbon flux corrections to be biome independent. Temporally and spatially high-resolution results utilizing biome-independent corrections provide insight into carbon dynamics in North America. In particular, we analyze hourly CO_2 mixing ratio data from a sparse network of eight towers in North America for 2004. A prior estimate of carbon fluxes due to Gross Primary Productivity (GPP) and Ecosystem Respiration (ER) is constructed from the SiB3 biosphere model on a 40 km grid. A combination of transport from the RAMS and the Parameterized Chemical Transport Model (PCTM) models is used to forge a connection between upwind biosphere fluxes and downwind observed CO_2 mixing ratio data. A Kalman filter procedure is used to estimate weekly corrections to biosphere fluxes based upon observed CO_2. RMSE-weighted annual NEE estimates, over an ensemble of potential inversion parameter sets, show a mean estimate 0.57 Pg/yr sink in North America. We perform the inversion with two independently derived boundary inflow conditions and calculate jackknife-based statistics to test the robustness of the model results. We then compare final results to estimates obtained from the CarbonTracker inversion system and at the Southern Great Plains flux site. Results are promising, showing the ability to correct carbon fluxes from the biosphere models over annual and seasonal time scales, as well as over the different GPP and ER components. Additionally, the correlation of an estimated sink of carbon in the South Central United States with regional anomalously high precipitation in an area of managed agricultural and forest lands provides interesting hypotheses for future work.

Correspondence to: A. E. Schuh
(aschuh@atmos.colostate.edu)

1 Introduction

Carbon dioxide inversion studies have generally been focused on improved estimation of terrestrial carbon fluxes such as Ecosystem Respiration (ER), Gross Primary Production (GPP), and Net Ecosystem Exchange (NEE) as a means to better understand the carbon cycle of the earth. Researchers have progressively increased the resolution, in both time and space, and accuracy of the carbon flux estimates

over the past decade. Early inversion studies were focused primarily with finding an explanation for the missing sink of carbon that can be easily identified from calculating a budget from annual fossil fuel emissions to the atmosphere, the effect of land use changes, and the oceanic carbon sink and comparing it to annual records of increasing atmospheric carbon dioxide concentrations. Given that the sink often represents a third of the annual fossil fuel emissions, it is of great interest to scientists and policy makers alike. Inversion results have been very effective at identifying large defining features of the terrestrial portion of the carbon sink (Fan et al., 1998; Gurney et al., 2002) although much debate remains even at extremely large scales (Stephens et al., 2007). However, the debate on a global scale has not deterred researchers from focusing these techniques on finer scale problems. In fact, criticism has been aimed at large scale global inversions because of the fact that their estimates can be biased on finer regional scales (Kaminski et al., 2001). The data available for regional inversion studies is increasing rapidly year after year, primarily within the developed industrial nations of the Northern Hemisphere. This provides researchers with some of the first opportunities to perform inversion studies in a very high-resolution setting.

Gerbig et al. (2003) provided the first major regional inversion paper. They used a receptor-oriented inversion approach to investigate a series of flights from the CO_2 Budget and Rectification Airborne (COBRA) study conducted in 2000. Results showed that the effect of biosphere carbon fluxes could be seen at altitude in mixed layer CO_2 observed by aircraft. The paper pointed out several areas for future improvements in regional inverse modeling including improving biosphere-atmosphere exchange and convective transport modeling. Peylin et al. (2005) followed this with a regional inversion based on western Europe in which he estimated daily fluxes for a month using relatively continuous measurements of CO_2 from towers in the inversion domain. The most similar effort made for North America comes from the ongoing CarbonTracker project (Peters et al., 2007). Peters et al. (2007) used a nested transport structure (TM5) with a relatively high-resolution 1-degree inner grid over North America. A priori carbon fluxes were estimated by modifying 1-degree by 1-degree monthly output from the Carnegie Ames Stanford Approach (CASA) model to provide diurnal variability by incorporating a Q_{10} temperature relationship for respiration and a linear scaling of GPP with solar radiance. NEE estimates were optimized by estimating linear correction factors for NEE for each of up to 19 ecoregion-based (Olsen et al., 1992) sub-areas of North America based upon a 5-week smoothing window. The coarseness of the inversion over North America is required in order to regularize the inversion problem in light of limited observations.

Our inversion framework has drawn upon certain techniques from previous inversions while including some new features. The aim of the inversion is to provide fine scale inversion results over North America for 2004. A novel feature of this inversion is the distinct estimation of GPP and ER instead of just NEE, which to our knowledge has not previously been performed, at least in the regional framework. We have drawn upon the spatial correlation constraints used by Rödenbeck et al. (2003) and Michalak et al. (2004), largely in order to regularize the inversion problem. We are largely using the spatial correlation in the prior error covariance structure to regularize the problem. Attempts were made to estimate the spatial correlation via the measurements but the data was not constraining enough. Future alternatives that might be possible would be to estimate parameters via a prior flux model as in Mueller et al. (2008) or Gourdji et al. (2008). However, it has been shown in practice that certain isotropic spatial error correlations can work well as a regularization agent. Carouge et al. (2008a, b) investigated the potential of a 10 tower network of CO_2 observing towers over Europe using a 50 km resolution grid over Europe. They found that 10 days temporal and 1000 km spatial averaging was required in order to obtain good agreement between estimate and "true" fluxes. Surprisingly, they found that these isotropic assumptions on the spatial errors performed better than an estimate of the spatial errors based on the "physical errors", those that could be calculated by knowing the "true" fluxes.

Large matrix inversions limited the inversion grid resolution to approximately 10 000 km^2 (60×36 grid composed of 100 km by 100 km grid cells). For sensitivity studies involving numerous inversion runs, a 40 000 km^2 grid (30×18 grid composed of 200 km by 200 km grid cells) is used. Many previous global inversions have been performed upon grid areas of around 5 to 10 times that size. In order to provide some contrast, CarbonTracker optimizes 17 bias correction factors for NEE over North America (with 4 of those representing less than 0.5% of the land area each) while this inversion typically optimizes 30×18=540 each (30×18 grid mentioned above) for ER and GPP. It is important to note that the employment of a spatial correlation constraint and decorrelation length scale, either due to a formal statistical model, or as a method of regularization, does reduce the effective degrees of freedom so that we certainly do not expect the optimization of 540 "independent" parameters. Nevertheless, it is important to note that Schuh et al. (2009) showed how biases can occur when using a relatively coarse fixed set of regions within an atmospheric inversion as opposed to a finer set of regions, even when assuming spatial-scale patterns of carbon flux on the order of 500 km and greater. The flexibility we have achieved by avoiding fixed inversion regions does not come without a cost since we cannot simultaneously optimize fluxes outside of North America. Therefore we used offline-derived boundary conditions and provided these as fixed contributions to the tower CO_2 budget.

Schuh et al. (2009) showed that considerable success could be achieved in estimating large spatial scale ER and GPP signals in the midst of small spatial scale variability in fluxes. We leveraged this result and put the problem in a Kalman

filter framework in order to allow higher resolution spatial estimation. This filter is of a somewhat simple variety and allowed us to work with all portions of the inversion, such as complete prior and posterior covariance matrices, explicitly. We then tested sensitivity to a number of pieces of the inversion considered uncertain, including parameters in the actual inversion as well as fixed contributions to the modeled CO_2 such as fossil fuel and boundary inflow. As far as we know this is also the first paper providing a comparison of inversion results derived by using two independent boundary inflow estimates. Additionally, the effect of including recently available high-resolution fossil fuel inventory data is quantified.

2 Methods

2.1 Prior flux model and transport

The Simple Biosphere model (SiB) is based on a land-surface parameterization scheme originally used to compute biophysical exchanges in climate models (Sellers et al., 1986), but later adapted to include ecosystem metabolism (Sellers et al., 1996a; Denning et al., 1996a). SiB has been coupled to the Brazilian version of the Regional Atmospheric Modeling System (RAMS; Pielke et al., 1992; Frietas et al., 2006) and used to study PBL-scale interactions among carbon fluxes, turbulence, and CO_2 mixing ratio (Denning et al., 2003) and regional-scale controls on CO_2 variations (Nicholls et al., 2004; Wang et al., 2006). This latest version of SiB is termed SiB3.

In SiB3, Net Ecosystem Exchange (NEE) is composed of two component fluxes, Gross Primary Productivity (GPP) and Ecosystem Respiration (ER), which includes autotrophic (canopy respiration and root respiration) and heterotrophic respiration terms (due to decomposition of dead organic matter),

$$\mathrm{NEE}(x,y,t) = \mathrm{ER}(x,y,t) - \mathrm{GPP}(x,y,t) \quad (1)$$

where x and y represent grid coordinates and t represents time. High-frequency time variations of photosynthesis and respiration are assumed to be well understood and easily modeled processes, i.e. due to diurnally varying quantities such as radiation, temperature, or longer term variations in modeled quantities such as soil moisture etc. Photosynthesis and assimilation are derived using a coupling of equations based upon the work of Farquhar, Collatz, and Ball (Farquhar et al., 1980; Collatz et al., 1992; Ball et al., 1987) while soil respiration is based upon a rather simple function of temperature and soil moisture and constrained in such a way that annual NEE is equal to zero (Raich et al., 1991; Denning et al., 1996).

Several papers have provided comparisons of models to observations, largely by using eddy flux towers to measure true fluxes of water, carbon, and energy (Baker et al., 2003, 2008; Hanan et al., 2005). Longer-term, more persistent biases are estimated by solving for unknown multiplicative biases in each component flux after smoothing in space and time. While these biases could result from incorrectly modeled short term processes, such as errors in the daily development of the planetary boundary layer, or short-term processes not in the model such as seasonal fertilization and irrigation, the main purpose is to capture longer-term processes not explicitly modeled such as land use change (Robertson et al., 2000; Peterson et al., 1998), disturbances, anthropogenic fertilization effects (Oren et al., 2001), managed forestry (Tillman et al., 2000), and large scale carbon removal (Ciais et al., 2007). This modeling is accomplished by convolving the *influence* functions generated from a lagrangian particle dispersion model, LPDM (Uliasz and Pielke, 1991; Uliasz, 1993, 1994; Uliasz et al., 1996; Zupanski, 2007), with gridded Gross Primary Productivity (GPP) and total Ecosystem Respiration (ER) at each time step in SiB3-RAMS. The LPDM transport scheme reverses advection derived from RAMS at very fine time scales and parameterizes vertical turbulent diffusion according to a Gaussian process. A large advantage of this model is the ability to simulate transport of atmospheric constituents at sub grid scales, reducing representation error that might be caused by associating an observing tower with a 40 km grid cell in the model. By tracking particles upwind, backward in time, from the towers, one may make inferences about the contribution of upstream GPP and ER sources.

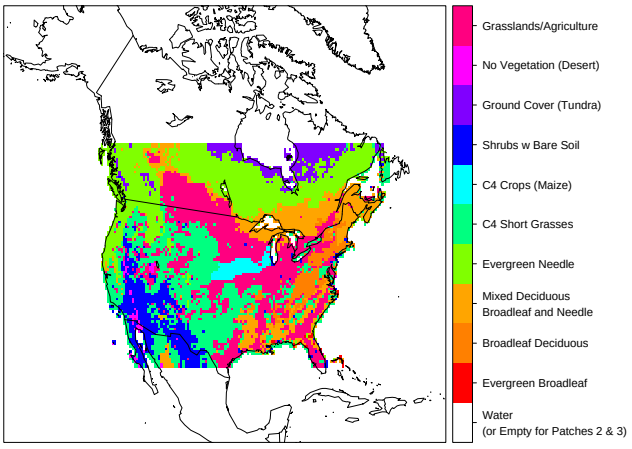

Fig. 1. Dominant SiB3 biome classes for the first biome patch derived from MODIS 12 Landcover product.

In particular, we have estimated regional fluxes from atmospheric mixing ratios by assuming that the model of the component fluxes is biased, and that the biases are smoother in time and space than the fluxes themselves:

$$\mathrm{NEE}(x,y,t) = (1+\beta_{\mathrm{RESP}}(x,y))\,\mathrm{ER}(x,y,t) - (1+\beta_{\mathrm{GPP}}(x,y))\,\mathrm{GPP}(x,y,t) \quad (2)$$

The model domain, shown in Fig. 1, consists of most of the United States as well as a large portion of Canada and the

northern portions of Mexico. Both SiB3 and RAMS were run on a single 150×90 grid of 40 km cells, with SiB3 utilizing 3 patches per cell to capture subgrid-scale variability in land cover. RAMS meteorology was nudged with 40 km forecast meteorology from the National Center for Environmental Protection's Eta model throughout the domain using a 4 Dimensional Data Assimilation (4DDA) scheme to produce more reliable wind fields. Soil classes were calculated from 5 min "%clay/% sand/% silt" soil data from the International Geosphere-Biosphere Programme (IGBP). Biomes were extracted from the UMD classification scheme of the MODIS 12 Landcover 1 km product and mapped to the most similar SiB biome class for all cells and for each of the three patches used. An exception are the C_4 vegetation classes, grasses and crops, which were projected onto the MODIS biomes from (Wang et al., 2006). The crop characterization is admittedly simple and more work is currently being done to incorporate more accurate crop maps and more realistic crop modeling into SiB (Lokupitiya et al., 2009). SiB has traditionally calculated fPAR, which defines the fraction of photosynthetically available radiation that is absorbed by the plant canopy, and Leaf Area Index (LAI) using satellite derived NDVI fields. The code was changed to use fPAR and LAI fields derived by the Moderate Resolution Imaging Spectroradiometer (MODIS) (Mu et al., 2007) and averaged over appropriate biome-areas based upon the three patch scheme. SiB3 was run with these 8-day fPAR and LAI products that were provided by the Numerical Terradynamics Simulation Group at the University of Montana who generated it for use in constructing the official Moderate Resolution Imaging Spectroradiometer GPP product.

Modeled carbon dioxide at the tower is calculated as the sum of 3 component fluxes convoluted by *time* and *tower* dependent transport.

$$\mathrm{CO_2}(\text{time, tower}) = \tag{3}$$
$$\mathrm{Transport}_{\text{time, tower}}\begin{pmatrix}\text{Boundary Inflow } (x,y,\text{time})\\ +\text{ Fossil Fuel } (x,y,\text{time})\\ +\text{ Domain Biogenic Fluxes } (x,y,\text{time})\end{pmatrix}$$

The boundary inflow component was calculated by convolving the influence functions from the LPDM model over boundary CO_2 fields derived using a global biosphere-transport model. At any point in time, the boundary inflow is the average of all upstream particles located in a 3 dimensional 40 km thick rectangular "ring" around the domain. CO_2 resulting from the transport of fossil fuels to the towers is calculated by convolving the influence functions from the LPDM model with surface fossil fuel flux estimates. In particular, the boundary CO_2 fields were calculated by combining transport from the Parameterized Chemistry Transport Model (PCTM) (Kawa et al., 2004; Parazoo, 2007) and pre-calculated archived hourly SiB3 fluxes (Baker et al., 2007) on a 1.25-degree by 1-degree global grid. The model was spun up for 2000–2004 and the CO_2 was centered around the Northern Hemispheric mean CO_2 for 2004. In addition to this, results from the CarbonTracker project, which provide globally optimized CO_2 concentration fields, are used for comparison purposes.

Fossil fuel fields were constructed using recently available high resolution Vulcan fossil fuel inventory fields (Gurney et al., 2008), at a 10 km horizontal spatial scale and hourly temporal scale. Previously available fossil fuel flux fields were derived by distributing country-level fossil fuel sources spatially as a function of population at a 1-degree resolution (Andres et al., 1995). The Vulcan fields provide many improvements including the incorporation of mobile emission sources and power plants, often located in areas distant from high density population centers, increased temporal resolution allowing the modeling of diurnal variability, and increased spatial resolution allowing better delineation of high density population centers. The sensitivity to the new fossil fuel fields is tested by running inversions using both the Vulcan fields as well as the Andres et al. (1995) fields.

The effect of this on boundary inflow estimates is that the PCTM-SiB3 calculated boundary CO_2 fields lacks the effect of sources or sinks in 2004. Given the consensus opinion of an annual mean sink for carbon resulting from the biosphere, this means that the CO_2 fields used will be biased somewhat by the effect of not including this expected global sink. We investigate the effect of this by including a comparison of the inversion using CarbonTracker optimized CO_2 concentration fields for boundary inflow, which includes the effects estimated sources/sinks outside of the regional modeling domain. As of this time, carbon dioxide resulting from forest fires is not included in the global PCTM-SiB3 inflow or domain SiB3 runs, but is included in the CarbonTracker inflow providing one more contrast between the two fields.

2.2 Observational data

Half-hourly averaged calibrated CO_2 observations were provided for eight measuring sites (WLEF, Harvard Forest; Urbanski et al., 2007; ARM, BERMS, Fraserdale, Western Peatland, WKWT, and Argyle – ME) for 2004 (Parazoo, 2007). Gerbig et al. (2003) found mean standard deviations on the order of 0.6 to 1 ppm when viewing morning and afternoon vertical profiles of CO_2 in the mixed layer. As a consequence, robust afternoon snapshot observations, at 12, 2, 4, and 6 p.m. LT, are used in order to avoid inversion model sensitivity to poor atmospheric transport modeling of extremely stable and stratified nocturnal atmospheric conditions near the ground. One exception is the WKWT tower in Moody, TX. For most days, data at this tower consistently showed high CO_2 concentrations in the 12 p.m. LT records that were more consistent with typical morning CO_2 than with well-mixed afternoon CO_2. For this tower, mixed boundary layer conditions appeared to be better represented by snapshot observations shifted by 2 h: 2, 4, 6, and 8 p.m. LT. The first 10 days of the year are not comparable due to a lack of transport preceding 2004. In all there were 2433 missing

observations, resulting in 4 (observations/day) × 8 (towers) × 355 (days) − 2433 (missing) = 8927 observations.

In a previous pseudo-data inversion using a very similar model (Zupanski et al., 2007), the errors on the observations were assumed to be 1 ppm for afternoon observations. Nevertheless, relative to the inversion techniques presented in the next section, the errors on these observations should include errors due to calibration error, mapping error, transport error, and representation error. For this inversion, transport error and representation error are likely the largest components which are notoriously tricky to quantify. Investigations into the sensitivity of inversion test results combined with initial maximum likelihood estimation results suggest errors in the range of 5–6 ppm are appropriate for this particular inversion. For the remaining inversions, the errors are assumed to be identical and independently distributed (i.i.d.) mean zero errors with standard deviation set to 5.5 ppm. This is a simple assumption and we certainly do not expect to the error to be completely homogeneous across towers although at what scale the observation error should be estimated is still somewhat uncertain. We also note that there certainly is expected to be autocorrelation in the errors within a daily time frame so that the "effective" number of observations is likely much less than 4 each day. The end result is that the observational error term over multiple observations is probably estimated as being somewhat lower than reality. For example, a mean of 4 afternoon observations has an estimated 2.75 ppm error, based on Gaussian 5.5 ppm independent errors for each observation. In reality, the error of the mean observation is probably larger due to likely temporal correlation in the observation errors.

2.3 Climatic conditions for 2004

The 2004 year was the 6th wettest in the contiguous United States over the preceeding 110 years (1894–2004). It was also warmer than on average. Nevertheless, there was a great amount of variability in precipitation and temperature as a function of location and season. Drought continued in the west through the summer of 2004, essentially prolonging a multi-year period of drought conditions. The spring was also very dry for the southeast, extending a period of dry conditions from late in 2003. However, summer brought increased precipitation to the east and southeast, culminating in enormous amounts of rain in late summer and early fall due to an extremely active hurricane season. The south (Texas, Louisiana, Mississippi, Arkansas, Oklahoma, and Kansas) had the wettest summer on record and was much cooler than average. These conditions were important as they provided initial conditions for SiB3 that involved soil moisture induced plant stress over large areas of the United States.

2.4 Inversion technique

Standard multivariate Gaussian assumptions are made and data are assimilated using a modified Kalman Filter algorithm (Kalman, 1960). In particular, for an initial length n CO_2 measurement vector $\boldsymbol{y}$ representing the first set of measurements, length m unknown CO_2 flux bias vector $\boldsymbol{\beta}$ (dimensionless), $n \times n$ observation error covariance matrix Σ (ppm^2), $n \times m$ Jacobian flux-transport matrix $\mathbf{G}$ (ppm), length m prior flux bias estimate $\boldsymbol{\beta}_0$ (dimensionless), and $m \times m$ model-prior mismatch covariance matrix Σ_0 (dimensionless), the Bayesian statistical assumptions are a Gaussian distribution on the "measurement" errors as well as a Gaussian distribution on the a priori distribution of $\boldsymbol{\beta}$, i.e.:

$$\boldsymbol{y}|\boldsymbol{\beta},\ \Sigma \sim N(\mathbf{G}\boldsymbol{\beta},\ \Sigma) \tag{4}$$

$$\boldsymbol{\beta} \sim N(\boldsymbol{\beta}_0,\ \Sigma_0)$$

The posterior distribution of the flux bias vector can be solved for analytically and is:

$$p(\boldsymbol{\beta}|\boldsymbol{y},\ \Sigma) \propto -\frac{1}{2} \tag{5}$$
$$\left[(\mathbf{G}\boldsymbol{\beta}-\boldsymbol{y})^T\Sigma^{-1}(\mathbf{G}\boldsymbol{\beta}-\boldsymbol{y}) + (\boldsymbol{\beta}-\boldsymbol{\beta}_0)^T\Sigma_0^{-1}(\boldsymbol{\beta}-\boldsymbol{\beta}_0)\right]$$
$$\sim N\left(\left(\Sigma_0^{-1}+\mathbf{G}^T\Sigma^{-1}\mathbf{G}\right)^{-1}\left(\Sigma_0^{-1}\boldsymbol{\beta}_0+\mathbf{G}^T\Sigma^{-1}\boldsymbol{y}\right),\right.$$
$$\left.\left(\left(\Sigma_0^{-1}+\mathbf{G}^T\Sigma^{-1}\mathbf{G}\right)\right)^{-1}\right)$$

With a little bit of algebra, one can rewrite the mean of the posterior distribution of the mean, giving the Kalman-filter updating equation for the mean.

$$E[\boldsymbol{\beta}] = \boldsymbol{\beta}_0 + \left(\mathbf{G}^T\Sigma^{-1}\mathbf{G} + \Sigma_0^{-1}\right)\mathbf{G}^T\Sigma^{-1}(\boldsymbol{y}-\mathbf{G}\boldsymbol{\beta}_0) \tag{6}$$

The posterior mean and variance of $\boldsymbol{x}$ are then fed into the next filter step with a new set of measurements. This particular inversion estimates biases over 7-day periods using available data from that 7-day period of time. Therefore, bias estimates for both ecosystem respiration and GPP as well as corresponding variance estimates are available for all of 2004 with the bias estimates changing with a weekly resolution.

Two difficulties often arise when using filter-style correction schemes. The filter estimates can drift away from realistic values if the data are not plentiful or precise enough to constrain it. Secondly, the nature of the Kalman filter at each step is to create posterior variance estimates that are in general smaller than the prior estimates. This can essentially cause the filter to get "stuck", when an explicit dynamical model of the biases is not available, and thus produce unrealistically small posterior variance estimates around the biases. There is generally no easy solution to this problem. Artificially inflating the posterior variance at each filter step is one method in which one can try to circumvent (Zupanski et al., 2007). This accommodates the fact the biases are likely to

change in reality and it allows the filter to consider a wider range of possibilities for the bias factors. However, it does not necessarily constrain the biases to any particular "reasonable" region of values allowing the bias estimates to drift into unrealistic parameter space. Therefore, we have chosen to weight the filter at each step with a "grand" prior. This effectively handles both of the preceding problems. With respect to our inversion, there will be three pieces of information at each step, the grand prior which is derived from the forward SiB3-RAMS model with an error assumption, the local prior which is derived from the previous filter step's posterior flux bias distribution, and the data which forms the statistical likelihood function. In some sense, this new piece of the covariance structure provides a bound upon how much the inversion can "learn" about the bias structure.

In order to quantify, we denote the grand prior as a multivariate Gaussian distribution around $\boldsymbol{\beta}_{\text{grand}}$ with covariance matrix $\sigma^2_{\text{grand}}\Sigma_{\text{grand}}$, and additional weight factor w, and we rewrite the expression given in Eq. (4) as:

$$p(\boldsymbol{\beta}|\boldsymbol{y},\ \Sigma) \propto -\frac{1}{2}\Big[(\mathbf{G}\beta-\boldsymbol{y})^T\sigma_{\text{obs}}^{-2}I(\mathbf{G}\beta-\boldsymbol{y}) + (\boldsymbol{\beta}-\boldsymbol{\beta}_0)^T\sigma_0^{-2}\Sigma_0^{-1}(\boldsymbol{\beta}-\boldsymbol{\beta}_0) + (\boldsymbol{\beta}-\boldsymbol{\beta}_{\text{grand}})^T \times w\sigma_{\text{grand}}^{-2}\Sigma_{\text{grand}}^{-1}(\boldsymbol{\beta}-\boldsymbol{\beta}_{\text{grand}})\Big] \tag{7}$$

Thus $\boldsymbol{\beta}$ is distributed as a multivariate Gaussian with parameters:

$$\begin{aligned}&\text{Mean}(\boldsymbol{\beta}) = E[\boldsymbol{\beta}] \\ &= \left(w^{-1}\sigma_{\text{grand}}^{-2}\Sigma_{\text{grand}}^{-1} + \sigma_0^{-2}\Sigma_0^{-1} + \mathbf{G}^T\sigma_{\text{obs}}^{-2}\mathbf{IG}\right)^{-1} \\ &\times \left(w\sigma_{\text{grand}}^{-2}\Sigma_{\text{grand}}^{-1}\boldsymbol{\beta}_{\text{grand}} + \sigma_0^{-2}\Sigma_0^{-1}\boldsymbol{\beta}_0 + \mathbf{G}^T\sigma_{\text{obs}}^{-2}\mathbf{I}\boldsymbol{y}\right) \\ &\text{Variance}(\boldsymbol{\beta}) = E[\boldsymbol{\beta}^2] - (E[\boldsymbol{\beta}])^2 \\ &= \left(\left(w\sigma_{\text{grand}}^{-2}\Sigma_{\text{grand}}^{-1} + \sigma_0^{-2}\Sigma_0^{-1} + \mathbf{G}^T\sigma_{\text{obs}}^{-2}\mathbf{IG}\right)\right)^{-1}\end{aligned} \tag{8}$$

Equation (7) specifically separates out the variance scalars, σ^2_{grand}, σ_0^2, and σ^2_{obs} from the covariance matrices, leaving the covariance matrices essentially scaled to 1. The w weight is a redundant factor and is simply included to facilitate easier interpretation of tightening/loosening of the grand prior covariance (around the SiB3 derived a priori carbon fluxes). Unless otherwise specified, this weight, w, on the grand covariance matrix is set to 2. This means that the initial variance around the grand prior is increased, thus providing a weaker constraint. For the initial filter step, only the grand prior is used. After that point, there exist both a grand prior and a prior (from the posterior of the previous filter step). The inversion is further constrained by the assumption of spatially correlated errors in the grand prior, i.e. the covariance matrix Σ_{grand} will take on the following form.

$$\Sigma_{\text{grand}} = \begin{bmatrix} \Sigma_{\text{Respg, prior}} & 0 \\ 0 & \Sigma_{\text{Assimn, prior}} \end{bmatrix} \tag{9}$$

The respiration and GPP covariance matrices are each formed from the exponential covariance function, where $t_{i,j}$ is the distance between points β_i and β_j.

$$\text{Cov}(\beta_i,\ \beta_j) = \begin{cases} \sigma_0^2(1-\alpha_0)\ \exp\left(\frac{-t_{i,j}}{h_0}\right), i \neq j \\ \alpha_0\sigma_0^2,\ i = j \end{cases} \tag{10}$$

The h_0 parameter is the decorrelation length scale parameter, giving the distance at which the covariance between two points is equal to $\sigma_0^2(1-\alpha_0)e^{-1}$. The σ^2 parameter is the scalar variance parameter and determines the variance of the marginal distribution of the particular flux component. The parameter α_0 controls what percentage of the covariance can be attributed to spatial covariance, as opposed to spatially independent errors, often termed "nugget" variance. While the "nugget" parameter is an important parameter if one is fitting a rigorous statistical spatial model to the errors, for regularization purposes it is often set to zero which is what we will do for the remainder of the paper.

It is important to note that the use of a high resolution grid for the inversion certainly does not imply that meaningful inferences can be made at the finest scale. Assumed decorrelation length scales of 500 km and greater certainly imply a strong constraint upon the solution effectively giving somewhat smoothed solutions spatially. For example, while 540 parameters are used spatially, there are only 8 towers providing information at any point in time (assuming no missing data) and those are only afternoon observations. In effect, if the wind is coming from N.W. portion of the domain to all the towers, then the inversion can only learn about the N. W. portion of the domain and only within the confines of the differences in upstream sampling footprints and the differences in the observed CO_2 at the towers. For example, based upon a 1000 km decorrelation length scale smoothing scheme with a two week assimilation cycle, the effective degrees of freedom of the data used in the paper might only be between 2 and 7, with the E dimension being estimate between 15 and 30 (Park and Xu, 2009). This can be visualized by noticing the scale of the corrections in many of the figures in the paper.

It was shown in Schuh et al. (2009), that under isotropic error type conditions (for assumed and "true" errors) that this inversion model is robust to small spatial scale random deviations in flux bias and that post-aggregated (in space) estimates can be very good even when using a fairly sparse network of towers observing CO_2. The usefulness of the high resolution grid allows one to separate the impact of a tower residual across space more effectively. For example, if a tower only saw a corner of a somewhat large inversion region than the correction imposed on that corner is essentially projected onto the entire inversion region. This essentially arises from a lack of uniform sampling over every inversion "grid cell". The effect of this potential error is of course dependent upon the "actual" structure of the errors which is not often known. Nevertheless, regardless of whether one

chooses to assume isotropic error conditions through a spatial smoothing such as ours, or larger inversion regions similar to Peters et al. (2007), given the unconstrained nature of the inversion problem, it is always important to assess the impact of varying certain unknown parameters in the inversion, such as the choice of inversion regions: grid vs biome, localization schemes, the spatial decorrelation length scales, the weight given to the "grand" prior, and the fixed CO_2 contributions from both the boundary inflow and fossil fuel sources.

2.5 Sensitivity

The inversion essentially guarantees some improvement in prediction of observed CO_2 (Eq. 5). However, when using a regression style approach in a heavily unconstrained environment, this improvement can often be overstated because of the great freedom the inversion has to fit the data. Therefore, it is often desirable to go beyond simply comparing observed carbon dioxide at the towers to model-based predicted carbon dioxide. Comparing model observations to independent observations not used in the inversion, comparing models which predict similar quantities, as well as testing the sensitivity of the model to variations in unknown parameters are all methods of generating more confidence in estimates.

We used a variety of different procedures to test the sensitivity of the inversion. Therefore, we first test the sensitivity of the inversion to varying the inflow of CO_2 at the boundaries. To do this, we derive boundary inflow to the 8 towers using the LPDM model and optimized carbon dioxide concentration fields from the CarbonTracker project (Peters et al., 2007). Inversion results are then compared with the results derived from the LPDM model and the PCTM inflow. Secondly, we vary several different variance parameters and derive annual domain-summed NEE and tower observation based RMSE based upon the varied parameters. Thirdly, we use a re-sampling procedure in which we create 45 different observation data subsets by holding out a randomly selected 50% of the observation data for each. Each set of data is run through the weekly inversion scheme and the sensitivity of the predicted CO_2 at the towers and the estimated flux biases is explored. This provides estimates of the variability of the flux correction factors and can be used to assess the sensitivity of the source/sink to the constraint provided by the data. Using the held out data as independent evaluation data and the complementing data as training data for the inversion, one may also derive a more accurate estimate of Root Mean-Squared Error (RMSE) of the inversion-optimized fluxes. We test the impact of the high resolution Vulcan fossil fuel inventory on the inversion results by comparing inversion results relying upon Vulcan to those results utilizing the Andres et al. (1995) fossil fuel inventory.

SiB3 has been evaluated at many sites and over many time periods, nevertheless, the particular model run used for the a priori flux estimates was not optimized to fit the flux data at any site in particular. Even though there is a mismatch in representation, with the flux towers representing footprints of less than a square kilometer and the inversion results representing flux estimates on the scale of thousands of square kilometers, we believe that these comparisons are of value, especially in locations that are more spatially homogeneous than others, such as grasslands and large forest reaches. This is then the fourth comparison we make.

3 Results

As was indicated in the previous section, there are a number of variables that the inversion will likely be sensitive to and therefore the results are expected to be quite variable. For results, we choose to present one particular case with a fixed set of inversion inputs as an initial case study and then use it to compare the effect of varying the boundary inflow and the source of the domain fossil fuel fluxes. With reference to the preceding section and Eq. (7) in particular, the following values are used for these inversions: σ_{grand}=0.25, σ_0=0.25, σ_{obs}=5.5 ppm, w=2, h_0=1000 km. In particular, a value of σ_{grand}=0.25 would mean that we expect that approximately 68% of the GPP and ER biases are within ±25% of the original SiB3 estimated fluxes, with 95% within ±50%. This variation when combined with positive spatial correlations was shown to provide a reasonable a priori range of annual domain-summed NEE. These deviations must generally be kept to less than 30–40% to ensure that posterior ER and GPP fluxes are not reduced by more than 100%, which makes no conceptual sense. We then test the sensitivity of the results over a number of varying inversion inputs using the PCTM boundary conditions and the Vulcan fossil fuel flux field.

3.1 General structure of results

CO_2 can be predicted by invoking the relationship shown in Eq. (3). The predicted mean observed CO_2 is derived as $\mathbf{G}\hat{x}$ where $\hat{x}$ represents one (for the prior fluxes) plus the inversion-optimized flux biases. Using the PCTM boundary conditions and the Vulcan fossil fuel inventory, a comparison of the inversion-corrected posterior predictions at the towers to the observations is shown in Fig. 2. For domain-summed temporal plots, NEE is calculated via Eq. (2) while ER and GPP are calculated via the two respective summands on right hand side of that equation. These domain-summed temporal results are shown in Fig. 3.

The observed carbon dioxide concentrations contain information that infers a dampening of the a priori annual GPP cycle, and hence the a priori annual ER cycle (due to the strong correlation of the annual sums of each). Since both GPP and ER are significantly dampened, it is not surprising that the NEE signal is dampened as well. Furthermore, the data suggest a weak temporal shift in the prior NEE signal. This manifests itself as a stronger, but more gradual onset

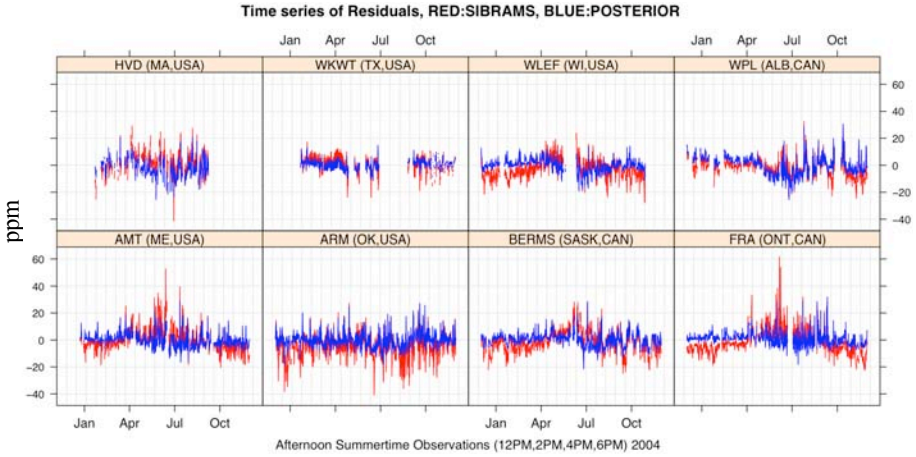

Fig. 2. Time series plots of carbon dioxide residuals based upon SiBRAMS prior (red) and inversion posterior (blue) (observations – model).

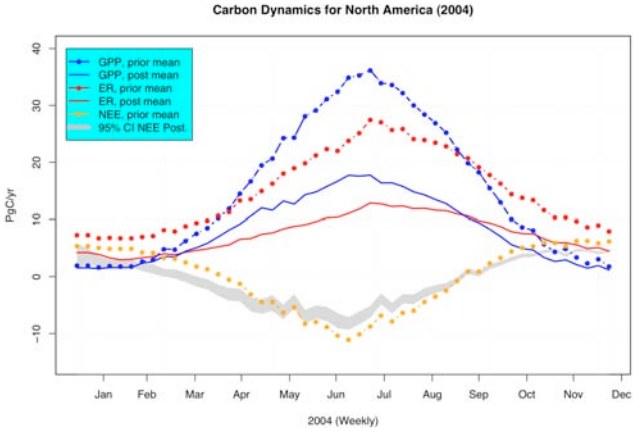

Fig. 3. Plots of prior and posterior estimates for GPP, ER, and NEE. Results are shown for a single inversion while the confidence intervals are derived from an ensemble of 45 inversions.

of spring, followed by a weaker overall carbon sink over the middle and late summer periods. It was brought to our attention by Steve Wofsy (Harvard U.) that this discrepancy in a priori and a posteriori GPP and respiration fluxes could arise from a bias in the meteorological data that was driving SiB3 to produce the a priori fluxes, in particular biases in shortwave radiation. Upon investigation and comparison of several different reanalysis products to recently available Ameriflux radiation observations, it does appear that nearly all of the reanalysis products investigated had somewhat uniformly, and far from insignificant, positive biases in shortwave radiation. This certainly could play a role in the a priori GPP and respiration fluxes being significantly larger than they should be. This is currently being investigated under the guise of the North American Carbon Program (NACP) by Daniel Riccuito (Oak Ridge National Laboratory), and a manuscript is currently in preparation describing further the differences found between observations and reanalysis products and the possible effect on biospheric carbon flux estimates. Nevertheless, this is an a priori estimate of fluxes, and although we certainly would like it to be close to the posterior estimate, it simply represents the best knowledge we currently have about the processes.

We use the resampling procedure, that was first mentioned in Sect. 2.5, to account for variability that might be associated with over fitting the model and which provides additional variability to the standard covariance estimates of the biases given in Eq. (6). Forty-five different inversions are run, each based upon a different subsample of the observations. Assuming temporal independence of the errors in the filter, one may simulate properties of the annual NEE probability density functions (pdf) for each of these 45 inversions by using the posterior covariance provided at each step of the Kalman Filter for each inversion. A 95% Confidence Interval (CI) for the entire domain can be calculated at each step of the filter for each of the 45 inversions. The CI shown in Fig. 3 then characterizes variability in the NEE by selecting the 95% CI of each set of 95% CIs for each weekly time step.

The ensemble mean of the domain summed annual NEE flux is approximately -0.68 Pg/yr while the standard deviation of this estimate is about 0.11 Pg/yr. It is important to note that this standard deviation estimate does appear to be too small, giving tighter bounds on the flux than found in other inversion papers (Gurney et al., 2002; Peters et al., 2007). An additional source of variability in the estimate is discussed later (Sect. 3.4) and likely provides another 0.1–0.15 Pg/yr to this standard deviation estimate. The spatial representation of these sources and sinks can be seen in the first panel of Fig. 7. Depictions of this variability in a spatial framework are shown in Fig. 4. This variability is partitioned into two pieces, variability associated with the spread of mean estimates over the 45 inversions (measure of over fitting) and variability associated with summing up the posterior variances at each filter step (regular KF variance)

Table 1. Biases in Tower CO_2 partitioned by season.

Tower	Winter.Prior.Bias	Winter.Posterior.Bias	Summer.Prior.Bias	Summer.Posterior.Bias
AMT (ME,USA)	−3.87	−1.03	8.10	2.10
ARM (OK,USA)	−4.40	0.14	−3.81	0.17
BERM (SASK,CAN)	−5.09	−0.92	8.07	3.88
FRA (ONT,CAN)	−6.99	−1.31	9.68	3.92
HVD (MA,USA)	−0.52	−0.49	4.74	−0.09
WKWT (TX,USA)	0.86	0.35	0.30	1.11
WLEF (WI,USA)	−5.15	0.33	3.47	0.88
WPL (ALB,CAN)	−3.76	0.54	2.89	0.69

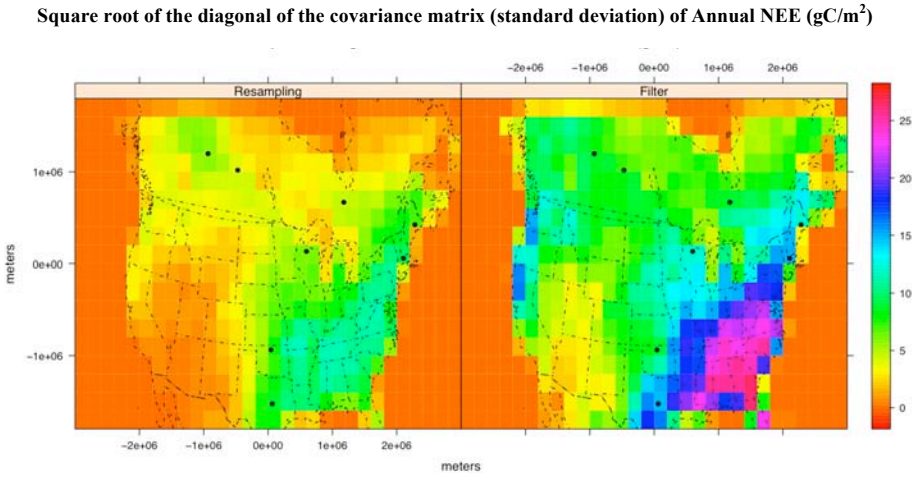

Fig. 4. Uncertainty in annual NEE. The left panel is the result of running 100 inversions each using a randomly selected 50% of the data and then calculating the variance of each cell's mean estimate, over the 100 inversions, and summing over each of the weekly filter cycles. Finally, the square root of this summed variance (standard deviation) is displayed and is a measure of the uncertainty of the mean estimate due to model over-fitting. For the right panel, the summed annual variance in NEE is calculated for each inversion, from the weekly filter estimates, and the the square root of this (standard deviation) is shown for each cell. These plots aim to provide a measure of the uncertainty of each cell's NEE estimate, incorporating the correlation between ER and GPP in each cell, but not incorporating the spatial correlation in the covariance matrices.

evaluated over all 45 inversions. Besides the spatial display of posterior variance information for NEE, which roughly tracks the convolution of the sampling footprint of the network and the prior ER/GPP signals, the results show that over fitting the model may provide a significant source of variability comparable to that which is normally constructed from each filter step's posterior covariance matrix.

The residuals from the model fit are generally symmetric and do not appear to deviate substantially from normality (Fig. 5). There is a slight but pronounced positive skew to the residuals indicating that when the residuals deviate most strongly from zero, the observed CO_2 is greater than the modeled CO_2. Biases remain in the inversion process, likely a result of residual pdfs' deviations from symmetry. Sites in the north and northeastern portion of the domain appear to be most sensitive to this, in particular AMT and Harvard Forest (Table 1). These sites seem to be affected more by a strong a priori seasonal cycle than the other sites. Additionally, we note that the these towers are in relatively close proximity to the most populated areas of North America and it is possible that occasional spikes in anthropogenic emissions from the northeast coast of the United States could impact tower concentrations. Weekly chi-square statistics were calculated to diagnose the model's performance. Values near to one indicate that the assumed errors are being estimated reasonably, a priori. The weekly chi-square innovation statistics are generally near 0.5 from January through May and then around 1 for the summer and remainder of year. The innovation statistics show more temporal variability in the summer time. The low value in the winter time in indicative of some heterogeneity in the model-data residuals, seasonally, and that the assumed errors in the winter might be too large. In essence, this might weight the model too heavily towards the prior which might imply that magnitude of the winter time NEE

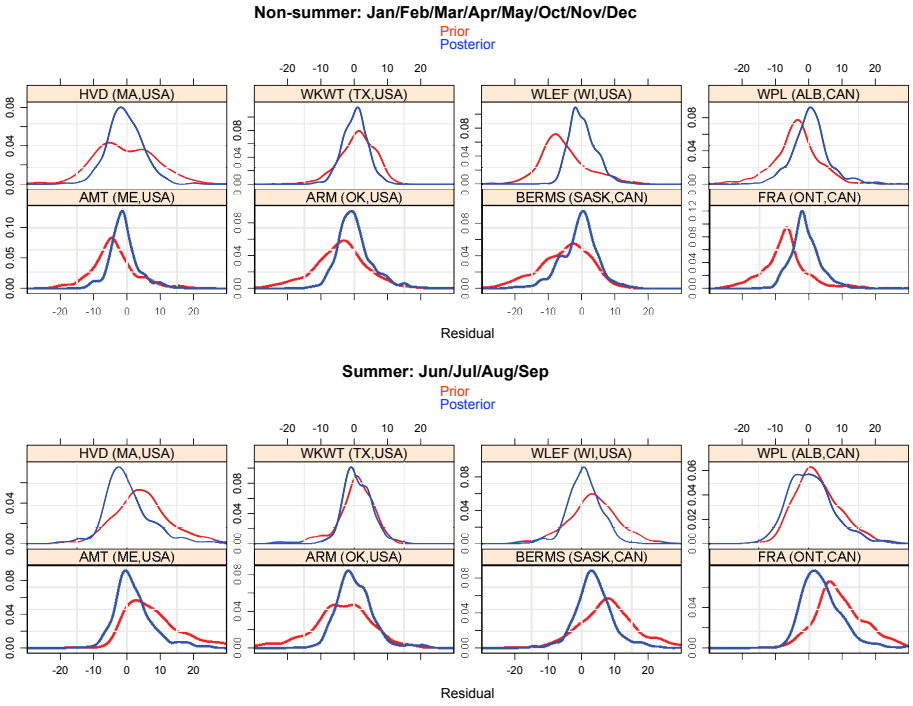

Fig. 5. Estimated probability density functions for modeled CO_2 residuals (observations – model), broken out by season and tower.

adjustment, which is generally a C sink under our a priori flux scenario, might be too weak.

3.2 Sensitivity and robustness of results to inflow

Inflow of CO_2 from the boundaries has typically been a large concern of regional models (Gerbig et al., 2003; Peylin et al., 2005). In extremely limited domain problems, the variance of the CO_2 coming in from the boundary can easily dwarf the changes inside the domain due to local biotic uptake and release. Therefore it is of interest to gauge the sensitivity of the inversion to varying boundary inflows. The boundary conditions included in this model were constructed from a global simulation using SiB3 and PCTM (Parazoo et al., 2007). The CarbonTracker project has provided CO_2 mixing ratio data based upon globally optimized fluxes (Peters et al., 2007). SiB3 has no annual source/sinks whereas CarbonTracker includes an annual source/sink estimated from observations of CO_2. A plot of the difference between the two inflows is shown in Fig. 6. The inflow annual mean and temporal pattern is very similar for PCTM and CarbonTracker with the main difference being a seasonally stronger cycle in the PCTM-SiB3 results, likely a result of the underlying biosphere model, SiB3, providing a stronger seasonal GPP/NEE signal than the corresponding CASA model used in CarbonTracker. In addition to running comparison inversions between these two CO_2 inflow estimates, we also run the inversion with a fixed inflow estimate of 378 ppm representing the annually averaged PCTM inflow over the period of the simulation in order to show the necessity of reasonable boundary inflow values in calculating source/sink estimates.

Figure 7 shows a comparison plot of maps of the annual mean NEE estimate based upon CarbonTracker (w/CASA), PCTM (w/SiB3), and the fixed inflow condition. The results are similar for the CarbonTracker and PCTM inflows. Both results have similar spatial and temporal characteristics but differ mainly in magnitude. The PCTM-based inversion results in a sink of 0.1–0.2 Pg/yr more than that of the CarbonTracker-based result. The PCTM-based boundary conditions do not account for the expected global carbon sink outside of the inversion domain, which forces the inversion to increase the North American sink to compensate. This results in the PCTM-inflow based inversion having a larger annual sink estimate than the CT-inflow based inversion. The sink estimated with the PCTM inflow was 0.65 Pg/yr while the sink estimated with the CarbonTracker inflow was estimated at 0.48 Pg/yr. It does seem somewhat surprising that the results from the two inflows are still close, within approximately 30% of one another. This indicates that local observations may be affected significantly more by local fluxes than by larger scale fluxes in distant locations outside of the model boundary.

3.3 Sensitivity of results to fossil fuel inventory

Until the release of the Vulcan fossil fuel inventory in 2008, most researchers were reliant upon the Andres et al. (1995) fossil fuel inventory, which was released at annual time

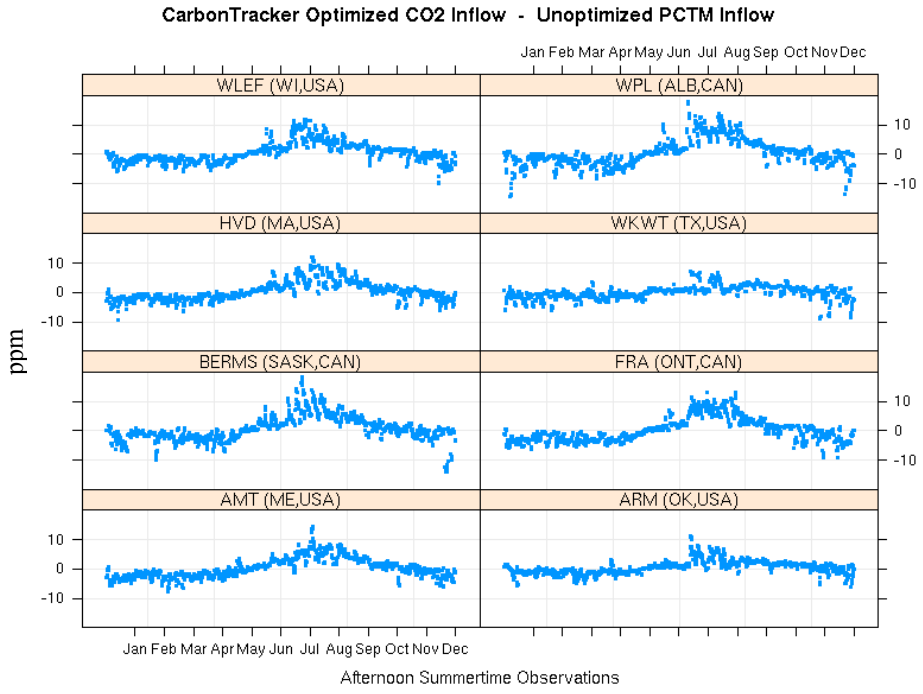

Fig. 6. Figure shows the effect of boundary inflow CO_2 upon tower CO_2 concentrations. In particular, this figure shows the "difference" between estimates of CO_2 arriving at tower due to two distinct boundary inflows (1420 sequential "12/2/4/6 p.m." observation sequences for each of 8 towers).

scales and at a 1-degree resolution over the globe. For many large-scale inversion applications, this inventory is adequate. However, for higher resolution studies within the United States, the Vulcan fossil fuel inventory provides a dramatic improvement in both space and time accounting of fossil fuel fluxes. The main difference between these inventories is the redistribution of some fossil fuel sources from population centers to more distant locations representing mobile sources and power plants. The Vulcan fossil fuel flux estimates are at a much higher resolution in both time and space. Previous inversions had to grapple with the fact that some observing stations are located within enormous fossil fuel flux regions. For example, a semi-rural location like Harvard Forest would very likely be located in the same grid cell as the large metropolitan city of Boston. Given no sub-annual temporal resolution to the fossil fuel fluxes, an observing tower located at Harvard Forest was often seeing a 24 h continuous stream of fossil fuel fluxes arising from a city over 100 km away. However, the 10 km horizontal resolution of the Vulcan inventory allows these to be separated and additionally provides a diurnal and seasonal estimate of these fluxes, which is important for inversions based upon hourly observations.

In order to gauge the impact of incorporating the Vulcan data, we first contrasted the contributions to each of the 8 towers from each of the inventories. For many of the stations, the afternoon differences between the two were very small. Differences at the ARM site in Oklahoma, the WLEF site in Wisconsin, the Canadian sites, and the Argyle, Maine site were on the order of a few ppm. Differences at the Moody, Texas tower were in the range of -5 to 5 ppm. While the differences across most towers were relatively small, the differences at Harvard Forest were between -25 and 30 ppm!

The difference in the annual NEE estimate is shown in Fig. 8. The effect on the inversion is far from trivial with differences of up to 150 g/m^2 per year recorded along the northeast coast of the United States, similar in magnitude to the maximum annual sinks estimated by the inversion. These differences are a result of coarse fossil fuel flux fields providing artificially high sources of CO_2 to the Harvard Forest tower which must be neutralized via a large local sink.

3.4 Sensitivity and robustness of results to prior variance structure

A test of the sensitivity and effect of the prior upon results is important because of the use of an informative Bayesian prior, that is, a prior flux estimate in which the inversion will likely be sensitive. With reference to Eqs. (5) and (7), the w, σ_0^2, and h_0 parameters are varied and results are shown in Fig. 9. These figures show that results are sensitive to nearly all of these parameters, providing different degrees of RMSE and sink strength depending upon the particular combination. In particular, sink estimates range between 0 and 1 Pg/yr. The ensemble of estimates, over the various possible

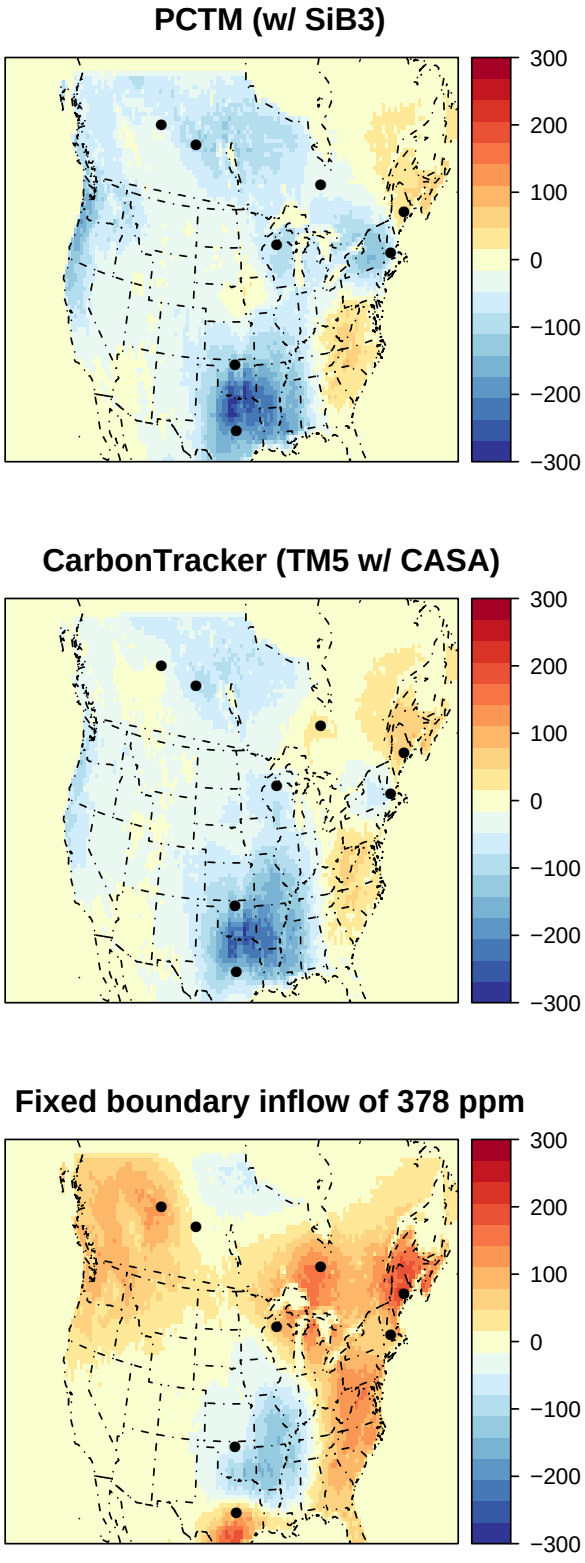

Fig. 7. Inversion estimates for three different inflow scenarios, one without modeled annual source/sink (PCTM w/SiB), one with modeled source/sink (CarbonTracker w/CASA), and a uniform fixed 378 ppm inflow. Negative values denote land uptake of carbon. Summed annual NEE is −0.65, −0.48, and 0.38 PgC/yr, respectively.

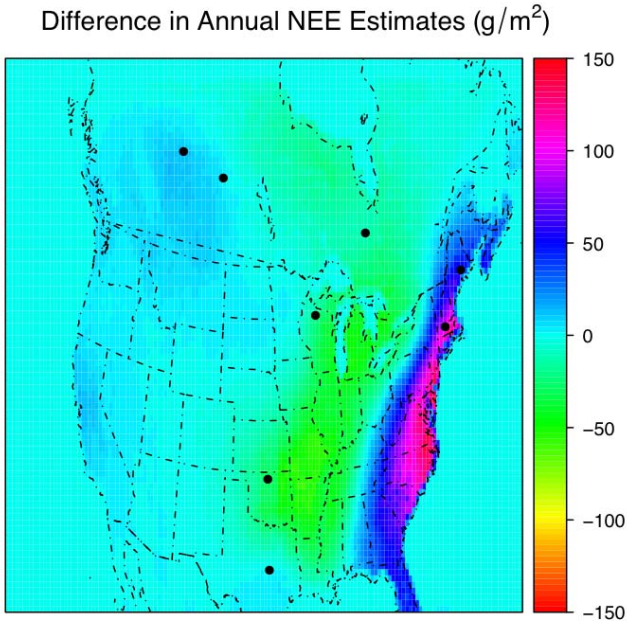

Fig. 8. Difference in annual sink inferred by inversions based upon the Vulcan fossil fuel inventory and the Andres et al. (1995) fossil fuel inventory. Positive values (purple) indicate carbon sinks were stronger using Andres inventory. Spatially-summed annual difference between Vulcan-based NEE estimate for 2004 and Andres (1995) based NEE estimate for 2004 is less than 0.01 PgC.

a priori variance parameters, has a standard deviation of approximately 0.2 PgC/yr. This likely contributes another 0.1 to 0.15 PgC/yr (depending upon the existence of correlation between the variance shown here and earlier variance estimates due to jackknife resampling and the Kalman filter posterior variances) to the initial standard deviation estimate of 0.11 Pg/yr given earlier. This would give an adjusted standard deviation estimate of approximately 0.2–0.25 PgC/yr to the posterior annual NEE estimate shown in Fig. 3.

An RMSE-weighted average of the sink estimates show a sink of 0.57 PgC/yr, 20% higher than our single case scenario that we have followed throughout these results. Values very near the lower left of the plot are somewhat unrealistic since low spatial correlation (h_0) and a low variance on the prior (σ_0^2) will not provide a reasonable enough range around the prior to provide a realistic posterior sink estimate which generally is thought to range between 0 and 1.5 PgC/yr (Schimel et al., 2000; Gurney et al., 2002) inter-annually. Increasing either the variance multiplier (along x-axis) or the spatial decorrelation length scale (along y-axis), or both jointly, increases the error variance around the a priori mean allowing more realistic domain-wide summed posterior flux estimates. Therefore if one "de-weights" these sink estimates occurring in the lower left hand portions of the panels in Fig. 9, the RMSE-weighted sink will likely increase to more than 0.57 PgC/yr.

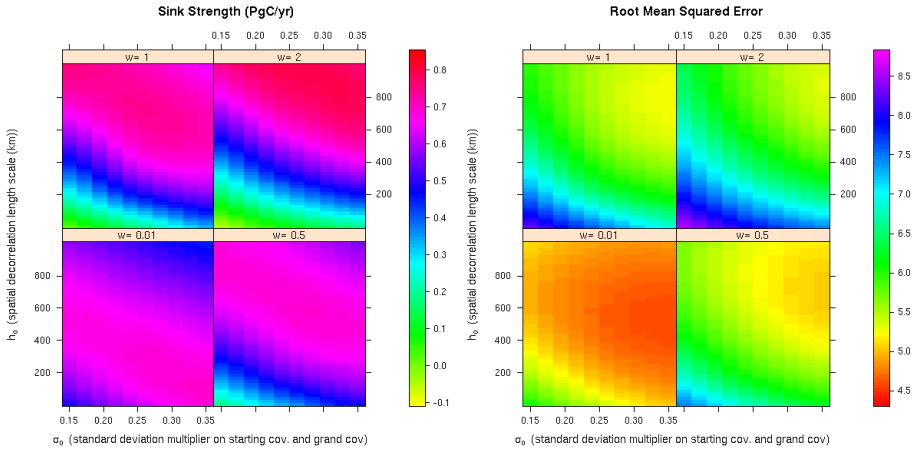

Fig. 9. Sensitivity of **(a)** sink estimate and **(b)** root mean squared error to varying covariance parameters in inversion. For example, a set of parameter values like w=0, h_0=600 km, σ_0=0.35 provides the estimate w/the lowest RMSE (b) and an estimated sink of approximately 0.55 PgC/yr (a). Nevertheless, qualitatively, this represents a maximum departure from the prior and thus must be viewed with some skepticism due to the likelihood of overfitting the data.

The weight of the grand prior (w) has two effects. First, it constrains solutions back towards the prior, essentially anchoring the Kalman filter so that, over time, it does not drift too far from the prior. Given the fact that this grand prior is fixed in time, it also provides a degree of variance inflation (over the regular KF) by providing a lower bound on the prior variance for each filtering step. It is interesting to note that, for cases in which the global prior is weaker (bottom two panels), the maximum sink estimate occurs on the inside of the plot bounds and not at the boundary. The Kalman filter becomes more entrenched without the grand prior since there is no lower limit on the prior variability at each inversion filter step and there is no inflation. Therefore it is likely that the initial reduction in respiration and associated "sink" of carbon in the early months of the year becomes entrenched and leaves a strong sink signature on the rest of the year resulting in the largest sink estimates. We did not test any additional forms of variance inflation on the model and acknowledge that additional efforts are needed to construct more robust filter techniques.

3.5 Comparison to CarbonTracker flux estimates

Given the fact that the majority of the underlying observations supporting the inversion were also used in the CarbonTracker project, one would expect posterior flux estimates to be somewhat similar. One of the most important differences between these inversions and CarbonTracker is the optimization of encompassing global fluxes, which affect CO_2 concentrations within our domain. However, this can be mitigated somewhat by the use of optimized CO_2 concentrations from CarbonTracker in the inversion. Under this scenario, one would expect the inversion results to be similar to CarbonTracker but there are still many differences. As can be seen in Fig. 10, the carbon fluxes in the priors, CASA and SiB3, play an important role in the posterior estimates. The posterior estimates of both inversion models display the signature of the a priori fluxes prominently. These results would lead one to believe that either the data does not provide sufficient constraint or the covariance structure is specified too tightly around the prior.

The results can be aggregated up to SiB biomes (Fig. 1) which are presented in Table 2. The aggregated results show somewhat close agreement with Peters et al. (2007). Because of the differences in land cover classifications between Peters et al. (2007) and the State of the Carbon Cycle Report (SOCCR, 2007), it is difficult to directly compare results. Furthermore, as was shown earlier, the magnitude of the domain-wide annual NEE sink is very sensitive to inflow assumptions although the spatial configuration of the sources and sinks seem much more robust. In this fashion, the proportion of the annual sink due to forests, both conifers and deciduous, ranges between 30% and 37% depending upon inflow choice. This is certainly within the confidence bounds of the estimate given in the SOCCR report as well as very similar to the estimates given in Peters et al. (2007).

One of the most significant contrasts is the placement of the carbon sink on agricultural lands. Peters et al. (2007) shows a large effective sink in the northern Great Plains centered near the state of Iowa where there are very large expanses of corn fields. Our results indicate a strong effective sink in the southern portion of the Great Plains more in the vicinity of large wheat growing operations. Ongoing research in this region of the United States (http://www.nacarbon.org/nacp/mci.html) seems to validate the existence of an effective sink in the northern Great Plains while

Table 2. Total Posterior Net Ecosystem Exchange by Biome (negative indicates "into biosphere").

Biomes	Using CarbonTracker boundary	Using PCTM boundary
Conifers (Evergreen Needle)	−83 TgC	−111 TgC
Mixed Deciduous Broadleaf and Needle, Braodleaf Deciduous, Evergreen Broadleaf	−49 TgC	−124 TgC
Grasslands and Agriculture	−261 TgC	−337 TgC
Shrublands, Desert and Ground Cover	−43 TgC	−54 TgC
Total	−436 TgC	−626 TgC

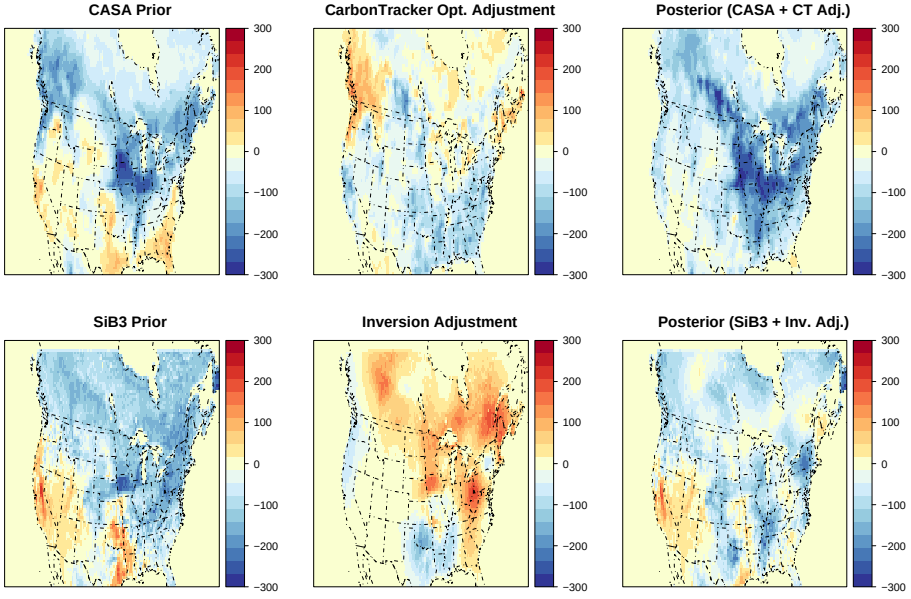

Fig. 10. July-August-September comparison. Top panels concern CarbonTracker and lower panels concern our inversion. Left panels show a priori NEE, middle panels show inversion adjustment, and right panels show a posteriori NEE.

agricultural statistics and other recent work (Riley et al., 2009) seem to validate a possible southern Great Plains effective sink as well.

3.6 Comparison to filled level 4 Ameriflux data at Southern Great Plains

Posterior respiration and GPP estimates from the model can also be compared to Ameriflux level 4 data. As indicated earlier, there is a spatial representation mismatch in doing so due to the fact that the model estimate is an average over approximately 1600 km^2 and the associated flux tower estimate is over a much smaller footprint, likely less than 1 km^2. Nevertheless, some useful comparisons and observations can be made. Figure 11 shows comparisons of the model to the observations for weekly ER and GPP at three Ameriflux sites, which appear in the more observation constrained portion of the model domain. The ARM site is one of the more constrained sites in the domain and lies in a relatively homogenous landscape making it an excellent candidate for analysis. The prior site NEE estimate appears to be improved on average by the posterior flux estimates. In particular, the prior model is corrected significantly in the summer when it predicts significant respiration occurring. Clearly one can see an early spring winter wheat signal in the observations, forming a significant amount of carbon drawdown over an 8–10 week period. SiB3 necessarily balances GPP and ER annually and is thus forced to redistribute this carbon into respiration in other portions of the year. This is the likely reason for displacement of the prior estimate in the summer. The posterior corrects for a large portion of this but the large distance between the prior and observed fluxes make a complete correction difficult. Just as important, but perhaps more subtle, is the fact that the inversion is able to provide significant corrections to ER and GPP separately. SiB3 appears to significantly overestimate GPP. However, due to the annual NEE balance constraint, SiB3 will overestimate ER as well, providing an NEE signal that appears very reasonable. If the forward model is only compared to NEE estimates at various

sites then this fact can be easily overlooked but is likely very important to biosphere dynamics on certain time scales.

3.7 Evaluation of annual NEE source/sinks against ancillary data and hypotheses

Using two sets of boundary conditions, we arrived at a final sink estimate of 0.5–0.7 PgC/yr±0.25 PgC/yr. This is similar in strength to CarbonTracker's sink estimate of 0.69 PgC per year (0.79 PgC/yr "natural" sink minus implicit 0.1 PgC/yr "fire" contribution) and other estimates currently emerging from an ongoing top-down synthesis project. It is clearly possible that other globally based inversions provide more constraint on certain areas of North America, such as the Pacific Northwest forest regions of North America, the Southeastern United States, or extreme Northeast Canada. Both of these areas have large annual GPP signals and are thus capable of being a strong source/sink of CO_2. However, our inversion results show a generous sink in the coastal N. W. forests while CarbonTracker shows little sink there. Furthermore, CarbonTracker's sink is largely located in the agricultural Midwest of the United States (and a portion of Canada), an area reasonably constrained by the observation network we have used.

On the other hand, perhaps the globally based sink estimates are too high. The recently completed SOCCR report provides an inventory-based sink estimate for North America of approximately 0.66 PgC per year (land sink) using a variety of data sources collected over the last ten to fifteen years. Uncertainty is presented as a 95% confidence interval, 0 to 1.32 PgC. This is similar to what we have recovered in these inversions. However, this is a mean sink estimate over many years and 2004 is believed to be a year in which the sink in North America was very strong, likely putting the SOCCR estimate closer to 0.8–0.9 PgC/yr, the upper range of their annual estimates. Stephens et al. (2007) called into question the magnitude of the Northern Hemispheric (and North American) global annual NEE sink which has been a cornerstone of inversion results for the last 10 years (Fan et al., 1998; Gurney et al., 2002; Peters et al., 2007) indicating that it may be much smaller than previously assumed. In any case, the rapid expansion of the calibrated CO_2 tower network (currently over 30 towers in North America) should soon provide significant additional data constraints to researchers performing atmospheric CO_2 based inversions.

The spatial character of the annual NEE estimate has several distinctive features. The most definitive feature of the annual NEE estimate shown in Fig. 7 is the large sink located over Texas, Louisiana, Arkansas, and portions of Oklahoma. This sink is located largely between, and to the east of, the ARM and WKWT sites in south central portion of the domain. At first glance this may appear to be an artifact of incorrect transport, poor boundary conditions, or incorrect fossil fuel emissions specifications. However, summing the ARM NEE observations for the year provides a sink estimate of approximately 275 g/m^2, similar to the estimates the inversion produces to the south of the ARM site (Fig. 7). A likely hypothesis for this sink is the lateral export of crops, primarily winter wheat that draws most of its carbon from the atmosphere in the spring and then is harvested and exported in early summer. The WKWT tower concentrations have proven to be somewhat difficult to model given a number of factors. CO_2 observations at the top of the tower did not appear to be well mixed until well after 12 p.m. LT.

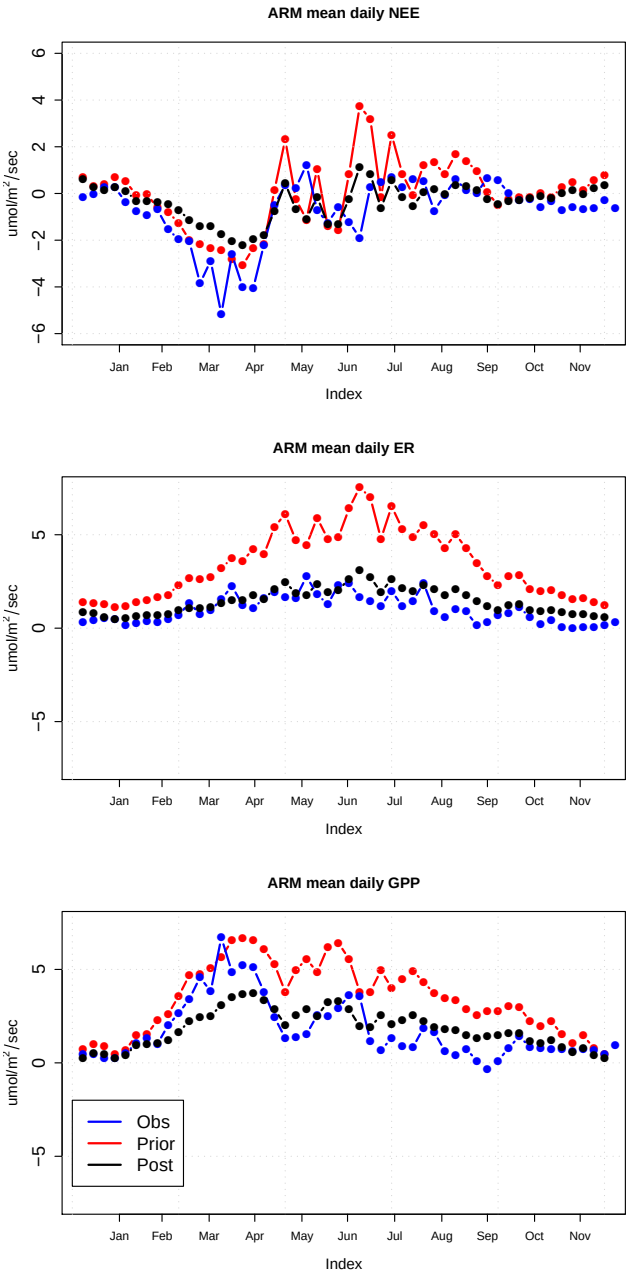

Fig. 11. Comparison of posterior fluxes of GPP, ER, and NEE with Ameriflux Level 4 flux tower data for ARM Site in OK. Pay particular attention to the fact that the y-axes are different scales.

Additionally, the tower is located relatively closely to both the model boundary and the ocean and is in close proximity to fossil fuel sources of major metropolitan areas and oil refining facilities near Houston and Galveston.

The aforementioned sink also extends to the east and northeast of the ARM tower. This is an area of significant crop production, with corn and soybeans being grown extensively in the northern portions while soybeans, rice, and other crops are grown to the south in the Arkansas/Mississippi region. This area is also covered by heavily managed forest regions, which produce large annual harvests of wood primarily for paper pulp. These managed forests are largely composed of very young productive loblolly pine trees providing a major source of carbon sequestration. This area is known for quite variable precipitation patterns and it would seem to reasonable to assume that young productive forests in this area would be very productive under the unusually wet and cool conditions of 2004.

It is interesting to note that the most intensely cultivated portion of the Midwestern United States, centered on the state of Iowa, shows little to no sink. This is an area typically planted extensively with corn, which has been shown to be an extremely effective consumer of atmospheric CO_2. The a priori estimate of NEE based upon SiB3 included a very strong summer time sink of carbon over the Iowa region using a C_4 photosynthesis scheme from Collatz et al. (1992). Lokupitiya et al. (2009) illustrated that a phenology-based model for the fluxes agricultural crops provided flux estimates much closer to those of eddy covariance towers in the region. Additionally, the area of crop production in the a priori model was very crude and did not match the spatial extent of crops, or the mix of different crop types, as given by United States Department of Agricultural maps. The general consensus, as mentioned by Peters et al. (2007), is that this sink occurs over a relatively small intensively farmed area of the country while the agricultural products produced (the effective sink) are distributed out uniformly over the country, effectively spreading out the associated respiration signal. Emerging research from the Mid-Continent Intensive portion of the North American Carbon Program appears to support this hypothesis to some extent (Tris West, personal communication, 2009). Therefore, it is likely that the "missing" sink in this area can be attributed to a poor agricultural crop prior in SiB3 and/or a lack of CO_2 measurements in the vicinity. Although the existence of a sink is widely supported by agricultural crop statistics, the strength of the sink is currently unknown and its estimation is complicated by a number of factors.

First, annual NEE estimates from the corn-planted Bondville, IL Ameriflux site indicate a sink on the order of 500–600 g/m^2. Soybeans can be expected to provide sinks of about half of this. Assuming steady state conditions over several years, these types of sinks can be attributed directly to the harvest. Approximately 20% of the corn harvest and 35% of the soy harvest is exported overseas, mostly for animal feed, while half of the corn and soy retained in the United States is used to feed livestock domestically (National Corn Growers Association website: http://www.ncga.com/files/pdf/2009WOC.pdf, Soy Stats, http://www.soystats.com). Most of the carbon in this livestock feed is then returned to the atmosphere as CO_2 and CH_4 at locations where it is consumed by livestock. Almost 70% of the feedlots in the United States are located in just 3 states: Texas, Kansas, and Nebraska (http://www.cattlenetwork.com). This may provide a partial explanation for the lack of an agriculturally-induced sink over Nebraska and Kansas, states with very high crop production and intense livestock operations, and the existence of sinks over portions of Arkansas, Mississippi, Missouri and Illinois, states with relatively high crop production but with significantly less livestock operations. A rapidly evolving ethanol industry in the area further complicates the picture. Currently, this is an area of intense research (http://www.nacarbon.org/nacp/mci.html)and one may expect a much more complete picture to emerge concerning the carbon balance of the Midwest United States within a few years. An important point to keep in mind is that the addition of a carbon sink in the Midwest United States would likely be correlated with weakened sinks (or increased respiration) in other areas of the domain in order to constrain the annual domain wide source/sink estimate.

Forested regions in the northwestern United States and boreal forests of Canada show slight sinks. However, variability estimates surrounding these sink estimates are typically much smaller than the variability estimates of similar sink magnitudes in the Midwest or southeastern United States showing relatively more confidence in the sink despite the lack of proximity to the observing towers. The sink estimate in the northwestern United States is not surprising since the northwestern coastal mountains of California, Oregon and Washington have been intensely managed over the last 50 years and are expected to provide a sink of carbon for many decades into the future (Alig et al., 2006). The estimate for the boreal forest regions appears much harder to objectively evaluate. Most studies have indicated that Canadian ecosystems should currently be a weak sink, although the projection of this weak sink into the future is highly uncertain. The inversion results show a fairly carbon neutral Canada on average, but shows the boreal forests of central Canada and the boreal and coastal forests of western Canada as slight sinks while the agricultural plains of Canada and the forests of eastern Canada provide slight sources. It is interesting to note that areas to the south of the two Canadian towers show an annual source of carbon in an area just to the east of large expansive forest ecosystems of British Columbia that have recently experienced unprecedented bark beetle invasions and tree mortality. It is important to note that forest fires were not included in the SiB3 domain run for the regional inversion. Average carbon emissions from Canadian forest fires were estimated at 27 ± 6 Tg/yr (Amiro et al.,

2001), a non-trivial amount that could increase the strength of the boreal forest sink predicted by the inversion.

4 Conclusions

GPP, ER, and NEE flux corrections implied by this inversion provide posterior annual NEE estimates similar to those provided by a number of independently derived models including CASA (via CarbonTracker optimized) and the MODIS 17 GPP product. NEE estimates for the entire domain appear on the low side of estimates derived from global models, which is understandable given the lack of constraint on some key regions of high annual GPP, and hence potentially high annual NEE. This was corroborated by a comparison to INTEX aircraft data which shows the existence of a deficit in GPP over the southeast which would, when all other things are considered equal, inflate the domain-wide sink closer to levels estimated from global models such as CarbonTracker. Results are relatively sensitive to a number of parameters in the inversion setup, which is also to be expected with an inversion constrained by such a sparse observing network. Using a temporally uniform boundary condition seems to produce a very unrealistic annual sink on the order of 0.38 Pg per year, supporting the notion that regional inversions require realistic boundary inflow of CO_2. However, much to our surprise, we find that two completely independent boundary inflow estimates provide similar results with the main difference being an approximately 30% difference in magnitude. This leads us to believe that, while probably not preferable to optimized global CO_2 fields, the inclusion of annual NEE balanced models (such as SiB3) in global models used to provide boundary inflow estimation does not significantly damage inversions based upon it.

In the course of trying to improve NEE estimates, we were able to find that the inversion was able to provide some degree of correction to the individual summands of NEE, ER and GPP, which are generally highly correlated at many different scales in time and space. Considering that SiB3 currently calculates ER as a relatively simple function of soil moisture and temperature such that annual ER equals annual GPP, the significant adjustment inferred upon GPP may prove to be valuable estimation of other quantities of interest in the biosphere. For example, while photosynthesizing, plants must generally release water to compensate, meaning that artificially high GPP may infer artificially high water exchange with the atmosphere and possibly associated latent heat fluxes.

The agricultural Midwestern United States appears to play a large role in the inversion results, providing a large sink. However, the sink does not correlate exactly with crop productivity, when compared to crop production maps from the United States Department of Agriculture, and several states with significant crop production such as Nebraska, Kansas, and Iowa, appear to be in approximate annual carbon balance. While the magnitude of this difference between carbon neutral states with crops and carbon sink states with crops is likely influenced by the lack of data in the inversion and the general unconstrained nature of the solution at fine scales, the discrimination between them seems likely to stay. One hypothesis proposed is the lateral movement of crops which has been shown to be a major portion of the carbon budget globally (Ciais et al., 2007). The main crops of interest in the domain are wheat, soy and corn. Soy and corn are grown across large expanses of the north-central Midwest and are primarily used to feed livestock. These livestock are typically fed in feedlots in the states of Iowa, Colorado, Nebraska, Kansas, and Texas, generally located to the west and south of the areas of growth and harvest. The end result would be that eastern states within the Midwest would be a sink because of the near complete export of crops grown there. However, states in the western portion of the Midwest would receive the majority of these crops where they would be fed to cattle and other animals, returned to the atmosphere as CO_2 and CH_4 and largely balance any local sinks due to crop production.

Technical considerations concerning the inversion could also affect these results. In particular, a large amount of missing data for the WKWT (Moody, TX) tower leaves the southern boundary inflow unconstrained beyond the normal PCTM inflow. This could result in the inflation of an Oklahoma/Texas sink to account for a positive bias in the inflow at the southern boundary, particularly after 1 July 2004 when the Midwest receives its heaviest influence from the Gulf of Mexico. The WLEF tower was also missing most of its observations for June, a time of intense drawdown for croplands to the south of the site.

In 2004, the southern states of Texas, Oklahoma, Kansas, Louisiana, Arkansas, and Mississippi had an extremely wet summer, potentially mitigating some degree of drought and providing an increase in GPP for the region which includes managed forests, a large percentage of the United States' exported wheat crop, and soybeans and other crops along the lower Mississippi river valley. Additional research is needed to determine if any of these could represent a plausible hypothesis that would result in the net carbon neutrality of large crop growing states in the western portions of the Great Plains and the expansive southern and Mississippi river valley sink predicted by the inversion.

Acknowledgements. I would like to acknowledge several people who provided their calibrated carbon dioxide data to me and without which this paper would not have been possible. A. Andrews (ESRL/National Oceanic and Atmospheric Administration) provided data for the WKWT (Texas, US) and Argyle (Maine, US) towers, M. Fischer/M. Torn provided data for the Southern Great Plains site (Oklahoma, US) in particular Data collection was supported by the Office of Biological and Environmental Research of the US. Department of Energy Contract No. DE-AC02-05CH11231 as part of the Atmospheric Radiation Measurement Program, S. Wofsy/B. Munger provided data for

Harvard Forest site (Massachusetts, US), and D. Worthy provided data for BERMS, Western Peatland, and Fraserdale sites (Canada). I also would like to acknowledge K. Gurney and B. Andres for their contributions of fossil fuel inventory data as well as A. Jacobsen and W. Peters for the Carbon Tracker boundary inflow CO_2 data and N. Parazoo for the PCTM boundary inflow CO_2 data. I would also like to acknowledge Steve Wofsy, Marc Fischer and the two BGD anonymous reviewers for many useful comments. Again, these were all very generous contributions without which, little of this research could have been done.

Edited by: A. Neftel

References

Alig, R. J., Krankina, O., Yost, A., and Kuzminykh, J.: Forest carbon dynamics in the Pacific Northwest (USA) and the St. Petersburg region of Russia: Comparisons and policy implications, Climatic Change, 79, 335–360, 2006.

Amiro, B. D., Todd, J. B., Wotton, B. M., Logan, K. A., Flannigan, M. D., Stocks, B. J., Mason, J. A., Martell, D. L., and Hirsch, K. G.: Direct carbon emissions from Canadian forest fires, 1959–1999, Can. J. Forest Res., 31(3), 512–525, 2001.

Andres, R. J., Marland, G., Fung, I., and Matthews, E.: A $1^\circ \times 1^\circ$ distribution of carbon dioxide emissions from fossil fuel consumption and cement manufacture, 1950–1990, Global Biogeochem. Cy., 10, 419–429, 1996.

Baker, I., Denning, A. S., Hanan, N., Prihodko, L., Uliasz, M., Vidale, P., Davis, K., and Bakwin, P.: Simulated and observed fluxes of sensible and latent heat and CO_2 at the WLEF-TW tower using Sib 2.5, Global Change Biol., 9, 1262–1277, 2003.

Baker, I., Denning, A., Prihodko, L., Schaefer, K., Berry, J., Collatz, G., Suits, N., Stockli, R., Philpott, A., and Leonard, O.: Global Net Ecosystem Exchange (NEE) of CO_2, available online (http://www.daac.ornl.gov), last access: 18 May 2010, from Oak Ridge National Laboratory Distributed Active Archive Center, Oak Ridge, Tennessee, USA, 2007.

Baker, I. T., Prihodko, L., Denning, A. S., Goulden, M., Miller, S., and da Rocha, H. R.: Seasonal drought stress in the Amazon: Reconciling 3 models and observations, J. Geophys. Res., 113, G00B01, doi:10.1029/2007JG000644, 2008.

Carouge, C., Bousquet, P., Peylin, P., Rayner, P. J., and Ciais, P.: What can we learn from European continuous atmospheric CO_2 measurements to quantify regional fluxes - Part 1: Potential of the 2001 network, Atmos. Chem. Phys., 10, 3107–3117, 2010, http://www.atmos-chem-phys.net/10/3107/2010/.

Carouge, C., Rayner, P. J., Peylin, P., Bousquet, P., Chevallier, F., and Ciais, P.: What can we learn from European continuous atmospheric CO_2 measurements to quantify regional fluxes - Part 2: Sensitivity of flux accuracy to inverse setup, Atmos. Chem. Phys., 10, 3119–3129, 2010, http://www.atmos-chem-phys.net/10/3119/2010/.

Case, J. L., Manobianco, J., Dianic, A. V., and Wheeler, M. M.: Verification of high-resolution RAMS forecasts over east-central Florida during the 1999 and 2000 Summer Months, Weather Forecast., 17(6), 1133–1151, 2002.

CCSP: The First State of the Carbon Cycle Report (SOCCR): The North American Carbon Budget and Implications for the Global Carbon Cycle, A Report by the US Climate Change Science Program and the Subcommittee on Global Change Research, edited by: King, A. W., Dilling, L., Zimmerman, G. P., Fairman, D. M., Houghton, R. A., Marland, G., Rose, A. Z., and Wilbanks, T. J., National Oceanic and Atmospheric Administration, National Climatic Data Center, Asheville, NC, USA, 242 pp., 2007.

Choi, Y., Vay, S., Vadrevu, K., Soja, A., Woo, J., Nolf, S., Sachse, G., Diskin, G., Blake, D., Blake, N., Singh, H., Avery, M., Fried, A., Pfister, L., and Fuelberg, H.: Characteristics of the atmospheric CO_2 signal as observed over the conterminous United States during INTEX-NA, J. Geophys. Res., 113, D07301, doi:10.10129/2007JD008899, 2008.

Ciais, P., Bousquet, P., Freibauer, A., and Naegler, T.: Horizontal displacement of carbon associated with agriculture and its impacts on atmospheric CO_2, Global Biogeochem. Cy., 21, GB2014, doi:10.1029/206GB002741, 2007.

Collatz, G. J., Ribas-Carbo, M., and Berry, J. A.: Coupled photosythesis-stomatal conductance model for leaves of C4 plants, Aust. J. Plant Physiol., 19, 519–538, 1992.

Denning, A. S., Collatz, J. G., Zhang, C., Randall, D. A., Berry, J. A., Sellers, P. J., Colello, G. D., and Dazlich, D. A.: Simulations of terrestrial carbon metabolism and atmospheric CO_2 in a general circulation model. Part 1: Surface carbon fluxes, Tellus B, 48, 521–542, 1996.

Denning, A. S., Nicholls, M., Prihodko, L., Baker, I., Vidale, P., Davis, K., and Bakwin, P.: Simulated variations in atmospheric CO_2 over a Wisconsin forest using a couple ecosystem-atmosphere model, Global Change Biol., 9, 1241–1250, 2003.

Denning, A. S., Zhang, N., Yi, C., Branson, M., Davis, K., Kleist, J., and Bakwin, P.: Evaluation of modeled atmospheric boundary layer depth at the WLEF Tower, Agr. Forest Meteorol., 148, 206–215, 2008.

Engelen, R. J., Denning, A. S., and Gurney, K. R.: On error estimation in atmospheric CO_2 inversions, J. Geophys. Res., 107(10), 1–13, 2002.

Fan, S., Gloor, M., Mahlman, J., Pacala, S., Sarmiento, J., Takahashi, T., and Tans, P.: A large terrestrial carbon sink in North America implied by atmospheric and oceanic carbon dioxide data and models, Science, 282, 442–446, 1998.

Freitas, S. R., Longo, K., Silva Dias, M., Silva Dias, P., Chatfield, R., Fazenda, Á., and Rodrigues, L. F.: The coupled aerosol and tracer transport model to the brazilian developments on the Regional Atmospheric Modeling System: validation using direct and remote sensing observations, International Conference on Southern Hemisphere Meteorology and Oceanography (ICSHMO), 2006.

Fuelberg, H. E., Porter, M. J., Kiley, C. M., Halland, J. J., and Morse, D.: Meteorological conditions and anomalies during the Intercontinental Chemical Transport ExperimentNorth America, J. Geophys. Res., 112, D12S06, doi:10.1029/2006JD007734, 2007.

Gerbig, C., Lin, J. C., Wofsy, S. C., Daube, B. C., Andrews, A. E., Stephens, B. B., Bakwin, P. S., and Grainger, C. A.: Toward constraining regional-scale fluxes of CO_2 with atmospheric observations over a continent: 1. Observed spatial variability from airborne platforms, J. Geophys. Res., 108(D24), 4756, doi:10.1029/2002JD003018, 2003.

Gourdji, S. M., Mueller, K. L., Schaefer, K., and Michalak, A. M., Global monthly-averaged CO_2 fluxes recovered using a geostatistical inverse modeling approach: 2. Results including

auxiliary environmental data, J. Geophys. Res., 113, D21115, doi:10.1029/2007JD009733, 2008.

Gurney, K. R., Law, R. M., Denning, A. S., Rayner, P. J., Baker, D., Bousquet, P., Bruhwiler, L., Chen, Y., Clals, P., Fan, S., Fung, I. Y., Gloor, M., Helmann, M., Higuchi, K., John, J., Maki, T., Maksyutov, S., Masarle, K., Peylin, P., Prather, M., Pak, B. C., Randerson, J., Sarmiento, J., Tagucki, S., Takahashi, T., and Yuen, C.: Towards robust regional estimates of CO_2 sources and sinks using atmospheric transport models, Nature, 415, 626–630, 2002.

Gurney, K. R., Seib, B., Ansley, W., Mendoza, D., Fischer, M., Miller, C., and Murtishaw, S.: The Vulcan Inventory, version 1.0, Purdue University, http://www.purdue.edu/eas/carbon/vulcan/research.html, last access: 18 May 2010, 2008.

Hanan, N. P., Berry, J. A., Verma, S. B., Walter-Shea, E. A., Suyker, A. E., Burba, G. G., and Denning, A. S.: Model analyses of biosphere-atmosphere exchanges of CO_2, water and energy in Great Plains tallgrass prairie and wheat ecosystems, Agr. Forest Meteorol., 131, 162–179, 2004.

Kalman, R. E.: A new approach to linear filtering and prediction problems, J. Basic Eng.-T. ASME, 82, 35–45, 1960.

Kaminiski, T., Rayner, P. J., Heimann, M., and Enting, I. G.: On aggregation errors in atmospheric transport inversions, J. Geophys. Res., 106, 4703–4715, 2001.

Kawa III, S. R.,Pawson, S., and Zhu, Z.: Global CO_2 transport simulations using meteorological data from the NASA data assimilation system, J. Geophys. Res., 109, D18312, doi:10.1029/2004JD004554, 2004.

Liang, Q., Jaeglé, L., Hudman, R. C., et al.: Summertime influence of Asian pollution in the free troposphere over North America, J. Geophys. Res., 112, D12S11, doi:10.1029/2006JD007919, 2007.

Lokupitiya, E., Denning, S., Paustian, K., Baker, I., Schaefer, K., Verma, S., Meyers, T., Bernacchi, C. J., Suyker, A., and Fischer, M.: Incorporation of crop phenology in Simple Biosphere Model (SiBcrop) to improve land-atmosphere carbon exchanges from croplands, Biogeosciences, 6, 969–986, 2009, http://www.biogeosciences.net/6/969/2009/.

McGrath-Spangler, E. L., Denning, A. S., Corbin, K. D., and Baker, I. T.: Implementation of a boundary layer heat flux parameterization into the Regional Atmospheric Modeling System (RAMS), Atmos. Chem. Phys. Discuss., 8, 14311–14346, 2008, http://www.atmos-chem-phys-discuss.net/8/14311/2008/.

Michalak, A. M., Bruhwiler, L., and Tans, P. P.: A geostatistical approach to surface flux estimation of atmospheric trace gases, J. Geophys. Res. 109, 1–19, 2004.

Mueller, K. L., Gourdji, S. M., and Michalak, A. M.: Global monthly-averaged CO_2 fluxes recovered using a geostatistical inverse modeling approach: 1. Results using atmospheric measurements, J. Geophys. Res., 113, D21114, doi:10.1029/2007JD009734, 2008.

Nicholls, M. E., Denning, A. S., Prihodko, L., Vidale, P., Davis, K., and Bakwin, P.: A multiple-scale simulation of variations in atmospheric carbon dioxide using a coupled biosphere-atmospheric model, J. Geophys. Res., 109, D18117, doi:10.1029/2003JD004482, 2004.

Olson, J. S., Watts, J. A., and Allison, L. J.: Major World Ecosystem Complexes Ranked by Carbon in Live Vegetation: A Database, ORNL/CDIAC-134, NDP-017, Carbon Dioxide Information Analysis Center, US Department of Energy, Oak Ridge National Laboratory, Oak Ridge, Tennessee, USA, 2001.

Oren, R., Ellsworth, D. S., Johnsen, K. H., Phillips, N., Ewers, B. E., Maler, C., Schafer, K. V., McCarthy, H., Hendrey, G., McNulty, S. G., and Katul, G. G.: Soil fertility limits carbon seqestration by forest ecosystems in a CO_2-enriched atmosphere, Nature, 411, 469–471, 2001.

Parazoo, N.: Investigating synoptic variations in atmospheric CO_2 using continuousobservations and a global transport model, Master's thesis, Colorado State University, 2007.

Park, S. and Xu, L.: Data Assimilation for Atmospheric, Oceanic and Hydrologic Applications, doi:10.1007/879-3-540-71056-14, Springer-Verlag, Berlin, Heidleberg, 2009.

Peters, W., Jacobson, A. R., Sweeney, C., Andrews, A. E., Conway, T. J., Masarie, K., Miller, J. B., Bruhwiler, L. M. P., Pétron, G., Hirsch, A. I., Worthy, D. E. J., van der Werf, G. R., Randerson, J. T., Wennberg, P. O., Krol, M. C., and Tans, P. P.: An atmospheric perspective on North American carbon dioxide exchange: CarbonTracker, P. Natl. Acad. Sci. USA, 104, 18925–18930, 2007.

Prince, S.: NPP Cropland: Gridded Estimates for the Central, USA 1982–1996', online available at: http://knb.ecoinformatics.org/knb/metacat?action=read&qformat=nceas&sessionid=&docid=nceas.184, last access: 18 May 2010, 2000.

Peterson, G. A., Halvorson, A. D., Havlin, J. L., Jones, O. R., Lyon, D. J., and Tanaka, D. L.: Reduced tillage and increasing cropping intensity in the Great Plains conserves soil C, Soil Till. Res., 47, 207–218, 1998.

Peylin, P., Rayner, P. J., Bousquet, P., Carouge, C., Hourdin, F., Heinrich, P., Ciais, P., and AEROCARB contributors: Daily CO_2 flux estimates over Europe from continuous atmospheric measurements: 1, inverse methodology, Atmos. Chem. Phys., 5, 3173–3186, 2005, http://www.atmos-chem-phys.net/5/3173/2005/.

Pielke, R. A., Cotton, W., Walko, R., Tremback, C., Lyons, W., Grasso, L., Nicholls, M., Moran, M., Wesley, D., Lee, T., and Copeland, J.: A comprehensive meteorological modeling system – RAMS, Meteorol. Atmos. Phys., 46, 69–91, 1992.

Raich, J. W., Rastetter, E. B., Melillo, J. M., Kicklighter, D. W., Steudler, P. A., Peterson, B. J., Grace, A. L., Moore III, B., and Vorosmarty, C. J.: Potential Net Primary Productivity in South America: Application of a Global Model, Ecol. Appl., 1(4), 399–429, 1991.

Robertson, G. P., Paul, E. A., and Harwood, R. R.: Greenhouse gases in intensive agriculture: contributions of individual gases to the radiative forcing of the atmosphere, Science, 289, 1922–1925, 2000.

Rödenbeck, C., Houweling, S., Gloor, M., and Heimann, M.: CO_2 flux history 1982-2001 inferred from atmospheric data using a global inversion of atmospheric transport, Atmos. Chem. Phys., 3, 1919–1964, 2003, http://www.atmos-chem-phys.net/3/1919/2003/.

Schimel, D. S., House, J. I., Hibbard, K. A., Bousquet, P., Ciais, P., Peylin, P., Braswell, B. H., Apps, M. J., Baker, D., Bondeau, A., Canadell, J., Churkina, G., Cramer, W., Denning, A. S., Field, C. B., Friedlingstein, P., Goodale, C., Heimann, M., Houghton, R. A., Melillo, J. M., Moore III, D. M., Noble, I., Pacala, S. W., Prentice, I. C., Raupach, M. R., Rayner, P. J.,

Scholes, R. J., Steffen, W. L., and Wirth, C.: Recent patterns and mechanisms of carbon exchange by terrestrial ecosystems, Nature, 414, 169–172, 2001.

Schuh, A. E., Denning, A. S., Uliasz, M., and Corbin, K. D.: Seeing the forest through the trees: recovering large scale carbon flux biases in the midst of small scale variability, J. Geophys. Res., 114, G03007, doi:10.1029/2008JG000842, 2009.

Sellers, P. J., Mintz, Y., Sud, Y. C., and Dalcher, A.: A simple biosphere model (SiB) for use within general circulation models, J. Atmos. Sci., 43, 505–531, 1986.

Sellers, P. J., Randall, D. A., Collatz, G. J., Berry, J. A., Field, C. B., Dazlich, D. A., Zhang, C., Collelo, G. D., and Bounoua, L.: A revised land surface parameterization (SiB2) for atmospheric GCMs, Part I: Model formulation, J. Climate, 9, 676–705, 1996.

Stephens, B. B., Gurney, K. R., Tans, P. P., Sweeney, C., Peters, W., Bruhwiler, L., Ciais, P., Ramonet, M., Bousquet, P., Nakazawa, T., Aoki, S., Machida, T., Inoue, G., Vinnichenko, N., Lloyd, J., Jordan, A., Heimann, M., Shibistova, O., Langenfelds, R. L., Steele, L. P., Francey, R. J., and Denning, A. S.: Weak northern and strong tropical land carbon uptake from vertical profiles of atmospheric CO_2, Science, 316, 1732–1735, 2007.

Tilman, D., Reich, P., Phillips, H., Menton, M., Patel, A., Vos, E., Petersion, D., and Knops, J.: Fire suppression and ecosystem carbon storage, Ecology, 81(10), 2680–2685, 2000.

Tripoli, G. J. and Cotton, W. R.: The Colorado State University three-dimensional cloud/mesoscale model – Part I General theoretical framework and sensitivity experiments, J. Recherches Atmospheriques, 16, 185–219, 1982.

Ulliasz, M. and Pielke, R. A.: Application of the receptor oriented approach in mesoscale dispersion modeling', in: Air Pollution Modeling and its Applications VIII, edited by: Van Dop, H. and Steyn, D. G., Plenum Press, New York, 399–408, 1991.

Urbanski, S., Barford, C., Wofsy, S., Kucharik, C., Pyle, E., Budney, J., McKain, K., Fitzjarrald, D., Czikowsky, M., and Munger, J. W.: Factors controlling CO_2 exchange on timescales from hourly to decadal at Harvard Forest, J. Geophys. Res.-Biogeo., 112(G2), G02020, doi:10.1029/2006JG000293, 2007.

Wang, J. W., Denning, A. S., Lu, L., Baker, I. T., and Corbin, K. D.: Observations and simulations of synoptic, regional, and local variations in atmospheric CO_2, J. Geophys. Res., 112, D04108, doi:10.1029/2006JD007410, 2006.

Wise, T. A.: Identifying the Real Winners from, US Agricultural Policies, Global Development and Environmental Institute, Working Paper No. 05-07, 2005, 2006.

Zupanski, D., Denning, A. S., Marek, U., Zupanski, M., Schuh, A. E., Rayner, P. J., Peters, W., and Corbin, K. D.: Carbon flux bias estimation employing maximum Likelihood Ensemble Filter (MLEF), J. Geophys. Res., 112, D17107, doi:10.1029/2006JD008371, 2007.

Tellus SERIES B CHEMICAL AND PHYSICAL METEOROLOGY
PUBLISHED BY THE INTERNATIONAL METEOROLOGICAL INSTITUTE IN STOCKHOLM

Tellus (2010)

TELLUS

North American gross primary productivity: regional characterization and interannual variability

By IAN T. BAKER[1]*, A. SCOTT DENNING[1] and RETO STÖCKLI[2], [1]*Atmospheric Science Department, Colorado State University, Fort Collins, CO, USA;* [2]*Climate Services, Climate Analysis, MeteoSwiss, Zurich, Switzerland*

(Manuscript received 31 December 2009; in final form 1 July 2010)

ABSTRACT

Seasonality and interannual variability in North American photosynthetic activity reflect potential patterns of climate variability. We simulate 24 yr (1983–2006) and evaluate regional and seasonal contribution to annual mean gross primary productivity (GPP) as well as its interannual variability. The highest productivity occurs in Mexico, the southeast United States and the Pacific Northwest. Annual variability is largest in tropical Mexico, the desert Southwest and the Midwestern corridor. We find that no single region or season consistently determines continental annual GPP anomaly. GPP variability is dependent upon soil moisture availability in low- and mid-latitudes, and temperature in the north. Soil moisture is a better predictor than precipitation as it integrates precipitation events temporally. The springtime anomaly is the most frequent seasonal contributor to the annual GPP variability. No climate mode (i.e. ENSO, NAM) can be associated with annual or seasonal variability over the entire continent. We define a region extending from the Northeast United States through the midwest and into the southwestern United States and northern Mexico that explains a significant fraction of the variability in springtime GPP. We cannot correlate this region to a single mechanism (i.e. temperature, precipitation or soil moisture) or mode of climate variability.

1. Introduction

Global atmospheric CO_2 concentrations have been increasing over the past 250 yr in response to anthropogenic sources in the form of human burning of fossil fuel and land cover change (Keeling et al., 1995). The net increase in CO_2 concentration represents the residual CO_2 from the anthropogenic contribution and large exchange of CO_2 between the atmosphere and surface (oceans and land). It has been shown that on an annual basis, only about 50% of the CO_2 emitted by fossil fuel burning and land cover change resides in the atmosphere; about half is taken up by the oceans and terrestrial biosphere (Oeschger et al., 1975; Tans et al., 1990; IPCC, 2007).

The annual atmospheric CO_2 increase is not linear, but has variability determined by seasonality and the spatial configuration of the continents and oceans (Tans et al., 1990). Northern hemisphere CO_2 concentration is lowest during the Boreal summer, when biospheric uptake is large. In winter when vegetation is dormant, northern hemisphere CO_2 concentration is higher. A similar signal, with smaller magnitude due to smaller land coverage, is seen in the southern hemisphere. There is also interannual variability in the magnitude of the CO_2 increase. For example, volcanic eruptions have been shown to attenuate the rate of atmospheric CO_2 increase (Roderick et al., 2001), presumably a biospheric response to increased diffuse light (Gu et al., 2002; Niyogi et al., 2004) due to increased aerosol loading, or alternatively, a decrease in ecosystem respiration due to decreased temperature.

Increased greenhouse gas concentration in the atmosphere is predicted to modify the radiative forcing of the atmosphere (Cox et al., 2000; IPCC, 2007) which will result in changes to the meteorological forcing at the surface. Changes in surface behaviour will modify the partitioning of energy flux returned to the atmosphere, as well as imposing further changes to the radiative forcing due to changes in surface carbon flux. The atmosphere and terrestrial biosphere are tightly coupled with respect to exchange of energy, mass and momentum; predictions of future climate are critically dependent upon our understanding of processes operating under present conditions.

It is tempting to correlate atmosphere–biosphere carbon flux with climate indexes such as the Northern Annular Mode [NAM; here considered synonymous with the North Atlantic Oscillation (NAO)] or El-Niño/Southern Oscillation (ENSO) as a way to link

*Corresponding author.
1371 Campus Delivery,
Colorado State University,
Fort Collins, CO 80523-1371, USA
e-mail: baker@atmos.colostate.edu
DOI: 10.1111/j.1600-0889.2010.00492.x

regional carbon flux to large-scale climate dynamics. Demonstrable causal links between modes of climate variability and ecophysiological behaviour may provide insight into future climate if these modes exhibit secular trends. Russell and Wallace (2004) showed a correlation between NAM and rate of increase of global CO_2 concentration. In this case, the decreased rate of CO_2 growth was tied to greenness as measured by normalized difference vegetation index (NDVI) over the Eurasian continent, in the form in increased growing season length due to stronger warm onshore flow during the positive phase of the NAM. This finding was consistent with that of Schaefer et al. (2002), who also found that interannual variability in tropical net ecosystem exchange (NEE) of carbon was correlated to ENSO, as a response to changes in precipitation patterns. Surface carbon flux feeds back into atmospheric circulation and climate. Identifying strong mechanistic feedbacks, while not completely 'closing the loop' between surface and atmosphere, will strengthen scientific underpinnings for predictions of future climate.

To date, most studies have focused on the Northern Hemisphere, due to the large land fraction. However, with the exception of the aforementioned link between Eurasian carbon flux and the NAM, strong coupling between the terrestrial biosphere and atmosphere has defied explanation. In particular, studies have not shown consistent results in North America (NA). Zhou et al. (2001) looked at 19 yr of NDVI data and found a consistent response in Eurasia, both in greenness and length of growing season, but a more 'fragmented' situation in NA. Buermann et al. (2003) correlated greenness, temperature/precipitation and NAM/ENSO using meteorological and NDVI data for years 1982–1998, and corroborated the strong link between vegetation and warm onshore flow in Eurasia during the positive phase of the NAM. Again, the results for NA were not as coherent, suggesting more complex interactions between meteorological forcing and surface processes.

A strong causal link between the NAM and carbon uptake has been found in Eurasia, while determination of North American ecophysiology and the forcing mechanisms that determine it have been more ambiguous. In this paper, we will focus on gross primary productivity (GPP) over the North American continent, by evaluating 24 yr of model simulations. By taking a bottom-up approach, we hope to gain insight into one aspect of ecosystem behaviour that may inform our understanding of North American biophysics and carbon dynamics. The goal of this study is multiple: Is it possible to partition the continent into regions that are dominant in terms of explaining large-scale interannual GPP variability? Are there patterns in temporal behaviour that we can identify? Can we describe regions in NA that have identifiable reliance on particular atmospheric drivers of GPP? For example, can we identify regions where an early spring is indicative of an annual increase in GPP, or regions where anomalously high midsummer precipitation results in a large positive excursion in annual GPP? Ultimately, we will attempt to correlate North American GPP variability to modes of climate variability such as NAM and ENSO. Although multiple modes of teleconnection have been identified, it has been proposed (Quadrelli and Wallace, 2004) that most, if not all of these modes represent a linear combination of these two most dominant modes. Rather than compare ecosystem behaviour with many climate modes, we prefer to start with a conservative analysis. With a model we can isolate biospheric uptake of carbon from efflux (respiration or anthropogenic sources) and atmospheric transport, and provide a basic description of biospheric response to climate dynamic processes with spatial and temporal resolution higher than the continental/annual scale often reported in inversion studies (i.e. Gurney et al., 2002, 2008; Rödenbeck et al., 2003; Baker et al., 2006).

This paper is organized as follows: Section 2 gives a model synopsis and reviews previous results, as well as giving an overview of the statistical techniques used in the analysis. Analysis of NA GPP is contained in Section 3. This encompasses mean behaviour, regional decomposition and statistical evaluation. Summary and conclusions are given in Section 4.

2. Methods

2.1. Model description

The simple biosphere model (SiB) is a land-surface parameterization scheme originally used to simulate biophysical processes in climate models (Sellers et al., 1986), but later adapted to include ecosystem metabolism (Denning et al., 1996; Sellers et al., 1996a). SiB is a model that is useful to meteorologists for its ability to simulate exchanges of mass, energy and momentum between the atmosphere and terrestrial biosphere, and useful to ecologists for its ability to do so in a process-based framework that allows for simulation of explicit biophysical mechanisms. The parameterization of photosynthetic carbon assimilation is based on enzyme kinetics originally developed by Farquhar et al. (1980), that are linked to stomatal conductance and thence to the surface energy budget and atmospheric climate (Collatz et al., 1991, 1992; Sellers et al., 1996a; Randall et al., 1996).

The soil representation is similar to that of CLM (Dai et al., 2003), with 10 soil layers and soil column depth of 10 meters. Root distribution follows Jackson et al. (1996). SiB has been updated to include prognostic calculation of temperature, moisture and trace gases in the canopy air space (Baker et al., 2003; Vidale and Stöckli, 2003). We refer to this version of the code as SiB3.

Model photosynthesis rate is tightly coupled to total latent heat flux through transpirational losses of moisture through stomates. Photosynthesis is calculated as the minimum of rate-limitation by light, enzyme kinetics, and electron transport (Collatz et al., 1991; Sellers et al., 1992). Photosynthesis is further scaled downward from an optimum rate by limitation imposed by temperature, relative humidity and moisture availability in the soil (Sellers et al., 1992). Leaf-level temperature,

humidity and internal CO_2 concentration are coupled via the Ball–Berry process (Ball et al., 1987) and solved simultaneously. Moisture availability, defined by the combination of root density and soil water concentration in individual model soil layers, imposes a fundamental constraint on photosynthesis and hence evaporation. Commonly, models have defined water availability in terms of soil depth or root density alone, which is unrealistic when compared to actual plant behaviour. We find that coupling root and reservoir characteristics (Baker et al., 2008) provides a more realistic simulation framework.

2.2. Model runs

For this analysis, we ran a global simulation of SiB on a 1×1 degree cartesian grid. Vegetation type is determined by maps as described in DeFries and Townshend (1994), and soil character is specified by IGBP (Global Soil Data Task Group, 2000). In this simulation, SiB3 uses a 10-min timestep forced with 6-hourly regridded meteorological analysis products from the National Centers for Environmental Prediction (NCEP Reanalysis-2; Kalnay et al., 1996; Kanamitsu et al., 2002) interpolated to the model timestep for the years 1983–2006. SiB3 ingests temperature, pressure, precipitation, wind and radiation as forcing variables. Vegetation phenology is provided by the GIMMSg NDVI product (Brown et al., 2004; Tucker et al., 2005; Pinzon et al., 2006) which is used to calculate Leaf Area Index (LAI) and fraction of Photosynthetically Active Radiation absorbed (fPAR) following Sellers et al. (1996b).

Reanalysis products such as NCEP have known biases in precipitation (i.e. Costa and Foley, 1998) and other variables (Zhao and Running, 2006; Zhang et al., 2007a). As precipitation can be expected to have considerable influence on photosynthetic processes, we scale the NCEP precipitation to a data set that incorporates satellite and surface observations, in this case the Global Precipitation Climatology Project (GPCP; Adler et al., 2003). Using monthly precipitation values from GPCP, we scale the NCEP precipitation for consistency. We do not create precipitation events, although we may remove precipitation if the GPCP product indicates no precipitation at a location for a given month.

The model was initialized with saturated soil, and the entire 24 yr period (1983–2006) was simulated twice as a spinup, with the model re-initialized with ending (31 December 2006) model state at 1 January 1983. Ecosystem respiration was scaled to obtain annual carbon balance following Denning et al. (1996). Model diagnostics were output as monthly averages on the global grid, and subsampled for NA.

2.3. Model validation

Before evaluating model results for detailed analysis of ecosystem response to meteorological variability for NA, we wish to demonstrate a baseline of model performance. Continental-scale observations of surface flux do not exist so we compare SiB results with a variety of other sources as a means of establishing confidence in model output. We can appraise SiB behaviour when compared against leaf-level measurements, against observations of latent and sensible heat and carbon flux as observed by eddy covariance observation towers and against fluxes inverted from flask measurements and atmospheric transport to demonstrate model competence. These comparisons are not the focus of this paper, but can provide a foundation for trust in model simulation of less observable quantities such as regional ecophysiological variability. If we can demonstrate model skill at multiple scales, then inferences made about regional-scale ecophysiology will be more robust. Although the emphasis in this paper is on GPP, there are no direct measurements of fundamental photosynthetic uptake at either the canopy or regional scale. However, SiB is a 'third generation' surface scheme (Sellers et al., 1997) that contains self-consistency in the equation set that links radiative transfer, evaporation and ecophysiology. Internal consistency and multiple constraints make it possible to extend a degree of confidence to modelled GPP by comparing model output to observed quantities. In this regard, SiB has a demonstrable ability to simulate landsurface processes.

SiB was developed with the intended use as a lower boundary for Atmospheric General Circulation Models (AGCMs). Sato et al. (1989) describe implementation of SiB into an AGCM, and show that surface behaviour over diurnal to seasonal scales are realistic in the fully coupled model. Randall et al. (1996) describe the 'greening' of the Colorado State University AGCM when SiB phenological behaviour is upgraded from tabular values to those derived from satellite NDVI observations. Noncoupled [offline, driven by European Centre for Medium-Range Weather Forecasts (ECMWF) reanalysis products] global SiB GPP is shown to be consistent with accepted values in Zhang et al. (1996). SiB has been utilized as a lower boundary for the Regional Atmospheric Modeling System (RAMS; Cotton et al., 2003; Pielke et al., 1992) as well (Denning et al., 2003; Nicholls et al., 2004; Wang et al., 2007; Corbin et al., 2008). Denning et al. (2003) and Nicholls et al. (2004) describe how biological processes couple with meteorological process to define the regional carbon budget over Wisconsin, USA. Wang et al. (2007) and Corbin et al. (2008) extend the analysis to the central North American continent.

From its inception in 1986, SiB (versions 1, 2 and 3) has also been evaluated by confronting the model with local observations. Sellers and Dorman (1986) compare modelled energy flux, stomatal resistance, albedo and leaf water potential to observations over periods from several days to 1 month at multiple sites. Colello et al. (1998) confirm that SiB can reproduce diurnal cycles of energy, moisture and carbon flux at a grassland over periods of several days using FIFE data, and Hanan et al. (2005) show that incorporation of heterogeneous C3/C4 physiology maps into SiB improve modelled annual cycles and interannual variability at a grassland site in Oklahoma. Effective radiative

temperature, soil wetness and energy fluxes at a Tibetan prairie are successfully reproduced during growing season months in the study of Gao et al. (2004). Baker et al. (2003) and Schaefer et al. (2008) compare SiB energy and carbon fluxes to eddy covariance observations taken at mid-latitude forest sites: diurnal, monthly and interannual variability are captured by the model, although SiB is biased towards slightly high Bowen ratio when canopy cover is very dense. The mechanisms that control seasonal variability at a site in tropical Amazonia are incorporated into SiB by Baker et al. (2008), with the result that previously out-of-phase simulated annual flux cycles at this site are brought into agreement with observations.

Regional carbon exchange is not a directly measurable quantity. Flask observations of CO_2 are inverted with transport data by Gurney et al. (2008) to obtain estimates of carbon flux for the globe when partitioned into 22 oceanic and terrestrial regions. Figure 1 shows SiB NEE for years 1984–2004 (black line, symbols) compared to the results of Gurney et al. (2008) for Boreal and Temperate NA. There are eight global 'networks' for the inversion data, as changing numbers of flask locations makes a single estimate unreasonable. It is important to note that there is frequently disagreement between the inverted fluxes from different networks (i.e. 1997–1998 in Boreal NA; 1988–1989 and 1993–1996 in Temperate NA), underscoring the fact that absolute measurement of regional carbon flux does not exist. When our modelled flux is compared against the inversion results, SiB captures most, but not all, of the major variability seen in the inversion results. In Boreal NA, the efflux (positive values) event of 1990–1992 is well represented by SiB, as is the uptake event of 1997–1998, although that event is only captured by two of the inversion networks. The relative maximum of 2001–2002 is consistent between SiB and the inversion results, although the SiB peak is higher in magnitude. In temperate NA, general trends are consistent between SiB and inversion results. Local minima in 1991–1992 and 1996–1998 are consistent, as are maxima in 1994, 2000 and 2002. It is important to reiterate that inversion results are not conclusive, as represented by the disagreement between different inversion networks. Flask coverage is sparse (especially in Boreal NA), and transport was interannually uniform in the inversion exercise, which can be a cause for ambiguity (Gurney et al., 2008). It is crucial to acknowledge that there is uncertainty in regional flux estimates from either models (such as SiB) or inversions. However, we believe that SiB fluxes, when compared to inversion products, are reasonable and demonstrate an ability to capture the larger features of ecosystem variability across broad spatial domains. This ability is critical to the results we present later in this paper.

2.4. *Statistical tools*

A model is merely a tool to assist in our understanding of a particular system, in this case the spatiotemporal behaviour of the terrestrial biosphere. We acknowledge that uncertainty exists in model output due to parameterizations, subgrid scale heterogeneity and reanalyzing meteorological observations into forcing data sets. For these reasons, we keep our statistical toolbox small. With the inherent confidence bounds in the model system, we believe that relationships that cannot be seen with simple tools may simply be an artefact of the mathematical manipulations being applied. Therefore, we attempt to limit statistical tools to linear regression, explained variance and correlation coefficient. To test for significance, we use a two-ended Student's *t*-test at the 90% level. We take a conservative approach and assume that each year comprises an independent sample, giving

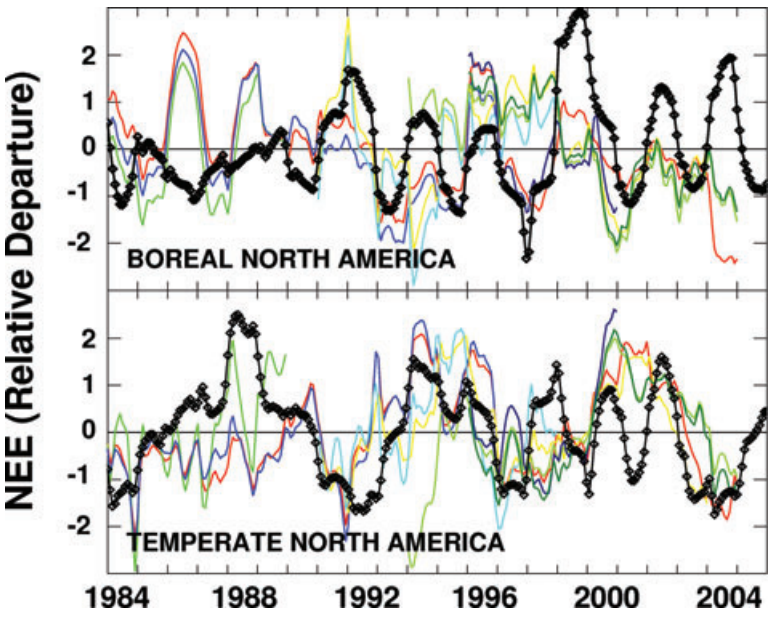

Fig. 1. Modelled net ecosystem exchange (black line, symbols) superimposed on NEE estimated by inversion of eight flask networks (Gurney et al., 2008). Modelled flux has 13-month trapezoidal running mean applied. Both model and flask-based time series have been standardized, so units are relative.

us 24 samples in the modelling period (for a two-tailed test we subtract two, giving 22 degrees of freedom). At this level, the probability that a particular value is the result of random chance requires a t-statistic value of $t < 1.72$.

We also use singular value decomposition to obtain the principle component (PC) time series, which we can regress GPP and meteorological anomalies onto to determine if there are patterns that explain large fractions of continental-scale variability. Eigenvalues are tested for significance following North et al. (1982). We found that the significance of the eigenvalues was critically dependent upon the degrees of freedom specified, which we calculated (following Bretherton et al., 1998) as

$$N^* = \frac{1 - r^2(\Delta t)}{1 + r^2(\Delta t)}, \tag{1}$$

where N^* is the degrees of freedom, r^2 is the lag-one autocorrelation and Δt is the timestep of the data.

Intuitively, we can think of the spatiotemporal persistence of anomalies in GPP as the dependence of an anomaly upon the previous month, season or year's environmental conditions. Plots of lag-one autocorrelation of monthly GPP (not shown) show a spatial variability in this dependence: In the northeast, in an area bounded approximately by 50° north latitude and 90° west longitude, there is very little variability explained by the lag-one autocorrelation, less than 20% on even a monthly basis. In the more arid regions of the continent (desert southwest, arctic), the lag-one autocorrelation on a monthly basis is much higher. When annual anomalies are used, the region of spatial independence becomes larger still, with only the desert southwest suggesting that GPP in a given year is dependent upon conditions in the previous year. For this reason, we continue to use 22 as our degrees of freedom, which is not only smaller than the area-mean value found using eq. (1), but consistent with our theme of using conservative statistics throughout the analysis.

3. Analysis

3.1. Mean North American GPP

For this analysis, we define NA as the region northward of 15° north latitude between 50° and 170° west longitude. The spatial distribution of simulated annual mean GPP is shown in Fig. 2 (panel a). Maximum uptake of CO_2 is in the tropical forest of southern Mexico, over 3.5 kg m^{-2} yr^{-1} in some areas. The southeastern United States and Pacific Northwest are the next largest in terms of annual assimilation of carbon, at approximately 2 kg m^{-2} yr^{-1}. The desert southwest and arctic tundra regions show smallest annual GPP, which is not unexpected given the harshness of the climate and lack of biomass in these regions.

The standard deviation of annual GPP (Fig. 2, panel b) shows that the tropical forest in southern Mexico has large interannual variability, but the productive regions in the southeast and Pacific Northwest do not. GPP in the Monsoon region in Mexico is highly variable, as is the California coast south of San Francisco Bay. There is also a belt of relatively large variability centred on 100° west longitude, from Southern Texas to the prairie provinces of Canada. This midwestern band of large standard deviation deserves attention because it exists as a natural boundary between the productive east and the relatively dry intermountain west. This region encompasses the 'dry line' that often focuses severe weather, as well as the region effected by the cold, fast-moving airmasses ('Alberta Clippers') that intrude into the mid-latitude United States from Canada. It is intuitive that this region will not only experience large variability in

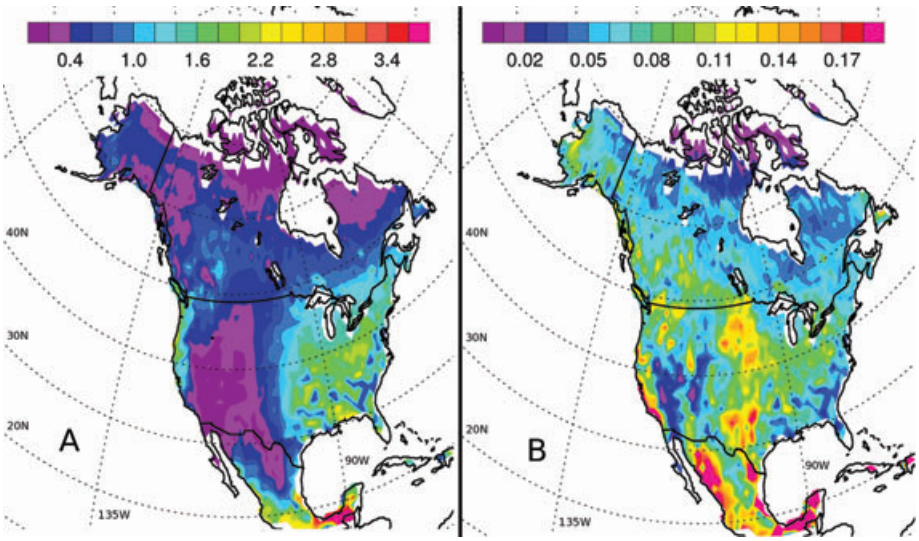

Fig. 2. Panel a: Annual mean GPP, in kg carbon, for North America, as simulated by SiB3, years 1983–2006. Panel b: GPP standard deviation, in kg carbon.

ecosystem function, but that overall variability here has the potential to impact continental-scale carbon characteristics.

The coefficient of variation (defined as the standard deviation divided by the mean; not shown) for GPP is largest in the desert southwest, and smallest in the local maxima GPP regions in the southeast United States and Pacific Northwest, as well as in the Boreal Forest of Canada. In general, large coefficient of variation is found where mean annual GPP is low.

Any analysis of North American GPP must include consideration of seasonality. In the extreme north, cold winters and brief warm summers ensure that annual GPP is completed in only a few months. For example, in Barrow AK there are only 3 months (June, July and August) that have mean monthly temperature above 273 K, with mean annual temperature amplitude of almost 50 K. As one moves south, temperature seasonality is damped and mean annual temperature is larger. The mean monthly temperature for locations such as Miami FL and Mexico City is above freezing in all months, and the amplitude of the annual cycle is 10 K or less. There are periodic cold air intrusions southwards (more so in the SE United States than in Mexico or Central America), but mean conditions are suitable for photosynthetic activity throughout the year. Precipitation seasonality plays a role as well, especially in the southern regions where temperature is not as variable. Figure 3 (panel a) shows the month where mean maximum GPP occurs, and Fig. 3 (panel b) shows the fraction of annual GPP that occurs during the month of greatest activity. In the arctic, maximum monthly GPP happens in July or August, and 1 month can comprise upwards of 40% of the annual total. By contrast, in the southern United States (with the exception of the southern Rockies), maximum photosynthetic activity occurs in April or May, and no individual month contributes more than 15% to the annual total. In the monsoon region of Mexico, maximum GPP occurs in August/September, after seasonal rains have replenished moisture in the soil.

3.2. North American GPP variability

Continents are commonly partitioned by vegetation type (i.e. Peters et al., 2007) as a means to determine more detailed relationships. In this study, we prefer a regional discretization, based roughly on spatial coherence in the mean, standard deviation and coefficient of variability of GPP. These regions are shown in Fig. 4, and while we did not explicitly establish criteria to define continental subregions, these regions implicitly incorporate natural delineations of mean annual GPP, standard deviation and coefficient of variability, vegetation type, topography and climatological variables such as annual mean precipitation and temperature. These regions are listed in Table 2, along with the fraction of NA land area, fraction of mean annual NA GPP occurring in the region and the ratio of GPP fraction to land fraction. Several features of Table 1 are worth noting.

- The SouthWest and SouthEast regions have identical area, but the SouthEast region has over four times the fraction of mean annual NA GPP that the SouthWest region does.
- Over half (54%) of the mean annual NA GPP occurs in three regions: SouthEast, NorthEast and Mexico/CA. However, the variability in the SouthEast and NorthEast regions is small (Fig. 2, panel b), which may reduce the impact these regions impose on continental-scale GPP anomaly.
- The MidWest region contributes around 12% to mean annual NA GPP, but the relatively large standard deviation in annual GPP for the region suggests that this region may play a larger role in continental-scale behaviour.

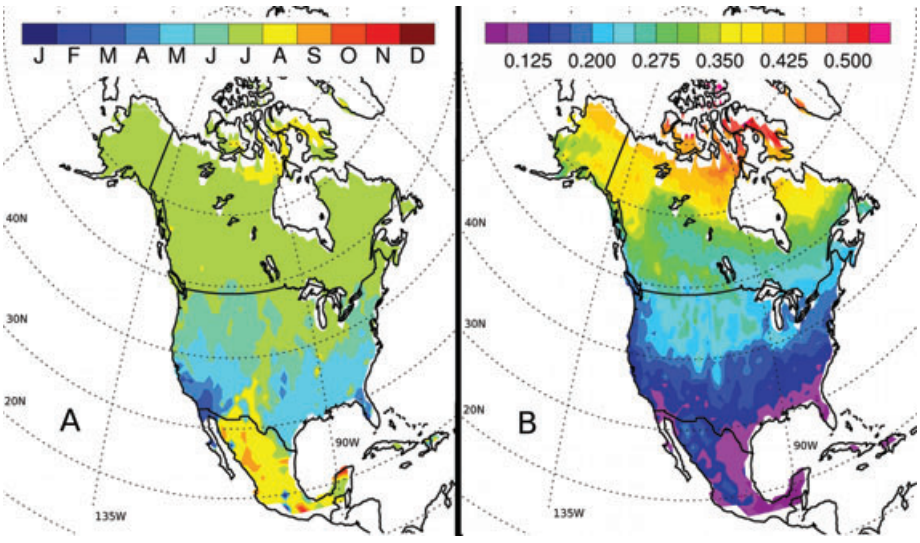

Fig. 3. Panel a: Month of maximum GPP. Panel b: Fraction of annual GPP occurring during the month of maximum GPP.

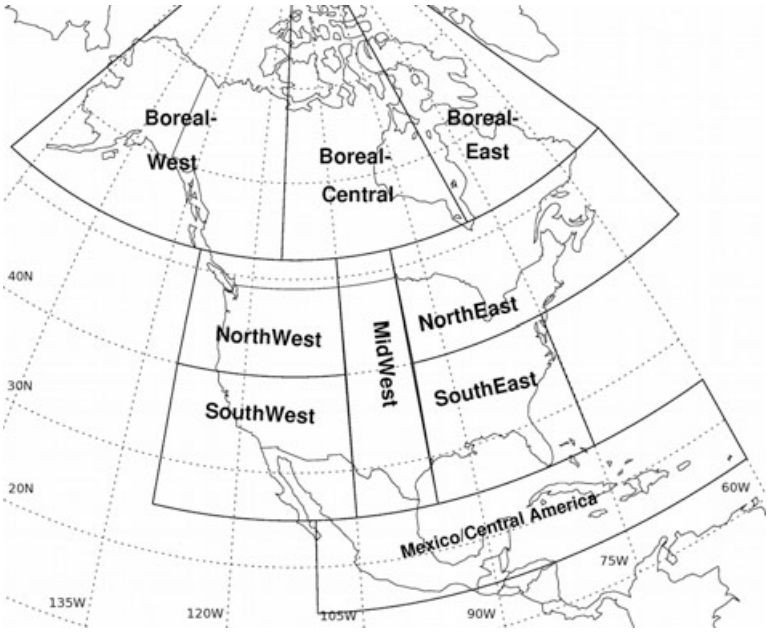

Fig. 4. Regional partition of North America.

Table 1. Ecophysiological subregions for the North American continent

Subregion	% area	% GPP	Ratio (GPP/area)
Mexico/Central America	6.4	15.7	2.45
SouthWest	8.8	4.3	0.49
SouthEast	8.8	18.0	2.05
NorthWest	9.6	8.1	0.84
NorthEast	13.4	20.3	1.51
MidWest	11.6	11.9	1.03
Boreal-East	7.6	2.8	0.37
Boreal-Central	15.6	7.8	0.50
Boreal-West	18.1	11.2	0.62

The annual anomaly in modelled GPP for 1983–2006 for the entire continent is shown in Fig. 5, with the regional anomalies superimposed. In this figure, the continental-scale anomaly is plotted as the solid line and the regional anomalies are sorted by magnitude, with smallest variation from the regional mean plotted closest to the zero line; larger anomalies are plotted further from the origin, demonstrating which regions contribute the most to that year's anomaly on the continental scale. In no year do all regional anomalies have identical sign; both positive and negative anomalies exist on a regional basis in all years. In 4 years (1996, 2000, 2002, 2005), all regions save one have similar sign. Interestingly, the southernmost region is the outlier for each of these years. For years with small overall anomaly (1990, 2001, 2004), there are relatively large, yet compensating, regional excursions from the mean.

Variability about the mean NA GPP is not consistently dependent on any single region. Of the nine regions, only eastern Boreal Canada (Boreal-East) and the Pacific Northwest (NorthWest) are never the largest anomaly for a given year, where all other regions contribute the largest anomaly to the annual variability at least once. Several regions stand out due to their frequent large excursions from the mean; Mexico/Central America, MidWest and Central/Western Boreal regions. The Boreal regions commonly exhibit similar sign (i.e. 1983, 1985, 1992) to the overall anomaly but not exclusively (2001, 2004) suggesting that these adjoining regions may respond to different forcing mechanisms that determine annual GPP variability.

The SouthWest is the largest anomaly three times; even though the mean GPP is small there, the coefficient of variability is the largest on the continent. The SouthWest can be an influence for either positive or negative anomalies—it is not just that it can contribute if it rains, although the largest contribution is during the large El Niño event of the early 1980s. This region is important for continental-scale carbon flux.

The continental-scale annual GPP anomaly is partitioned by seasonal contribution in Fig. 6. On a seasonal basis, all seasons except winter have at least 6 yr where that seasonal anomaly is the same sign as the annual anomaly and is largest during the year. Spring anomalies dominate the year the most (11 times) with Summer contributing the most to the annual anomaly 7 yr, and Fall 6. The two largest anomalies during the year are usually adjoining seasons (i.e. spring and summer, or summer and fall), but not exclusively. It is not uncommon for the two largest seasonal anomalies with the same sign to be opposing seasons (i.e. 1985, 2005), nor is it uncommon for adjoining seasons to have opposing signs (i.e. 1991, 2004) although in this

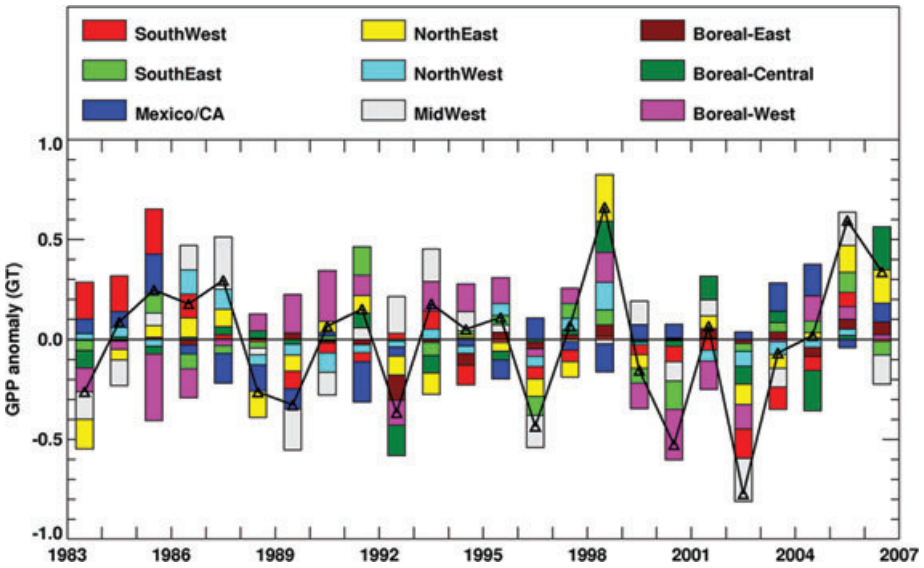

Fig. 5. Regional contribution to annual North America GPP anomaly, in GT carbon, for years 1983–2006. Continental-scale variability is shown as the solid black line, and regional contribution to the total is given by the coloured boxes. Smallest regional anomalies are plotted nearest the zero line, and largest anomalies further from the *x*-axis.

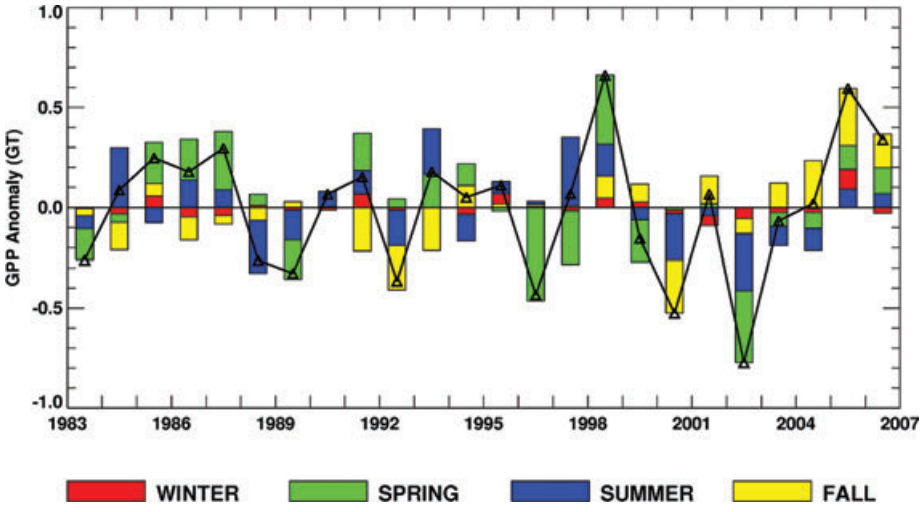

Fig. 6. Seasonal contribution to annual North America GPP anomaly, in GT carbon, for years 1983–2006. Continental-scale variability is shown as the solid black line, and seasonal contribution to the total is given by the coloured boxes. Smallest regional anomalies are plotted nearest the zero line, and largest anomalies further from the *x*-axis.

case the magnitude of the anomaly is generally small and winter is usually one of the seasons. For each season, the distribution between positive and negative is fairly evenly distributed; both positive and negative excursions from the mean are found in the simulation record.

3.3. Correlation to physical mechanism

3.3.1. Annual GPP variability. Ultimately, we wish to link ecophysiological behaviour to modes of climate variability, but doing so directly requires a causal jump across the meteorological mechanisms that influence ecosystem behaviour. In this section we make simple statistical comparisons of GPP to meteorological forcing such as temperature, radiation, and precipitation. We also include a comparison to soil moisture availability, as precipitation alone may neglect features of precipitation distribution that may be misleading. For example, a large precipitation event will suggest a positive anomaly, but if a large fraction of that precipitation is lost as runoff then the potential benefit to vegetation will be lost. Furthermore, the effect of wintertime precipitation anomalies may be attenuated or exacerbated by the nature of the spring warmup. Using soil moisture as a diagnostic

tool takes advantage of its integrative nature, which may not be possible if precipitation alone is used.

We regress variability in annual GPP against variability in annual precipitation, soil moisture availability, temperature, and radiation. The fraction of GPP variability explained by the various mechanisms is calculated along with a Pearson's correlation coefficient to help determine the nature of the relationship. Significance is determined using a Student's *t*-statistic, calculated for 90% significance assuming 22 degrees of freedom (assuming each year as an independent sample).

For the North American continent, we aggregate the results and show the mechanism that explains the largest fraction in annual GPP in Fig. 7 (panel a). Figure 7 (panel b) shows the amount of variance explained by the mechanism that explains the most variance. We plot the mechanisms as grid-boxes (not contoured) because the classification used is discrete. Blank spots reflect gridcells where no single mechanism is able to explain interannual variability in GPP at the 90% significance level. Soil moisture availability explains the most GPP variability for a significant fraction of the continent, from Mexico and Central America through the southern tier of the United States. The midwestern United States and the southern boundary of the Canadian Prairie provinces are responsive to soil moisture availability, as is most of Alaska and parts of Arctic Canada. The fraction of variance explained by soil moisture availability is largest in the Yucatan Peninsula, northwest Mexico/Southwest United States and the Colorado Plateau. In this region, variance explained can exceed 95%. In the southern plains, variance explained is in the 20–40% range, while there is a local maximum in soil moisture influence over the Dakotas and southern Manitoba of around 75%. In the arctic, the variance explained is lower, generally between 20% and 40% (with small local maxima).

Temperature explains most of the GPP variability in the east-central United States and over most of Canada. Temperature influence in Canada is intuitive, as an early spring can be expected to lead to anomalously large GPP. However, the fraction of variability explained by temperature is small everywhere where temperature is the dominant mechanism, generally between 10% and 40%. Radiation variability explains the most variance over small pockets in the Pacific Northwest and Ohio River Valley. The fraction of GPP variability explained by radiation is generally small.

3.3.2. Spring GPP variability. We identified spring as the season that most frequently makes the largest contribution to annual GPP variability (Fig. 6). We can repeat the analysis that we performed on annual anomalies for springtime GPP, and in addition to regressing springtime GPP onto springtime meteorology, we can regress springtime GPP onto winter meteorology to look for a lagged response.

When focus is isolated on spring, the intuitive result is borne out from the statistical analysis: Spring GPP responds positively to anomalously warm temperature across a large fraction of NA. The largest response, in terms of fraction of spring GPP variability explained by temperature variability, extends along a band from New England, along the United States–Canada border into the Pacific Northwest. There is a narrow strip through central Mexico where 20–50% of the springtime GPP variability is explained by temperature, yet in this region the relationship is inverted-cooler spring enhances productivity. The annual pattern shown previously (Fig. 5) in NW Mexico/SW United States holds in the spring as well-increased soil moisture availability is strongly correlated with enhanced GPP.

When we regress springtime GPP against winter meteorological variability, the same relationships seen during the same

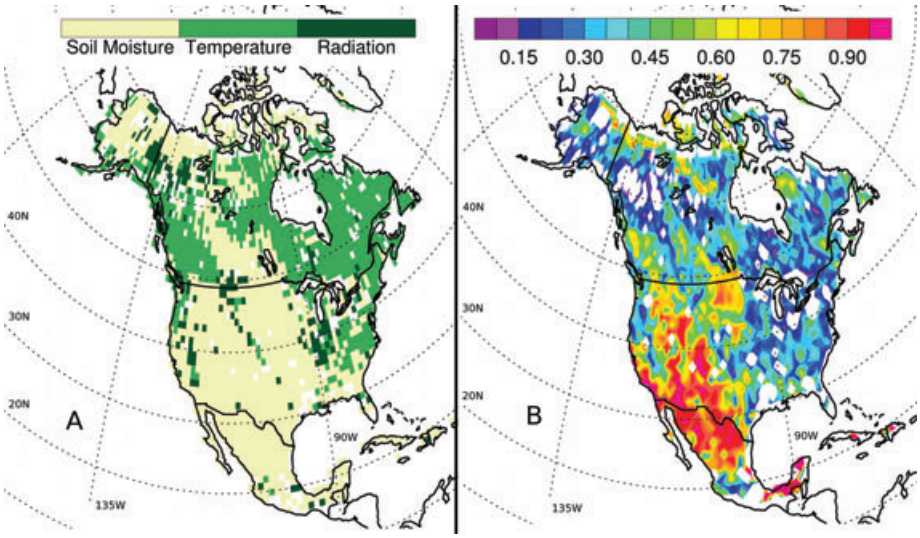

Fig. 7. Panel a: Biophysical mechanism that explains the largest fraction of annual GPP variability, limited to significance at the 90% level. Mechanisms are (1) Soil moisture availability, (2) Temperature and (3) Radiation. Blank spots occur where no single mechanism is significant at the 90% level. Panel b: Fraction of annual GPP variability explained by the dominant mechanism.

season (spring/spring) regression hold, albeit with slightly different spatial structure. This is likely due to the fact that anomalously large winter precipitation has an opportunity to be integrated into the soil prior to springtime GPP onset for large areas of the continent. When the seasonal lag is included into the analysis, anomalous precipitation in winter or spring is similar for the purpose of statistical regression and the patterns we retrieve. The positive temperature relationship to GPP is significant over a much smaller area, centred on Northwestern Quebec.

3.4. Modes of climate variability

Ultimately, we wish to link modes of large-scale climate variability (MCV) such as ENSO or NAM to continental-scale photosynthetic behaviour. However, partitioning continental GPP into regional or temporal components (Figs 5 and 6) does not reveal consistent or coherent patterns, suggesting that ecosystem linkage to large-scale climatic modes may be a difficult prospect.

However, the lack of continental-scale coherence does not preclude regional relationships between modes of climate variability and ecosystem function. To test this idea, we regress GPP anomalies against the two main indices that measure modes of climate variability: the Multivariate ENSO Index (MEI: Wolter and Timlin, 1993; Wolter and Timlin, 1998), and the Northern Annular Mode (NAM; Thompson and Wallace, 2000). We regress anomalies of GPP, temperature and precipitation against these indices as a way to draw out mechanisms that influence vegetation behaviour. As we did for meteorological mechanisms, we calculate a Pearson's correlation coefficient, and test for significance using a two-tail Student's t-statistic at the 90% level.

The data may be dissected in several ways. Modes of climate variability show power over multiple timescales (Rasmussen and Carpenter, 1982; Barnston and Livezy, 1987; Enfield and Birkes, 1993; Hurrell, 1995), and many index values are only evaluated during winter/spring months. We might expect to see a coupling between annual GPP anomaly and annual MCV index in some cases, and a higher-frequency response in others. We might also expect to see a lag between the mechanism invoked by variability of a climate index and environmental response. Furthermore, we focus seasonal attention on the spring (MAM) and summer (JJA) seasons, as these are the seasons with largest GPP and variability, and thus the seasons most likely to influence annual carbon uptake anomaly. Therefore, we conducted the following regressions:

- Annual GPP anomaly onto annual index: Can we relate annual GPP anomaly to low-frequency (annual) variability in a climate index?
- Annual GPP anomaly onto winter, spring, or summer index: Does seasonal-scale variability in a climate index translate to an annual anomaly in GPP?
- Spring GPP anomaly onto winter index, or summer GPP onto spring index (lag-one seasonal comparison): Is there a delay in atmospheric or ecosystem response to climatic forcing?
- Spring GPP anomaly onto spring index or summer onto summer (lag-zero): Immediate ecosystem response to changes in forcing invoked by index variability.

Results are summarized later; no obvious relationship between a single MCV and GPP variability emerged on the large-scale, although there are multiple responses on the regional scale between climate indices, GPP, and the mechanisms that influence GPP that are intuitive and consistent with current knowledge of manifestation of climate variability on meteorology.

3.4.1. Multivariate ENSO Index: MEI. For example, we have shown a relationship between soil moisture availability and GPP in the desert southwest (i.e. Fig. 7, panel a). There is a well-known link between positive ENSO index and high winter precipitation in this region (Sheppard et al., 2002; Mauget, 2003), although an inverse relationship is seen during the monsoon season of the late summer (Higgins et al., 1999). Therefore, we might expect a correlation between GPP and ENSO index here. We do not see large areas of correlation between annual GPP and annual MEI, but we do see a significant relationship in the desert southwest and Pacific Northwest from winter through spring. When spring (MAM) GPP is regressed against the winter MEI, we see between 20% and 30% of the variability in the desert southwest explained, and up to 45% of the GPP variability in Washington, British Columbia and western Alberta explained. This relationship is reinforced when spring GPP is regressed against spring MEI. By summer, the influence in the southwest has moved slightly northeast into the Colorado Plateau, and the correlation in the Pacific Northwest is gone. In the desert southwest, the ENSO influence is in the form of enhanced precipitation, and the positive correlation between MEI and GPP to the north is due to warmer temperatures resulting in extended growing season.

3.4.2. Northern annular mode. The characteristic frequency of the NAM is much shorter than that of ENSO, so we may expect that correlation between annual mean index and annual mean GPP are non-existent. However, we do see a suppression of GPP along the Canadian arctic coast between 100 and 120 west longitude, although it explains less than 25% of the variability. There is no statistical significance between NAM and temperature or precipitation in this region, so the exact mechanism by which NAM influences GPP is not clear.

We see an influence on annual temperature anomaly by seasonal NAM index. A high springtime NAM is associated with positive annual temperature anomaly in a region from central Alaska through the Yukon-NW Territories border, where the NAM explains up to 30% of the temperature variability. Similarly, a high summertime NAM can explain up to 40% of the variability in annual temperature over a sizable fraction of Wyoming and eastern Montana. However, in neither of these regions do

we see a correlation between GPP and either spring or summer NAM. This suggests that other mechanisms (water availability, relative humidity) play a larger role in regulating GPP in these regions than temperature does.

One-season lagged comparison shows no significance when spring GPP is compared to winter NAM. This is likely due to low ecosystem activity in the region of influence (generally far north latitudes) until later in the year. When we correlate summer ecosystem activity to spring NAM index, we see that high NAM is associated with suppressed GPP along the Canadian arctic coast noted earlier.

When NAM is compared to same-season quantities, we see an arc of anomalously high GPP along an arc from central Alaska along the eastern slope of the Canadian Rockies to the Canada–USA border. This GPP anomaly is associated with a positive temperature anomaly, implying early warming and extension of growing season.

The net result is that no continental-scale relationship emerges, with respect to temperature, precipitation or GPP. This is consistent with the previously cited studies such as Zhou et al. (2001) or Buermann et al. (2003). The extensive continental dependence on soil moisture suggests that subtle interactions between precipitation, temperature and radiation are responsible for large-scale GPP variability, and these interactions are heterogeneous in space and time. We are not, at this time, able to make predictions about NA ecophysiological behaviour based on ENSO or NAM index.

3.5. *EOF/PC analysis*

To determine if coherent patterns exist for GPP variability on annual and seasonal scales independent of reliance on physical mechanism, we performed singular value decomposition (SVD) analysis to obtain the PC time series for GPP anomalies. We tested eigenvalues for significance following North et al. (1982).

On an annual basis, we found no significant pattern, nor did one emerge for summertime GPP. However, the first eigenvalue for springtime showed separation, suggesting that a spatially consistent pattern of GPP variability exists for this season. The GPP anomaly regressed upon the first PC time series is shown in Fig. 8, and shows a spatially coherent region extending from around 90° to 105° west longitude, bounded by the Rio Grande in the south and extending into the Prairie Provinces of Canada to the north. This region branches northeastward up the Ohio River valley towards New England. There is also an associated region of coherence in the Monsoon region of Mexico and the southwestern United States. This EOF implies that there is a large region that behaves consistently, and explains most of

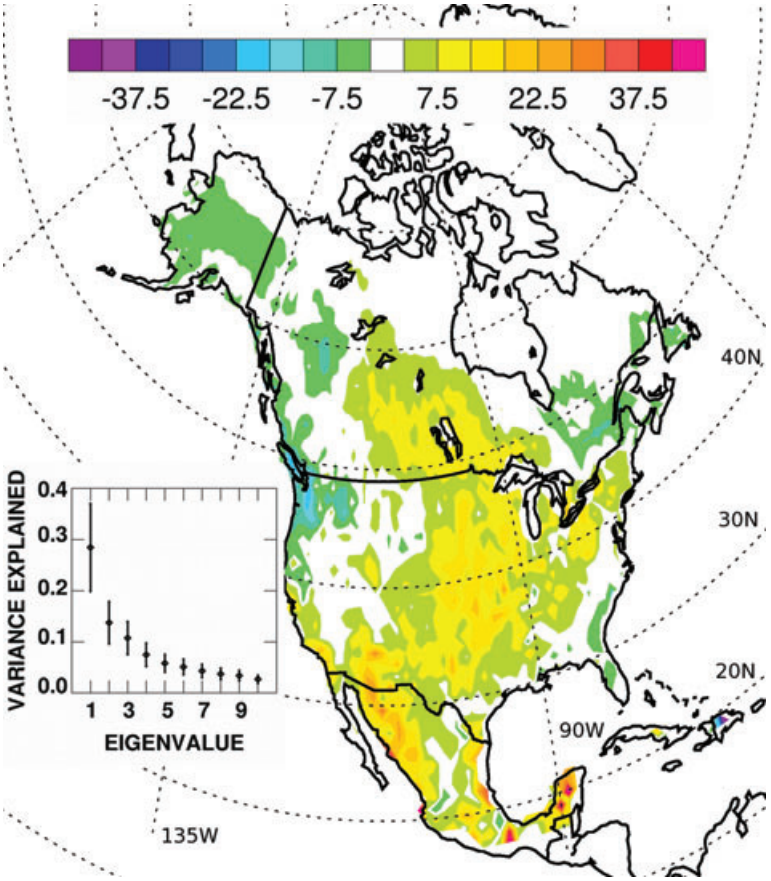

Fig. 8. First EOF of springtime GPP variability. Contour intervals are 5g of carbon. Inset shows separation of the eigenvalues and fraction of variability explained by each.

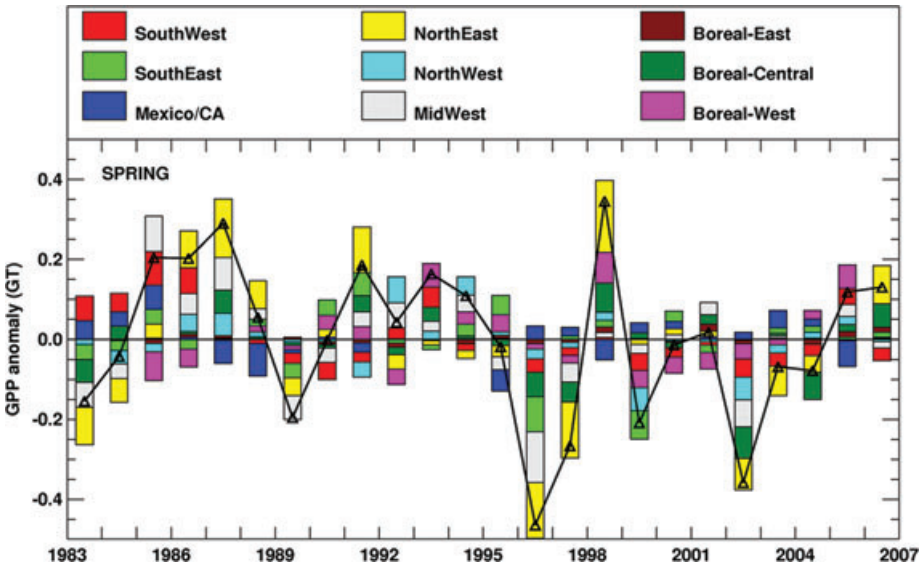

Fig. 9. Regional contribution to springtime North America GPP anomaly, in GT carbon for years 1983–2006. Continental-scale variability is shown as the solid black line, and regional contribution to the total is given by the coloured boxes. Smallest regional anomalies are plotted nearest the zero line, and largest anomalies further from the *x*-axis.

the variability in springtime GPP. If we look at the subregions that describe this region (Fig. 4), it falls mainly in the Mid-Western, NorthEast and Boreal-Central regions. The spring GPP anomalies, broken out by subregion contribution, are shown in Fig. 9, and it is easily seen that the three aforementioned regions play a large role in determining the seasonal variability. The largest spring anomaly (of the same sign as the continental-scale seasonal anomaly) is from the MidWest, NorthEast or Boreal-Central region in 16 of 24 yr, one of the top two in 20 of 24 yr, and at least one of these regions is in the top three anomalies in 23 of 24 yr. In 4 yr (1983, 1987, 1997, 2002), these three regions all have the same sign on their anomaly, and are the top three anomalies in terms of the magnitude of GPP variability that determines continental-scale GPP variability in spring.

Temperature is the driving mechanism for a large portion of the springtime variability in this region. Generally, an early spring results in increased GPP. However, there are also portions of Texas and the Dakotas where, even in spring, the available soil moisture explains most of the variability when compared with other mechanisms.

Springtime GPP variability, when correlated with modes of climate variability, show no strong relationships over the region shown in Fig. 8 when compared concurrently or with a 1-season lag. ENSO index is positively correlated with warmer temperatures along the southern edge of the Great Lakes and in Alaska/Yukon when springtime temperature is compared with winter index. The northern area moves eastward and expands in size when spring temperature is correlated to spring ENSO index. The correlation to GPP is smaller, partially due to low spring GPP in the north. There is virtually no correlation between the NAM and either temperature or GPP at a lag of one season (spring GPP/temperature correlated with winter NAM index). When concurrent NAM index and temperature/GPP are compared in spring, there is a large band extending from Alaska through the Prairie Provinces where temperature is positively correlated to the NAM. The GPP correlation is strongest for a region extending from Oklahoma through Louisiana. Therefore, although there are portions of the pattern shown in Fig. 8 where GPP anomaly can be tied a particular climate index, no one index or mechanism explains the region-wide behaviour.

3.6. *Comparison with observations*

Rigorous comparison of our results with observational data is not possible, but we can compare our results from Fig. 7 with studies from the literature. In general, we find that grasslands are most sensitive to soil moisture as a mechanism that influences GPP. This is consistent with the results of Flanagan et al. (2002), who looked at 3 yr of meteorological and eddy covariance flux data from Lethbridge (49°N/112°W). Meyers (2001) also show strong dependence between soil moisture and GPP in an Oklahoma grassland (35°N/98°W) when evaluating multiple years of observations. Kjelgaard et al. (2008) report a strong correlation between precipitation and GPP in the Texas 'Hill Country' of the southern plains (30–32°N/100–105°W), which is inconsistent with our findings. However, in this case the locally shallow soil (<50 cm) may reduce the importance of soil moisture storage. SiB uses globally uniform soil depth, and so cannot reproduce this result at this time. Zhang et al. (2007b) compared a piecewise regression model of GPP to flux tower data and to GPP modelled using MODIS over the high plains region of the United States. Although soil moisture was not a

component of the model, the authors allude to the importance of moisture holding capacity to GPP in the region.

We find that GPP variability in the northeastern quadrant of NA is principally dependent on temperature. Conceptually, this can be thought of as a lengthening of the growing season correlating to high seasonal or annual GPP. This result is consistent with that of Richardson et al. (2009), who found growing season length was a significant driver of GPP variability at two flux tower sites in the northeastern United States. Urbanski et al. (2007) found temperature to be a driver of GPP variability at Harvard Forest in Massachusetts. During the 13 yr of their study, the largest annual GPP occurred during a year with extremely early canopy development. The year with the smallest annual GPP was also a year with an early canopy. However, in this case low temperature and insolation in early summer acted to suppress GPP. They found that soil moisture was unrelated to seasonal or annual GPP variability, except during the late summer. This suggests that temperature, while an important driver of GPP variability, is not the sole influencing factor. This is supported by Fig. 7, which shows that while temperature is the dominant driver of GPP variability the fraction of variability explained is relatively low.

Three different-aged Douglas-fir stands on Vancouver Island (British Columbia, Canada) were studied by Jassal et al. (2009). They found that summertime GPP was water limited. However, they also noted that winter season GPP is energy (or light) limited, and the largest annual GPP occurred during the warmest year of their observational record. This variability in the Pacific Northwest is not wholly inconsistent with our results. We find a heterogeneous situation in the region (Fig. 7, panel a), with pixels showing highest GPP dependence on soil moisture, temperature and radiation in close proximity to each other. These results, although not conclusive, indicate a general correspondence between several observational studies and our results as indicated in Fig. 7. We have not found observational studies that directly contradict our analysis of the mechanisms that drive variability in GPP.

4. Summary and Conclusions

As global atmospheric CO_2 levels rise, the exchange between the atmosphere and terrestrial biosphere is important for two reasons: First, around half of the anthropogenic CO_2 currently emitted is taken up by the oceans and land (the 'missing sink'), and secondly, vegetation behaviour plays an important role in determining the exchange of energy, mass and momentum between the atmosphere and land surface. Understanding of present-day ecophysiological behaviour is critical to predictions of future climate.

There has been an observed increase in the positive phase of the NAM (or NAO; Hurrell, 1995; Hurrell et al., 2001) in recent years, which has been positively correlated to increased carbon uptake in Eurasia (Schaefer et al., 2002; Buermann et al., 2003; Russell and Wallace, 2004). The causal links are simple to follow. A tightening of the polar vortex results in anomalous intrusions of warm maritime air onto the continent, resulting in an extension of growing season due to warmer spring and/or fall. If we have a scientific basis for predicting a continued persistence in the positive phase of the NAM, we can make predictions of ecophysiological response with considerable confidence.

In NA, the situation is much less clear. We have not been able to find a consistent, continent-wide vegetation response to either ENSO or NAM, and this result is consistent with previous work (i.e. Zhou et al., 2001; Schaefer et al., 2002; Russell and Wallace, 2004). Part of the problem is the large latitudinal extent of NA, further complicated by the presence of large mountain chains running along almost the entire western continental boundary from north to south. These mountains influence and disrupt circulation, and have a large impact on weather and climate. Secondly, while the situation in Eurasia can be easily attributed to temperature, in NA temperature and precipitation are secondary in importance to soil moisture availability. This can be seen in Fig. 10, which shows the lag-correlated coefficient of determination (R^2), calculated as

$$R^2 = \frac{\overline{X'G'}}{\overline{X'^2}}, \tag{2}$$

where R^2 is the coefficient of determination, X' is the meteorogical forcing anomaly and G' is the GPP anomaly.

In eq. (2), the overbar represents the mean of all gridcells on the continent (weighted by cosine of latitude), and covariance is calculated for multiple lags (zero, one, two, etc. months to the end of the year). With these plots, we can determine what fraction of the variability of a particular month's GPP anomaly is explained by the variability in meteorological forcing during the same or a prior month. To read Fig. 10, locate the desired month on the y-axis and move horizontally to the diagonal line. The value or colour at this point represents the lag-zero relationship between GPP and the chosen meteorological variable. Moving to the right, the explained variability in GPP at increasing lag is shown. The vertical axis shows the month of the forcing anomaly, and the x-axis shows the month of GPP response.

There are several interesting features of Fig. 10. First, the lack of variability explained solely by temperature is dramatic. A slight signal in the spring and fall can be seen, with spring having a longer influence than fall. There is a slight negative influence of temperature in midsummer, which is intuitive. A hot summer can impose stress on vegetation. Precipitation has more overall influence than temperature, mainly during the summer months when ecosystems can respond quickly to precipitation events. Radiation has almost no influence, on a continental basis.

The idea that soil moisture availability has the most power to explain North American GPP variability is supported by the lower right panel in Fig. 10. The fraction of variability explained is much higher that any other mechanism, and the lag covariance has influence for a much longer period of time. Up to 25% of

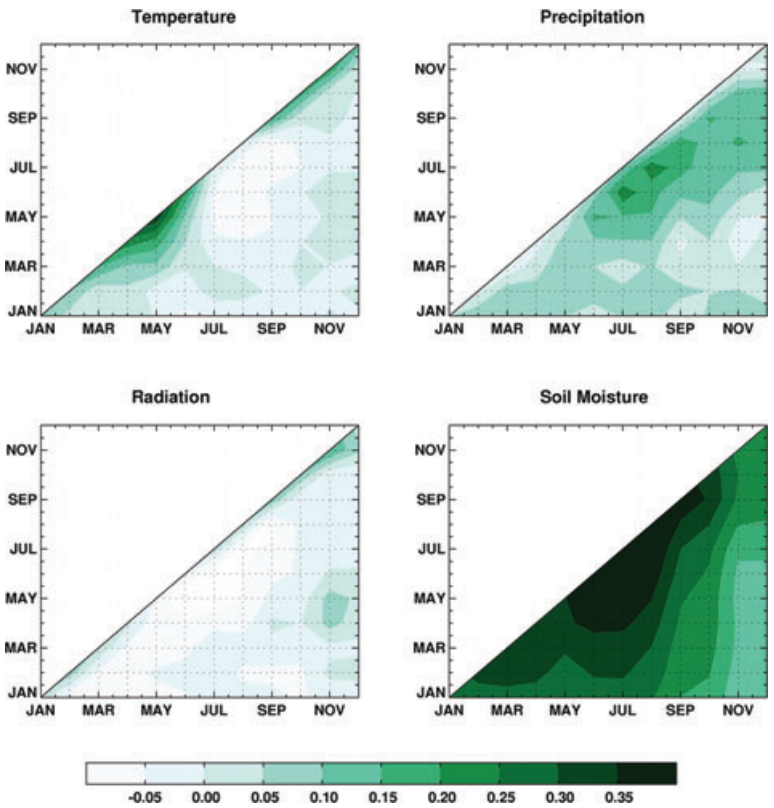

Fig. 10. Lag covariance (divided by total variance) of GPP to anomalies in temperature (upper left), precipitation (upper right), radiation (lower left) and soil moisture availability (lower right). Axes represent time, shading shows increasing covariance from light to dark. Lag covariance is found by following the position of a month on the vertical axis towards the right along the dashed horizontal line. Numerical value represents fraction of total variance for GPP in a given month explained by variance in forcing mechanism.

August GPP variability can be explained by January/February soil moisture anomaly. This reinforces the idea that we cannot point to a single meteorological driver to explain vegetation response on the continent. Soil moisture availability is defined by unique combinations of precipitation and temperature, and is necessarily integrated through time with respect to both snow and infiltration rate.

When continental GPP is partitioned temporally, spring is the season that most frequently contributes more to the annual anomaly than any other season. However, for a given region, the annual variability is not confined to spring—it is common to see almost any season except winter contain the largest fraction of the annual anomaly for a region. Springtime meteorological variability, generally in the form of anomalously warm (cool) temperature, is correlated with anomalously high (low) GPP over large areas north of the 40th parallel. The desert southwest, not surprisingly, is tightly coupled with precipitation and soil moisture availability on both an annual and seasonal basis.

It is intuitive that spring is the season that most commonly determines the annual GPP anomaly. One would expect that an early or late spring bud-burst and leaf-out would have an impact on annual carbon budget. EOF analysis reveals a coherent region of the continent, extending along 95° degrees west longitude from the Gulf of Mexico through the prairie provinces of Canada and extending into New England, that exhibits consistent springtime variability. This region commonly determines the sign of the continental GPP anomaly for the spring. As spring is the largest seasonal anomaly for almost half of the simulated years, this region is the closest we can find to a bellwether for continental-scale GPP variability. This region is not tightly coupled to any single measurement of climate variability.

At present, we cannot make statements about North American carbon uptake based on the values of climate indices. For example, Hurrell (1995) reports on a persistent elevation of the NAO index during the 1980s, but we see no corresponding response in either regional- or continental-scale GPP. A high positive-phase ENSO may suggest anomalously large GPP in the southwestern United States in the spring, or a tightening of the polar vortex may imply an early spring in northern Canada, but neither effect is large enough to have implications on continental-scale carbon flux on a seasonal or annual basis. The pattern in coherent springtime GPP variability that we find must be explained by another method.

5. Acknowledgments

This research was sponsored by the National Science Foundation Science and Technology Center for Multi-Scale Modeling of Atmospheric Processes, managed by Colorado State University under cooperative agreement No. ATM-0425247. This research

was also funded by Department of Commerce/National Oceanic and Atmospheric Administration contract NA08AR4320893, NASA contracts NNX06AC75G and NNX08AM56G, Department of Energy contract DE-FG02-06ER64317 and NICCR contract MTU050516Z14. The authors would like to acknowledge D.W.J. Thompson and A.H. Butler for assistance with statistical analysis, and M.D. Branson for graphical support.

References

Adler, R. F., Huffman, G. J., Chang, A., Ferraro, R., Xie, P. and co-authors. 2003. The Version 2 Global Precipitation Climatology Project (GPCP) Monthly Precipitation Analysis (1979-Present). *J. Hydrometeor.* **4**, 1147–1167.

Baker, D. F., Law, R. M., Gurney, K. R., Rayner, P., Peylin, P. and co-authors. 2006. TransCom 3 inversion intercomparison: impact of transport model errors on the interannual variability of regions CO_2 fluxes, 1988-2003. *Global Biogeochem. Cycles* **20**, GB1002, doi:10.1029/2004GB002439.

Baker, I. T., Denning, A. S., Hanan, N., Prihodko, L., Vidale, P.-L. and co-authors. 2003. Simulated and observed fluxes of sensible and latent heat and CO_2 at the WLEF-TV Tower using SiB2.5. *Global Change Biol.* **9**, 1262–1277.

Baker, I. T., Prihodko, L., Denning, A. S., Goulden, M., Milller, S. and co-authors. 2008. Seasonal drought stress in the Amazon: reconciling models and observations. *J. Geophys. Res.* **113**, G00B01, doi:10.1029/2007JG000644.

Ball, J. T., Woodrow, I. E. and Berry, J. A. 1987. A model predicting stomatal conductance and its contribution to the control of photosynthesis under different environmental conditions. *Prog. Photosyn. Res.* IV, ISBN 9024734533, J. Biggens ed., Hijhoff Publishers, the Netherlands.

Barnston, A. G. and Livezy, R. E. 1987. Classification, seasonality, and persistence of low-frequency atmospheric circulation patterns. *Mon. Wea. Rev.* **115**(6), 1083–1126.

Brown, M. E., Pinzon, J. and Tucker, C. J. 2004. New vegetation index dataset available to monitor global change. *EOS Trans.* **85**, 565, doi:10.1029/2004EO520003.

Bretherton, C. S., Widmann, M., Dymnikov, V. P., Wallace, J. M. and Bladé, I. 1998. The effective number of spatial degrees of freedom of a time-varying field. *J. Clim.* **12**, 1990–2009.

Buermann, W., Anderson, B., Tucker, C. J., Dickinson, R. E., Lucht, W. and co-authors. 2003. Interannual covariability in Northern Hemisphere air temperatures and greenness associated with El Niño-Southern Oscillation and the Arctic Oscillation. *J. Geophys. Res.* **108**(D13), 4396, doi:10.1029/2002/JD002630.

Collatz, G. J., Ball, J. T., Grivet, C. and Berry, J. A. 1991. Physiological and environmental regulation of stomatal conductance, photosynthesis and transpiration: a model that includes a laminar boundary layer. *Agric. Forest Meteor.* **54**, 107–136.

Collatz, G. J., Ribas-Carbo, M. and Berry, J. A. 1992. Coupled photosynthesis-stomatal conductance model for leaves of C4 plants. *Aust. J. Plant Physiol.* **19**(5), 519–538.

Colello, G. D., Grivet, C., Sellers, P. J. and Berry, J. A. 1998. Modelling of energy, water and CO_2 flux in a temperate grassland ecosystem with SiB3: May-October 1987. *J. Atmos. Sci.* **55**, 1141–1169.

Corbin, K. D., Denning, A. S., Lu, L., Wang, J.-W. and Baker, I. T. 2008. Possible representation errors in inversions of satellite CO_2 retrievals. *J. Geophys. Res.* **113**, D02301, doi:10.1029/2007JD008716.

Costa, M. H. and Foley, J. A. 1998. A comparison of precipitation datasets for the Amazon basin. *Geophys. Res. Lett.* **25**(2), 155–158.

Cotton, W. R., Pielke, R. A., Walko, R. L., Liston, G. E., Tremback, C. J. and co-authors. 2003. RAMS 2001: current status and future directions. *Meteorol. Atmos. Phys.* **82**, 5–29.

Cox, P. M., Betts, R. A., Jones, C. D., Spall, S. A. and Totterdell, I. J. 2000. Acceleration of global warming due to carbon-cycle feedback in a coupled climate model. *Nature* **408**, 184–187.

Dai, Y., Zeng, X., Dickinson, R. E., Baker, I., Bonan, G. and co-authors. 2003. The common land model (CLM). *B. Am. Meteorol. Soc.* **84**, 1013–1023.

DeFries, R. S. and Townshend, J. R. G. 1994. NDVI-derived land cover classification at a global scale. *Int. J. Remote Sens.* **15**(17), 3567–3586.

Denning, A. S., Collatz, G. J., Zhang, C., Randall, D. A., Berry, J. A. and co-authors. 1996. Simulations of terrestrial carbon metabolism and atmospheric CO_2in a general circulation model. Part 1: Surface carbon fluxes. *Tellus B* **48B**, 521–542.

Denning, A. S., Nicholls, M., Prihodko, L., Baker, I., Vidale, P.-L. and co-authors. 2003. Simulated and observed variations in atmospheric CO_2 over a Wisconsin forest using a coupled ecosystem-atmosphere model. *Global Change Biol.* **9**, 1241–1250.

Enfield, D. B. and Birkes, D. S. 1993. Probabilistic outlooks for El Niño recurrences. Tropical Oceans Global Atmosphere (TOGA) Notes, No. 11, 1–4, April 1993.

Farquhar, G. D., von Caemmerer, S. and Berry, J. A. 1980. A biochemical model of photosynthetic CO_2 assimilation in leaves of C3 species. *Planta* **149**, 78–90.

Flanagan, L. B., Wever, L.A. and Carlson, P. J. 2002. Seasonal and interannual variation in carbon dioxide exchange and carbon balance in a northern temperate grassland. *Global Change Biol.* **8**, 599–615.

Gao, Z., Chae, N., Kim, J., Hong, J., Choi, T. and co-authors. 2004. Modeling of surface energy partitioning, surface temperature, and soil wetness in the Tibetan prairie using the Simple Biosphere Model 2 (SiB2). *J. Geophys. Res.* **109**, D06102, doi:10.1029/2003JD004089.

Global Soil Data Task Group. 2000. Global Gridded Surfaces of Selected Soil Characteristics (IGBP-DIS). [Global Gridded Surfaces of Selected Soil Characteristics (International Geosphere-Biosphere Programme—Data and Information System)]. Data set. Available at: http://www.daac.ornl.gov from Oak Ridge National Laboratory Distributed Active Archive Center, Oak Ridge, Tennessee, USA, doi:10.3334/ORNLDAAC/569.

Gu, L., Baldocchi, D., Verma, S. B., Black, T. A., Vesala, T. and co-authors. 2002. Advantages of diffuse radiation for terrestrial ecosystem productivity. *J. Geophys. Res.* **107**(D6), doi:10.1029/2001JD001242.

Gurney, K. R., Law, R. M., Denning, A. S. Rayner, P. J., Baker, D. and co-authors. 2002. Towards robust regional estimates of CO_2 sources and sinks using atmospheric transport models. *Nature* **415**, 626–629.

Gurney, K. R., Baker, D., Rayner, P. and Denning, A. S. 2008. Interannual variations in continental-scale net carbon exchange and sensitivity to observing networks estimated from atmospheric CO_2 inversions for the period 1980 to 2005. *Global Biogeochem. Cycles* **22**, GB3025, doi:10.1029/2007GB003082.

Hanan, N. P., Berry, J. A., Verma, S. B., Walter-Shea, E. A. Suyker, A. E. and co-authors. 2005. Testing a model of CO_2, water and energy exchange in Great Plains tallgrass prairie and wheat ecosystems. *Agric. Forest Meteor.* **131**, 162–179.

Higgins, R. W., Chen, Y. and Douglas, A. V. 1999. Interannual variability of the North American warm season precipitation regime. *J. Clim.* **12**, 653–680.

Hurrell, J. W. 1995. Decadal trends in the North Atlantic Oscillation: regional temperatures and precipitation. *Science* **269**, 676–679.

Hurrell, J. W., Kushnir, Y. and Visbeck, M. 2001. The North Atlantic Oscillation. *Science* **291**, 603–605.

IPCC (2007), Climate Change 2007. *The Physical Science Basis. Contribution of Working Group I to the Fourth Assessment Report of the Intergovernmental Panel on Climate Change* (eds. Solomon, S., D. Qin, M. Manning, Z. Chen, M. Marquis, K.B. Averyt, M. Tignor and H.L. Miller). Cambridge University Press, Cambridge, UK and New York, USA, 996 pp.

Jackson, R. B., Canadell, J., Ehleringer, J. R., Mooney, H. A., Sala, O. E. and co-authors. 1996. A global analysis of root distributions for terrestrial biomes. *Oecologia* **180**(3), 389–411.

Jassal, R. S., Black, T. A., Spittlehouse, D. L., Brümmer, C. and Nesic, Z. 2009. Evapotranspiration and water-use efficiency in different-aged Pacific Northwest Douglas-fir stands. *Agric. Forest Meteor.* **149**, 1168–1178.

Kalnay, E., Kanamitsu, M., Kistler, R., Collins, W., Deaven and co-authors. 1996. The NCEP/NCAR 40-year reanalysis project. *Bull. Am. Met. Soc.* **77**(3), 437–471.

Kanamitsu, M., Ebisuzaki, W., Woollen, J., Yang, S.-K., Hnilo, J. J. and co-authors. 2002. NCEP-DOE AMIP-II Reanalysis (R-2). *Bull. Am. Meterol. Soc.* **83**(11), 1631–1643.

Keeling, C. D. and Whorf, T. P., Whalen, M. and van der Plicht, J. 1995. Interannual extremes in the rate of rise of atmospheric carbon dioxide since 1980. *Nature* **375**, 666–670.

Kjelgaard, J. F., Heilman, J. L., McInnes, K. J., Owens, M. K. and Kamps, R. H. 2008. Carbon dioxide exchange in a subtropical mixed C_3/C_4 grassland on the Edwards Plateau, Texas. *Agric. Forest Meteor.* **148**, 953–963.

Mauget, S. A. 2003. Intra- to multidecadal climate variability over the continental United States: 1932-99. *J. Clim.* **16**, 2215–2231.

Meyers, T. P. 2001. A comparison of summertime water and CO_2 fluxes over rangeland for well watered and drought conditions. *Agric. Forest Meteor.* **106**, 205–214.

Nicholls, M. E., Denning, A. S., Prihodko, L., Vidale, P.-L. Baker, I. T. and co-authors. 2004. A multiple-scale simulation of variations in atmospheric carbon dioxide using a coupled biosphere-atmosphere model. *J. Geophys. Res.-Atmos.* **109**, D18117, doi:10.1029/2003JD004482.

Niyogi, D., Chang, H.-I. Saxena, V. K., Holt, T., Alapaty, K. and co-authors. 2004. Direct observation of the effects of aerosol loading on net ecosystem CO_2 exchanges over different landscapes. *Geophys, Res. Lett.* **31**, L20506, doi:10.1029/2004GL020915.

North, G. R., Bell, T. L., Cahalan, R. F. and Moeng, F. J. 1982. Sampling errors in the estimation of empirical orthogonal functions. *Mon. Wea. Rev.* **110**, 699–706.

Oeschger, H., Seigenthaler, U., Schotterer, U. and Gugelman, A. 1975. A box diffusion model to study the carbon dioxide exchange in nature. *Tellus* **17**(2), 168–192.

Peters, W., Jacobsen, A. R., Sweeney, C., Andrews, A. E., Conway, T. J. and co-authors. 2007. An atmospheric perspective on north American carbon dioxide exchange: CarbonTracker. *Proc. Nat. Acad. Sci.* **104**(48), 18 925–18 930, doi:10.1073/pnas.0708986104.

Pielke, R. A., Cotton, W. R., Walko, R. L., Tremback, C. J., Lyons, W. A. and co-authors. 1992. A comprehensive meteorological modeling system: RAMS. *Meteorol. Atmos. Phys.* **49**, 69–91.

Pinzon, J., Brown, M. E. and Tucker, C. J. 2006. Satellite time series correction of orbital drift artifacts using empirical mode decomposition. In: *Applications of Empirical Mode Decomposition*, Chapter 10, Part II, ed. N. Huang.

Quadrelli, R. and Wallace, J. M. 2004. A simplified linear framework for interpreting patterns of northern hemisphere wintertime climate variability. *J. Clim.* **17**(19), 3728–3744.

Randall, D. A., Dazlich, D. A., Zhang, C., Denning, A. S., Sellers, P. J. and co-authors. 1996. A revised land surface parameterization (SiB2) for GCMs. Part III: The greening of the Colorado State University general circulation model. *J. Clim.* **9**(4), 738–763.

Rasmussen, E. M. and Carpenter, T. H. 1982. Variations in tropical sea surface temperature and surface wind fields associate with the southern oscillation/El Niño. *Mon. Wea. Rev.* **110**, 354–384.

Richardson, A. D., Hollinger, D. Y., Dail, D. B., Lee, J. T., Munger, J. W. and co-authors. 2009. Influence of spring phenology on seasonal and annual carbon balance in two contrasting New England forests. *Tree Physiol.* **29**, 321–331, doi:10.1093/treephys/tpn040.

Rödenbeck, C., Houweling, S., Gloor, M. and Heimann, M. 2003. CO_2 flux history 1982-2001 inferred from atmospheric data using a global inversion of atmospheric transport. *Atmos. Chem. Phys.* **3**, 1919–1964.

Roderick, M. L., Farquhar, G. D., Berry, S. L. and Noble, I. R. 2001. On the direct effect of clouds and atmospheric particles on the productivity and structure of vegetation.*Oecologia*, **129**, 21–30, doi:10.1007/s004420100760.

Russell, J. L. and Wallace, J. M. 2004. Annual carbon dioxide drawdown and the Northern Annular Mode. *Global Biogeochem. Cycles* **18**, GB1012, doi:10.1029/2003GB002044.

Sato, N., Sellers, P. J., Randall, D. A., Schneider, E. K., Shukla, J. and co-authors. 1989. Implementing the Simple Biosphere Model (SiB) in a General Circulation Model: Methodologies and results. NASA Contractor Report 195509, 76pp.

Schaefer, K., Denning, A. S., Suits, N., Kaduk, J., Baker, I. and co-authors. 2002. Effect of climate on interannual variability of terrestrial CO_2 fluxes. *Global Biogeochem. Cycles* **16**(4), 1102, doi:10.1029/2002GB001928.

Schaefer, K., Collatz, G. J., Tans, P., Denning, A. S., Baker, I. and co-authors. 2008. The combined Simple Biosphere/Carnegie-Ames-Stanford Approach (SiBCASA) terrestrial carbon cycle model. *J. Geophys. Res.* **113**, G03034, doi:10.1029/2007JG000603.

Sellers, P. J., Mintz, Y., Sud, Y. C. and Dalcher, A. 1986. A Simple Biosphere Model (SiB) for use within General Circulation Models. *J. Atmos. Sci.* **43**(6), 505–531.

Sellers, P. J. and Dorman, J. L., 1986. Testing the Simple Biosphere Model (SiB) using point micrometeorological and biophysical data. *L. Clim. Appl. Meteor.* **26**, 622–650.

Sellers, P. J., Berry, J. A., Collatz, G. J., Field, C. B. and Hall, F. G. 1992. Canopy reflectance, photosynthesis, and transpiration III. A reanalysis using improved leaf models and a new canopy integration scheme. *Remote Sens. Environ.* **42**, 187–216.

Sellers, P. J., Randall, D. A., Collatz, G. J., Berry, J. A., Field, C. B. and co-authors. 1996a. A revised land surface parameterization (SiB2) for atmospheric GCMs. Part I: Model formulation. *J. Clim.* **9**(4), 676–705.

Sellers, P. J., Los, S. O., Tucker, C. J., Justice, C. O., Dazlich, D. A. and co-authors. 1996b. A revised land surface parameterization (SiB2) for atmospheric GCMs. Part II: The generation of global fields of terrestrial biophysical parameters from satellite data. *J. Clim.* **9**(4), 706–737.

Sellers, P. J., Dickinson, R. E., Randall, D. A., Betts, A. K., Hall, F. G. and co-authors. 1997. Modeling the exchanges of energy, water, and carbon between continents and the atmosphere. *Science* **275**, 502–509.

Sheppard, P. R., Comrie, A. C., Packin, G. D., Angersbach, K. and Hughes, M. K. 2002. The climate of the US Southwest. *Clim. Res.* **21**, 219–238.

Tans, P. P., Fung, I. Y. and Takahashi, T. 1990. Observational constraints on the global atmospheric CO_2 Budget. *Science* **247**(4949), 1431–1438.

Thompson, D. W. J. and Wallace, J. M. 2000. Annular modes in the extratropical circulation. Part I: month-to-month variability. *J. Clim.* **13**, 1000–1016.

Tucker, C. J., Pinzon, J., Brown, M. E., Slayback, D. A., Pak, E. W. and co-authors. 2005. An extended AVHRR 8-km NDVI data set compatible with MODIS and SPOT vegetation NDVI data. *Int. J. Rem. Sens.* **26**(20), 4485–4498.

Urbanski, S., Barford, C., Wofsy, S., Kucharik, C., Pyle, E. and co-authors. 2007. Factors controlling CO_2 exchange on timescales from hourly to decadal at Harvard Forest. *J. Geophys. Res.* **112**, G02020, doi:10.1029/2006JG000293.

Vidale, P. L. and Stöckli, R. 2003. Prognostic canopy air solutions for land surface exchanges. *Theor. Appl. Climatol.* **80**, 245–257.

Wang, J.-W., Denning, A. S., Lu, L., Baker, I. T., Corbin, K. D. and co-authors. 2007. Observations and simulations of synoptic, regional, and local variations in atmospheric CO_2. *J. Geophys. Res.* **112**, D04108, doi:10.1029/2006JD007410.

Wolter, K. and Timlin, M. S. 1993. Monitoring ENSO in COADS with a seasonally adjusted principal component index. In: *Proceedings of the 17th Climate Diagnostics Workshop, Norman, OK, NOAA/NMC/CAC, NSSL, Oklahoma Climate Survey*, CIMMS and the School of Meteorology, University of Oklahoma, 52–57.

Wolter, K. and Timlin, M. S. 1998. Measuring the strength of ENSO events - how does 1997/98 rank? *Weather* **53**, 315–324.

Zhang, C., Dazlich, D. A., Randall, D. A., Sellers, P. J. and Denning, A. S. 1996. Calculation of the global land surface energy, water and CO_2 fluxes with an off-line version of SiB2. *J. Geophys. Res.* **101**(D14), 19 061–19 075.

Zhang, K., Kimball, J. S., Zhao, M., Oechel, W. C., Cassano, J., and co-authors. 2007a. Sensitivity of pan-Arctic terrestrial net primary productivity simulations to daily surface meteorology from NCEP-NCAR and ERA-40 reanalyses. *J. Geophys. Res.* **112**, G01011, doi:10.1029/2006JG000249.

Zhang, L., Wylie, B., Loveland, T., Fosnight, E., Tieszen, L. L. and co-authors. 2007b. Evaluation and comparison of gross primary production estimates for the Northern Great Plains grasslands. *Remote Sens. Environ.* **106**, 173–189.

Zhao, M. and Running, S. W., 2006. Sensitivity of Moderate Resolution Imaging Spectroradiometer (MODIS) terrestrial primary production to the accuracy of meteorological reanalyses. *J. Geophys. Res.*, **112**, G01002, doi:10.1029/2004JG000004.

Zhou, L., Tucker, C. J., Kaufmann, R. K., Slayback, D., Shabanov, N. V. and co-authors. 2001. Variations in northern vegetation activity inferred from satellite data of vegetation index during 1981 to 1999. *J. Geophys. Res.* **106**(D17), 20 069–20 083.

Tellus
SERIES B
CHEMICAL
AND PHYSICAL
METEOROLOGY
PUBLISHED BY THE INTERNATIONAL METEOROLOGICAL INSTITUTE IN STOCKHOLM

Tellus (2010), 62B, 550–572

TELLUS

Using continental observations in global atmospheric inversions of CO_2: North American carbon sources and sinks

By M. P. BUTLER[1]*, K. J. DAVIS[1], A. S. DENNING[2] and S. R. KAWA[3], [1]*Department of Meteorology, The Pennsylvania State University, University Park, PA 16802, USA*; [2]*Department of Atmospheric Science, Colorado State University, Fort Collins, Colorado*; [3]*NASA Goddard Space Flight Center, Greenbelt, MD, USA*

(Manuscript received 30 December 2009; in final form 22 July 2010)

ABSTRACT

We evaluate North American carbon fluxes using a monthly global Bayesian synthesis inversion that includes well-calibrated carbon dioxide concentrations measured at continental flux towers. We employ the NASA Parametrized Chemistry Tracer Model (PCTM) for atmospheric transport and a TransCom-style inversion with subcontinental resolution. We subsample carbon dioxide time series at four North American flux tower sites for mid-day hours to ensure sampling of a deep, well-mixed atmospheric boundary layer. The addition of these flux tower sites to a global network reduces North America mean annual flux uncertainty for 2001–2003 by 20% to 0.4 Pg C yr^{-1} compared to a network without the tower sites. North American flux is estimated to be a net sink of 1.2 $\pm$ 0.4 Pg C yr^{-1} which is within the uncertainty bounds of the result without the towers. Uncertainty reduction is found to be local to the regions within North America where the flux towers are located, and including the towers reduces covariances between regions within North America. Mid-day carbon dioxide observations from flux towers provide a viable means of increasing continental observation density and reducing the uncertainty of regional carbon flux estimates in atmospheric inversions.

1. Introduction

About half of the anthropogenic carbon emitted into the atmosphere remains in the atmosphere each year. The remainder is taken up by the ocean and terrestrial ecosystems through the processes responsible for the natural exchange of carbon between the atmosphere and terrestrial vegetation and the surface ocean (Denman et al., 2007; Forster et al., 2007). Numerous studies (Myneni et al., 2001; Nemani et al., 2003; Potter et al., 2003) show that climate cycles, local weather and ecosystem conditions all affect the interannual variability of this uptake of carbon. Our understanding of the mechanisms governing the dynamics of the carbon cycle has been hampered by a limited ability to locate and quantify these exchanges at sufficiently fine temporal and spatial resolution (Bousquet et al., 2000; Gurney et al., 2002; Ciais et al., 2005; Baker et al., 2006; Peters et al., 2007). Accurate and precise quantification of sources and sinks at regional and continental scales is likely to be increasingly important for evaluation and monitoring of carbon management policies.

Global atmospheric inversions have been used to infer sources and sinks of carbon (both natural and anthropogenic) at continental and ocean basin scale from atmospheric measurements of carbon dioxide using tracer transport models. Model intercomparison projects, including the TransCom (Atmospheric Tracer Transport Model Intercomparison Project) series (Gurney et al., 2002; Gurney et al., 2004; Baker et al. 2006), have been designed to attribute the uncertainties in the continental and ocean basin fluxes estimated by this method. These studies show that transport model differences and the uneven and sparse global distribution of atmospheric carbon dioxide measurements contribute to the uncertainty of the inverse flux estimates. While transport models are improving and the global measurement network for carbon dioxide is expanding, there are still fundamental representation and aggregation errors (Kaminski et al., 2001; Engelen et al., 2002) inherent in the global atmospheric inversion method. There is a mismatch in space and time resolution between the transport models (grid boxes and minutes), the observations (points in space and time) and the inversion solution (continents or subcontinents and months or weeks). Observations are subject to local atmospheric variations. These subgrid

*Corresponding author.
e-mail: mpbutler@meteo.psu.edu
DOI: 10.1111/j.1600-0889.2010.00501.x

scale mesoscale variations are not explicitly accounted for in the transport models; however, we use these local observations to constrain continental and ocean basin results. In addition, global inversions typically require strong and uncertain assumptions about the correlation of fluxes and observations in space and time. If the inversion solution is constructed at the continental scale, for example, it is not possible to evaluate changes in fluxes from subregions within the continent. These strong assumptions about correlations of fluxes in space and time are a weakness; the strengths of such a continental scale global inversion method are the minimum number of unknowns and the global coverage. Some assumptions about coherence in space and time are essential; atmospheric observations will always be uneven and sparse at some level of resolution.

A compelling approach is to invert on the grid and time scale of the transport model (Kaminski et al., 2001; Engelen et al., 2002). Global atmospheric inversions at the spatial resolution of the transport model (e.g. Rödenbeck et al., 2003a; Gourdji et al., 2008; Mueller et al., 2008), aim for the finest resolution possible to minimize representation assumptions, at the expense of larger posterior covariances. Subsequent aggregation into coarser regional and temporal resolution is then used to lessen the posterior error. Regional atmospheric inversions target a geographically limited domain with finer spatial and temporal resolution (Gerbig et al., 2003; Peylin et al., 2005; Lauvaux et al., 2008; Schuh et al., 2009). Both of these approaches involve many more unknowns, which cannot be resolved independently given the current observation density. The underlying assumptions may be minimized, but at the expense of building prior covariance matrices and the increased computational costs required by the finer resolution.

In this experiment we take a pragmatic, middle-ground approach to the continental-scale global inversion by choosing a number of regions roughly matched to the observation density currently available. If we have chosen observation sites that are representative of the regions and sensitive to the surface exchanges in these regions, then we expect that posterior uncertainties and spatial correlations will be reduced and that the problem will be computationally tractable using simple inversion methods. Inversion results can be aggregated to the larger TransCom continental regions for comparison with published results. We can also test the ability of the expanded network to constrain the smaller regions with this method.

Typically global atmospheric measurement network sites have been chosen to facilitate sampling background concentrations of trace gases including carbon dioxide. These background measurement networks have yielded important understanding of interhemispheric gradients in carbon dioxide mixing ratios (Tans et al., 1990; Denning et al., 1995; Keeling et al., 1996) and of the mean annual cycles of carbon emissions and uptake (e.g. Keeling et al., 1995). These data, however, provide limited understanding of the continental carbon cycle. We cannot diagnose continental or regional scale fluxes and determine the factors influencing terrestrial fluxes without observing sites over the continents. Continental carbon dioxide measurements are characterized by strong diurnal and seasonal cycles that reflect a combination of biological fluxes and atmospheric boundary layer dynamics (Bakwin et al., 1998; Yi et al., 2001; Davis et al., 2003). Continental data also contain strong gradients driven by weather (e.g. Hurwitz et al., 2004; Wang et al., 2007; Parazoo et al., 2008). These strong, rapidly varying gradients in the observations may be difficult to simulate in the transport, but the continental data contain information needed to resolve regional sources and sinks of carbon with increasing spatial and temporal resolution.

In this paper, we use the Bayesian synthesis inversion method to demonstrate the impact of including more continental measurement sites in the global measurement network. The added sites are long-running eddy covariance flux towers with high precision carbon dioxide measurements calibrated to global standards. Carbon dioxide measurements at flux towers do not need to be calibrated to global standards for the calculation of net ecosystem exchange of carbon dioxide using the eddy covariance method. The sites used in this study, however, are part of a growing network where the calibration is done with the intent of providing data suitable for application to atmospheric inversion studies. The five towers used in this study have data available during the 2000–2004 time period. Increasing numbers of flux towers are incorporating the calibration processes into their routine processing; this offers opportunities for extending this research in the future.

We focus here on the effect on the North American carbon balance, recognizing the danger that, in an ill-conditioned problem such as this, increasing the density of observations in North America may introduce new challenges. For example, global inversions typically exhibit dipole behaviour or 'pair-sum' relationships (Rödenbeck et al., 2003a) where the flux as a sum for two regions can be constrained, while the individual regions cannot. Within North America we may discover dipoles between the subregions that were not apparent in the continental-scale inversion. With the exception of Boreal Asia, the Northern Hemisphere is well represented in the networks tested (Fig. 2). Concentrating observation sites in North America may highlight dipole relationships between Boreal Asia and other regions of the Northern Hemisphere. Some recent inversions, for example, find a larger terrestrial carbon sink in Europe (Baker et al., 2006; Mueller et al., 2008) and others in Asia (Rödenbeck et al., 2003a; Peters et al., 2007). Published inversion results also frequently disagree with estimates of carbon fluxes from biogeochemical models (Janssens et al., 2003; Peters et al., 2007; Potter et al., 2007). We will examine our results in this light, but concentrate on the uncertainty improvement of the added measurement sites in this paper.

In Section 2, we describe the estimation method. In Section 3, we present global and North American results for two typical global measurement networks and a third network including five additional continental sites. The results are discussed in

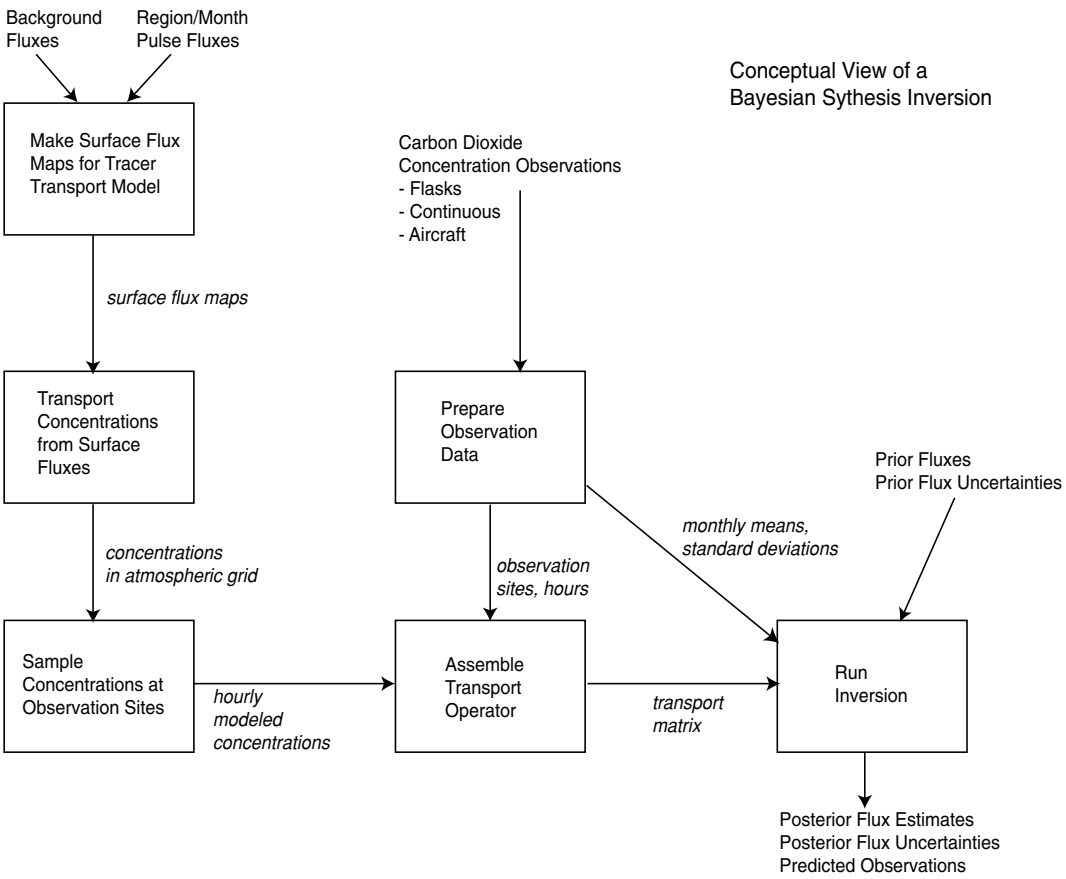

Fig. 1. Overview of the Bayesian synthesis inversion method.

Section 4. We conclude in Section 5 with recommendations for applicability of the method to future experiments.

2. Methods

2.1. Estimation method

The Bayesian synthesis inversion method used is shown in Fig. 1 and described by Enting (2002) and Tarantola (2005), with the experimental protocol (Gurney et al., 2000) following closely that of the TransCom interannual variability model intercomparisons (Baker et al., 2006; Gurney et al., 2008). We depart from the TransCom inversion method in a few important respects. (1) For observation data, we use monthly means and standard deviations derived directly from site observations of carbon dioxide (Rödenbeck et al., 2003b) instead of using a smoothed data product, such as GLOBALVIEW-CO2 (GLOBALVIEW-CO2, 2007) and assigned uncertainties (Baker et al., 2006). (2) We use annually varying meteorological driver data in our transport modelling. (3) Finally, we include biomass burning emissions explicitly.

The solution is for monthly carbon source/sink estimates (2000–2004) for 47 subcontinental regions and ocean basins using monthly mean carbon dioxide mixing ratio measurements. Figure 2 shows the region definitions and locations of the observing sites. The problem is ill-constrained due to the sparse and uneven distribution of observations; the method solves for adjustments to natural land– and ocean–atmosphere exchanges (referred to here as background fluxes) within the constraint of imposed prior uncertainties. Fossil fuel emissions and biomass burning emissions are assumed to be correct and not adjusted in the inversion process.

Following Baker et al. (2006), the atmospheric carbon dioxide at a measuring site can be represented as the linear combination of responses at the location to the background fluxes and to the unknown adjustment fluxes from each of the regions and months,

$$\mathbf{c}_{\mathrm{obs}} = \mathbf{c}_{\mathrm{fwd}} + \mathbf{H}\mathbf{x}, \tag{1}$$

where $\mathbf{c_{obs}}$ is the time series of monthly carbon dioxide observations, $\mathbf{c_{fwd}}$ is the modelled concentration time series using the background fluxes, $\mathbf{H}$ is a transport matrix (described below) and $\mathbf{x}$ are the unknown monthly adjustments to the background terrestrial and ocean fluxes for each of the 47 regions. Solving for the unknown monthly adjustments $\mathbf{x}$ is done, using a singular value decomposition approach for numerical stability (Rayner

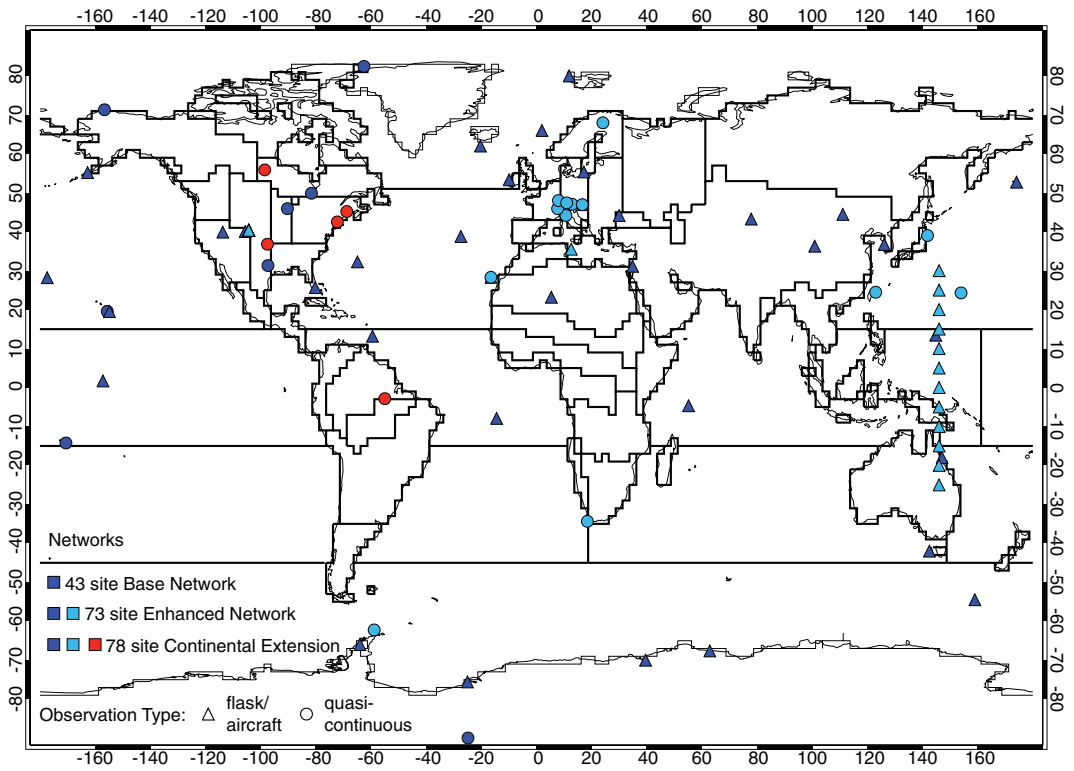

Fig. 2. Solid lines define the spatial scale of the inversion solution (36 land regions and 11 ocean regions). Symbols mark locations of the observation sites in the three networks tested: Base network (blue); Enhanced network (blue and cyan); Continental Extension network (blue, cyan, red). Symbol shapes indicate the type of observation: quasi-continuous (circle) and discrete (triangle).

et al., 1999), to the minimization of the cost function

$$J = (\mathbf{c_{obs}} - \mathbf{c_{fwd}} - \mathbf{Hx})^T \mathbf{R}^{-1} (\mathbf{c_{obs}} - \mathbf{c_{fwd}} - \mathbf{Hx}) + (\mathbf{x} - \mathbf{x_0})^T \mathbf{P}_0^{-1} (\mathbf{x} - \mathbf{x_0}) \quad (2)$$

where $\mathbf{R}$ is the covariance matrix specifying the observation, transport and representation error of the data, $\mathbf{x_0}$ are a priori estimates of the solution and $\mathbf{P_0}$ is the covariance matrix of uncertainties of these a priori estimates. In this experiment both $\mathbf{R}$ and $\mathbf{P_0}$ are described by diagonal matrices, as has been common practice in previous TransCom experiments (Gurney et al., 2002; Gurney et al., 2004; Baker et al., 2006). This cost function minimization is a least squares solution weighted by the variability of the observations and penalized for deviation from the a priori estimates. The analytical solution for the flux adjustments $\hat{\mathbf{x}}$ is

$$\hat{\mathbf{x}} = \left(\mathbf{H}^T \mathbf{R}^{-1} \mathbf{H} + \mathbf{P}_0^{-1}\right)^{-1} \left(\mathbf{H}^T \mathbf{R}^{-1} (\mathbf{c_{obs}} - \mathbf{c_{fwd}}) + \mathbf{P}_0^{-1} \mathbf{x_0}\right) \quad (3)$$

and the a posteriori covariance matrix is given by

$$\mathbf{P}^{-1} = \mathbf{P}_0^{-1} + \mathbf{H}^T \mathbf{R}^{-1} \mathbf{H} \quad (4)$$

allowing examination of the covariances for independence of the solution. This analytical a posteriori uncertainty is a function of the uncertainty of the prior flux estimate and the uncertainty attributed to the observations and assumes that the problem meets the requirements of the method. We have oversimplified both the data errors (uncertainty of observations and transport) and the model errors (prior flux uncertainty) by assuming they are independent and can be modelled using Gaussian distributions. Tarantola (2005) warns that the a posteriori solution may not be robust and may be particularly sensitive to outlier data points if these assumptions are not met. As a consequence, the accuracy of the a posteriori covariance is limited by the assumptions inherent in the a priori flux uncertainty and data uncertainty assignments. Even if the a posteriori covariance is optimistic, analysis of the region–region covariances provides valuable information about the flux estimates and the extent of the constraint provided by the network. Another product of this inversion method is a set of predicted observations, the carbon dioxide concentration values that would be expected at each observation site given the a posteriori flux solution. The predicted observations provide a basis for analysis of the data residuals, which cannot be done with the fluxes.

The analytical solution delivers an adjustment to the background fluxes for each region and month in 2000–2004. Results for the central years 2001–2003 are retained for analysis. The first and final year of the solution are discarded to minimize edge effects, including inaccuracies introduced by the spinup method described below and the length of time it takes an atmospheric signal to reach distant observation sites. All results reported here are the adjusted land and ocean fluxes including the assumed biomass burning emissions for each month in

order to compare with published results. The assumed background fossil emissions are not included. Choices for the components of the method shown in Fig. 1 follow.

2.2. Background fluxes

The terrestrial background flux is the annually varying hourly SiB3 terrestrial flux (Baker et al., 2008) as prepared for the TransCom continuous experiment (Law et al., 2008; Patra et al., 2008). An alternative terrestrial flux with monthly (but not diurnal or annual) variability, the CASA climatology (Randerson et al., 1997) used in previous TransCom experiments, is also tested to investigate the solution dependence on the terrestrial background flux used and the time resolution of the flux. The ocean background flux is the monthly climatology of Takahashi et al. (2002), also as used in the TransCom continuous experiment. The seasonally varying fossil fuel emissions, as described by Erickson et al. (2008), are based on the 1995 spatial distribution of Brenkert (1998) and Li (1996), with annual totals scaled to the appropriate years based on Marland et al. (2007). The interannually varying monthly biomass burning emissions are from the Global Fire Emissions Database version 2 (GFED2) (Giglio et al., 2006; van der Werf et al., 2006). Each background flux (4 tracers $\times$ 5 yr) is regridded to the horizontal spatial grid of the transport model and used as a surface boundary condition for a forward run from the beginning of the applicable year to the end of 2004. The model output is sampled hourly to allow for matching of sampling of the transport model output with the observations (see Section 2.8) when constructing the $c_{\mathbf{fwd}}$ time series represented in eq. (1).

2.3. Transport response functions

The 47 regions specified for the solution are shown in Fig. 2 and listed in Table 1. The 11 ocean regions are the same as those used in the TransCom experiments. The 36 land regions are conformable to the TransCom land regions. The Boreal Asia, Temperate Asia, Tropical Asia and Australia regions are defined as in TransCom. Remaining TransCom regions are subdivided into subregions: Boreal North America (3 regions); Temperate North America (7); Tropical America (3), Temperate South America (2), Europe (7), Northern Africa (5) and Southern Africa (5). These continental regions are subdivided, roughly according to biome, to test the degree to which the solutions can be constrained given current and future observing sites. For North America and Europe the number of regions is similar to the number of available continental observing sites. The results for these regions are aggregated to larger regions for reporting and comparison with published results.

To construct the transport matrix **H**, emissions of known magnitude (1 month duration at an annual rate of 1 Pg carbon emission) are run forward as inert species through the transport model for each region-month (47 regions $\times$ 12 months $\times$ 5 yr), beginning in the applicable month and year and ending after 25 months of transport or the end of 2004. Model output is sampled hourly at each observation location through the 25 months (or less) of each region-month transport run, and then assumed to remain at a constant well-mixed, residual level after the transport is terminated through the end of 2004. Longer transport runs showed that the assumption of a well-mixed concentration beyond 25 months is justified.

The flux spatial distributions (or flux patterns) for the transport response functions within each terrestrial region are based on annual NPP simulated by CASA monthly climatology (Randerson et al., 1997), scaled to the transport model grid cells within each region. The pattern is derived from the similar regional patterns in the TransCom experiments (Gurney et al., 2000) and regridded to the spatial resolution of the transport model used here. There is no variation by model grid cell within the ocean regions. These land and ocean flux patterns constitute a hard constraint in this inversion method. The inversion solution specifies the adjustment to the background flux for the region as a whole; the distribution of the flux within the region is fixed by these flux patterns.

2.4. Tracer transport model

The tracer transport model used in this experiment is the Colorado State University version of the NASA Parametrized Chemistry Tracer Model (PCTM), described in Kawa et al. (2004) which has participated in TransCom experiments. Winds, temperatures, diffusion coefficients and convective mass fluxes are from the NASA Goddard Earth Observation System 4 (GEOS-4) data assimilation system (Bloom et al., 2005). The 6-hourly meteorological driver data are linearly interpolated to the 15-min time step of the model. The model is run on a 2.5° longitude by 2.0° latitude grid, with 25 hybrid vertical layers. The model exhibited intermediate performance in the TransCom Interannual Variability model intercomparisons (Baker et al., 2006; Gurney et al., 2008) and is also one of the three models used in the Gurney et al. (2005) study of the potential bias in inversions caused by using non-varying background fossil emissions. Gurney et al. (2005) chose PCTM for its intermediate performance among the TransCom models with regard to key transport characteristics: the simulated annual zonal mean surface carbon dioxide concentration responses to non-varying fossil fuel emissions and, separately, to the neutral biosphere flux. The responses to these surface fluxes are dependent on the volume in which the surface fluxes are mixed (the planetary boundary layer depth), the seasonal phasing of the surface fluxes and the transport and the subgrid-scale parametrization used for vertical mixing. For PCTM, the interhemispheric gradient established by the fossil emissions is relatively large compared to the other TransCom models (Gurney et al., 2005), but there is a relatively weak seasonal rectifier (covariance of the terrestrial background flux and seasonal differences in vertical mixing close to the model

Table 1. Spatial resolution of the inversion with prior specifications and 2001–2003 mean annual posterior flux solution for the continental extension network. All units are in Pg C yr^{-1}. Aggregated land regions are shown in bold. Net posterior flux plus biomass burning emissions, but not fossil emissions

	Mean Annual Prior Specifications				Annual Mean Posterior Results		
	Prior Flux	Prior Error	Fossil Emiss.	Burning Emiss.	Post. Flux	Net Post. Flux	Post. error
Land Regions							
Boreal North America	**0.00**	**1.27**	**0.01**	**0.02**	**−0.06**	**−0.04**	**0.34**
Western Boreal	0.00	1.09	0.01	0.01	−0.22	−0.20	0.38
Northern Boreal	0.00	0.22	0.00	0.00	0.05	0.05	0.19
Eastern Boreal	0.00	0.62	0.00	0.01	0.09	0.11	0.22
Temperate North America	**0.00**	**1.24**	**1.88**	**0.01**	**−1.18**	**−1.17**	**0.42**
Pacific Northwest	0.00	0.47	0.08	0.01	−0.34	−0.33	0.35
Central Plains	0.00	0.55	0.14	0.00	−0.03	−0.03	0.22
North Central	0.00	0.30	0.13	0.00	−0.10	−0.10	0.17
Northeast	0.00	0.84	0.78	0.00	−0.67	−0.67	0.25
Southwest	0.00	0.16	0.30	0.00	−0.09	−0.09	0.08
Southeast	0.00	0.37	0.38	0.00	0.08	0.08	0.26
Subtropical	0.00	0.21	0.07	0.00	−0.04	−0.03	0.19
Tropical America	**0.00**	**1.25**	**0.14**	**0.20**	**−0.04**	**0.16**	**0.81**
Central America	0.00	0.43	0.11	0.05	−0.07	−0.02	0.36
Northern Amazon	0.00	0.75	0.03	0.04	−0.05	−0.01	0.49
Southern Amazon	0.00	0.90	0.00	0.11	0.08	0.19	0.75
Temperate South America	**0.00**	**1.56**	**0.13**	**0.12**	**0.51**	**0.63**	**0.89**
Northern	0.00	1.53	0.12	0.12	0.50	0.63	0.91
Southern	0.00	0.27	0.01	0.00	0.00	0.01	0.25
Northern Africa	**0.00**	**1.31**	**0.12**	**0.61**	**0.27**	**0.98**	**0.67**
Mediterranean Coast	0.00	0.14	0.05	0.00	0.10	0.10	0.11
Northern Arid	0.00	0.14	0.04	0.00	−0.02	−0.02	0.13
Northern Dry Savanna	0.00	0.67	0.01	0.12	0.02	0.14	0.58
Northern Mesic Savanna	0.00	1.10	0.02	0.48	0.28	0.76	0.74
Horn	0.00	0.17	0.00	0.01	−0.01	0.00	0.17
Southern Africa	**0.00**	**1.51**	**0.13**	**0.61**	**−1.22**	**−0.62**	**0.68**
Western Forest	0.00	0.43	0.02	0.06	−0.07	−0.00	0.42
Southern Mesic Savanna	0.00	1.39	0.01	0.46	−0.95	−0.49	0.64
Southern Dry Savanna	0.00	0.34	0.10	0.06	−0.16	−0.10	0.27
Southern Arid	0.00	0.14	0.00	0.00	−0.04	−0.04	0.14
Madagascar	0.00	0.14	0.00	0.02	−0.01	0.01	0.14
Boreal Asia	**0.00**	**3.42**	**0.14**	**0.21**	**−0.49**	**−0.28**	**0.52**
Temperate Asia	**0.00**	**0.95**	**2.16**	**0.04**	**−0.26**	**−0.22**	**0.34**
Tropical Asia	**0.00**	**0.47**	**0.53**	**0.24**	**−0.35**	**−0.11**	**0.31**
Australia	**0.00**	**0.51**	**0.10**	**0.16**	**−0.29**	**−0.12**	**0.38**
Europe	**0.00**	**1.94**	**1.86**	**0.04**	**−0.62**	**−0.58**	**0.47**
British Isles	0.00	0.15	0.18	0.00	−0.02	−0.02	0.12
Scandinavia	0.00	0.36	0.08	0.00	0.03	0.03	0.14
North Central	0.00	1.69	0.49	0.03	−1.15	−1.12	0.60
Western	0.00	0.28	0.31	0.00	0.03	0.03	0.16
Central	0.00	0.39	0.41	0.00	−0.06	−0.06	0.20
Eastern	0.00	0.71	0.32	0.01	0.53	0.54	0.36
Iberia	0.00	0.16	0.09	0.00	0.03	0.03	0.14
Ocean Regions							
North Pacific	−0.49	0.53	0.02	0.00	−0.28	−0.27	0.24
Tropical West Pacific	0.11	0.10	0.00	0.00	0.05	0.05	0.09
Tropical East Pacific	0.51	0.44	0.00	0.00	0.24	0.24	0.30
South Pacific	−0.26	0.29	0.00	0.00	−0.32	−0.32	0.24

Table 1. Continued

	Mean Annual Prior Specifications				Annual Mean Posterior Results		
	Prior Flux	Prior Error	Fossil Emiss.	Burning Emiss.	Post. Flux	Net Post. Flux	Post. error
Northern	−0.29	0.25	0.00	0.00	−0.26	−0.26	0.16
North Atlantic	−0.28	0.32	0.02	0.00	−0.14	−0.14	0.18
Tropical Atlantic	0.13	0.11	0.00	0.00	0.10	0.10	0.11
South Atlantic	−0.13	0.14	0.00	0.00	−0.14	−0.14	0.13
Southern	−0.65	0.58	0.00	0.00	−0.38	−0.38	0.20
Tropical Indian	0.19	0.18	0.00	0.00	0.17	0.17	0.16
South Indian	−0.48	0.44	0.00	0.00	−0.28	−0.28	0.28

surface, resulting in an elevated annual mean mixing ratio in the atmospheric boundary layer relative to the free troposphere (Denning et al., 1995)). The interhemispheric exchange time, as defined in Denning et al. (1999), is slightly faster than average among the TransCom models (Kawa et al., 2004). Additional detail about the transport model performance can be found in Parazoo et al. (2008).

To establish the atmospheric interhemispheric gradient of carbon dioxide, we used a spin up procedure that differs from the technique used in TransCom-IAV (Baker et al., 2006), where there is no annual variability in the modelled responses used to construct the transport matrix **H**. The background fluxes were emitted as boundary conditions for 1 yr and the transport was continued for an additional 24 months for each model that participated in TransCom-IAV. In a similar manner the tracer response functions are the result of forward runs with one month of emission and the following 36 months of transport only. Each participating modeller made his own choice of transport fields. In constructing the transport matrix **H**, the same 36 months of responses are reused, beginning in each year of the inversion period. In TransCom-IAV, with its long analysis period, the first years are discarded in the analysis as they contain only the first years of responses. In our case, our goal was to use transport fields to match the years of the carbon dioxide observations. We had available only 5 yr of transport fields (2000–2004) at the time the forward runs were executed. In order to maximize an already short analysis period, we augmented the year 2000 responses with representative model response data to simulate responses to background fluxes and monthly response functions from years before 2000. We then discarded inversion results from the year 2000 in our analysis results to minimize any potential effects of this procedure.

2.5. *A priori constraints*

The a priori constraint consists of a flux term and an uncertainty specification at monthly resolution for each region-month flux adjustment in the inversion solution and for the background fluxes. The region-month a priori flux adjustments in this experiment are set at zero, implying 'no correction' to the monthly background terrestrial and ocean fluxes, as well as the fossil fuel and biomass burning emissions. This procedure differs from some other methods that may incorporate best guess adjustments or biomass burning emissions or other land use change fluxes in the a priori specifications. The terrestrial background flux is annually neutral; the ocean background flux specifies a global annual sink of 1.6 Pg C; biomass burning emissions are ∼2 Pg C annually; fossil flux emissions are ∼7 Pg C annually for this period. In order to balance the global growth in atmospheric carbon dioxide concentration, there is an expectation that the inversion-adjusted terrestrial and ocean region-month fluxes will be a net sink. The region-month uncertainties used to populate the variances in the diagonal values of $\mathbf{P}^0$, the a priori flux covariance matrix, vary by month, summing globally to 5.4 Pg C annually. This range is larger than the 2.8 Pg C annual uncertainty used in the TransCom interannual variability control (Baker et al., 2006) and network sensitivity (Gurney et al., 2008) experiments. The magnitude of the monthly uncertainties is intended to be loose enough to allow the inversion to make substantial adjustments to the background terrestrial and ocean fluxes while remaining biogeochemically realistic. These region-month uncertainties are calculated as the sum of the magnitudes of three months of the applicable background flux (terrestrial or ocean) for the region centred on each month. This allows the inversion 'room' to correct for timing differences in seasonal cycles and generally allows for more latitude for adjustment in months when the fluxes are of largest magnitude.

2.6. *Observation site networks*

Observation site locations are shown on the map in Fig. 2. Table 2 details the observation site names, locations, responsible agencies, references and the range of monthly variability of observations. The observation sites include observatories, tall towers, flask sampling sites and an aircraft vertical

Table 2. Observation Sites

Site	Location		Networks[a]			Variability[b]		[c]Agency	Reference
	Lat.	Lon.	B	E	CE	Min	Max		
Continuous/Quasi-Continuous									
Alert (ALT)	82.45	−62.52	X	X	X	0.50	2.72	EC	Higuchi et al. (2003)
Barrow (BRW)	71.32	−156.60	X	X	X	0.53	3.69	NOAA ESRL	Thoning et al. (2007)
Pallas_Sammaltunturi (PAL)[ns]	67.97	24.12		X	X	0.74	5.38	FMI	Hatakka et al. (2003), Aalto et al. (2002)
Northern Old Black Spruce	55.88	−98.48			X	1.21	11.93	Harvard	Dunn et al. (2006)
Fraserdale (FRD)	49.88	−81.57	X	X	X	0.95	5.95	EC	Higuchi et al. (2003)
Schauinsland (SCH)[ns]	48.00	8.00		X	X	1.24	5.03	UBA	Uhse (2006)
Schneefernerhaus (ZSF)[ns]	47.42	10.98		X	X	1.06	4.09	UBA	Uhse (2006)
Sonnblick (SNB)[ns]	47.05	12.05		X	X	1.23	4.06	UBAA	Friedbacher et al. (2007)
Hegyhatsal (HUN)[ns]	46.95	16.65		X	X	2.35	10.31	HMS	Haszpra et al. (2008)
Plateau Rosa (PRS)[ns]	45.93	7.70		X	X	0.76	3.44	CESI RICERCA	Apadula et al. (2003)
Park Falls 396m (LEF)[ns]	45.93	−90.27	X	X	X	1.24	8.11	NOAA ESRL	Andrews et al. (2008)
Howland Forest	45.20	−68.74			X	1.57	8.29	USDA FS	Hollinger et al. (1999)
Monte Cimone (CMN)[ns]	44.18	10.70		X	X	1.35	3.69	IAFMS	Santaguida (2008)
Harvard Forest	42.53	−72.17			X	2.61	11.16	Harvard	Urbanski et al. (2007)
Ryori (RYO)[ns]	39.03	141.82		X	X	1.58	8.61	JMA	Esaki (2009)
Southern Great Plains	36.80	−97.50			X	1.66	9.37	DOE LBNL	Fischer (2005), Fischer et al. (2007)
Moody 457m (WKT)[ns]	31.32	−97.33	X	X	X	0.93	6.27	NOAA ESRL	Andrews et al. (2008)
Tenerife (IZO)[ns]	28.30	−16.48		X	X	0.57	1.78	AEMET	Gomez-Pelaez et al. (2006)
Yonagunijima (YON)	24.47	123.02		X	X	0.94	3.78	JMA	Tsutsumi et al. (2006), Esaki (2009)
Minamitorishima (MNM)	24.30	153.98		X	X	0.53	2.30	JMA	Esaki (2009)
Mauna Loa (MLO)[ns]	19.54	−155.58	X	X	X	0.50	0.99	NOAA ESRL	Thoning et al. (2007)
Tapajos	−2.86	−54.96			X	1.53	8.28	Harvard	Hutyra et al. (2007)
Tutuila (SMO)	−14.24	−170.57	X	X	X	0.51	1.21	NOAA ESRL	Thoning et al. (2007)
Cape Point (CPT)	−34.35	18.49		X	X	0.50	0.99	SAWS	Brunke (2007)
Jubany (JBA)	−62.23	−58.82		X	X	0.58	0.98	PNRA, CNR-ICES, DNA	Ciattaglia et al. (1999), Ciattaglia et al. (2008)
South Pole (SPO)	−89.98	−24.80	X	X	X	0.53	0.72	NOAA ESRL	Thoning et al. (2007)
Discrete–surface sampling									
Ny-Alesund (ZEP)[ns]	80.00	11.88	X	X	X	0.57	3.43	NOAA ESRL	Conway et al. (2008)
Station M (STM)	66.00	2.00	X	X	X	0.51	2.98	NOAA ESRL	Conway et al. (2008)
Storhofdi (ICE)	62.00	−20.29	X	X	X	0.53	3.28	NOAA ESRL	Conway et al. (2008)
Baltic Sea (BAL)	55.35	17.22	X	X	X	1.93	9.35	NOAA ESRL	Conway et al. (2008)
Cold Bay (CBA)	55.20	−162.72	X	X	X	0.50	2.96	NOAA ESRL	Conway et al. (2008)
Mace Head (MHD)	53.33	−9.90	X	X	X	0.50	3.54	NOAA ESRL	Conway et al. (2008)
Shemya Island (SHM)	52.72	174.10	X	X	X	0.59	3.79	NOAA ESRL	Conway et al. (2008)
Hegyhatsal (HUN)[ns]	46.95	16.65	X			1.35	10.36	NOAA ESRL	Conway et al. (2008)
Sary Taukum (KZD)[ns]	44.45	77.57	X	X	X	0.79	5.27	NOAA ESRL	Conway et al. (2008)

Table 2. Continued

Site	Location		Networks[a]			Variability[b]		[c]Agency	Reference
	Lat.	Lon.	B	E	CE	Min	Max		
Ulaan Uhl (UUM)	44.45	111.10	X	X	X	0.67	6.41	NOAA ESRL	Conway et al. (2008)
Black Sea (BSC)	44.17	30.00	X	X	X	0.71	12.76	NOAA ESRL	Conway et al. (2008)
Niwot Ridge (NWR)[ns]	40.05	−105.58	X	X	X	0.51	2.95	NOAA ESRL	Conway et al. (2008)
Wendover (UTA)	39.90	−113.72	X	X	X	0.51	3.38	NOAA ESRL	Conway et al. (2008)
Azores (AZR)	38.77	−27.38	X	X	X	0.50	3.18	NOAA ESRL	Conway et al. (2008)
Tae-Ahn Peninsula (TAP)	36.73	126.13	X	X	X	0.70	7.98	NOAA ESRL	Conway et al. (2008)
Mt. Waliguan (WLG)[ns]	36.29	100.90	X	X	X	0.66	3.42	NOAA ESRL	Conway et al. (2008)
Lampedusa (LMP)	35.52	12.62		X	X	0.53	4.36	ENEA	Artuso et al. (2009), Apadula et al. (2005)
Tudor Hill (BMW)	32.27	−64.88	X	X	X	0.56	3.46	NOAA ESRL	Conway et al. (2008)
Sede Boker (WIS)	31.13	34.88	X	X	X	0.52	3.71	NOAA ESRL	Conway et al. (2008)
Tenerife (IZO)[ns]	28.30	−16.48	X			0.53	1.52	NOAA ESRL	Conway et al. (2008)
Sand Island (MID)	28.21	−177.38	X	X	X	0.51	2.19	NOAA ESRL	Conway et al. (2008)
Key Biscayne (KEY)	25.67	−80.20	X	X	X	0.53	4.48	NOAA ESRL	Conway et al. (2008)
Assekrem (ASK)[ns]	23.18	5.42	X	X	X	0.50	1.20	NOAA ESRL	Conway et al. (2008)
Cape Kumakahi (KUM)	19.52	−154.82	X	X	X	0.56	1.91	NOAA ESRL	Conway et al. (2008)
Mariana Islands (GMI)	13.43	144.78	X	X	X	0.50	1.38	NOAA ESRL	Conway et al. (2008)
Ragged Point (RPB)	13.17	−59.43	X	X	X	0.52	1.70	NOAA ESRL	Conway et al. (2008)
Christmas Island (CHR)	1.70	−157.17	X	X	X	0.55	0.97	NOAA ESRL	Conway et al. (2008)
Mahe Island (SEY)	−4.67	55.17	X	X	X	0.54	1.74	NOAA ESRL	Conway et al. (2008)
Ascension Island (ASC)	−7.92	−14.42	X	X	X	0.50	1.06	NOAA ESRL	Conway et al. (2008)
Cape Ferguson (CFA)	−18.00	147.06	X	X	X	0.54	2.71	CSIRO	Francey et al. (2003), Langenfelds et al. (2002)
Cape Grim (CGO)	−42.00	142.50	X	X	X	0.52	0.88	NOAA ESRL	Conway et al. (2008)
Macquarie Island (MQA)	−54.48	159.97	X	X	X	0.51	0.99	CSIRO ESRL	Francey et al. (2003), Langenfelds et al. (2002)
Palmer Station (PSA)	−66.00	−64.00	X	X	X	0.51	0.85	NOAA ESRL	Conway et al. (2008)
Mawson (MAA)	−67.62	62.87	X	X	X	0.51	0.84	CSIRO	Francey et al. (2003), Langenfelds et al. (2002)
Syowa Station (SYO)	−70.00	39.58	X	X	X	0.50	0.87	NOAA ESRL	Conway et al. (2008)
Halley Station (HBA)	−75.58	−25.00	X	X	X	0.50	0.81	NOAA ESRL	Conway et al. (2008)
Discrete–aircraft sampling									
Briggsdale 3000m (CAR)[ns]	40.37	−104.30		X	X	0.52	4.49	NOAA ESRL	NOAA, C. Sweeney
Briggsdale 4000m (CAR)[ns]	40.37	−104.30		X	X	0.53	3.41	NOAA ESRL	NOAA, C. Sweeney
Briggsdale 5000m (CAR)[ns]	40.37	−104.30		X	X	0.54	3.25	NOAA ESRL	NOAA, C. Sweeney
Briggsdale 6000m (CAR)[ns]	40.37	−104.30		X	X	0.52	1.82	NOAA ESRL	NOAA, C. Sweeney
Briggsdale 7000m (CAR)[ns]	40.37	−104.30		X	X	0.54	1.64	NOAA ESRL	NOAA, C. Sweeney
Briggsdale 8000m (CAR)[ns]	40.37	−104.30		X	X	0.57	2.06	NOAA ESRL	NOAA, C. Sweeney
JAL (WPO)[ns]	30.00	146.00		X	X	0.57	2.90	MRI NIES	Matsueda et al. (2008)
JAL (WPO)[ns]	25.00	146.00		X	X	0.56	2.79	MRI NIES	Matsueda et al. (2008)
JAL (WPO)[ns]	20.00	146.00		X	X	0.57	2.18	MRI NIES	Matsueda et al. (2008)

Table 2. Continued

	Location		Networks[a]			Variability[b]			
Site	Lat.	Lon.	B	E	CE	Min	Max	[c]Agency	Reference
JAL (WPO)[ns]	15.00	146.00		X	X	0.54	1.82	MRI NIES	Matsueda et al. (2008)
JAL (WPO)[ns]	10.00	146.00		X	X	0.50	1.71	MRI NIES	Matsueda et al. (2008)
JAL (WPO)[ns]	5.00	146.00		X	X	0.50	1.27	MRI NIES	Matsueda et al. (2008)
JAL (WPO)[ns]	0.00	146.00		X	X	0.54	1.58	MRI NIES	Matsueda et al. (2008)
JAL (WPO)[ns]	−5.00	146.00		X	X	0.51	1.48	MRI NIES	Matsueda et al. (2008)
JAL (WPO)[ns]	−10.00	146.00		X	X	0.52	1.05	MRI NIES	Matsueda et al. (2008)
JAL (WPO)[ns]	−15.00	146.00		X	X	0.54	0.96	MRI NIES	Matsueda et al. (2008)
JAL (WPO)[ns]	−20.00	146.00		X	X	0.51	1.32	MRI NIES	Matsueda et al. (2008)
JAL (WPO)[ns]	−25.00	146.00		X	X	0.50	2.04	MRI NIES	Matsueda et al. (2008)

[a]**Sites** are included in the networks marked: **B**, base; **E**, enhanced; **CE**, continental extension. A superscript of ns after the site identifier indicates that the site is treated as a non-surface layer site in model sampling.

[b]**Variability** indicates the minimum and maximum calculated monthly observation standard deviation in ppm CO_2.

[c]**Agency** is the responsible observing agency in 2000–2004: **AEMET** Meteorological State Agency of Spain, **CESI RICERCA** Environment and Sustainable Development Department (Italy), **CNR-ICES** International Center for Earth Sciences (Italy), **DNA** Antarctic Institute (Argentina), **CSIRO** CSIRO Marine and Atmospheric Research GASLAB (Australia), **DOE LBNL** Department of Energy Lawrence Berkeley National Lab, **EC** Environment Canada, **ENEA** Italian National Agency of New Technologies, Energy and Environment, **FMI** Finnish Meteorological Institute, **Harvard** Harvard University, **HMS** Hungarian Meteorological Service, **IAFMS** Italian Air Force Meteorological Service, **JMA** Japan Meteorological Agency, **MRI NIES** Meteorological Research Institute, National Institute for Environmental Studies (Japan), **NOAA** National Oceanic and Atmospheric Administration, Earth System Research Laboratory, Global Monitoring Division (USA), **PNRA** Italian Antarctic Program, **SAWS** South African Weather Service, **UBA** Umweltsbundesamt Germany, **UBAA** Umweltsbundesamt Austria, **USDA FS** US Department of Agriculture Forest Service.

Data Sources: NOAA ESRL: Observatories (ftp://ftp.cmdl.noaa.gov/ccgg/co2/in-situ/), NOAA Surface Flasks. (ftp://ftp.cmdl.noaa.gov/ccgg/co2/flask/event), NOAA Aircraft Vertical Profile from C. Sweeney (NOAA request 3346215).

Flux Tower CO_2: Harvard Forest, Howland Forest, Tapajos from Ameriflux (http://public.ornl.gov/ameriflux/dataproducts.shtml), Northern Old Black Spruce from Harvard University (http://www.seas.harvard.edu/lab/index.html Data Exchange), Southern Great Plains from ARM DAAC (http://www.archive.arm/gov/).

Pallas-Sammaltunturni from J. Hatakka, personal communication (March 2009).

All other data from World Data Center for Greenhouse Gases (http://gaw.kishou.go.jp/wdcgg/wdcgg.html).

profile from the NOAA ESRL network (http://www.esrl.noaa.gov/gmd/ccgg/index.html), sites from other measurement programs with data archived at the World Meteorological Organization (WMO) Global Atmosphere Watch World Data Center for Greenhouse Gases (//gaw.kishou.go.jp/wdcgg/wdcgg.html) and carbon dioxide time series from five flux towers. We have selected quasi-continuous measurement programs (in-situ measurements available as hourly averages) preferentially over discrete measurement programs (sampled approximately weekly in flasks for later analysis). We have excluded colocated measurement programs, retaining the highest samples from tall towers and the quasi-continuous measurement programs that are colocated with discrete measurement programs. The goal is to use measurements calibrated to the WMO standards for carbon dioxide (Zhao et al., 1997; Tans et al., 2003; Zhao and Tans, 2006). Calibration to WMO standards across multiple measurement methods and agencies has proved to be a challenge (Masarie et al., 2001). Law et al. (2003) show that the impact of interagency calibration offsets can be accommodated in inversions on synoptic time scales (∼5 d), but may be significant on the monthly time scale we use in this experiment. To the extent that we have included observations from multiple measurement programs, we may have introduced bias into our results.

Stations are selected based on data availability to minimize bias introduced by gap filling. An upper limit of 12 missing months during the 2000–2004 time period was allowed, with a few exceptions for sites which began operation after 2000 (tall tower in Moody, Texas; flux towers at Southern Great Plains and Tapajos). This requirement prohibited the use of a number of sites that would be used if a smoothed, extrapolated data product such as GLOBALVIEW (GLOBALVIEW-CO2, 2007) were used. Three networks are tested in this experiment. The first is a 43-site base network, sourced from three agencies: National Oceanic and Atmospheric Administration Earth System Research Laboratory (NOAA ESRL), Environment Canada (EC) and CSIRO Marine and Atmospheric Research GASLAB in Australia. All of the observation sites in this network are also used in CarbonTracker (Peters et al., 2007; CarbonTracker 2008, http: //carbontracker.noaa.gov); we cannot use some of the CarbonTracker network sites due to the completeness of record requirement of our method. A 73-site enhanced network includes sites from other agencies, including high altitude aircraft and mountain top sites, archived at the World Data Center for Greenhouse Gases. These sites are used to improve global coverage. The last network, the 78-site continental extension network, adds the five flux tower observation sites. A primary objective of this experiment is to show the effect on the inversion estimates of including the four added North American continental sites.

2.7. *Observation data preparation*

Observations are selected with minimal screening for data quality issues identified by the observing agencies. For quasi-continuous continental sites, mid-day hours are selected (12–16 local standard time), except for mountain top sites where midnight hours are used. This selection is intended to maximize the contribution to the monthly mean of the hours representing well-mixed atmospheric conditions; these are conditions most likely to be modelled correctly in the tracer transport model. Monthly means are calculated from all available hours in the daily selection time periods without regard to meteorological conditions. Data uncertainties for each month are computed as the standard deviations of the available data for the month, with an imposed minimum of 0.5 ppm. These uncertainties, as variances, are used to populate the diagonal data covariance matrix **R** (eqs 2, 3 and 4). We have not included additional model-data mismatch error in **R** to account for errors in model transport or the representation of regions by point observation sites; we have equated synoptic monthly variability of the selected hours of observations with the total data error. Preliminary experiments with added model-data mismatch error effectively de-weighted observations to the point of overreliance on the a priori fluxes, with minimal adjustments to the background fluxes and large data residuals. This aspect of our method warrants further research. Table 2 includes the range of monthly variability for each station. Compared to the TransCom interannual variability experiment (Baker et al., 2006), these uncertainties are larger by ∼0.2 ppm at the minimum and up to two times larger at the maximum for remote sites. For continental and coastal sites, the minimum uncertainties are comparable and maximum uncertainties are at least as large as those in Baker et al. (2006), which used the GLOBALVIEW smoothed data product for the observation data time series and added model-data mismatch error for some observation sites.

For this analytical solution method, a regular time resolution is implied, making it necessary to fill gaps in the data for months with no observations. For observation sites that are represented in GLOBALVIEW (GLOBALVIEW-CO2, 2007), gaps are filled with the average of the GLOBALVIEW site data for the weeks corresponding to the month to be filled. For stations with no GLOBALVIEW representation, a climatology is constructed of the monthly departure of existing observations at the station from the GLOBALVIEW marine boundary layer (MBL) value for the station latitude. This difference climatology is applied to the MBL value for the missing months to fill the gap. The uncertainty for each gap-filled month is assigned as either the climatologic observation variability for the month for the station in 2000–2004 or a mean variability for all months with existing observations for the 2000–2004 time series for the station.

2.8. *Model sampling*

Model sampling is accomplished by saving vertical profiles of tracer concentration, pressure and temperature at the model grid cell nearest to each observing site hourly for the duration of

the forward runs of the tracer transport model. Coastal stations are sampled in an off-shore grid cell to approximate observation protocol for flask sampling of background air. For surface observing stations the concentration samples are taken from the surface layer in the chosen grid cell. For elevated stations, noted as non-surface in Table 2, vertical pressure interpolation is used to resolve the concentration sample to an equivalent elevation. Hourly samples from all transport model forward runs were saved as described in Sections 2.2 and 2.3. The hourly samples that match the measurement time stamps of the observations are selected for use in the construction of the transport matrix **H** (eq. 2), a concept referred to as cosampling (Peters et al., 2007). For the discrete flask and aircraft observation sites, 3 h of model samples centred on the hour of each observation are used to smooth discrepancies in timing of weather events in the transport. Monthly mean model samples are calculated from these cosampled hours for each observation site from the forward runs for each of the region-month pulses and the background fluxes and used to populate the transport matrix **H**.

In the event of a month-long gap in the observation data, a default model sampling strategy is required. In this case model samples are chosen from the same hours that an observation sample would have been taken (daily selected hours for quasi-continuous sites and on 5 d during the month for flask sampling sites). The default hours for flask sampling are based on the distribution of hours when samples were taken during 2000–2004 at the respective sampling sites. Monthly means computed from these selected hours are used to fill in the gaps in the cosampled transport matrix **H**.

3. Results

All results shown are the adjusted land and ocean a posteriori flux estimates including the fixed biomass burning emissions, but not the fossil fuel emissions. This convention allows comparisons to previous work in the literature. Error bars in the figures are ± the mean annual uncertainty from the a posteriori covariance.

3.1. Global results

Figure 3 shows the mean annual estimated fluxes and analytically-derived uncertainties for the analysis period (2001–2003) for the three networks tested (triangles for the base network, diamonds for the enhanced network and squares for the continental extension), aggregated to the 22 TransCom continent and ocean basin regions. Results for the continental extension network are also listed in Tables 1 and 3. The CarbonTracker 2008 (http://carbontracker.noaa.gov) results for the same time period are shown as a benchmark reference (circles in Fig. 3). For all three networks in our experiment the increase in the global atmospheric burden of carbon (from the net of the estimated global sink and the assumed biomass burning and fossil fuel emissions) is consistent within 0.1 Pg C yr^{-1} of the ∼ +2.1 ppm average annual increase in global surface carbon dioxide

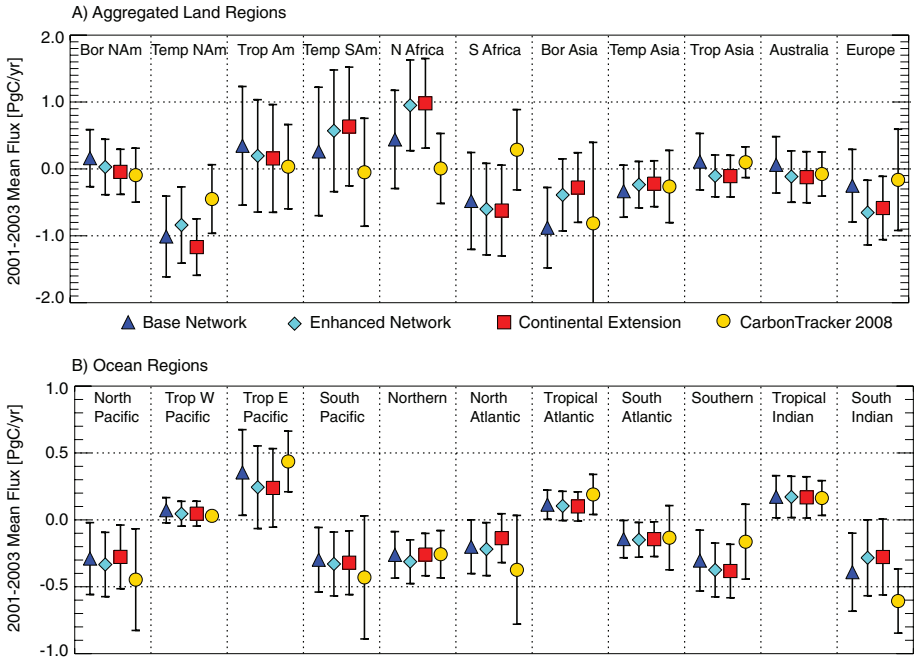

Fig. 3. Mean annual estimated flux and uncertainty for 2001–2003 in Pg C yr^{-1} for (a) aggregated land regions and (b) ocean regions for three networks: 43-site base network (triangles); 73-site enhanced network (diamonds); 78-site continental extension network (squares). CarbonTracker2008 results for the same time period are shown for reference (circles). All flux estimates include biomass burning emissions, but not fossil emissions.

Table 3. Comparisons of 2001–2003 mean annual flux and uncertainty estimates from the continental extension network of this study using SiB3 and CASA background terrestrial fluxes, the NASA PCTM and 13-model mean results from the TransCom IAV network sensitivity experiment (95-site network in Gurney et al., 2008) and CarbonTracker2008. All units are Pg C yr^{-1}. Flux estimates include biomass burning emissions, but not fossil fuel emissions

	This Study SiB3 Bio Background	This Study CASA Bio Background	TransCom IAV PCTM	TransCom IAV Model Mean	CarbonTracker 2008
Aggregated Land Regions					
Boreal North America	−0.04 ± 0.34	−0.17 ± 0.31	−0.39 ± 0.11	−0.41 ± 0.35	−0.07 ± 0.40
Temperate North America	−1.17 ± 0.42	−1.25 ± 0.39	−0.92 ± 0.20	−0.82 ± 0.50	−0.47 ± 0.51
Tropical America	0.16 ± 0.81	−0.60 ± 0.63	0.72 ± 0.54	1.51 ± 1.49	0.05 ± 0.63
Temperate South America	0.63 ± 0.89	0.58 ± 0.83	−0.01 ± 0.57	−0.09 ± 0.84	−0.07 ± 0.81
Northern Africa	0.98 ± 0.67	1.05 ± 0.64	0.86 ± 0.45	0.77 ± 1.01	0.01 ± 0.52
Southern Africa	−0.62 ± 0.68	−0.27 ± 0.65	−0.19 ± 0.44	−0.50 ± 1.30	0.27 ± 0.60
Boreal Asia	−0.28 ± 0.52	−0.51 ± 0.47	0.14 ± 0.19	0.03 ± 0.43	−0.69 ± 1.21
Temperate Asia	−0.22 ± 0.34	−0.03 ± 0.37	−0.79 ± 0.22	−0.98 ± 0.67	−0.25 ± 0.54
Tropical Asia	−0.11 ± 0.31	−0.08 ± 0.31	0.21 ± 0.29	−0.10 ± 0.53	0.10 ± 0.23
Australia	−0.12 ± 0.38	0.07 ± 0.37	−0.15 ± 0.19	−0.02 ± 0.26	−0.07 ± 0.33
Europe	−0.58 ± 0.47	−0.44 ± 0.41	−0.41 ± 0.16	−0.35 ± 0.66	−0.16 ± 0.76
Ocean Regions					
North Pacific Ocean	−0.28 ± 0.24	−0.34 ± 0.23	−0.58 ± 0.14	−0.79 ± 0.32	−0.43 ± 0.38
Tropical West Pacific Ocean	0.05 ± 0.09	0.06 ± 0.09	−0.08 ± 0.13	−0.05 ± 0.30	0.03 ± 0.02
Tropical East Pacific Ocean	0.24 ± 0.30	0.36 ± 0.29	0.45 ± 0.17	0.48 ± 0.23	0.44 ± 0.23
South Pacific Ocean	−0.32 ± 0.24	−0.27 ± 0.24	−0.55 ± 0.19	−0.46 ± 0.38	−0.41 ± 0.46
Northern Ocean	−0.26 ± 0.16	−0.17 ± 0.15	−0.03 ± 0.08	−0.27 ± 0.25	−0.26 ± 0.18
North Atlantic Ocean	−0.14 ± 0.18	−0.14 ± 0.18	−0.22 ± 0.13	−0.27 ± 0.18	−0.40 ± 0.41
Tropical Atlantic Ocean	0.10 ± 0.11	0.11 ± 0.11	0.09 ± 0.15	0.11 ± 0.23	0.19 ± 0.15
South Atlantic Ocean	−0.14 ± 0.13	−0.20 ± 0.13	−0.28 ± 0.12	−0.24 ± 0.20	−0.12 ± 0.24
Southern Ocean	−0.38 ± 0.20	−0.38 ± 0.20	−0.21 ± 0.10	−0.27 ± 0.24	−0.19 ± 0.28
Tropical Indian Ocean	0.17 ± 0.16	0.14 ± 0.15	0.02 ± 0.17	0.39 ± 0.30	0.16 ± 0.13
South Indian Ocean	−0.28 ± 0.28	−0.27 ± 0.28	−0.36 ± 0.11	−0.44 ± 0.19	−0.60 ± 0.24

for this period. The proportion of the global sink attributed to land regions across the three networks (58% for the base network, 46% for the enhanced network and 53% for the continental extension) shows, at the global level, some sensitivity of the solution to the composition of the network. Although the tropical and southern regions are not individually well-constrained, for all three networks the tropical land/ocean source and the southern land/ocean sink sum to a 0.3 Pg C yr^{-1} source. The tropical plus southern latitudinal band is constrained by these networks, but the flux distribution within these bands is not well-defined. The ocean region fluxes are mainly consistent within uncertainties across the solutions obtained from the three networks.

The three networks attribute 71–77% of the northern sink of 3.0–3.1 Pg C yr^{-1} to the land regions, with the sink for the ocean regions (North Pacific, North Atlantic and Northern Oceans) consistent at 0.7–0.9 Pg C yr^{-1} across the three solutions. However, the distribution of the land fluxes among continents depends very much on the network. For the base network, the land sink is split between Asia (Boreal and Temperate Asia regions accounting for 52%) and North America (Boreal and Temperate North America regions accounting for 37%), leaving Europe with 11%. Introducing east Asian observation sites, the western Pacific high altitude aircraft observations and mountain-top observations in Europe in the enhanced network shifts some of the Asian flux to Europe for an Asia:North America:Europe balance of 30%:39%:31%. This flux redistribution is accompanied by reductions in uncertainty for Europe and Asian regions (for example, Tropical Asia region annual uncertainty changes from 0.42 to 0.31 Pg C yr^{-1} and Europe from 0.54 to 0.48 Pg C yr^{-1}). The continental extension network with the four additional continental North American sites shifts more of the flux to North America (22%:53%:25%), with a reduction in uncertainty in North America (from 0.51 to 0.40 Pg C yr^{-1}), but not in Asia or Europe. The absence of observation sites in Boreal Asia and North Central Europe makes these regions under-constrained.

Two network-related shifts are seen in ocean fluxes between the base network and the enhanced network: the first is a transfer of source from the Tropical East Pacific and Tropical America to Temperate South America; the second is a shift of the distribution of the sink between the Southern Ocean and the South Indian Ocean with only modest reductions in uncertainty.

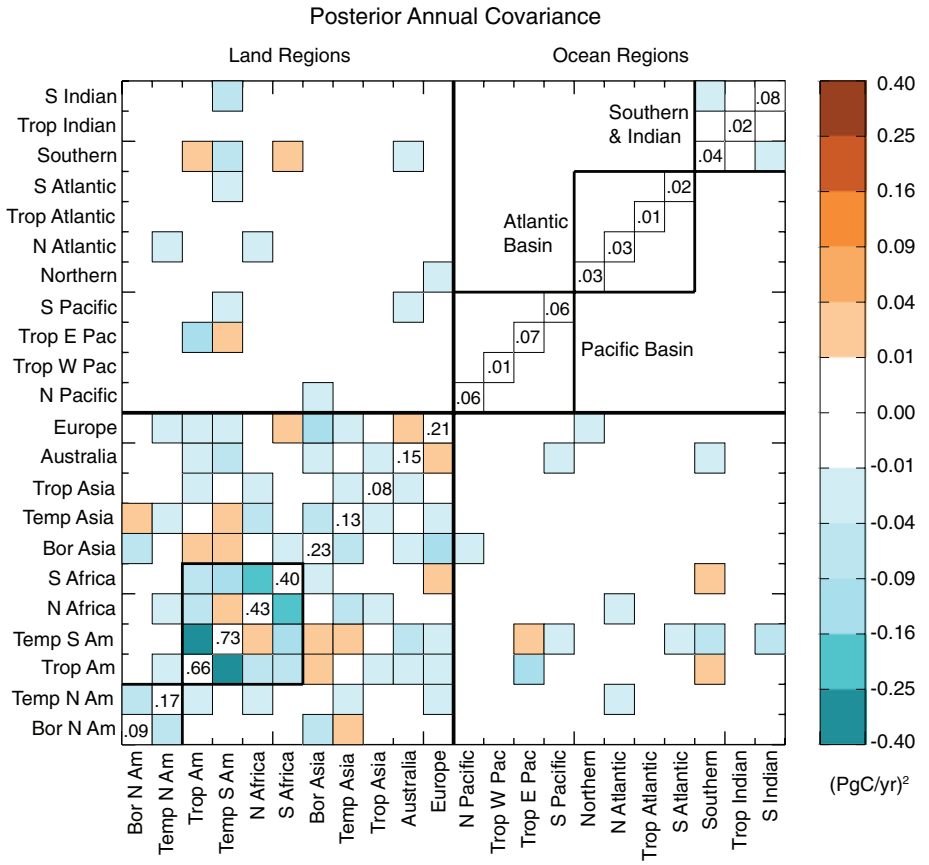

Fig. 4. Posterior covariance matrix for 2002 for the continental extension network solution for the 22 aggregated continental and ocean basin regions. Error covariances in (Pg C yr^{-1})^2 are shown on the diagonal. Shaded boxes contribute $\geq$0.1 Pg C yr^{-1} to the aggregated regional annual uncertainty.

Southern Hemisphere observation site additions in the enhanced network include Jubany Bay in Antarctica, Cape Point in southern Africa and the southern branch of the high altitude western Pacific aircraft flights. The flux tower in the Amazon in the continental extension network makes little difference in either flux or uncertainty in the aggregated South American regions. The seasonality of the modeled atmospheric concentration of carbon dioxide at this site fits the data poorly before the inversion and the post-inversion predicted concentration here is the worst fit of all of the observation sites used. This issue of correctly modeling the terrestrial carbon flux in the Amazon is partially addressed by Baker et al. (2008). The poor model fit to the site observation and the lack of any other observations on the South American continent likely account for the lack of improvement in the certainty of estimated fluxes here.

A fully independent solution using this analytic method would have no off-diagonal entries in the a posteriori covariance matrix. Here we examine an annually summarized example to illustrate how well the continental network solution conforms to this expectation. The a posteriori covariance matrix for 2002 annual fluxes for the aggregated TransCom regions and the continental extension network is presented in Fig. 4. Error variances are reported on the diagonal. The off-diagonal values indicate the covariances between the annual flux solutions in different regions and, therefore, show the independence of the estimates. Shaded off-diagonal values, in variance units of (Pg C yr^{-1})^2, impact the annual uncertainty of the aggregated regions by 0.1 Pg C or more; this cut-off is equivalent to the smallest annual error variance of the 22 aggregated regions. The largest covariance between ocean regions is slightly larger than –0.01 in units of variance between the Southern Ocean and the South Indian Ocean. The largest covariances are between Tropical America and Temperate South America (–0.37 in units of variance), North Africa and South Africa (–0.21), Temperate South America and South Africa (–0.14) and Europe and Boreal Asia (–0.12). The negative covariances among the Tropical America, Temperate South America, North Africa and South Africa aggregated regions, bounded by heavy black lines in Fig. 4, indicate that the estimates for the two continents should not be treated as independent. The total flux may be constrained, but the partitioning is not certain. Introducing the observation site in South America, where there were none in the enhanced network, is not enough to improve the overall continental constraint. In North America, however, the four added observations reduce the 2002 annual variance for Boreal North America from 0.16 to 0.09 (Pg C yr^{-1})^2, for Temperate North America from 0.33 to 0.17

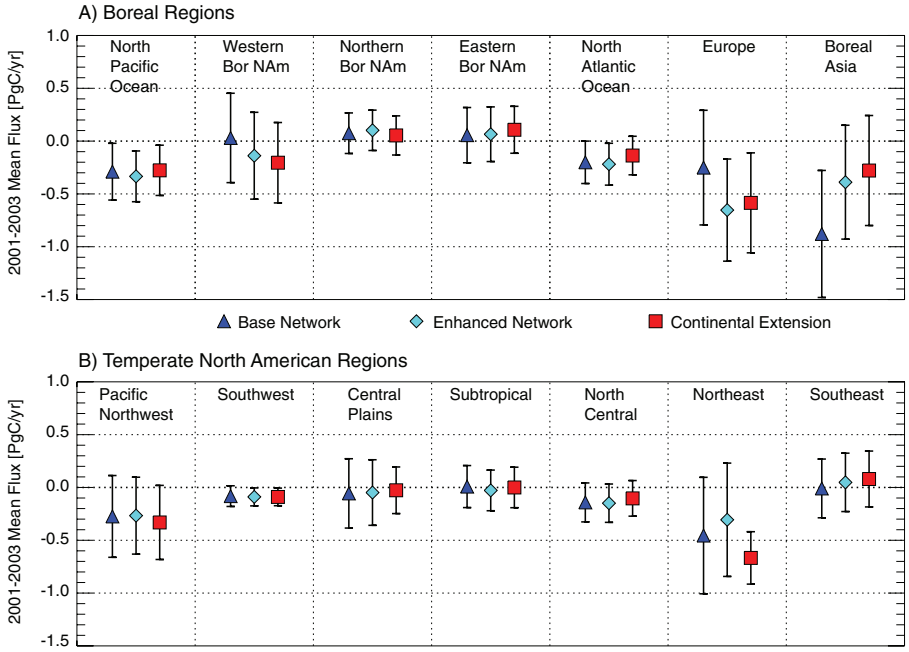

Fig. 5. Mean annual fluxes and uncertainties in Pg C yr^{-1} for 2001–2003 for the regions within (a) Boreal North America and (b) Temperate North America for three networks: base network (triangles); enhanced network (diamonds); continental extension network (squares). Also shown in (a) are other boreal aggregated regions. All fluxes include biomass burning emissions, but not fossil emissions.

(Pg C $yr^{-1})^2$ and the covariance between them from −0.12 to −0.05 (Pg C $yr^{-1})^2$ (bounded by heavy black lines in the lower left corner of Fig. 4). Rödenbeck et al. (2003a) examined a posteriori flux errors from the perspective of the correlation coefficients of the long-term fluxes for a period in the late 1990s in their fig. 13, finding several of the same "pair-sum" relationships that we see here.

3.2. *North American results*

Figure 5 shows the 2001–2003 mean annual North American fluxes and uncertainties along with the bordering North Atlantic and North Pacific ocean regions as well as Europe and Boreal Asia. Here it is evident that the uncertainty reduction in the regions with the added sites in the continental extension network (Eastern Boreal North America, Central Plains and Northeast in Temperate North America) accounts for nearly all of the uncertainty reduction in North America seen in Fig. 3. Within North America, the flux estimates change appreciably only in the Northeast region with the two added flux towers, unlike the change in balance between Boreal Asia and Europe when adding the European mountain top and additional sites in the eastern Asia. Uncertainty in the regions upstream of the added observations in North America (for example, Western Boreal and Pacific Northwest) is not much improved in the continental extension network.

The mean annual uncertainty reductions, relative to the a priori specifications ($1–\sigma_{post}/\sigma_{prior}$, expressed as a percent, where σ_{post} is the 2001–2003 mean annual posterior uncertainty and σ_{prior} is the annualized prior uncertainty), for the regions in North and South America are shown in Fig. 6 for the base network (triangles), enhanced network (diamonds) and continental extension network (squares). The annualized prior uncertainty and mean annual posterior uncertainty for each region are also listed in Table 1. Figure 6 again demonstrates that uncertainty reduction is achieved in the regions local to the added observations, a finding consistent with results from grid-scale inversions (e.g. Peylin et al., 2005; Gourdji et al., 2008; Lauvaux et al., 2008; Mueller et al., 2008). In regions where there are no observation sites in any of these three networks (for example, the Subtropical region within Temperate North America and most regions in South America), there is no reduction in uncertainty. Introducing one or two sites in a previously unrepresented region can result in a significant reduction in uncertainty. The Northeast region within Temperate North America shows little improvement in the enhanced network compared to the base network (36% vs. 34%); adding two flux tower observation sites in the continental extension network results in an uncertainty reduction of 70% from the prior uncertainty with a mean annual posterior uncertainty of 0.25 Pg C yr^{-1} compared to 0.54 Pg C yr^{-1} for the enhanced network. The South American flux tower is on the border between the Northern and Southern Amazon regions within Tropical America. The percentage reduction in uncertainty in the Northern Amazon compared to the prior doubles in the continental extension network compared to the base and enhanced networks (16% for the base network, 18% for the enhanced

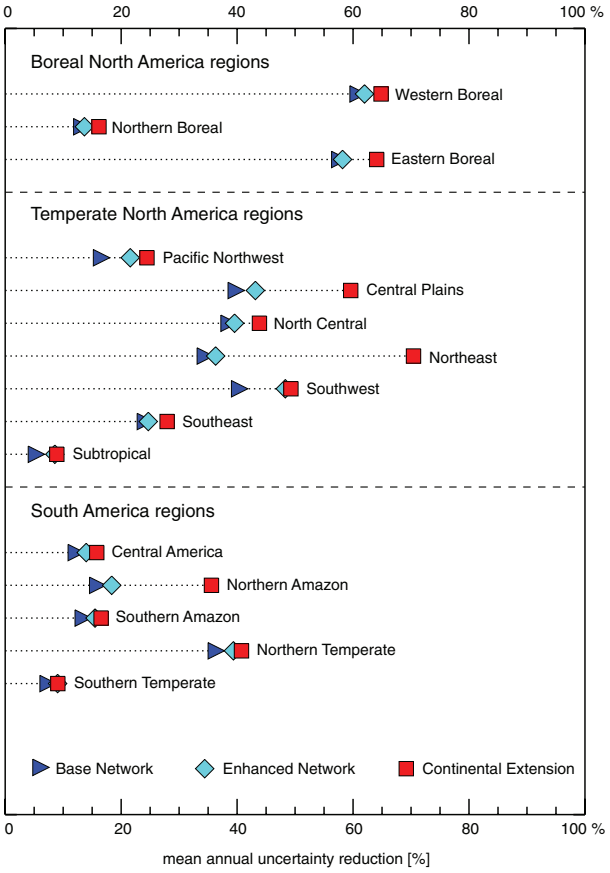

Fig. 6. Mean annual uncertainty reduction for 2001–2003 (in per cent) for North and South American regions for three networks: base network (right-facing triangles), enhanced network (diamonds), and continental extension network (squares).

network, 36% for the continental extension). The Southern Amazon region shows no improvement at all. Parazoo et al. (2008), using the same transport model and analyzed meteorological fields, found that atmospheric mixing in this region is dominated by vertical convection rather than the horizontal transport by synoptic weather systems prevalent in the mid-latitude continents. It is not surprising, therefore, that one observation site in South America constrains only the immediate region.

Regions within North America already partially constrained by local observations show some improvement, but less than for the first observation site. The Southwest, Central Plains and Eastern Boreal regions contain one observation site in the base network (Niwot Ridge, WKT tall tower and Fraserdale tower, respectively). Adding the aircraft vertical profile observations at Carr, Colorado, to the Southwest region in the enhanced network results in a modest improvement from 40% to 48% from the prior specification. After adding a flux tower to the Central Plains region and the Eastern Boreal region in the continental extension network, the percentage reduction of the uncertainty improves from 43 to 60% for the Central Plains and from 58 to 64% for the Eastern Boreal region.

Similar improvements in the covariances can be shown in the non-aggregated, 47-region 2002 annual covariance matrix for the continental extension network (not shown). The covariances among the regions within North America are reduced; the covariance between Eastern Boreal and Northeast Temperate regions is reduced from –0.06 to –0.02 (Pg C $yr^{-1})^2$, and the variances for Central Plains and Northeast are improved [0.11–0.05 (Pg C $yr^{-1})^2$ for the Central Plains and 0.30–0.05 (Pg C $yr^{-1})^2$ for the northeast]. Covariances between the North American regions and non-North American regions are reduced except for a negative covariance between Western Boreal North America and Boreal Asia. Results are more modest in South America, where the only appreciable improvement is the reduction in the covariance between Northern and Southern Amazon regions from -0.11 to -0.07 (Pg C $yr^{-1})^2$. Covariances within South America and between South American and African regions are reduced but not eliminated. We cannot justify the inversion solution for the subregions within South America as independent with the networks tested.

The monthly flux solutions for two Temperate North American regions for the three networks are shown in Fig. 7. The base network results are shown in blue, the enhanced network in cyan and the continental extension in red. Dotted lines indicate the extent of the constraint provided by the prior uncertainty. Shading represents the a posteriori uncertainty (from the diagonal of the posterior covariance matrix) of the solution for the continental extension network. On the left in Fig. 7 is the Pacific Northwest region which has no local observation sites in any of these networks, and is upstream of all the added North American

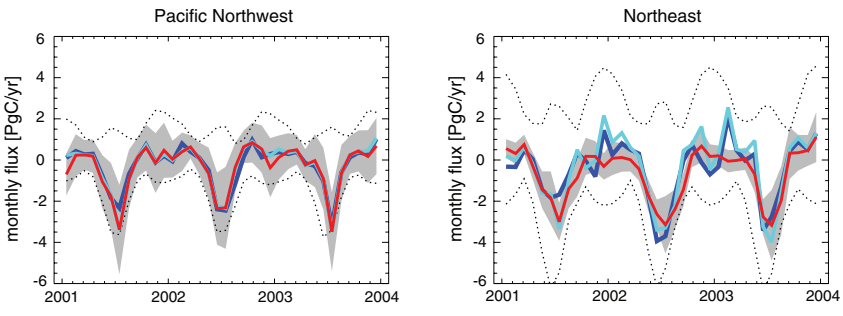

Fig. 7. Monthly posterior fluxes in Pg C yr^{-1} for two Temperate North America regions: Pacific Northwest (left) and Northeast (right) for three networks: base network (blue); enhanced network (cyan); continental extension network (red). Shading represents posterior monthly uncertainty of the continental extension network solution. Dotted lines define the prior uncertainty (background terrestrial flux ± assigned prior flux uncertainty).

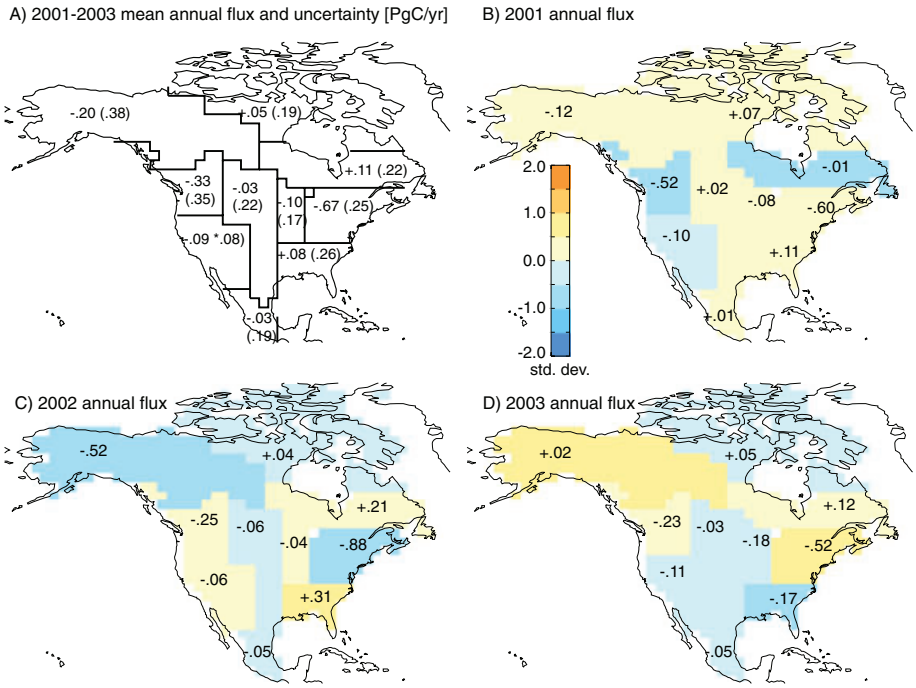

Fig. 8. (a) Mean annual flux (uncertainty) for North American regions for 2001–2003 for the continental extension network. (b), (c) and (d) show annual results for 2001, 2002 and 2003. Shading on the annual maps indicates the number of standard deviations from the 3-yr mean flux as an indication of annual variability. All units are Pg C yr^{-1}. Fluxes do not include fossil fuel emissions.

observation sites. Other than a correction to the timing of the seasonal cycle of the terrestrial background flux, there is little change from the background flux and no difference in the a posterior flux estimate for the three networks tested. The Northeast region is shown in the right panel of Fig. 7. This region has no local observations in the base or enhanced networks, and the two flux towers with well-calibrated CO_2 measurements in the continental extension network. The a posteriori flux estimate for the continental extension network is smoothed, of smaller amplitude and reduced uncertainty relative to the prior. Similar uncertainty reductions that can be attributed to the presence of local observations is evident in the monthly flux solutions for Central Plains and Eastern Boreal regions, where the two other North American flux towers in the continental extension network are located.

Figure 8 shows the annual variability of the flux solutions for the continental extension network for the North American regions. The mean annual flux estimates and uncertainties (in parentheses) for 2001–2003 in Pg C yr^{-1} are shown by region in panel A. The other panels show the results for each of the years 2001–2003. Shading indicates the fractional standard deviation of the annual flux from the 3-yr mean. For example, the Southeast region has a strong source deviation with severe drought in summer of 2002 (Waple et al., 2003), but a strong sink anomaly in the wet summer of 2003 (Levinson and Waple, 2004). The variability in the Northeast region exhibits the reverse behavior for these 2 yr. The 47-region covariance matrix shows an annual covariance of -0.01 (Pg C $yr^{-1})^2$ between these two regions. The negative covariance, although small, might be an indication of some dipole behavior between these two regions. All of the anomalies are within 1 standard deviation of the 3-yr means.

4. Discussion

4.1. Impact of added measurement sites

The added continental measurement sites contribute to local uncertainty reduction without undue disruption to the global flux solution. We choose to use mid-day observations and matching transport model samples for continental surface sites based on comparisons of mid-day and all-hours sampling for both the observations and transport model output. As these mid-day hours are most likely to represent the desired well-mixed background state, they are also likely to represent an area much broader than the immediate vicinity of the observation site. This subsampling avoids the issue of nocturnal boundary layer representation in the transport models and driver meteorological data. Representation error is still possible; choice of site is critical. The competing roles of multiple sites in the same solution region (e.g. Howland Forest and Harvard Forest in the Northeast region of Temperate North America) warrant further research. There are a number of additional North American flux towers where carbon dioxide measurements are now well-calibrated. These present an

opportunity for improving the uncertainty of the North American carbon balance as determined by atmospheric inversions. The use of these stations is, however, dependent on the continuity of the measurement time series, and the degree to which the site is representative of the area for flux estimation. The inversion method used here requires continuous observation time series and an unchanging network. Other methods may be more amenable to the addition and deletion of observation sites for an inversion solution for long periods of time.

4.2. *Results using an alternative background terrestrial flux*

We used an alternative background terrestrial flux, the CASA monthly mean flux, to compare the a posteriori results for the continental extension network with the results using the SiB3 terrestrial flux which has diurnal, monthly and annual variability. The results for the 22 aggregated TransCom regions are documented in Table 3 and as squares in Fig. 9. Ocean region results are similar, as might be expected. The two background fluxes have differences in both amplitude and timing of the seasonal cycle in North America. In well-constrained regions, such as the Northeast Temperate North America, both background terrestrial fluxes are adjusted to a result that is consistent within the a posteriori uncertainty. The results for CASA and SiB3 are less consistent for under-constrained regions; Tropical America is a good example of this. The sensitivity to the background fluxes warrants further research.

We have found the model samples from the forward runs of SiB3 overestimate observed seasonal amplitudes of carbon dioxide concentrations by as much as 40% at observation sites in some northern temperate and boreal regions in North America. This can be seen in the prior uncertainty ranges (derived from the SiB3 fluxes) in Fig. 7, especially in the Northeast Temperate North America region. The CASA terrestrial background flux has smaller annual amplitude in these same regions, and the modelled seasonal amplitudes are within 10% of the observed amplitudes at the same locations that are overestimated by SiB3. As can be seen in Fig. 9, the inversion solutions using the alternative background fluxes are similar in regions that are well constrained.

4.3. *Comparison to published results*

The results of this inversion are placed in the context of other contemporary inversions for the same time period in Fig. 9 and Table 3. Included in the table and figure are the SiB3 and CASA versions of our experiment (squares in Fig. 9), CarbonTracker 2008 (circles) from http://carbontracker.noaa.gov, model mean results (diamonds) from the 95-site network in the TransCom Interannual Variability (IAV) network sensitivity study (Gurney et al., 2008), and the NASA GSFC PCTM model results (triangles) from the same IAV study. All results are for 2001–2003. The uncertainties shown in Table 3 and Fig. 9 for the TransCom IAV model mean are the total error including the model spread. The 95-site network used in the TransCom IAV

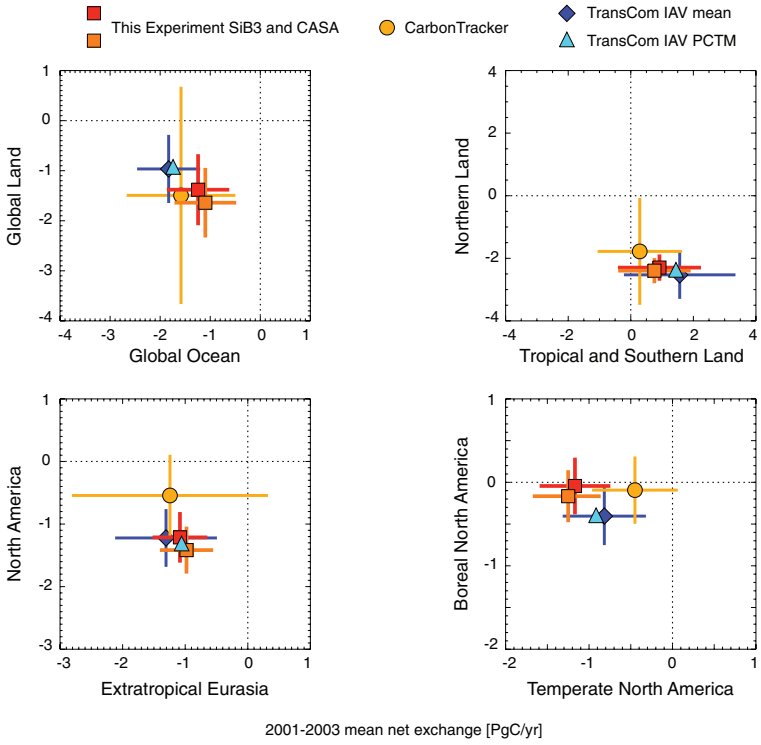

Fig. 9. Comparison of partitioning of annual mean fluxes for 2001–2003. Results are from this study (squares) using both SiB3 and an alternative background terrestrial flux (CASA), TransCom IAV 13-model mean (diamonds), NASA GSFC PCTM contribution to the 13-model TransCom IAV mean (triangles), and CarbonTracker2008 (circles). Posterior uncertainties are indicated by the error bars. The TransCom IAV model mean uncertainty is a total uncertainty including the model spread.

network sensitivity study is similar to our enhanced network, except that the GLOBALVIEW smoothed data product is used for observation data and colocated measurement programs are not excluded. In Fig. 9 we show inversion solutions using different data sources, different transport models and meteorological driver data, different background ocean and terrestrial fluxes, and different inversion methods. One very obvious difference in the partitioning results in Fig. 9 is in the greater magnitude of the uncertainties estimated by CarbonTracker. This is a methodological difference and an attempt to incorporate transport model error more comprehensively (Peters et al., 2007) when using only one transport model. Other studies have suggested that the transport model used and the uneven and sparse spatial distribution of observation sites are equal contributors to the differences in results (Gurney et al., 2002; Rödenbeck et al., 2003a,b; Gurney et al., 2008). The other a posteriori uncertainties shown in Fig. 9 are derived analytically (with the addition of model spread for the TransCom-IAV model mean). In general our SiB3 and CASA results, which share the same transport, network composition and data selection protocol, are much closer to each other than to the other inversions in this comparison.

Figure 9 shows that the TransCom IAV-PCTM result tracks very closely to the TransCom IAV model mean except in the partitioning between North America and Extratropical Eurasia where the TransCom IAV-PCTM more closely resembles the results of our study. Our results in the partitioning between Global Land and Global Ocean are more like CarbonTracker than the TransCom IAV model mean and TransCom IAV-PCTM results with greater land sink than ocean sink. All of the inversion results report a net source for the combined Tropical and Southern Land.

In contrast to CarbonTracker, however, our results place more of the northern land sink in North America than in extratropical Eurasia (Europe, Boreal Asia and Temperate Asia) in agreement with the TransCom IAV model mean and TransCom IAV-PCTM. Only the CarbonTracker results in Fig. 9 are in line with an independent estimate of -0.50 Pg C/yr (not including fossil fuel emissions) (CCSP, 2007) for North America. This illustrates again that there is not yet a convergence in carbon flux estimates between top-down and bottom-up methods. Our results differ from all of the other examples here in the partitioning of flux between Boreal and Temperate North America; our results show Boreal North America as approximately neutral with most of the sink in Temperate North America.

4.4. *Adjustments of the background ocean fluxes*

Our inversion results are generally consistent in zonal distribution with the ocean air-sea flux estimates of Takahashi et al. (2002), which we use as our background ocean flux. Our flux solution reduces the net global ocean sink from 1.6 Pg C to 1.2 Pg C annually, with smaller sinks in temperate waters and smaller sources in the tropics. Our experiment reduces the Southern Ocean sink specified by Takahashi et al. (2002), but not by as much as CarbonTracker (see Table 3) or the update to these air-sea fluxes (Takahashi et al., 2009) for the climatologic year 2000, which shows little or no net annual flux in the Southern Ocean due to offsetting effects of biological drawdown and upwelling of carbon-rich waters.

4.5. *Subcontinental flux partitioning*

The relatively large (with respect to CarbonTracker) Temperate North America terrestrial sink found in this study is not evenly distributed across the continent. Table 1 and Fig. 5b) suggest that the northeastern U.S. is responsible for more than half of this sink. The additional data constraint provided by the flux tower mixing ratio time series suggests that, within the limits of the uncertainties assessed here, this finding is significant. It is possible that this could be the result of transport errors, network biases, or other systematic errors that this study is not able to resolve. It is also notable that in Europe, the other relatively densely instrumented continent, the North Central region presents a dominant sink and the Eastern region a source, both significant with respect to the bounds of our uncertainty estimates. These subcontinental results show the promise of enhanced continental networks and, while preliminary, deserve further study.

4.6. *Uses of the posterior covariance matrix*

We have used the analytic product of the inversion method, the a posteriori covariance matrix, in three different ways in this experiment. We have used the magnitudes of the matrix elements as an indication of the uncertainty of the flux estimates. We have also used a change in magnitude as an indication of the value of adding sites to the network. Finally, we have used the a posteriori covariance to assess the spatial correlations between regions in the flux solutions. As we noted in Section 2.1, the accuracy of the a posteriori covariance is limited by the assumptions inherent in the a priori flux uncertainty and model-data errors, both of which are difficult to test. The magnitudes of the a posteriori uncertainties, as reported in Tables 1 and 3 and in the figures, are dependent upon the accuracy of our assumed prior uncertainties. The other uses of the a posteriori covariance should, however, be largely independent of the magnitude of the prior uncertainty estimates and thus more robust. CarbonTracker (Peters et al., 2007) includes a broader uncertainty assessment including some analysis of uncertainty caused by atmospheric transport. This may explain the larger error bounds in the CarbonTracker flux estimates.

5. Conclusions

We have shown the value of additional continental observations in a standard Bayesian global atmospheric inversion. We have removed some of the methodological simplifications used in previous Bayesian synthesis inversions by using transport fields

appropriate to the years of the observation data, by using real observation data, and by explicit inclusion of biomass burning emissions. We have also incorporated careful examination of the a posteriori covariance in the evaluation of the quality of the inversion output. Specific findings include the following:

1. Using a judicious combination of region size and location of additional continental observation sites, the a posteriori flux uncertainty and region-to-region covariance are significantly reduced.

2. Flux towers are typically sites in representative ecosystems and have existing measurement infrastructure. With some additional instrumentation and a careful calibration of carbon dioxide concentrations to global standards, these sites can be used in the global measurement network used for atmospheric inversions. With the extent of the current global flux network, there is a major opportunity for improved coverage in the observation networks used for global and regional atmospheric inversions.

3. The transport model and analysed meteorological fields appear to have more impact on our flux estimates than the added observation sites or the background terrestrial flux. For the well-constrained aggregated region of North America, the TransCom-IAV PCTM results are more like our findings than CarbonTracker. Transport uncertainty is an important problem that this study does not address.

4. We confirm the findings of other researchers (e.g. Baker et al., 2006; Jacobson et al., 2007a,b) that the tropical and southern land regions are underconstrained to the extent that the inversion source/sink estimates for these regions cannot be considered independently. The observation networks tested in this experiment do not improve this situation. An increase in observation density, for example from satellite observations, is required to change this situation.

5. In our experiment, we find that the Northeast subregion of Temperate North America dominates the North American sink. While this is a preliminary finding, based on our limited experiment, it does suggest that increasing both the coverage of the observation network and the number of regions in the inversion, can help to localize critical source and sink regions for the global carbon budget.

6. Acknowledgments

We thank three anonymous reviewers for their recommendations for improvements to the manuscript. This work would not be possible without the efforts of those responsible for the precise measurement and calibration of carbon dioxide measurements world-wide; we acknowledge the continued leadership of NOAA ESRL in measurement and calibration. We thank the following for the carbon dioxide time series from the flux towers: D. Hollinger for Howland Forest; J. W. Munger and S. Wofsy for Harvard Forest, Tapajos and Northern Old Black Spruce; M. Fischer and M. Torn for Southern Great Plains. Data collection at the Southern Great Plains site was supported by the Office of Biological and Environmental Research of the U.S. Department of Energy under contract DE-AC02–05CH11231 as part of the Atmospheric Radiation Measurement Program. The CarbonTracker team at NOAA ESRL makes their methods and results available (http://carbontracker.noaa.gov); we thank them, especially Andy Jacobson, for advice and encouragement. We thank the TransCom modeling community for making the inversion method available (http://www.purdue.edu/transcom/) and Kevin Gurney for providing results from the TransCom IAV network sensitivity study. Our research was funded in part by the U.S. Department of Commerce, National Oceanic and Atmospheric Administration (NOAA), Office of Global Programs, Global Carbon Cycle program, grant number NA040AR4310124 and by the Office of Science (BER) U.S. Department of Energy. M.P.B. greatly appreciates the technical support and funding provided by a NASA GSFC Graduate Student Research Program fellowship.

References

Aalto, T., Hatakka, J., Paatero, J., Tuovinen, J.-P., Aurela, M. and co-authors. 2002. Tropospheric carbon dioxide concentrations at a northern boreal site in Finland: basic variations and source areas. *Tellus* **54B**, 110–126.

Andrews, A. E., Kofler, J., Bakwin, P. S., Zhao, C. and Tans, P. 2008. Carbon dioxide and carbon monoxide dry air mole fractions from the NOAA ESRL Tall Tower Network, 1992–2008. Version: 11 Dec 2008, Path: ftp://ftp.cmdl.noaa.gov/ccg/towers/.

Apadula, F., Gotti, A., Pigini, A., Longhetto, A., Rocchetti, F. and co-authors. 2003. Localization of source and sink regions of carbon dioxide through the method of the synoptic air trajectory statistics. *Atmos. Environ.* **37**, 3757–3770. doi:10.1016/S1352-2310(03)00505-3.

Apadula, F., Artuso, F., Chamard, P., De Nile, F., di Sarra, A. and co-authors. 2005. The network for background CO_2 measurement in Italy, 12th WMO/IAEA Meeting of Experts on Carbon Dioxide Concentration and Related Tracer Measurement Techniques. World Meteorological Organization Global Atmosphere Watch Report no. 161 (WMO TD no. 1275), 173–175.

Artuso, F., Chamard, P., Piacentino, S., Sferlazzo, D., De Silvestri, L. and co-authors. 2009. Influence of transport and trends in atmospheric CO_2 at Lampedusa. *Atmos. Environ.* **43**(19), 3044–3051.

Baker, D. F., Law, R. M., Gurney, K. R., Rayner, P., Peylin, P. and co-authors. 2006. TransCom 3 inversion intercomparison: Impact of transport model errors on the interannual variability of regional CO_2 fluxes, 1988–2003. *Global Biogeochem. Cycles* **20**, GB1002. doi:10.1029/2004GB002439.

Baker, I. T., Prihodko, L., Denning, A. S., Goulden, M., Miller S. and co-authors. 2008. Seasonal drought stress in the Amazon: Reconciling models and observations. *J. Geophys. Res.* **113**, G00B01. doi:10.1029/2007JG000644.

Bakwin, P. S., Tans, P. P., Hurst, D. F. and Zhao, C. 1998. Measurements of carbon dioxide on very tall towers: results of the NOAA/CMDL program. *Tellus* **50B**, 401–415.

Bloom, S., da Silva, A. and Dee, D. 2005. *Documentation and Validation of the Goddard Earth Observing System, Version 4*. Technical Report Series on Global Modeling and Data Assimilation, Greenbelt, MD.

Bousquet, P., Peylin, P., Ciais, P., LeQuéré, C., Friedlingstein, P. and co-authors. 2000. Regional changes in carbon dioxide fluxes of land and oceans since 1980. *Science* **290**, 1342–1346.

Brenkert, A. L. 1998. Carbon dioxide emission estimates from fossil-fuel burning, hydraulic cement production, and gas flaring for 1995 on a one degree grid cell basis. **NDP-058A**, *Carbon Dioxide Inf. Anal. Cent.* Oak Ridge Natl. Lab., Oak Ridge, Tenn., USA.

Brunke, E. 2007. Atmospheric CO_2 hourly concentration data, Cape Point Global Atmosphere Watch station. In: *World Data Center for Greenhouse Gases*. Japan Meteorol. Agency, Tokyo. Version: 18 Mar 2008, Available at: http://gaw.kishou.go.jp/wdcgg.html.

CCSP. 2007. The First State of the Carbon Cycle Report (SOCCR): the North American Carbon Budget and Implications for the Global Carbon Cycle. In: *A Report by the U.S. Climate Change Science Program and the Subcommittee on Global Change Research* (eds A. W. King, L. Dilling, G. P. Zimmerman, D. M. Fairman, R. A. Houghton, and co-editors). National Oceanic and Atmospheric Administration, National Climatic Data Center, Asheville, NC, USA, 242.

Ciais, P., Reichstein, M., Viovy, N., Granier, A., Ogée, J. and co-authors. 2005. Europe-wide reduction in primary productivity caused by the heat and drought in 2003. *Nature* **437**, 529–533. doi:10.1038/nature03972.

Ciattaglia, L., Colombo, T. and Masarie, K. A. 1999. Continuous measurements of atmospheric CO_2 at Jubany Station, Antarctica. *Tellus* **51B**, 713–721.

Ciattaglia, L., Rafanelli, C., Araujo, J. and Rodriguez, H. 2008. Long-term measurements of the atmospheric carbon dioxide concentration measured at Jubany Station indicate a relationship with "El Niño". *Berichte zur Polar und Meeresforschung*. AWI Bremerhaven, 571–2008, 390–396.

Conway, T. J., Lang, P. M. and Masarie, K. A. 2008. Atmospheric Carbon Dioxide Dry Air Mole Fractions from the NOAA ESRL Carbon Cycle Cooperative Global Air Sampling Network, 1968–2007. Version: 2008–07-24, Path: ftp://ftp.cmdl.noaa.gov/ccg/co2/flask/event/.

Davis, K. J., Bakwin, P. S., Yi, C., Berger, B. W., Zhao, C. and co-authors. 2003. The annual cycles of CO_2 and H_2O exchange over a northern mixed forest as observed from a very tall tower. *Global Change Biol.* **9**, 1278–1293.

Denman, K. L., Brasseur, G., Chidthaisong, A., Ciais, P., Cox, P. M. and co-authors. 2007. Couplings between changes in the climate system and biogeochemistry. In: *Climate Change 2007: The Physical Science Basis. Contribution of Working Group I to the Fourth Assessment Report of the Intergovernmental Panel on Climate Change* (eds S. Solomon, D. Qin, M. Manning, Z. Chen, M. Marquis, and co-editors). Cambridge University Press, Cambridge, United Kingdom and New York, NY, USA, 501–588.

Denning, A. S., Fung, I. Y. and Randall, D. A. 1995. Latitudinal gradient of atmospheric CO_2 due to seasonal exchange with land biota. *Nature* **376**, 240–243.

Denning, A. S., Holzer, M., Gurney, K. R., Heimann, M., Law, R. M. and co-authors. 1999. Three-dimensional transport and concentration of SF_6–A model intercomparison study (TransCom 2). *Tellus*, **51B**, 266–297.

Dunn, A. L., Barford, C. C., Wofsy, S. C., Goulden, M. L. and Daube, B. C. 2006. A long-term record of carbon exchange in a boreal black spruce forest: means, responses to interannual variability, and decadal trends. *Global Change Biol.* **12**, doi:10.1111/j.1365-2486.2006.01221.x.

Engelen, R. J., Denning, A. S., Gurney, K. R., Law, R. M., Rayner, P. J. and co-authors. 2002. On error estimation in atmospheric CO_2 inversions. *J. Geophys. Res.* **107**, 4635. doi:10.1029/2002JD002195.

Enting, I. G. 2002. *Inverse Problems in Atmospheric Constituent Transport*. Cambridge Univ. Press, Cambridge, UK, 392.

Erickson, D. J., III, Mills, R. T., Gregg, J., Blasing, T. J., Hoffman, F. M. and co-authors. 2008. An estimate of monthly global emissions of anthropogenic CO_2: Impact on the seasonal cycle of atmospheric CO_2. *J. Geophys. Res.* **113**, G01023. doi:10.1029/2007JG000435.

Esaki, Y. 2009. *Atmospheric CO_2 Hourly Concentration Data, Minamitorishima, Ryori and Yonagunijima*. World Data Center for Greenhouse Gases, Japan Meteorol. Agency, Tokyo. Version: 18 Mar 2008, Available at: http://gaw.kishou.go.jp/wdcgg/wdcgg.html.

Fischer, M. 2005. Carbon Dioxide Flux Measurement Systems Handbook. Atmospheric Radiation Measurement Tech Report: ARM-TR048.

Fischer, M., Billesbach, D. P., Berry, J. A., Riley, W. J. and Torn, M. S. 2007. Spatiotemporal variations in growing season exchanges of CO_2, H_2O, and sensible heat in agricultural fields of the Southern Great Plains. Lawrence Berkeley National Laboratory Professional Paper: LBNL-63014.

Forster, P., Ramaswamy, V., Artaxo, P., Berntsen, T., Betts, R. and co-authors. 2007. Changes in atmospheric constituents and in radiative forcing. In: *Climate Change 2007: The Physical Science Basis. Contribution of Working Group I to the Fourth Assessment Report of the Intergovernmental Panel on Climate Change* (eds S. Solomon, D. Qin, M. Manning, Z. Chen, M. Marquis, and co-editors).Cambridge University Press, Cambridge, United Kingdom and New York, NY, USA, 131–234,

Francey, R. J., Steele, L. P., Spencer, D. A., Langenfelds, R. L., Law, R. M. and co-authors. 2003. The CSIRO (Australia) measurement of greenhouse gases in the global atmosphere. In: *Report of the 11th WMO/IAEA Meeting of Experts on Carbon Dioxide Concentration and Related Tracer Measurement Techniques* (eds S. Toru and S. Kazuto). World Meteorological Organization Global Atmosphere Watch, Tokyo, Japan, September 2001, 97–111.

Friedbacher, E., Froehlich, M. and Spangl, W. 2007. *Atmospheric CO_2 hourly concentration data, Sonnblick*. World Data Center for Greenhouse Gases, Japan Meteorol. Agency, Tokyo. Version: 18 Mar 2008, Available at: http://gaw.kishou.go.jp/wdcgg.html.

Gerbig, C., Lin, J. C., Wofsy, S. C., Daube, B. C., Andrews, A. E. and co-authors. 2003. Toward constraining regional-scale fluxes of CO_2 with atmospheric observations over a continent: 2. Analysis of COBRA data using a receptor-oriented framework. *J. Geophys. Res.* **108**, 4757. doi:10.1029/2003JD003770.

Giglio, L., van der Werf, G. R., Randerson, J. T., Collatz, G. J. and Kasibhatla, P. S. 2006. Global estimation of burned area using MODIS active fire observations. *Atmos. Chem. Phys.* **6**, 957–974.

GLOBALVIEW-CO2. 2007. Cooperative Atmospheric Data Integration Project–Carbon Dioxide. CD-ROM, NOAA ESRL, Boulder, Colorado. [Also available on Internet via anonymous FTP to ftp.cmdl.noaa.gov, Path: /ccg/co2/GLOBALVIEW]

Gomez-Pelaez, A. J., Ramos, R. and Perez-delaPuerta, J. 2006. Methane and carbon dioxide continuous measurements at Izana GAW station

(Spain). In: *GAW Report (No. 168) of the 13th WMO/IAEA Meeting of Experts on Carbon Dioxide and Related Tracer Measurement Techniques* (ed. J. B. Miller). World Meteorological Organization, (TD No. 1359), Boulder, Colorado, USA, 19–22 September 2005 180–184.

Gourdji, S. M., Mueller, K. L., Schaefer, K. and Michalak, A. M. 2008. Global monthly averaged CO_2 fluxes recovered using a geostatistical inverse modeling approach: 2. Results including auxiliary environmental data. *J. Geophys. Res.* **113**, D21115. doi:10.1029/2007JD009733.

Gurney, K. R., Law, R., Rayner, P. and Denning, A. S. 2000. *TransCom 3 Experimental Protocol*. Paper 707, Department of Atmospheric Science, Colorado State University, USA.

Gurney, K. R., Law, R. M., Denning, A. S., Rayner, P. J., Baker, D. and co-authors. 2002. Towards robust regional estimates of CO_2 sources and sinks using atmospheric transport models. *Nature* **415**, 626–630.

Gurney, K. R., Law, R. M., Denning, A. S., Rayner, P. J., Pak, B. C. and co-authors. 2004. Transcom 3 inversion intercomparison: Model mean results for the estimation of seasonal carbon sources and sinks. *Global Biogeochem. Cycles* **18**, GB1010. doi:10.1029/2003GB002111.

Gurney, K. R., Chen, Y-H., Maki, T., Kawa, S. R., Andrews, A. and co-authors. 2005. Sensitivity of atmospheric CO_2 inversions to seasonal and interannual variations in fossil fuel emissions. *J. Geophys. Res.* **110**, D10308. doi:10.1029/2004JD005373.

Gurney, K. R., Baker, D., Rayner, P. and Denning, S. 2008. Interannual variations in continental-scale net carbon exchange and sensitivity to observing networks estimated from atmospheric CO_2 inversions for the period 1980 to 2005. *Global Biogeochem. Cycles* **22**, GB3025. doi:10.1029/2007GB003082.

Haszpra, L., Barcza, Z., Hidy, D., Szilágyi, I., Dlugokencky, E. and co-authors. 2008. Trends and temporal variations of major greenhouse gases at a rural site in Central Europe. *Atmos. Environ.* **42**, 8707–8716. doi:10.1016/j.atmosenv.2008.09.012.

Hatakka, J., Aalto, T., Aaltonen, V., Aurela, M., Hakola, H. and co-authors. 2003. Overview of the atmospheric research activities and results at Pallas GAW station. *Boreal Environ. Res.* **8**, 365–383.

Higuchi, K., Worthy, D., Chan, D. and Shashkov, A. 2003. Regional source/sink impact on the diurnal, seasonal and inter-annual variations in atmospheric CO_2 at a boreal forest site in Canada. *Tellus* **55B**, 115–125.

Hollinger, D. Y., Goltz, S. M., Davidson, E. A., Lee, J. T., Tu, K. and co-authors. 1999. Seasonal patterns and environmental control of carbon dioxide and water vapour exchange in an ecotonal boreal forest. *Global Change Biol.* **5**, 891–902.

Hurwitz, M. D., Ricciuto, D. M., Bakwin, P. S., Davis, K. J., Wang, W. and co-authors. 2004. Transport of carbon dioxide in the presence of storm systems over a northern Wisconsin forest. *J. Atmos. Sci.* **61**, 607–618.

Hutyra, L. R., Munger, J. W., Saleska, S. R., Gottlieb, E., Daube, B. C. and co-authors. 2007. Seasonal controls on the exchange of carbon and water in an Amazonian rain forest. *J. Geophys. Res.* **112**, G03008. doi:10.1029/2006JG000365.

Jacobson, A. R., Mikaloff Fletcher, S. E., Gruber, N., Sarmiento, J. L. and Gloor, M. 2007a. A joint atmosphere-ocean inversion for surface fluxes of carbon dioxide: 1. Methods and global-scale fluxes. *Global Biogeochem. Cycles* **21**, GB1019. doi:10.1029/2005GB002556.

Jacobson, A. R., Mikaloff Fletcher, S. E., Gruber, N., Sarmiento, J. L. and Gloor, M. 2007b. A joint atmosphere-ocean inversion for surface fluxes of carbon dioxide: 2. Regional results. *Global Biogeochem. Cycles* **21**, GB1020. doi:10.1029/2006GB002703.

Janssens, I. A., Freibauer, A., Ciais, P., Smith, P., Nabuurs, G.-J. and co-authors. 2003. Europe's terrestrial biosphere absorbs 7 to 12% of European anthropogenic CO_2 emissions. *Science* **300**, 1538–1542. doi:10.1126/science.1083592.

Kaminski, T., Rayner, P. J., Heimann, M. and Enting, I. G. 2001. On aggregation errors in atmospheric transport inversions. *J. Geophys. Res.* **106**(D5), 4703–4715.

Kawa, S. R., Erickson, D. J., III, Pawson, S. and Zhu, Z. 2004. Global CO_2 transport simulations using meteorological data from the NASA data assimilation system. *J. Geophys. Res.* **109**, D18312. doi:10.1029/2004JD004554.

Keeling, C. D., Whorf, T. P., Wahlen, M. and Van Der Pilcht, J. 1995. Internannual extremes in the rate of rise of atmospheric carbon dioxide since 1980. *Nature* **375**, 666–670.

Keeling, R. F., Piper, S. C. and Heimann, M. 1996. Global and hemispheric CO_2 sinks deduced from changes in atmospheric O_2 concentrations. *Nature* **381**, 218–221.

Langenfelds, R. L., Francey, R. J., Pak, B. C., Steele, L. P., Lloyd, J. and co-authors. 2002. Interannual growth rate variations of atmospheric CO_2 and its $\delta^{13}C$, H_2, CH_4 and CO between 1992 and 1999 linked to biomass burning. *Global Biogeochem. Cycles* **16**, 1048. doi:10.1029/2001GB001466.

Lauvaux, T., Uliasz, M., Sarrat, C., Chevallier, F., Bousquet, P. and co-authors. 2008. Mesoscale inversion: First results from the CERES campaign with synthetic data. *Atmos. Chem. Phys.* **8**, 3459–3471.

Law, R. M., Rayner, P. J., Steele, L. P. and Enting, I. G. 2003. Data and modelling requirements for CO_2 inversions using high-frequency data. *Tellus* **55B**, 512–521.

Law, R. M., Peters, W., Rödenbeck, C., Aulagnier, C., Baker, I. and co-authors. 2008. TransCom model simulations of hourly atmospheric CO_2: Experimental overview and diurnal cycle results for 2002. *Global Biogeochem. Cycles* **22**, GB3009. doi:10.1029/2007GB003050.

Levinson, D. H. and Waple, A. M. 2004. State of the climate in 2003. *Bull. Am. Meteorol. Soc.* **85**, S1-S72.

Li, Y.-F. 1996. Global Population distribution 1990: Terrestrial area and country name information on a one by one degree grid cell basis. *ORNL/CDIAC-96*, DB1016, Carbon Dioxide Inf. Anal. Cent., Oak Ridge, Tenn., USA.

Marland, G., Boden, T. A. and Andres, R. J. 2007. Global, regional, and national fossil fuel CO_2 emissions. In: *Trends, A Compendium of Data on Global Change*. Carbon Dioxide Inf. Anal. Cent., Oak Ridge Natl. Lab., U.S. Dep. of Energy, Oak Ridge, Tenn., USA.

Masarie, K. A., Langenfelds, R. L., Allison, C. E., Conway, T. J., Dlugokencky, E. J. and co-authors. 2001. NOAA/CSIRO Flask Air Intercomparison Experiment: A strategy for directly assessing consistency among atmospheric measurements made by independent laboratories. *J. Geophys. Res.* **106**(D17), 20445–20464.

Matsueda, H., Machida, T., Sawa, Y., Nakagawa, Y., Hirotani, K. and co-authors. 2008. Evaluation of atmospheric CO_2 measurements from new flask air sampling of JAL airliner observations. *Meteorol. Geophys.* **59**, 1–17. doi:10.2467/mripapers.59.1.

Mueller, K. L., Gourdji, S. M. and Michalak, A. M. 2008. Global monthly averaged CO_2 fluxes using a geostatistical inverse modeling approach:

1. Results using atmospheric measurements. *J. Geophys. Res.* **113**, D21114. doi:10.1029/2007JD009734.

Myneni, R. B., Dong, J., Tucker, C. J., Kaufmann, R. K., Kauppi, P. E. and co-authors. 2001. A large carbon sink in the woody biomass of Northern forests. *Proc. Natl. Acad. Sci. USA* **98**, 14784–14789. doi:10.1073/pnas.261555198.

Nemani, R. R., Keeling, C.D., Hashimoto, H., Jolly, W. M., Piper, S. C. and co-authors. 2003. Climate-driven increases in global terrestrial net primary production from 1982 to 1999. *Science* **300**, 1560–1563. doi:10.1126/science.1082750.

Parazoo, N. C., Denning, A. S., Kawa, S. R., Corbin, K. D., Lokupitiya, R. S. and co-authors. 2008. Mechanisms for synoptic variations of atmospheric CO_2 in North America, South America and Europe. *Atmos. Chem. Phys.* **8**, 7239–7254.

Patra, P. K., Law, R. M., Peters, W., Rödenbeck, C., Takigawa, M. and co-authors. 2008. TransCom model simulations of hourly atmospheric CO_2: Analysis of synoptic-scale variations for the period 2002–2003. *Global Biogeochem. Cycles* **22**, GB4013. doi:10.1029/2007GB003081.

Peters, W., Jacobson, A. R., Sweeney, C., Andrews, A. E., Conway, T. J. and co-authors. 2007. An atmospheric perspective on North American carbon dioxide exchange: CarbonTracker. *Proc. Natl. Acad. Sci. USA* **104**, 18925–18930. doi:10.1073/pnas.0708986104.

Peylin, P., Rayner, P. J., Bousquet, P., Carouge, C., Hourdin, F. and co-authors. 2005. Daily CO_2 flux estimates over Europe from continuous atmospheric measurements: 1, inverse methodology. *Atmos. Chem. Phys.* **5**, 3173–3186.

Potter, C., Klooster, S., Steinbach, M., Tan, P., Kumar, V. and co-authors. 2003. Global teleconnections of climate to terrestrial carbon flux. *J. Geophys. Res.* **108**, 4556. doi:10.1029/2002JD002979.

Potter, C., Klooster, S., Huete, A. and Genovese, V. 2007. Terrestrial carbon sinks for the United States predicted from MODIS satellite data and ecosystem modeling. *Earth Interact.* **11**, 11–013. doi:10.1175/EI228.1.

Randerson, J. T., Thompson, M. V., Conway, T. J., Fung, I. Y. and Field, C. B. 1997. The contribution of terrestrial sources and sinks to trends in the seasonal cycle of atmospheric carbon dioxide. *Global Biogeochem. Cycles* **11**, 535–560.

Rayner, P. J., Enting, I. G., Francey, R. J. and Langenfelds, R. 1999. Reconstructing the recent carbon cycle from atmospheric CO_2, $\delta^{13}C$ and O_2/N_2 observations. *Tellus* **51B**, 213–232.

Rödenbeck, C., Houweling, S., Gloor. M. and Heimann, M. 2003a. CO_2 flux history 1982–2001 inferred from atmospheric data using a global inversion of atmospheric transport. *Atmos. Chem. Phys.* **3**, 1919–1964.

Rödenbeck, C., Houweling, S., Gloor, M. and Heimann, M. 2003b. Time-dependent atmospheric CO_2 inversions based on interannually varying tracer transport. *Tellus* **55B**, 488–497.

Santaguida, R. 2008. *Atmospheric CO_2 hourly concentration data, Monte Cimone*. World Data Center for Greenhouse Gases, Japan Meteorol. Agency, Tokyo. Version: 18 Mar 2008, Available at: http://gaw.kishou.go.jp/wdcgg.html.

Schuh, A. E., Denning, A. S., Uliasz, M. and Corbin, K. D. 2009. Seeing the forest for the trees: Recovering large-scale carbon flux biases in the midst of small-scale variability. *J. Geophys. Res.* **114**, G03007. doi:10.1029/2008JG000842.

Takahashi, T., Sutherland, S. C., Sweeney, C., Poisson, A., Metzl, N. and co-authors. 2002. Global sea-air CO_2 flux based on climatological surface ocean pCO_2 and seasonal biological and temperature effects. *Deep-Sea Res. II* **49**, 1601–1622.

Takahashi, T., Sutherland, S. C., Wanninkhof, R., Sweeney, C., Feely, R. A. and co-authors. 2009. Climatological mean and decadal change in surface ocean pCO_2, and net sea-air CO_2 flux over the global oceans. *Deep-Sea Res. II* **56**, 554–577. doi:10.1016/j.dsr2.2008.12.009.

Tans, P. P., Fung, I. Y. and Takahashi, T. 1990. Observational constraints on the global atmospheric CO_2 budget. *Science* **247**, 1431–1438.

Tans, P., Zhao, C. and Masarie, K. 2003. Maintenance and propagation of the WMO Mole Fraction Scale for carbon dioxide in air. In: *Report of the Eleventh WMO Meeting of Experts on Carbon Dioxide Concentration and Related Tracer Measurement Techniques* (ed. S. Toru). World Meteorological Organization, Geneva, Tokyo, Japan, 25–28. September 2001.

Tarantola, A. 2005. *Inverse Problem Theory and Methods for Model Parameter Estimation*. Society for Industrial and Applied Mathematics, Philadelphia, PA, USA, 342.

Thoning, K. W., Kitzis, D. R. and Crotwell, A. 2007. Atmospheric Carbon Dioxide Dry Air Mole Fractions from quasi-continuous measurements at Barrow, Alaska; Mauna Loa, Hawaii; American Samoa; and South Pole, 1973–2006. Version: 2007–10-01, Path: ftp://ftp.cmdl.noaa.gov/ccg/co2/in-situ/.

Tsutsumi, Y., Mori, K., Ikegami, M., Tashiro, T. and Tsuboi, K. 2006. Long-term trends of greenhouse gases in regional and background events observed during 1998–2004 at Yonagunijima located to the east of the Asia continent. *Atmos. Environ.* **40**, 5868–5879. doi:10.1016/j.atmosenv.2006.04.036.

Uhse, K. 2006. *Atmospheric CO_2 hourly concentration data, Schauinsland, Zugspitze/Schneefernerhaus*. World Data Center for Greenhouse Gases, Japan Meteorol. Agency, Tokyo. Version: 18 Mar 2008, Available at: http://gaw.kishou.go.jp/wdcgg.html.

Urbanski, S., Barford, C., Wofsy, S., Kucharik, C., Pyle, E. and co-authors. 2007. Factors controlling CO_2 exchange on timescales from hourly to decadal at Harvard Forest. *J. Geophys. Res.* **112**, G02020. doi:10.1029/2006JG000293.

van der Werf, G. R., Randerson, J. T., Giglio, L., Collatz, G. J., Kasibhatla, P. S. and co-authors. 2006. Interannual variability in global biomass burning emissions from 1997 to 2004. *Atmos. Chem. Phys.* **6**, 3423–3441.

Wang, J.-W., Denning, A. S., Lu, L., Baker, I. T., Corbin, K. D. and co-authors. 2007. Observations and simulations of synoptic, regional, and local variations in atmospheric CO_2. *J. Geophys. Res.* **112**, D04108. doi:10.1029/2006JD007410.

Waple, A. M., Lawrimore, J. H., Alexander, L., Horton, B., Ambenje, P. and co-authors. 2003. State of the climate in 2002. *Bull. Am. Meteorol. Soc.* **84**, S1-S68.

Yi, C., Davis, K. J., Berger, B. W. and Bakwin, P. S. 2001. Long-term observations of the dynamics of the continental planetary boundary layer. *J. Atmos. Sci.* **58**, 1288–1299.

Zhao, C. L., Tans, P. P. and Thoning, K. W. 1997. A high precision manometric system for absolute calibrations of CO_2 in dry air. *J. Geophys. Res.* **102**, 5885–5894.

Zhao, C. and Tans, P. P. 2006. Estimating uncertainty of the WMO mole fraction scale for carbon dioxide in air. *J. Geophys. Res.* **111**, D08S09. doi:10.1029/2005JD006003.

Tellus (2010)

TELLUS

Assessing the impact of crops on regional CO_2 fluxes and atmospheric concentrations

By K. D. CORBIN[1]*, A. S. DENNING[2], E. Y. LOKUPITIYA[2], A. E. SCHUH[2], N. L. MILES[3], K. J. DAVIS[3], S. RICHARDSON[3] and I. T. BAKER[2], [1]*Commonwealth Scientific and Industrial Research Organization (CSIRO), Marine and Atmospheric Research, Aspendale, Victoria, Australia;* [2]*Department of Atmospheric Science, Colorado State University, Fort Collins, CO, USA;* [3]*Department of Meteorology, Pennsylvania State University, University Park, PA, USA*

(Manuscript received 22 December 2009; in final form 30 June 2010)

ABSTRACT

Human conversion of natural ecosystems to croplands modifies not only the exchange of water and energy between the surface and the atmosphere, but also carbon fluxes. To investigate the impacts of crops on carbon fluxes and resulting atmospheric CO_2 concentrations in the mid-continent region of the United States, we coupled a crop-specific phenology and physiology scheme for corn, soybean and wheat to the coupled ecosystem–atmosphere model SiB3–RAMS. Using SiBcrop–RAMS improved carbon fluxes at the local scale and had regional impacts, decreasing the spring uptake and increasing the summer uptake over the mid-continent. The altered fluxes changed the mid-continent atmospheric CO_2 concentration field at 120 m compared to simulations without crops: concentrations increased in May and decreased >20 ppm during July and August, summer diurnal cycle amplitudes increased, synoptic variability correlations improved and the gradient across the mid-continent region increased. These effects combined to reduce the squared differences between the model and high-precision tower CO_2 concentrations by 20%. Synoptic transport of the large-scale N–S gradient caused significant day-to-day variability in concentration differences measured between the towers. This simulation study shows that carbon exchange between crops and the atmosphere significantly impacts regional CO_2 fluxes and concentrations.

1. Introduction

The conversion of natural ecosystems to croplands is one of the most direct manifestations of human activity within the biosphere (Ramankutty and Foley, 1998). Land use and land cover change affect the phenology of the vegetation, modify biophysical properties of the land surface (e.g. surface roughness and albedo) and alter biogeochemical cycles (Betts, 2005). Modelling studies have shown that these perturbations change the weather and climate on regional and global scales (Copeland et al., 1996; Bonan, 1997; Lawrence and Slingo, 2004; Osborne et al., 2007).

Although the conversion of forests and grasslands to agricultural land initially leads to a net release of carbon to the atmosphere (Houghton, 2003), the role of croplands on the carbon cycle remains uncertain. Studies over Europe suggest that on annual time-scales croplands are net carbon sources due to soil carbon loss, although these estimates are sensitive to land history, soil properties and management practices (Vleeshouwers and Verhagen, 2002; Janssens et al., 2003). On the global scale, Bondeau et al. (2007) found that including crops reduces the carbon sink in the land biosphere, as compared with simulations of the potential natural vegetation only.

To investigate regional carbon fluxes over a densely cultivated region, the North American Carbon Program (NACP) launched the Mid-Continent Intensive (MCI) Campaign (Ogle et al., 2006). The MCI region is centred over the Midwestern United States (Fig. 1), and the primary focus of the campaign is to compare and reconcile regional fluxes on hourly to annual time scales from top-down atmospheric budgets with bottom-up ecosystem model-based inventories. The MCI campaign funded dense inventory and flux measurements throughout the summer and fall of 2007. The region hosts networks of eddy-covariance flux towers, several long-term agricultural experimental sites with time series of carbon stocks, forestry data collected through the U.S. Department of Agriculture (USDA) Forest and Inventory Analysis (FIA) program, annual crop yield data collected by USDA National Agricultural Statistics Service (NASS) and fossil fuel emissions estimates from the Environmental Protection Agency (EPA) Fuel Emission Statistics. In addition to local

*Corresponding author.
e-mail: katherine.corbin@csiro.au
DOI: 10.1111/j.1600-0889.2010.00485.x

COLOUR

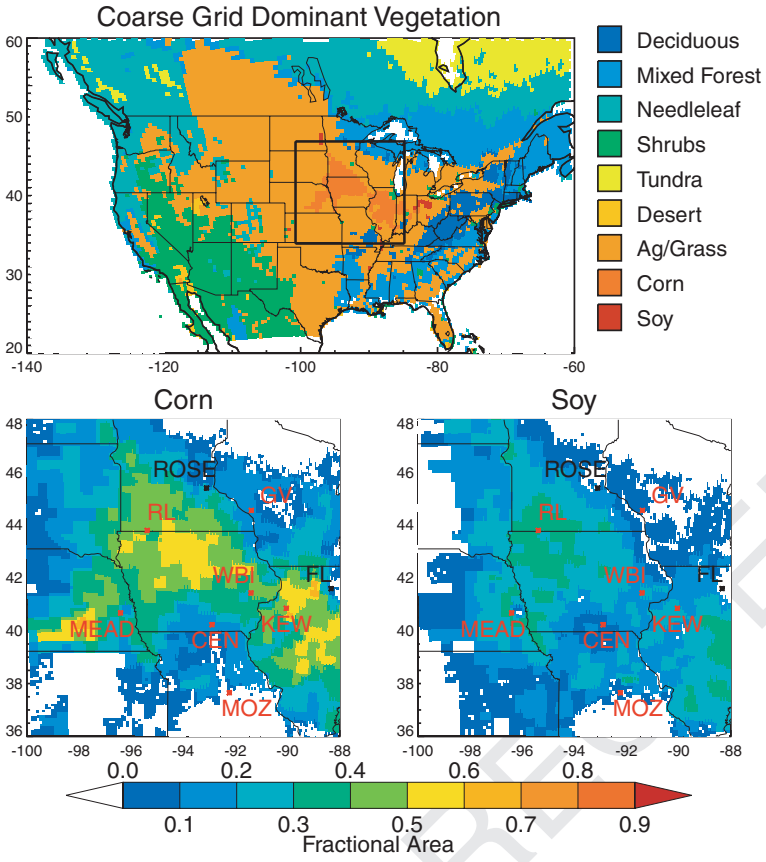

Fig. 1. Grid setup for the SiB3–RAMS simulations. (Top panel) The coarse domain and the dominant vegetation type. The interior grid, corresponding to the MCI region, is outlined on the coarse domain. (Bottom left panel) The fractional coverage of corn in the nested grid. Red tower labels indicate the continuous atmospheric CO_2 sites, and black tower labels indicate AmeriFlux sites. (Bottom right panel) The fractional coverage of soybean in the nested grid.

flux measurements and crop yields, high-precision atmospheric CO_2 concentrations are sampled at seven communications towers throughout the region, beginning spring 2007 (Richardson et al., 2009).

The dense network of data from the MCI can be used for a variety of studies not only to investigate carbon fluxes between the land and atmosphere, but also to enhance our knowledge of the carbon cycle. Regional models provide a way to quantitatively map sources and sinks of CO_2 using a variety of different observations (i.e. soil maps, vegetation maps, topography, meteorology). Model simulations compared with field measurements from the MCI campaign will lead to the advancement of our understanding of the processes and mechanisms driving the variability in these fields. In addition to providing atmospheric inversions with initial flux estimates that include all known mechanisms, coupled ecosystem–atmosphere models can help interpret the high-frequency variability in atmospheric CO_2 concentrations. Because CO_2 concentrations contain information about all sources and sinks of carbon, understanding the mechanisms driving the CO_2 variability will help us better predict carbon fluxes.

To evaluate and analyse atmospheric CO_2 concentrations, it is essential that carbon fluxes be modelled as accurately as possible using all available information. Due to physiological and phenological differences from natural ecosystems, crops strongly modify both the seasonality and magnitude of carbon fluxes by having shorter growing seasons with more intense drawdown (de Noblet et al., 2004; Gervois et al., 2004; Lokupitiya et al., 2009); and land surface models typically do not represent crop fluxes well due to their short but vigorous photosynthetic uptake. Traditionally, models use remotely sensed vegetation parameters, such as the normalized difference vegetation index (NDVI), leaf-area index (LAI) and the fraction of photosynthetically active radiation (FPAR) to estimate carbon dynamics; however, using satellite data does not accurately capture planting, growth, and harvest events of crops due to temporal and spatial compositing. Remotely sensed products use temporal composites, generally 8-day to monthly, to minimize cloud contamination. Because the LAI and FPAR for crops rapidly changes, using these coarse time resolutions do not accurately capture the magnitude of the crop growth and unrealistically extend the timing of the growing season. Spatial compositing also occurs and leads to misrepresentations between the data and the actual field conditions.

To better predict carbon exchanges for crops, Lokupitiya et al. (2009) developed crop-specific phenology and physiology sub-models for corn (maize), soybean and wheat and coupled them to the Simple Biosphere Model (SiBcrop). The sub-models replace remotely sensed leaf area index (LAI) and the FPAR as

used in SiB for estimating carbon dynamics. Using a phonologically based model substantially improved the prediction of LAI for crops, and the use of crop-specific physiology increased the carbon fluxes for a specified LAI to better predict the net ecosystem exchange (NEE) as compared with observed data at flux tower sites in the U.S. mid-continent region (Lokupitiya et al., 2009).

To predict regional-scale carbon exchanges and the resulting atmospheric CO_2 concentrations, we coupled the corn, soybean and wheat sub-models to the ecosystem–atmosphere model SiB3–RAMS. In this study, we will investigate the impact of crops on atmospheric CO_2 concentrations. To evaluate simulated carbon fluxes, we will compare modelled NEE to eddy-covariance derived NEE from flux towers. We will also evaluate atmospheric CO_2 concentrations by comparing the modelled CO_2 field to continuous concentrations sampled on towers at 30 and 120 m during the MCI campaign. In addition, we will examine the cause of the variability in the CO_2 gradient between the towers.

2. Methods

2.1. Model: SiB3–RAMS

The base model used in this study is the Simple Biosphere Model Version 3 (SiB3; Baker and Denning, 2008) coupled to the Brazilian version of the Colorado State Regional Atmospheric Modelling System (RAMS; Frietas et al., 2005). The coupled model, SiB3–RAMS, has been evaluated and used in a variety of carbon budget studies. Denning et al. (2003) used the coupled model to investigate the influence of ecosystem fluxes on atmospheric CO_2 concentrations in Wisconsin; and in a companion paper, Nicholls et al. (2004) showed that katabatic winds, vertical wind shear and circulations in the vicinity of lakes caused atmospheric CO_2 variations. Lu et al. (2005) used the model to investigate mesoscale circulations and atmospheric CO_2 variability in South America. Wang et al. (2007) investigated synoptic variability in atmospheric CO_2 concentrations over North America; and Corbin et al. (2008) used SiB–RAMS to evaluate atmospheric CO_2 spatial and temporal variability. Throughout these studies, various SiB–RAMS modelled fields have been evaluated against observations, including temperature, wind speed, wind direction, radiation, water vapour mixing ratio, latent heat, sensible heat, NEE and atmospheric CO_2 concentrations. Because this is a model comparison study to investigate the impact of crops on carbon fluxes and atmospheric concentrations, we focus on NEE and atmospheric CO_2 concentrations, referring the reader to these previous studies for further model evaluation.

Traditionally, SiB used remotely sensed NDVI to calculate LAI and FPAR; however, due to both spatial and temporal compositing, these satellite data do not accurately capture the timing of planting and harvest events and underestimate the maximum LAI and FPAR values for crops. To more accurately simulate croplands, we coupled SiB3–RAMS to the crop module developed by Lokupitiya et al. (2009). The crop module explicitly calculates the LAI and FPAR for corn, soy and wheat. These simulated values replace remotely sensed data for these vegetation classifications. Phenology events and growth stages for crops were determined by the growing degree days and the number of days since planting, and the crop module allocated photosynthetic carbon to four different plant pools depending on phenological development. The daily carbon allocation to leaves was used to update LAI, which was then used to calculate the NEE.

SiB3–RAMS utilizes a variety of data sets. All the data are for 2007 and are re-gridded from their native resolutions to the SiB3–RAMS domain. The land cover classification is derived from the Moderate Resolution Imaging Spectroradiometer (MODIS) data with 1 km horizontal resolution, which is distributed by the Land Processes Distributed Active Archive Center (LP DAAC) located at the U.S. Geological Survey (USGS) Earth Resources Observation and Science (EROS) Center (lpdaac.usgs.gov). The land cover is converted from the University of Maryland (UMD) classification scheme to SiB biome types. Corn, soybean and wheat are integrated into the vegetation map based on county-level ground-based data from the National Agricultural Statistics Service (NASS) and the Census of Agriculture (AgCensus) (Lokupitiya et al., 2007).

Rather than calculating LAI and FPAR from remotely sensed NDVI, SiB3–RAMS uses direct estimates of these parameters from satellite data. Both LAI and FPAR are 8-day composites derived from MODIS 1-km resolution data, and these products are provided by the Numerical Terradynamics Simulation Group at the University of Montana (Zhao et al., 2005). Due to the minimal land cover classification information provided with the data, the 1-km resolution data are combined to provide one estimate of LAI and FPAR per grid cell. For grid cells that include crops, the LAI and FPAR values for corn, soybean and wheat are replaced by calculated values from the crop module.

The soil classification is derived from a 5-min resolution soil type map by the International Geosphere Biosphere Programme (IGBP) (IGBP, 2000). Meteorological fields are initialized and nudged to the National Centers for Environmental Prediction (NCEP) North American Regional Reanalysis (NARR) meteorological analyses, which covers the North American domain with a 32-km horizontal resolution, 3-h temporal resolution and 50-hPa vertical resolution (Mesinger et al., 2006). The NCEP NARR data are provided by the NOAA/OAR/ESRL Physical Sciences Division located in Boulder, CO, USA, from their web site at http://www.esrl.noaa.gov/psd/. Fossil fuel emissions are prescribed from the high-resolution Vulcan fossil fuel inventory (Gurney et al., 2009). Since the Vulcan emissions represent 2002, they are scaled to match the total estimated 2007 emissions from the Energy Information Administration (EIA, 2007), and these fluxes are added to the first model level. Initial values for carbon

pools, soil moisture and other prognostic variables are calculated for every grid cell from a 10-yr offline SiBcrop simulation using NARR driver data from 1997 to 2007. The initial atmospheric CO_2 concentration field and the lateral boundary concentrations are set and nudged to 3-hourly global CO_2 concentrations on a $1.25^\circ \times 1^\circ$ grid from the Parameterized Chemical Transport Model (PCTM; Parazoo et al., 2008).

2.2. Case descriptions

Three SiB3–RAMS simulations over North America are performed for 1 May 2007 through 31 August 2007. The coarse grid for all cases has 200×120 grid points with 40-km horizontal grid increments, 46 vertical levels up to 24 km and a 90 s time-step. To capture subgrid-scale variability in land cover, SiB3–RAMS used three vegetation patches per grid cell. The dominant vegetation cover for the coarse grid is shown in Fig. 1 (top panel). The landcover in the MCI region is dominated by corn, soybean and C3 grasses/agriculture.

The first case, which will be referred to as BASE, uses the original SiB3–RAMS (without the crop module) and resets all the corn, soybean and wheat biomes to the generic agriculture/grassland vegetation type. The second case, CROP, uses the crop phenology module to replace the remotely sensed LAI and FPAR for corn, soybean and wheat. The model also uses crop-specific physiology to replace the generic grassland/agricultural parameters. The third case, CROPN, uses the crop module and includes a nested grid over the MCI region to capture the extensive corn and soybean cover (Fig. 1, bottom panel). The horizontal grid spacing for the interior grid is 10 km.

2.3. Observations

Because SiB3–RAMS calculates both carbon fluxes and concentrations, we will evaluate the model performance using measurements of both eddy-covariance derived NEE and CO_2 concentrations. For carbon fluxes, eddy-covariance derived NEE data for 2007 are available at three AmeriFlux towers in the mid-continent region: the Mead Rainfed site in Nebraska (MEAD; 41.12°N, 96.44°W; Verma et al., 2005), the Rosemount G21 conventional management corn/soybean rotation site in Minnesota (ROSE; 44.71°N, 93.09°W; Griffis et al., 2008) and the Fermi Agricultural conventional tillage corn/soybean rotation site in Illinois (FL; 41.86°N, 88.22°W; Matamala et al., 2008; Xiao et al., 2008). At all towers, the NEE estimates are derived from measurements of carbon flux and storage, and we use the gap-filled data products. Corn grew at the Mead and Rosemount sites during the summer of 2007, while soybean grew at the Fermi site. The data were obtained from FLUXNET and are available on-line at http://www.fluxnet.ornl.gov (Baldocchi, 2006).

To compare these flux measurements to SiB3–RAMS fluxes, we sample the model at the grid-cell including the tower. Because SiB3–RAMS has three patches per grid cell, only the patch with the corresponding vegetation type is used for comparison (i.e. grass/agriculture for BASE and either corn or soy for CROP). For the CROP and CROPN cases, the fluxes at the towers are nearly identical despite the difference in horizontal resolution, and we only present the results from the CROPN case.

To evaluate modelled CO_2 concentrations, we compare simulated concentrations to continuous tower measurements. As part of the MCI campaign, Pennsylvania State University (PSU) collected continuous atmospheric CO_2 concentrations on five communications towers and in the mid-continent region (Richardson et al., 2009). These measurements were sampled using cavity ring-down spectroscopy instruments from Picarro (Crosson, 2008). In addition, PSU sampled continuous, well-calibrated CO_2 concentrations on the AmeriFlux tower at Missouri Ozarks, which is located in the transitional zone between the central hardwood region and the central agricultural region of the U.S. Atmospheric CO_2 concentrations for 2007 were also collected at West Branch, Iowa (WBI) by the National Oceanic and Atmospheric Administration (NOAA) Global Monitoring Division (GMD). High-accuracy CO_2 concentrations were sampled at WBI using a non-dispersive infrared spectroscopy CO_2 analyser, and the data are publicly available at http://esrl.noaa.gov/gmd (Andrews et al., 2009). The reference names and letters, locations and sampling heights at all six towers are displayed in Table 1 and Fig. 1, bottom panel. Nearly all the towers measure CO_2 concentrations both near the surface and in the mid-troposphere, except the Missouri Ozark tower, which only collects samples at 30 m. We will compare measurements sampled closest to 30-and 120 m at each tower to model results from the matching location at the same vertical level. To reconcile an offset, the four-month mean modelled atmospheric CO_2 concentrations were corrected to match the four-month mean observed CO_2 concentration among the towers.

3. Results

3.1. Crop impacts on NEE

Simulating corn and soybean explicitly using crop-specific physiology and phenology rather than using the generic agriculture/grassland biome significantly alters both the timing and the magnitude of NEE (Fig. 2). In the BASE case, the NEE is similar at all three sites, with a diurnal mean NEE of $\sim 3\ \mu\text{mol m}^{-2}\ \text{s}^{-1}$ throughout the summer. The NEE remains relatively constant due to the remotely sensed LAI and FPAR for this time period, as the satellite data has reduced seasonality due to both temporal and spatial compositing. In addition, re-gridding the data to the SiB3–RAMS domain causes further smoothing. Because the remotely sensed vegetation data associated with the LAI and FPAR has limited land cover classifications and does not contain crops, all the satellite pixels within a SiB3–RAMS grid cell are included to create a mean value. Because crops have a much shorter, more intense growing season than natural vegetation,

Table 1. Reference name, location and sampling height for the towers measuring continuous atmospheric CO_2 concentrations in the MCI region

Reference	Abbreviation	Site	Latitude	Longitude	Sampling heights
A	MEAD	Mead, NE	41.14°N	96.46°W	30/122 m
B	RL	Round Lake, MN	43.53°N	95.41°W	30/110 m
C	CEN	Centerville, IA	40.79°N	92.88°W	30/110 m
D	WBI	West Branch, IA	41.73°N	91.35°W	31/99/379 m
E	GV	Galesville, WI	44.09°N	91.34°W	30/122 m
F	KEW	Kewanee, IL	41.28°N	89.97°W	30/140 m
G	MOZ	Missouri Ozark, MO	38.74°N	92.20°W	30 m

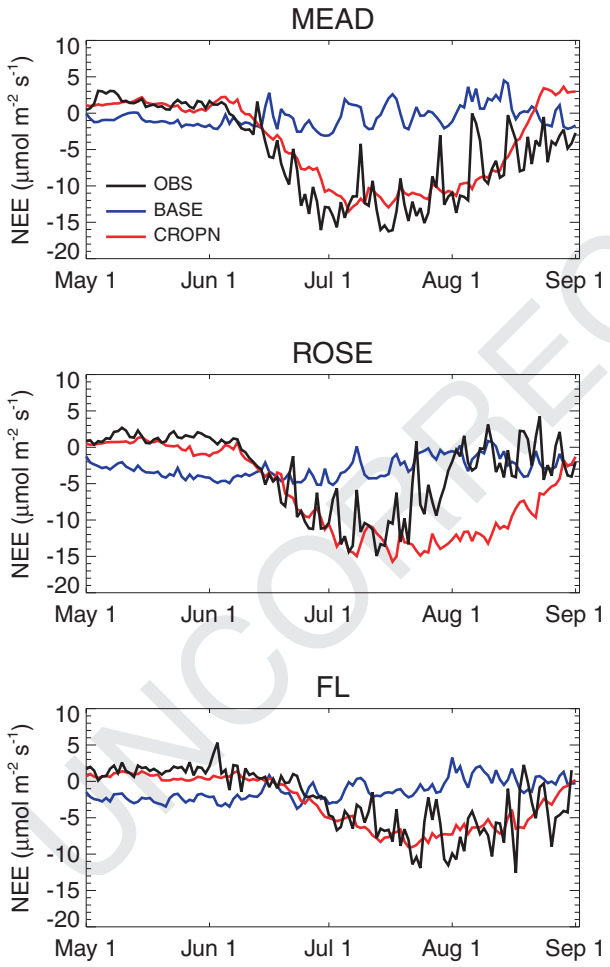

Fig. 2. Diurnal mean net ecosystem exchange (NEE) at the Mead site (top panel), the Rosemount G21 site (middle panel) and the Fermi site (bottom panel). Observations are solid black, modelled NEE from the BASE simulation is dark grey solid dot, and modelled NEE from the CROPN simulation is dashed grey.

averaging over all satellite pixels further lengthens the growing season and reduces the amplitude of the seasonality in LAI and FPAR. These temporal and spatial compositing effects combine to yield relatively constant NEE from May to August.

In the simulations with crops, the NEE varies between sites and more closely matches the observations. Over the two corn sites (MEAD and ROSE), the NEE remains small until the beginning of June when the corn begins to grow rapidly. The NEE uptake rapidly increases through June, reaching maximum daily carbon uptake throughout July in both the eddy-covariance derived NEE estimates and the simulations by the crop model. The uptake then decreases throughout August; however, at the Rosemount site the carbon uptake in the model does not decrease as rapidly as seen in the observations.

Compared with corn, soybean starts to grow later in the year and assimilates less carbon (FL; Fig. 2, bottom panel). At the soybean site, the crop module captures the minimal drawdown from May until mid-June, the rapid increase in uptake throughout late June and July, and the decrease in uptake in late August. Modelling corn and soy explicitly yields a shorter, more intense growing season than using natural ecosystems to represent crops, which better represents the eddy-covariance derived fluxes at both corn and soybean sites.

Atmospheric CO_2 concentrations are influenced not only by local carbon fluxes, but also by more distant fluxes through atmospheric mixing and transport. Because the MCI region is located in the middle of the United States, it is important to understand the fluxes over the entire country. The mean spring (May) and summer (JJA) NEE from the CROP simulation are displayed in Fig. 3 (left panel). In May of 2007, the majority of the country is taking up carbon at the onset of the growing season, except heavily cultivated areas including the MCI region. Since corn and soybean have not started growing, the central United States is neutral to a slight source of carbon due to bare fields at these locations. During the summer of 2007, the model shows that the southeastern United States is a source of CO_2. Photosynthesis is severely reduced due primarily to temperature and humidity stress. During the daytime, high temperatures significantly above optimal conditions decrease the assimilation while enhancing the respiration, and the dry atmospheric conditions create a vapour pressure deficit which further restricts carbon uptake. According to the National Climatic Data Center, the summer of 2007 was the sixth warmest for the United States in the past 113 yr, with temperatures being the highest in the

COLOUR

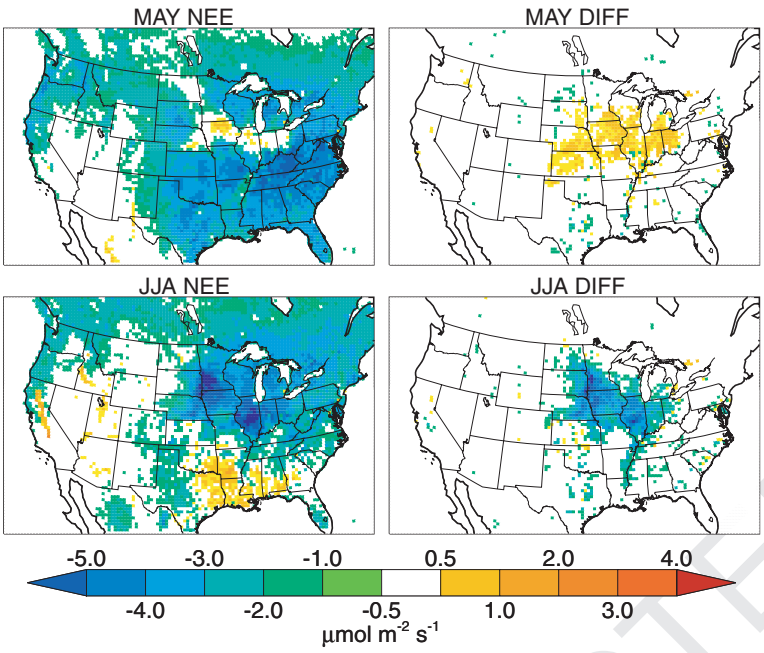

Fig. 3. (Top left panel) Mean May NEE from the CROPN simulation. (Bottom left panel) Mean summertime (June/July/August) NEE from the CROPN simulation. (Top right panel) Mean May NEE differences between the BASE and CROPN simulations (CROPN–BASE). (Bottom right panel) Mean summertime NEE differences.

southeast and in the west. The southeastern United States experienced a heat wave in August, breaking over 70 records for all-time high temperatures and for the most days above 32 °C, and the 3-month Standardized Precipitation Index for June through August 2007 shows that the southeastern United States was exceptionally dry (National Oceanic and Atmospheric Administration National Climatic Data Center; http://lwf.ncdc.noaa.gov/climate-monitoring/index.php). Central California was also very hot and moderately dry according to the Climatic Data Center, and this region is also a summer source of CO_2 due to temperature and humidity stress. The northern half of the United States and Canada are summer sinks of carbon. The MCI region is a particularly large summer sink, with some heavily cultivated regions taking up more than 8 μmol m^{-2} s^{-1} carbon on average.

Simulating crops alters the modelled NEE across the entire MCI region (Fig. 3, right panel). In May, the CROPN case has reduced monthly mean uptake over the MCI and Midwest regions compared to the BASE simulation, with mean differences of ∼1–3 μmol m^{-2} s^{-1}. These differences are caused by the lack of uptake in corn and soybean during this month while the crops are sown as compared with the BASE case, which has photosynthesizing natural vegetation. A few individual grid cells have enhanced uptake over the central United States, and these pixels correspond to wheat crops that are nearing maturity after being planted in the winter. The mean May fluxes over the MCI region do not change between the CROP and CROPN simulations.

In the summer, modelling crops explicitly enhances the uptake over the MCI region, with differences greater than 5 μmol m^{-2} s^{-1} in the seasonal average. The enhanced summer uptake from including crops is due to the intensity of assimilation by both corn and soybean compared with the basic agricultural and natural grassland fluxes. Simulating corn and soybean rather than generic agriculture has the largest impact on the NEE, as the majority of the summer difference is seen between the CROP and BASE cases. Adding the nested grid contributes an additional ∼1–2 μmol m^{-2} s^{-1} to the mean summer sink.

3.2. *Crop impacts on atmospheric CO_2 concentrations*

Mean atmospheric CO_2 concentrations at 120 m in the CROPN simulation reflect the 2007 NEE distribution (Fig. 4, left panel). In May, concentrations are lower in the southeast, central United States, and eastern Canada compared to higher concentrations in the west and the MCI region. In contrast, summer (JJA) concentrations are high over the southeast, where the region is a source of carbon, whereas lower concentrations exist over the northern United States and Canada, where the vegetation is a sink. High concentrations appear over southern California and the east coast from fossil fuel emissions. The high southern and eastern concentrations and low northern concentrations create a large-scale horizontal gradient in atmospheric CO_2 concentrations, with near-surface differences at 120 m greater than 20 ppm across the central states just to the south of the MCI region.

Including crops causes significant, spatially coherent changes in the 120 m atmospheric CO_2 concentrations (Fig. 4, right panel). The CROPN simulation has higher concentrations over the MCI region in May compared to the BASE case. The increased concentrations occur due to the lack of uptake over croplands before planting, and the May differences between the CROP and CROPN simulations are minimal (<1 ppm). In the

COLOUR

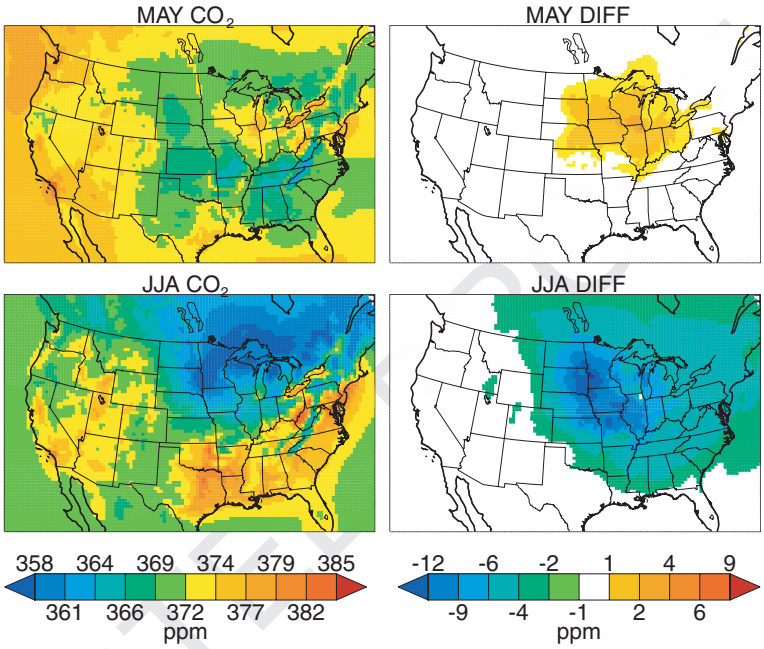

Fig. 4. (Top left panel) Mean May atmospheric CO_2 concentrations at 120 m from the CROPN simulation. (Bottom left panel) Mean summer (JJA) atmospheric CO_2 concentrations at 120 m from the CROPN simulation. (Top right panel) Mean May 120 m CO_2 concentration differences between BASE and CROPN (CROPN–BASE). (Bottom panel) Mean summer (JJA) 120 m CO_2 concentration differences.

summer, the CROPN simulation has significantly lower concentrations than the BASE case. Maximum differences occur in July, when 120 m concentration differences are greater than 15 ppm. Approximately, half of the net differences seen between the CROPN and BASE cases are due to adding crops on the coarse domain, the other half are due to including the nested grid over the MCI region. Throughout the summer, the influence of crops extends to Canada due to atmospheric transport, although the magnitude of the differences decreases with increasing distance from the MCI region.

The impact of crops on atmospheric CO_2 concentrations can be quantitatively assessed by evaluating the concentrations at the seven towers in the MCI region. The root mean square errors (RMSE) between the full time-series of tower observations and the SiB3-RAMS simulations are shown in Table 2. At 120 m, including the crop module lowered the RMSE at all towers. Including crops on the coarse domain caused the largest reduction, while increasing the spatial resolution to capture the extensive crop coverage further reduced the errors. The RMSE reduction is more than 25% at Round Lake and Kewanee, the two towers with the greatest coverage of corn and soybean; however, the error reduction at the Galesville tower is minimal. Overall, the mean RMSE at 120 m for the CROPN simulation is approximately 20% lower (2.4 ppm) than that for the BASE case. Model errors near the surface (30 m) are higher than those at 120 m, and the improvements in the CROP and CROPN simulations are less significant, except at WBI where the improvement is larger near the surface. The mean RMSE for the CROPN simulation is approximately 13% lower (2.4 ppm) than the BASE simulation, although the errors at both Mead and Galesville increase

Table 2. Root mean square errors (RMSE), in ppm, using the complete time series

	RMSE at 120 m (ppm)				RMSE at 30 m (ppm)			
Site	BASE	CROP	CROPN	% Error reduction	BASE	CROP	CROPN	% Error reduction
MEAD	12.5	11.6	11.1	12%	14.5	15.7	15.5	−7%
RL	14.1	10.5	10.1	28%	16.4	13.7	13.2	20%
CEN	15.2	12.6	11.9	22%	16.2	15.0	14.2	13%
WBI	17.5	14.7	14.0	20%	26.0	27.9	18.5	29%
GV	13.0	12.7	12.7	3%	19.6	20.4	20.5	−5%
KEW	15.8	13.1	11.4	28%	17.5	17.3	13.8	21%
MOZ	–	–	–	–	20.3	19.0	17.8	14%

Note: The left-hand columns show the errors at 120 m, and the right-hand columns display the errors at 30 m. The errors for the BASE, CROP and CROPN simulations are shown at each tower for both vertical levels, as is the percent error reduction between the BASE and CROPN simulations.

slightly when crops are modelled. The net error reductions show that including crops substantially improves the SIB3-RAMS simulations, particularly at the locations in heavily cultivated areas.

The improvement in the atmospheric CO_2 concentrations is caused by changes in the spring and summer drawdown, the diurnal cycle, and synoptic variability. Focusing on the Kewanee tower, which has the largest percentage of crop coverage, mid-afternoon mean concentrations and a ten-day mid-July time-series from both the tower CO_2 observations and all three model simulations are shown in Fig. 5. The BASE case does not capture the seasonality of the concentrations, with lower than observed CO_2 concentrations in May and June (>10 ppm differences) and higher values in July and August (>15 ppm differences). Simulating crops more closely matches the spring and summer drawdown by increasing the May concentrations and decreasing the mid-summer concentrations. Coarsely simulating crops helps to capture the seasonality, while modelling the region at higher resolution leads to further improvement. Including crops improves the synoptic variability at Kewanee, as specific events are captured in both the CROP and CROPN cases. The diurnal cycle also matches the observations more closely in the runs with crops, as the BASE simulation tends to underestimate the amplitude of the diurnal cycle. Improved summer drawdown and diurnal and synoptic variability all combine to cause the reduction in RMSE seen at Kewanee. Although the RMSE from the full time-series remains relatively large, the reduction from crops is still substantial and will improve both forward and inverse models. In particular, not capturing the correct magnitudes of concentrations in May and July by inaccurately modelling the spring drawdown will lead to biases in forward modelling applications and thus cause biases in carbon fluxes from inverse modelling studies.

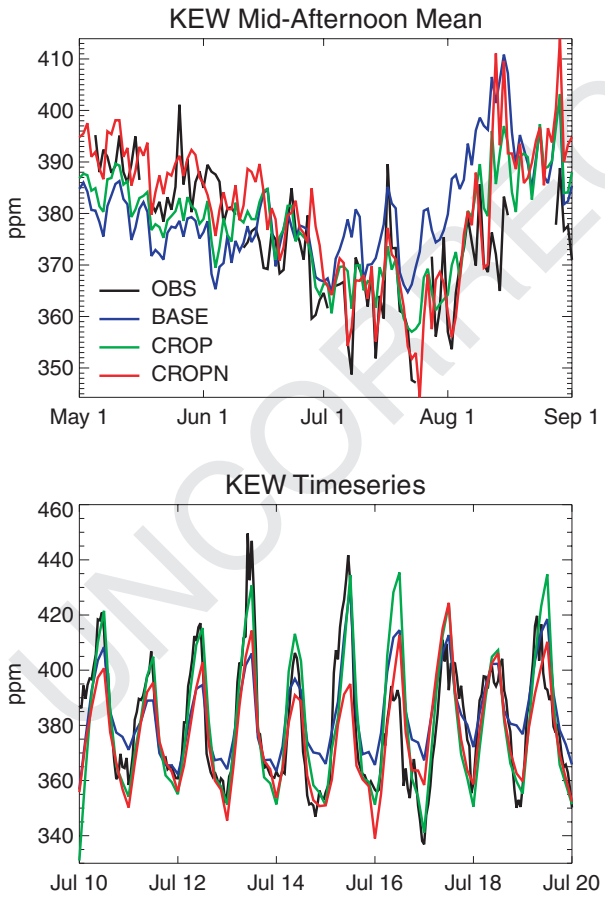

Fig. 5. (Top panel) Time-series of the mean mid-afternoon (12 p.m.–6 p.m.) atmospheric CO_2 concentrations at 120 m for the Kewanee tower, which is the tower with the greatest corn and soybean coverage. Observations are solid black, modelled CO_2 from the BASE simulation is dark grey solid dot, modelled CO_2 from the CROP simulation is grey dot and modelled CO_2 from the CROPN simulation is dashed grey. (Bottom panel) Mid-July 120 m time-series at the Kewanee tower.

In addition to Kewanee, all the towers in the MCI region show that modelling crops improves the spring draw-down, the diurnal cycle, and synoptic variability. Fig. 6(a) shows daytime monthly mean concentrations at each of the towers. The observations have high concentrations in May and low concentrations in July, with a spring drawdown of more than 20 ppm at some towers. The gradient between the towers increases throughout the growing season: in May, the towers are all within 5 ppm of each other, while in August the spread has increased to nearly 15 ppm. In July, three of the towers have daytime mean concentrations lower than 360 ppm.

The BASE simulation does a poor job capturing the drawdown during spring months, with mean concentrations remaining stable between May and July. The BASE case simulates an increase in the gradient between the towers located in cultivated areas; however, the model underestimates the May and June concentrations at the Missouri Ozark site. Including crops dramatically improves the simulated carbon uptake during the spring and summer. The CROP simulation increases the seasonality, and the CROPN case simulates even greater drawdown between spring and summer. The CROPN simulation still underestimates the May and June concentrations, particularly at Missouri Ozark. The CROPN case captures the increasing gradient between the towers and simulates the June and July spread reasonably well; however, it underestimates the monthly-mean May concentration at Missouri Ozark and overestimates the spread in August. In May, the highest concentrations amongst the agricultural towers occur at Round Lake, a densely cultivated region with minimal spring photosynthetic uptake, while the lowest concentrations occur at Centerville, located in a less-densely cropped region. In August, the lowest CO_2 concentrations occur at Round Lake and the highest concentrations occur at the Missouri Ozark site in both the observations and in the crop cases.

Monthly mean near-surface diurnal amplitudes at each tower are displayed in Fig. 6(b). The amplitude of the diurnal cycle increases throughout the growing season amongst the cropland

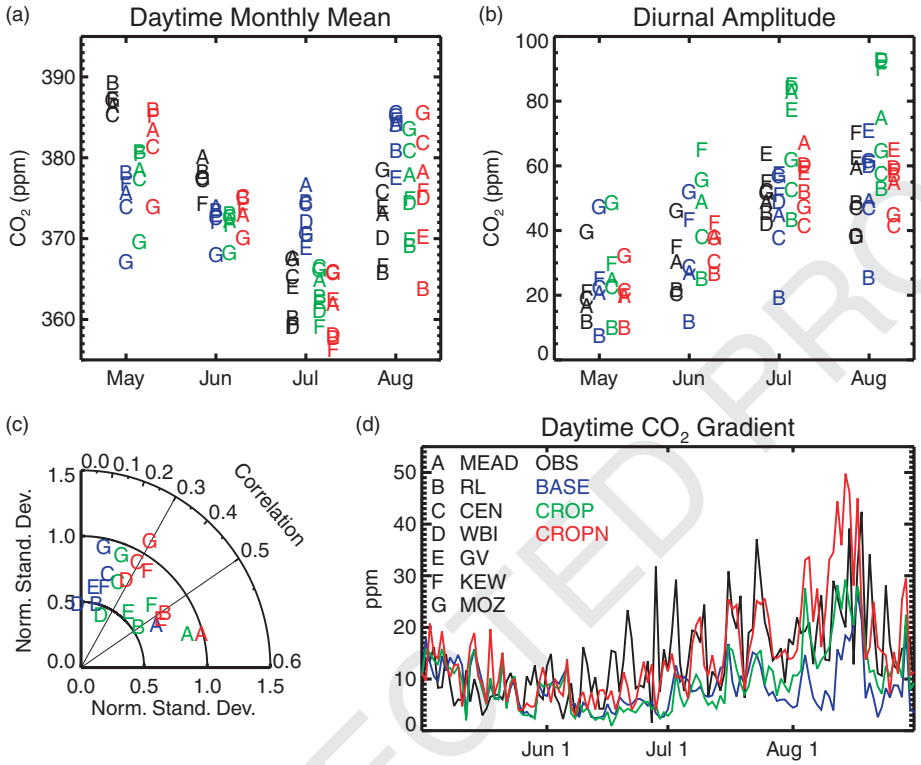

Fig. 6. (a) Mid-afternoon (12 p.m.–6 p.m.) monthly mean concentrations at 120 m (except MOZ, at 30 m) for each of the towers, which are indicated by individual letters. Observations are shown in black (left column), BASE in blue (mid-left column), CROP results in green (mid-right column) and CROPN results in red (right column). (b) Monthly mean diurnal amplitudes at 30 m for each of the towers. (c) Taylor diagram of the mean mid-afternoon (12 p.m.–6 p.m.) atmospheric CO_2 concentrations at 120 m (except MOZ, at 30 m) for the BASE (blue), CROP (green) and CROPN (red) cases. A spline fit to the concentrations has been subtracted at every tower to remove seasonality to isolate synoptic variability. (d) Atmospheric CO_2 concentration gradient between the towers (obs, black; BASE, blue; CROP, green; CROPN, red). The gradient is the difference between the lowest and highest mid-afternoon 120 m (except MOZ, at 30 m) CO_2 concentration between the towers.

towers. In May, the diurnal amplitudes at the six heavily cultivated towers are less than 20 ppm, with a spread of 10 ppm. The minimal amplitudes are due to limited spring crop uptake, while the diurnal amplitude at the transitional site, Missouri Ozark, is considerably higher. In May, the BASE simulation overestimates the amplitude of the atmospheric CO_2 diurnal cycle at all the towers except Round Lake. The model simulates an increase in the amplitude of the diurnal cycle of CO_2 concentrations throughout the summer; however, it continues to underestimate the amplitude at Round Lake the entire summer. Including crops again generally matches the observations more closely, as both crop cases simulate smaller amplitudes over croplands in May that increase throughout the summer; however, the CROP case over-estimates the diurnal amplitudes in July and August. The CROPN case captures the magnitudes of the diurnal amplitude reasonably well, which is likely due not only to the inclusion of crops but also to the increased horizontal resolution in the simulation improving the boundary layer dynamics in the model.

To investigate synoptic variability, a Taylor diagram of daytime mean atmospheric CO_2 concentrations, with the springtime drawdown removed, is displayed in Fig. 6(c). Including the crop module increases the correlation at all the towers, indicating that the timing of the synoptic variability is better simulated when crops are modelled explicitly. Nesting over the MCI region further increases the correlations. Except at Missouri Ozark, the normalized standard deviations are all closer to unity in the CROPN simulation, indicating the magnitude of synoptic events has increased in the model and is closer to observed. At Missouri Ozark, the transitional site, the standard deviation is overestimated in the CROPN simulation. This is caused by a significant increase in concentrations during mid-August.

In addition to evaluating the atmospheric CO_2 concentrations at the individual towers, the magnitude of the gradient between towers can also be evaluated. Fig. 6(d) displays the time-series of the CO_2 gradient, which is the difference between the towers with the highest and lowest daytime mean concentrations. As indicated previously, the gradient increases from a mean magnitude of $\sim$10 ppm in May to mid-August, when the gradient is more than 20 ppm across the MCI region. Fig. 6(d) shows the gradient also has considerable day-to-day variability. The BASE simulation does not capture the increase in the gradient

and poorly simulates the timing and magnitude of the variability in the gradient. By including crops, the CROP simulation captures the increase in the gradient during August. The CROPN simulation does a reasonable job at capturing both the magnitude as well as the timing of the day-to-day variations, particularly in July; however, this case overestimates the gradient the first half of August.

The cause of the day-to-day variability in the CO_2 differences amongst the towers can be investigated by analysing a time period in the CROPN case when both the model and the observations show a large change in the gradient. On 24 July the gradient across the towers is one of the largest seen during the summer, with a change of ∼35 ppm across the MCI region. The CO_2 concentration map shows that the large-scale gradient is shifted northward by strong near-surface winds (Fig. 7, left panel). Zooming in to the MCI region shows that the gradient occurs through the centre of the towers. The Mead tower has higher concentrations (greater than 360 ppm), while the Kewanee tower has very low concentrations (less than 335 ppm) both from local crops as well as from the enhanced uptake over Illinois being advected northward. Two days later, on 26 July, the atmospheric CO_2 concentration difference between the towers is less than 10 ppm. Relatively low concentrations extend across the entire MCI region, as the low northerly concentrations are advected south due to a low pressure system cantered over the Great Lakes (Fig. 7, right panel). The large-scale gradient is shifted southward and lies completely below the MCI region, and all of the towers see lower concentrations that are within 10 ppm.

Although the atmospheric CO_2 concentrations are only displayed for two days, we investigated other cases when the CO_2 gradient jumped between high and low values and found similar results. High gradients occur when the mean wind is southerly, causing high concentrations from the south to be advected northward. This synoptic weather pattern causes the large-scale gradient to shift over the MCI region, thus causing large differences in the concentrations between the towers. On days when the gradient between the towers is low, the wind is from the north, advecting lower CO_2 further south and causing all the towers in the MCI region to have lower, relatively similar concentrations. The simulated gradient overestimation in August is due to very high concentrations seen at the Missouri Ozark and Mead towers, suggesting the model may be overestimating the stress in the southeast during the heat wave. The CROPN simulation shows that changes in the magnitude of the gradient are due to synoptic weather patterns shifting the location of the large-scale gradient between the high southeastern CO_2 concentrations and the low central and northern concentrations.

COLOUR

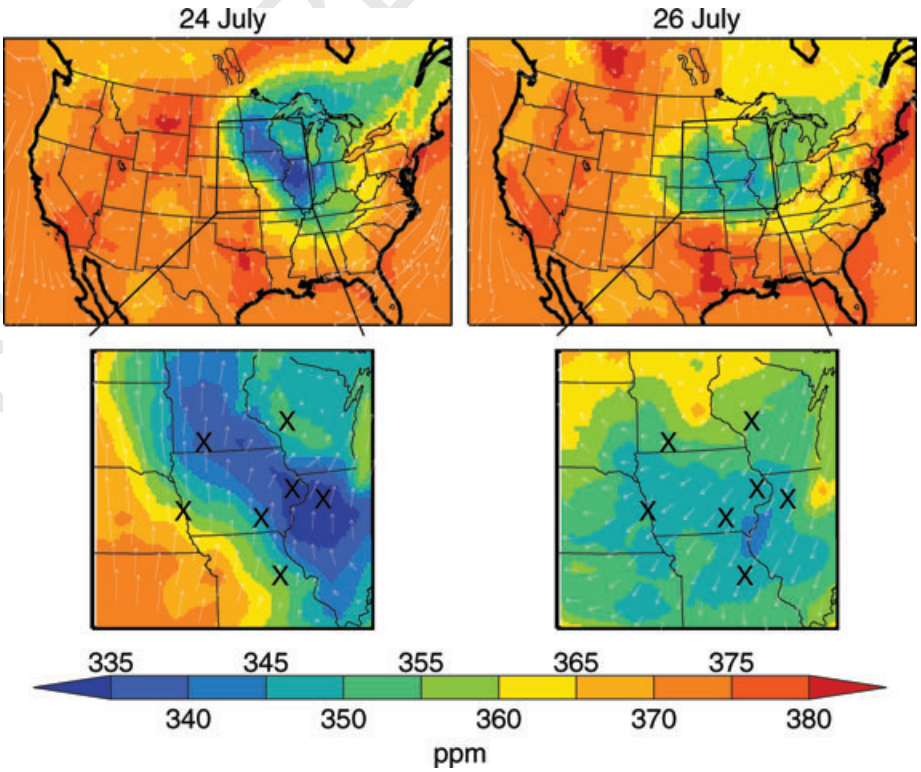

Fig. 7. (Left panel) Mean CROPN daytime atmospheric CO_2 concentrations at 120 m on 24 July 2007, with the corresponding mean wind vectors overlaid. The top panel shows the concentrations from the coarse domain, and the bottom panel shows the concentrations from the nested grid. The towers are indicated by the black Xs. (Right panel) Mean CROPN daytime atmospheric CO_2 concentrations at 120 m on 26 July 2007.

4. Conclusions

Simulating corn and soybean explicitly has a significant impact on both the timing and the magnitude of carbon fluxes. Compared to the generic agriculture land cover classification, the growing season for both corn and soybean is shortened and intensified, and crop-specific fluxes more closely match available observations. Since the mid-continent region of the U.S. is heavily cultivated, crops alter carbon fluxes on regional scales. In May, the monthly-mean carbon uptake over the central U.S. was reduced compared to natural vegetation, while the summer (JJA) carbon sink increased by more than 1.7 kg C m^{-2}.

Altering the carbon fluxes impacted the atmospheric CO_2 concentrations. Modelling corn and soybean enhanced the springtime drawdown, causing increased atmospheric CO_2 concentrations in May and significantly decreased concentrations during the summer, when daytime monthly-mean values less than 360 ppm occurred in both the model and in observations. These CO_2 concentration differences between modelling generic biomes and specific crop types were coherent over the mid-continent region in May and even extended to the eastern U.S. and Canada during the summer, causing changes greater than 15 ppm near the surface. Simulating crops explicitly increased the amplitude of the diurnal cycle in July and August and improved the timing and magnitude of CO_2 variability due to synoptic events. Compared with continuous CO_2 concentrations collected across the mid-continent region, the crop module significantly improved the concentrations, reducing the average RMSE at 120 m by 20%.

Including crops in the model captured the day-to-day variability in the mid-continent region and increased the atmospheric CO_2 concentration gradient across the mid-continent region, more closely matching the observed gradient in the central United States. Analysing the simulation with crops revealed that the considerable day-to-day variability in the gradient was due to synoptic variability. The summer of 2007 was exceptionally hot and dry over the southeastern United States, creating a summertime source of carbon in that region. This source increased the atmospheric CO_2 concentrations, and combined with fossil fuel emissions across the east coast, established a large-scale CO_2 gradient across the mid-continent. This large-scale near-surface gradient of over 30 ppm shifted with the weather patterns: southerly mean flow shifted the gradient northwards into the mid-continent causing high concentration differences between the towers, whereas northerly mean flow associated with low-pressure systems across northern United States and Canada shifted the large-scale gradient south and minimized the concentration differences seen across the mid-continent.

Crops significantly altered both carbon fluxes and atmospheric CO_2 concentrations on regional spatial scales and monthly time scales. Using natural vegetation to represent crops creates biases in forward models, and thus will create errors in source and sink estimates from atmospheric inverse models. Because crops are physiologically and phenologically different compared to forests and grasslands, it is essential to represent them in land surface models used for carbon studies, as these differences dramatically changed the regional carbon source and sink estimates, as well as regional atmospheric CO_2 concentrations.

5. Acknowledgments

The authors thank Arlyn Andrews at NOAA/ESRL for the CO_2 concentration data at WBI, John Baker (USDA-ARS) and Tim Griffis (University of Minnesota) for the flux data at Rosemount, Roser Matamala from the Argonne National Laboratory for the data at the Fermi Agricultural site, and Shashi Verma at the University of Nebraska-Lincoln for the Mead flux data. The authors also thank Rachel Law (CSIRO) for all of her help and suggestions and to Ying-Ping Wang (CSIRO) for constructive comments on the manuscript. Support for the writing of this work has been granted as part of the Australian Climate Change Science Program, funded jointly by the Department of Climate Change, the Bureau of Meteorology, and CSIRO. This research was funded by the National Oceanic and Atmospheric Administration (NOAA) contract NA08OAR4320893, the National Institute for Climate Change Research (NICCR) grant MTU 050516Z14 and the Department of Energy contract DE-FG02-06ER64317. The authors thank the constructive comments by two anonymous reviewers, which improved the quality of the paper.

References

Andrews, A. E., Kofler, J. D., Bakwin, P. S., Zhao, C. and Tans, P. 2009. Carbon dioxide and carbon monoxide dry air mole fractions from the NOAA ESRL tall tower network, 1992–2009. Version: 2009–05-12, ftp://ftp.cmdl.noaa.gov/ccg/towers/.

Baker, I. T. and Denning, A. S. 2008. SiB3 modeled global 1-degree hourly biosphere-atmosphere carbon flux, 1998–2006. In: *Data set*. Oak Ridge National Laboratory Distributed Active Archive Center, Oak Ridge, TN, USA, http://daac.ornl.gov/.

Baldocchi, D. 2006. Fluxnet: a global network measuring and assessing spatial-temporal variability of carbon dioxide, water vapor, and energy fluxes between the terrestrial biosphere and the atmosphere. National Science Foundation Research Coordination Networks in Biological Sciences. Report NSF 06-567.

Betts, R. A. 2005. Integrated approaches to climate-crop modelling: needs and challenges. *Phil. Trans. R. Soc. B* **360**, 2049–2065, doi:10/1098/rstb.2005.1739.

Bonan, G. B. 1997. Effects of land use on the climate of the United States. *Climatic Change* **37**, 449–486.

Bondeau, A., Smith, P. C., Zaehle, S., Schaphoff, S., Lucht, W. and co-authors. 2007. Modelling the role of agriculture for the 20th century global terrestrial carbon balance. *Global Change Biol.* **13**, 679–706, doi:10.1111/j.1365-2486.2006.01305.x.

Q2

Copeland, J. H., Pielke, R. A. and Kittel, T. G. F. 1996. Potential climatic impacts of vegetation change: a regional modeling study. *J. Geophys. Res.-Atmos* **101**(D3), 7409–7418.

Corbin, K. D., Denning, A. S., Lu, L., Wang, J.-W. and Baker, I. T. 2008. Using a high resolution coupled ecosystem-atmosphere model to estimate representation errors in inversions of satellite CO_2 retrievals. *J. Geophys. Res.-Atmos* **113**(D02301), doi:10.1029/2007JD008716.

Crosson, E. R. 2008. A cavity ring-down analyzer for measuring atmospheric levels of methane, carbon dioxide, and water vapor. *Appl. Phys. B* **92**(3), 403–408.

Denning, A. S., Nicholls, M., Prihodko, L., Baker, I. T., Vidale, P.-L. and co-authors. 2003. Simulated variations in atmospheric CO_2 over a Wisconsin forest using a coupled ecosystem-atmosphere model. *Global Change Biol.* **9**, 1241–1250.

De Noblet-Ducoudre, N., Gervois, S., Ciais, P., Viovy, N., Brisson, N. and co-authors. 2004. Coupling the Soil-Vegetation-Atmosphere-Transfer Scheme ORCHIDEE to the agronomy model STICS to study the influence of croplands on the European carbon and water budgets. *Agronomie* **24**, 397–407, doi:10.1051/agro:2004038.

Energy Information Administration. 2007. Emissions of greenhouse gases. Report DOE/EIA-0573. Office of Integrated Analysis and Forecasting. U.S. Department of Energy, Washington, DC, 64.

Frietas, S. R., Longo, K. M., Silva Dias, M. A. F., Silva Dias, P. L., Chatfield, R. and co-authors. 2005. Monitoring the transport of biomass burning emissions in South America. *Environ. Fluid Mech.* **5**(1–2), 135–167.

Gervois, S., de Noblet-Ducoudre, N., Viovy, N. and Ciais, P. 2004. Including croplands in a global biosphere model: methodology and evaluation at specific sites. *Earth Interact.* **8**(16), 25.

Q3

Griffis, T. J., Sargent, S. D., Baker, J. M., Lee, X., Tanner, B. D. and co-authors. 2008. Direct measurement of biosphere-atmosphere isotopic CO_2 exchange using the eddy covariance technique. *J. Geophys. Res.-Atmos.* **113**(D08304), doi:10.1029/2007JD009297.

Gurney, K. R., Mendoza, D. L., Zhou, Y., Fischer, M. L., Miller, C. C. and co-authors. 2009. High resolution fossil fuel combustion CO_2 emission fluxes for the United States. *Environ. Sci. Technol.* **43**, doi:10.1021/es900806c.

Houghton, R. A. 2003. Revised estimates of the annual net flux of carbon to the atmosphere from changes in land use and land management 1850–2000. *Tellus* **55B**, 378–390.

International Geosphere Biosphere Programme (IGBP). 2000. Global soil data products CD-ROM (IGBP-DIS). In: *Global Soil Data Task*. Data and Information System, Potsdam, Germany. Available from Oak Ridge National Laboratory Distributive Active Archive Center, Oak Ridge, TN, USA, http://www.daac.ornl.gov.

Janssens, I. A., Freibauer, A., Ciais, P., Smith, P., Nabuurs, G.-J. and co-authors. 2003. Europe's terrestrial biosphere absorbs 7 to 12% of European anthropogenic CO_2 emissions. *Science* **300**(5625), 1538–1542.

Lawrence, D. M. and Slingo, J. M. 2004. An annual cycle of vegetation in a GCM. Part II: Global impacts on climate and hydrology. *Climate Dyn.* **22**, 107–122, doi:10.1007/s00382-003-0367-8.

Lokupitiya, E., Breidt, F. J., Lokupitiya, R., Williams, S. and Paustian, K. 2007. Deriving comprehensive county-level crop yield and area data for U.S. cropland. *Agron. J.*, **99**(3), 673–681.

Lokupitiya, E., Denning, A. S., Paustian, K., Baker, I. T., Schaefer, K. and co-authors. 2009. Incorporation of crop phenology in Simple Biosphere Model (SiBcrop) to improve land-atmosphere carbon exchanges from croplands. *Biogeosciences* **6**, 969–986.

Lu, L., Denning, A. S., da Silva-Dias, M. A., da Silva-Dias, P., Longo, M. and co-authors. 2005. Mesoscale circulations and atmospheric CO_2 variations in the Tapajos Region, Para, Brazil. *J. Geophys. Res.-Atmos.* **110**(D21102), doi:10.1029/2004JD005757.

Matamala, R., Jastrow, D. J., Miller, R. M. and Garten, C. 2008. Temporal changes in the distribution of C and N stocks in a restored tallgrass prairie in the U.S. Midwest. *Ecol. Appl.* **18**, 1470–1488.

Mesinger, F., DiMego, G., Kalnay, E., Mitchell, K., Shafran, P. C. and co-authors. 2006. North American Regional Reanalysis. *Bull. Am. Meteorol. Soc.* **87**(3), 343–360.

Nicholls, M. E., Denning, A. S., Prihodko, L., Vidale, P.-L., Baker, I. T. and co-authors. 2004. A multiple-scale simulation of variations in atmospheric carbon dioxide using a coupled biosphere-atmospheric model. *J. Geophys. Res.-Atmos.* **109**(D18117), doi:10.1029/2003JD004482.

Ogle, S., Davis, K. J., Andrews, A., Gurney, K. R., West, T. and co-authors. 2006. Mid-continent intensive campaign of the North America Carbon Program. *Sci. Plan.*, http://www.nacarbon.org/nacp/mci.html.

Osborne, T. M., Lawrence, D. M., Challinor, A. J., Slingo, J. M. and Wheeler, T. R. 2007. Development and assessment of a coupled crop-climate model. *Global Change Biol.* **13**, 169–183, doi:10.1111/j.1365-2486.2006.01274.x.

Parazoo, N. C., Denning, A. S., Kawa, S. R., Corbin, K. D., Lokupitiya, R. S. and co-authors. 2008. Mechanisms for synoptic variations of atmospheric CO_2 in North America, South America, and Europe. *Atmos. Chem. Phys.* **8**, 7239–7254.

Ramankutty, N. and Foley, J. A. 1998. Characterizing patterns of global land use: an analysis of global croplands data. *Global Biogeochem. Cycles* **12**(4), 667–685.

Richardson, S. J., Miles, N. L., Davis, K. J., Crosson, E., Van Pelt, A. D. and co-authors. 2009. *EOS Trans. AGU* **90**(52), Fall Meet. Suppl., Abstract B51E-0343.

Verma, S. B., Dobermann, A., Cassman, K. G., Walters, D. T., Knops, J. M. and co-authors. 2005. Annual carbon dioxide exchange in irrigated and rainfed maize-based agroecosystems. *Agric. Forest. Met.* **131**(1–2), 77–96.

Vleeshouwers, L. M. and Verhagen, A. 2002. Carbon emission and sequestration by agricultural land use: a model study for Europe. *Global Change Biol.* **8**, 519–530.

Wang, J.-W., Denning, A. S., Lu, L., Baker, I. T., Corbin, K. D. and co-authors. 2007. Observations and simulations of synoptic, regional, and local variations in atmospheric CO_2. *J. Geophys. Res.-Atmos.* **112**(D04108), doi:10.1029/2006JD007410.

Xiao, J. F., Zhuang, Q. L., Baldocchi, D. D., Law, B. E., Richardson, A. D. and co-authors. 2008. Estimation of net ecosystem carbon exchange for the conterminous United States by combining MODIS and AmeriFlux data. *Agric. Forest Met.* **148**(11), 1827–1847.

Zhao, M., Heinsch, F. A., Nemani, R. R. and Running, S. W. 2005. Improvements of the MODIS terrestrial gross and net primary production global data set. *Rem. Sens. Environ.* **95**, 164–176.

Queries

Journal: TEB
Paper: teb_485

Dear Author

During the copy-editing of your paper, the following queries arose. Please respond to these by marking up your proofs with the necessary changes/additions. Please write your answers on the query sheet if there is insufficient space on the page proofs. Please write clearly and follow the conventions shown on the corrections sheet. If returning the proof by fax do not write too close to the paper's edge. Please remember that illegible mark-ups may delay publication.

Query Reference	Query	Remarks
Q1	Author: A running head short title was not supplied; please check if this one is suitable and, if not, please supply a short title that can be used instead.	
Q2	Author: Please provide location for reference 'Baldocchi (2006)'.	
Q3	Author: Please supply the doi code or page range (or both) for reference 'Gervois (2004)', or indicate if it is a one-page reference.	

MARKED PROOF

Please correct and return this set

Please use the proof correction marks shown below for all alterations and corrections. If you wish to return your proof by fax you should ensure that all amendments are written clearly in dark ink and are made well within the page margins.

Instruction to printer	*Textual mark*	*Marginal mark*
Leave unchanged	··· under matter to remain	✓
Insert in text the matter indicated in the margin	⌇	New matter followed by ⌇ or ⌇ (x2)
Delete	/ through single character, rule or underline or ⊢⊣ through all characters to be deleted	/ or / (x2)
Substitute character or substitute part of one or more word(s)	/ through letter or ⊢⊣ through characters	new character / or new characters /
Change to italics	— under matter to be changed	⌒
Change to capitals	≡ under matter to be changed	≡
Change to small capitals	= under matter to be changed	=
Change to bold type	~ under matter to be changed	~
Change to bold italic	≈ under matter to be changed	≈
Change to lower case	Encircle matter to be changed	≠
Change italic to upright type	(As above)	⊬
Change bold to non-bold type	(As above)	⊬
Insert 'superior' character	/ through character or ⌇ where required	Y or Y under character e.g. Y^{3} or Y^{3}
Insert 'inferior' character	(As above)	⌇ over character e.g. Y_{2}
Insert full stop	(As above)	⊙
Insert comma	(As above)	,
Insert single quotation marks	(As above)	Y or Y and/or Y or Y
Insert double quotation marks	(As above)	Y or Y and/or Y or Y
Insert hyphen	(As above)	⊢
Start new paragraph	⌐	⌐
No new paragraph	⌣	⌣
Transpose	⊔	⊔
Close up	linking ⁀ characters	⁀
Insert or substitute space between characters or words	/ through character or ⌇ where required	Y
Reduce space between characters or words	| between characters or words affected	⊤

Large amplitude spatial and temporal gradients in atmospheric boundary layer CO_2 mole fractions detected with a tower-based network in the U.S. upper Midwest

Natasha L. Miles,[1] Scott J. Richardson,[1] Kenneth J. Davis,[1] Thomas Lauvaux,[1] Arlyn E. Andrews,[2] Tristram O. West,[3] Varaprasad Bandaru,[3] and Eric R. Crosson[4]

Received 1 June 2011; revised 12 December 2011; accepted 17 December 2011; published 21 February 2012.

[1] This study presents observations of atmospheric boundary layer CO_2 mole fraction from a nine-tower regional network deployed during the North American Carbon Program's Mid-Continent Intensive (MCI) during 2007–2009. The MCI region is largely agricultural, with well-documented carbon exchange available via agricultural inventories. By combining vegetation maps and tower footprints, we show the fractional influence of corn, soy, grass, and forest biomes varies widely across the MCI. Differences in the magnitude of CO_2 flux from each of these biomes lead to large spatial gradients in the monthly averaged CO_2 mole fraction observed in the MCI. In other words, the monthly averaged gradients are tied to regional patterns in net ecosystem exchange (NEE). The daily scale gradients are more weakly connected to regional NEE, instead being governed by local weather and large-scale weather patterns. With this network of tower-based mole fraction measurements, we detect climate-driven interannual changes in crop growth that are confirmed by satellite and inventory methods. These observations show that regional-scale CO_2 mole fraction networks yield large, coherent signals governed largely by regional sources and sinks of CO_2.

Citation: Miles, N. L., S. J. Richardson, K. J. Davis, T. Lauvaux, A. E. Andrews, T. O. West, V. Bandaru, and E. R. Crosson (2012), Large amplitude spatial and temporal gradients in atmospheric boundary layer CO_2 mole fractions detected with a tower-based network in the U.S. upper Midwest, *J. Geophys. Res.*, *117*, G01019, doi:10.1029/2011JG001781.

1. Introduction

[2] Interest in quantifying carbon dioxide (CO_2) sources and sinks, both biogenic and anthropogenic, is growing with the increasing interest in monitoring and verifying CO_2 emissions [*Committee on Methods for Estimating Greenhouse Gas Emissions*, 2010]. The continuous tower-based CO_2 mole fraction measurement density is increasing in the United States and Europe, with the goal of using the data in inversion models to diagnose CO_2 fluxes. In North America, 6–8 towers within an area of 10^7 km^2 were available to past continental-scale studies [*Peylin et al.*, 2005; *Peters et al.*, 2007; *Schuh et al.*, 2010]. Other studies focused on regional scales, using CO_2 mole fractions measured at one tower in addition to aircraft [*Matross et al.*, 2006] and meteorological [*Tolk et al.*, 2009] data. *Lauvaux et al.* [2009], using data observed during the CarboEurope Regional Experiment [*Dolman et al.*, 2006], determined regional-scale fluxes using two towers within a 10^5 km^2 domain, representing an order of magnitude improvement in tower density. Still, the scarcity and limited time frame of tower-based measurements have hindered the determination of regional-scale fluxes [*Matross et al.*, 2006]. Uncertainties in the flux estimates remain large, but can be reduced by including additional towers [*Butler et al.*, 2010].

[3] The Mid-Continent Intensive (MCI) is the first targeted experimental campaign of the North American Carbon Program (NACP) [*Wofsy and Harriss*, 2002; *Denning*, 2005]. The primary objective of the MCI [*Ogle et al.*, 2006] is to compare regional-scale CO_2 fluxes derived from inventory data and biogeochemical models [*King et al.*, 2007; *Xiao et al.*, 2008; *West et al.*, 2008; *Gurney et al.*, 2009; *Ogle et al.*, 2010] to fluxes inferred from tower-based CO_2 measurements via inversion models [*Tans et al.*, 1990; *Peters et al.*, 2007; *Lauvaux et al.*, 2009; *Schuh et al.*, 2010]. The MCI campaign incorporates tower CO_2 mole fraction measurements at nine sites, USDA National Agricultural Statistics inventory data, ongoing eddy-covariance flux measurements from AmeriFlux towers in the region, other inventory data such as the Vulcan fossil fuel emissions product [*Gurney et al.*, 2009], USDA National Resources Inventory, USDA Forest Inventory and Analysis data, and airborne trace gas measurements [*Martins et al.*, 2009; *Crevoisier et al.*, 2010].

[1]Department of Meteorology, Pennsylvania State University, University Park, Pennsylvania, USA.
[2]Earth System Research Laboratory, Global Monitoring Division, National Oceanic and Atmospheric Administration, Boulder, Colorado, USA.
[3]Pacific Northwest National Laboratory, Joint Global Change Research Institute, University of Maryland, College Park, Maryland, USA.
[4]Picarro, Inc., Sunnyvale, California, USA.

0148-0227/12/2011JG001781

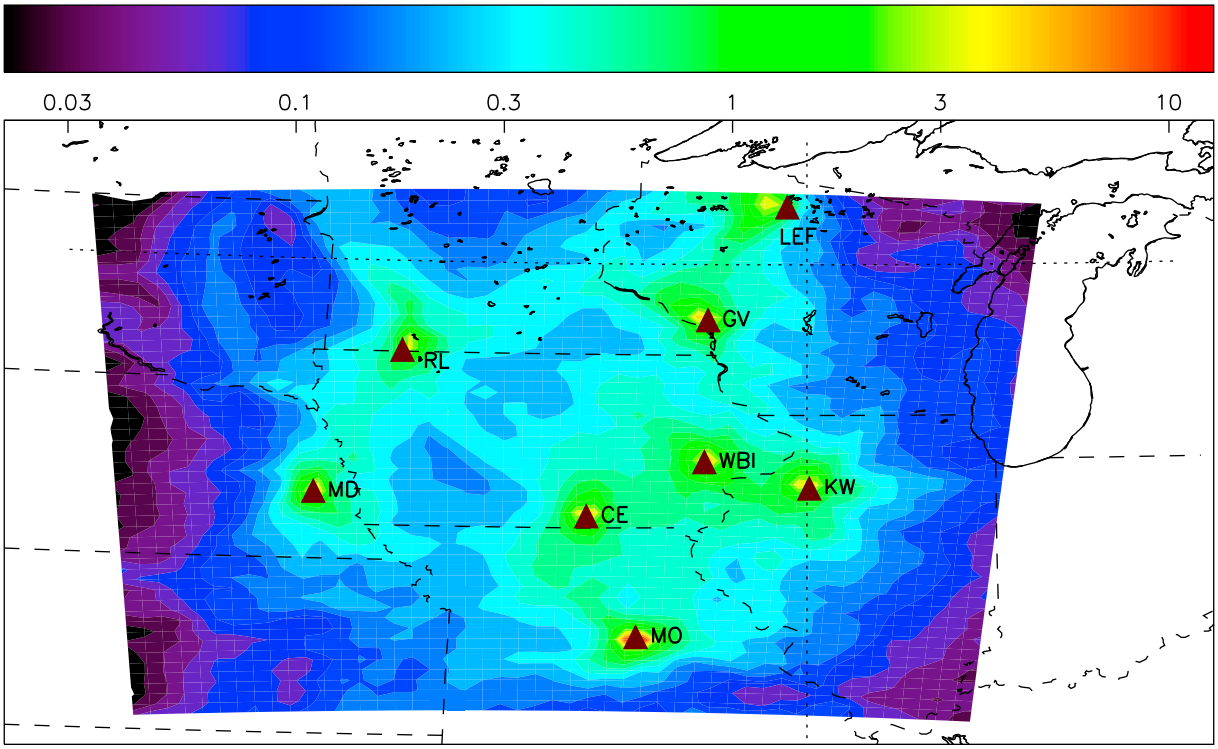

Figure 1. Footprint of the CO_2 mixing ratio tower network plotted on a natural logarithmic scale. The footprints (ppm/g CO_2 m^{-2} h^{-1}) are normalized such that the total is 100% times the number of towers; the color bar indicates the approximate percentage of the contribution (within the MCI domain) arising from each particular 20 km × 20 km pixel. The time frame is July–August 2007.

[4] Modeling results for the MCI region show the importance of vegetation type. Simulation of corn and soybean explicitly using crop-specific physiology and phenology results in improved modeled NEE [*Lokupitiya et al.*, 2009] and forward modeled CO_2 mole fractions [*Corbin et al.*, 2010]. While *Lauvaux et al.* [2011] present the regional CO_2 fluxes for June–December 2007 and explore model uncertainties resulting from inverse system assumptions, in this paper we focus on the CO_2 mole fraction measurements.

[5] Understanding of the characteristics (amplitudes, temporal persistence, and attribution to vegetation, weather, and climate) of atmospheric CO_2 is critical to the design of observational networks [*Committee on Methods for Estimating Greenhouse Gas Emissions*, 2010; *Nisbet and Weiss*, 2010]. Documenting the characteristics and causes of transient, weather-related regional mole fraction gradients has not, however, been possible to date because of very limited spatial sampling. Seasonal-scale characteristics have been previously reported at single sites [*Davis et al.*, 2003; *Haszpra et al.*, 2008] but not for a regional network. Previous studies of daily scale gradients have largely been limited to temporal analyses at single sites [*Hurwitz et al.*, 2004], modeling [*Wang et al.*, 2007] and aircraft studies [*Chan et al.*, 2004; *Gerbig et al.*, 2003]. While there are numerous satellite remote sensing design studies [*Houweling et al.*, 2010], real data to inform these studies are scarce [*Lin et al.*, 2004].

[6] The purposes of this paper are (1) to document the seasonal cycle of CO_2 mole fraction at several sites in a largely agricultural region; (2) to document the spatial CO_2 mole fraction gradients in the region on seasonal, daily, and interannual time scales; (3) to ascertain the degree to which regional-scale CO_2 mole fraction networks can yield coherent signals governed largely by regional sources and sinks of CO_2; and (4) to determine if signals in the tower-based CO_2 mole fraction data are correlated with both ground-based inventory data and estimates from satellite remote sensing.

2. Methods

2.1. Mid-Continent Intensive Region

[7] The U.S. upper Midwest (Figure 1) was the region selected for the Mid-Continent Intensive (MCI) because of its uncomplicated terrain and because the dominant crop ecosystems are extensively documented. The region is primarily agricultural, with cropland and grassland being the dominant vegetation types, but has forest cover in the southern and especially northern portions of the region (U.S. Geological Survey Land Cover Institute, 2010; see http://landcover.usgs.gov). Corn and soybeans are the dominant crops; in Iowa, the area planted with these crops is 52% and 41% of the total agricultural area, respectively [*U.S. Department of Agriculture National Agricultural Statistics Service* (*USDA-NASS*), 2010].

2.2. Tower CO_2 Measurements

[8] A total of nine communication tower-based CO_2 sensors were located within a 500 × 800 km^2 area within the MCI study region from May 2007 through November 2009

Table 1. Site Latitudes, Longitudes, Measurement Dates, and Sampling Level Used

	Centerville	Galesville	Kewanee	Mead	Missouri Ozarks	Round Lake	Rosemount	West Branch	Park Falls
Latitude (deg N)	40.7919	44.0910	41.2762	41.1386	38.7441	43.5263	44.6886	41.725	45.9459
Longitude (deg W)	92.8775	91.3382	89.9724	96.4559	92.2000	95.4137	93.0728	91.353	90.2723
Measurement dates	Apr 2007 to Nov 2009	Jun 2007 to Nov 2009	Apr 2007 to Nov 2009	Apr 2007 to Nov 2009	Sep 2006 to current	May 2007 to Nov 2009	Nov 2007 to current	Jul 2007 to current	1995 to current
Sampling level used (m AGL)	110	122	140	122	30	110	100	99	122

(see Table 1 and Figure 1). The mean distance of each tower to the closest neighboring tower is 188 km (Table 2). The National Oceanic and Atmospheric Administration (NOAA)'s Earth System Research Laboratory (ESRL) maintains measurements of CO_2 mole fractions at two long-term tall towers in the study region (LEF, Park Falls, Wisconsin, and WBI, West Branch, Iowa). These sites are part of the NACP's continental backbone observing network and serve as foci for the MCI experiment. LEF (Park Falls, Wisconsin) and WBI (West Branch, Iowa) are instrumented with NOAA-ESRL tall tower nondispersive infrared (NDIR) systems [*Bakwin et al.*, 1995; *Zhao et al.*, 1997]. With the goal of oversampling the MCI region, The Pennsylvania State University deployed instruments at five towers: Centerville (Iowa), Galesville (Wisconsin), Kewanee (Illinois), Mead (Nebraska), and Round Lake (Minnesota). These sites were instrumented with wavelength-scanned cavity ring-down spectroscopy (WS-CRDS) systems (Picarro, Inc., Santa Clara, California, model CADS) [*Crosson*, 2008]. *Chen et al.* [2010] document the accuracy and precision of a

Table 2. Distances Between Site Pairs, Magnitudes of the Median Intersite Differences and Gradients in Daily Daytime CO_2 Mole Fraction[a]

	Centerville	Galesville	Kewanee	Mead	Missouri Ozarks	Round Lake	Rosemount	West Branch	Park Falls
				Centerville					
Distance (km)		388	250	303	235	369	437	164	611
Median difference (ppm)		0.58	5.13	0.88	1.50	6.04	4.08	5.12	0.15
Median gradient (ppm/100 km)		0.2	2.1	0.3	0.6	1.6	0.9	3.1	0.0
				Galesville					
Distance (km)			332	532	600	333	156	263	223
Median difference (ppm)			4.45	0.51	2.84	5.43	0.60	3.96	1.43
Median gradient (ppm/100 km)			1.4	0.1	0.5	1.6	0.4	1.5	0.6
				Kewanee					
Distance (km)				543	340	512	459	125	520
Median difference (ppm)				5.37	7.42	0.48	3.04	0.97	6.43
Median gradient (ppm/100 km)				1.0	2.2	0.1	0.7	0.8	1.2
					Mead				
Distance (km)					450	279	483	430	730
Median difference (ppm)					0.17	5.14	1.36	4.73	0.11
Median gradient (ppm/100 km)					0.0	1.8	0.3	1.1	0.0
						Missouri Ozarks			
Distance (km)						597	669	340	817
Median difference (ppm)						9.02	5.89	8.44	4.13
Median gradient (ppm/100 km)						1.5	0.9	2.5	0.5
							Round Lake		
Distance (km)							228	388	487
Median difference (ppm)							4.72	1.22	6.47
Median gradient (ppm/100 km)							2.1	0.3	1.3
								Rosemount	
Distance (km)								361	260
Median difference (ppm)								1.84	0.67
Median gradient (ppm/100 km)								0.5	0.3
									West Branch
Distance (km)									477
Median difference (ppm)									6.02
Median gradient (ppm/100 km)									1.3

[a]Time period is 2007–2009 growing season (July and August). Sites are classified as either corn dominated (Kewanee, Round Lake, and West Branch), or non–corn dominated.

WS-CRDS (Picarro, Inc.) in laboratory testing and an aircraft deployment. *Richardson et al.* [2012] document the quality assessment of the instruments during the MCI; 8 months of testing against a NOAA-ESRL NDIR system in West Branch, Iowa, yielded median daytime-only differences of -0.13 ± 0.63 ppm. Two additional long-term sites measuring well-calibrated CO_2 mole fraction (University of Minnesota KCMP, Rosemount, Minnesota, and Pennsylvania State University (PSU)/Oak Ridge National Laboratory (ORNL, Missouri Ozarks, Missouri) are located within the region and used in this study. At the University of Minnesota Rosemount tower, CO_2 mole fraction is measured using a tunable diode laser [*Griffis et al.*, 2010]. The Missouri Ozarks CO_2 measurement site is colocated with an ongoing AmeriFlux site [*Gu et al.*, 2008] and employs a well-calibrated system based on a NDIR instrument (Licor, Inc., Lincoln, Nebraska, model LI-820). The system is dried using Nafion (Perma Pure, LLC, Toms River, New Jersey, model MD-070-96P-4) driers, calibrated every 4 h using four real-air standards (with hourly target and daily archive tests as well), temperature and pressure controlled, and automatically leak tested. Residuals from known tank values tested daily at the site are -0.11 ± 0.21 ppm [*Stephens et al.*, 2011].

[9] Although nighttime mole fractions provide useful information about respiration, in this study we focus on only the daytime (12:00–17:00 LST) average CO_2 mole fractions. Although these hours extend into the evening transition as defined by *Davis et al.* [2003], composited diurnal cycles of CO_2 in July are well mixed during these hours [*Bakwin et al.*, 1998, Figure 1]. During the daytime, the CO_2 mole fraction from the levels used in this study (100–140 m AGL for all sites except for Missouri Ozarks, which is 30 m AGL) is a reasonable approximation of the mixed layer value [*Bakwin et al.*, 1998; *Chan et al.*, 2004]. At West Branch during daytime in the peak growing seasons 2007–2009, the median difference between the 99 and 379 m AGL values is 1.0 ± 2.2 ppm and between the 31 and 99 m AGL values is 1.1 ± 1.5 ppm.

[10] To investigate seasonal-scale variability, we used a 31 day running mean to smooth the CO_2 mole fraction daily daytime average data. We required 60% of the days within each window to be good data. To avoid extending the smoothed product over areas with prolonged missing data, we also required that there be good data within 2 days of each smoothed point.

2.3. Tower Mole Fraction Footprints

[11] We simulated the tower mole fraction footprints using the nonhydrostatic mesoscale model WRF-Chem v3.1 [*Skamarock et al.*, 2008] at 10 km resolution. The WRF simulations used are described in more detail in the work of *Lauvaux et al.* [2011], but here we summarize the description of the main schemes, driver data, and resolution. The atmospheric boundary layer scheme used is the Mellor-Yamada-Nakanishi-Niino (MYNN) 2.5 scheme coupled to the Monin-Obukhov (Jancic Eta) scheme for the surface physics. The atmospheric vertical column is described by 60 levels, with 40 levels in the lower 2 km. We used the NOAH land surface model to describe the surface energy balance, and the NCEP Eta/NAM model output at 40 km resolution for the initial conditions and nudged over four pixels (40 km) to provide boundary conditions around our simulation domain. We simulated the influence functions with the Lagrangian Particle Dispersion Model [*Uliasz*, 1994]. We used the mean three-dimensional winds, potential temperature, and turbulent kinetic energy as input variables each 30 min to drive the particle motions from the receptor locations to the sources, as described in the work of *Lauvaux et al.* [2008]. We computed the footprints for each observation hour, at each tower location, by counting particles over a 20 km resolution grid. We then averaged the footprints corresponding to daytime hours only (06:00–18:00 LST) at a weekly time step, and summed over July–August 2007 to represent the area of influence at the surface during the growing season. The resulting summer time aggregated footprint represents the contribution of each surface pixel within the MCI domain to the summer drawdown observed in the daily daytime mole fractions. In addition, we quantified the influence of the boundaries (CO_2 mole fraction inflow) by counting particles at the boundaries. The boundary influence is a separate contribution, given by a global-scale model, in this case, CarbonTracker 2009 [*Peters et al.*, 2007]. We thus computed the fractional influence from outside the MCI domain, as well as the distribution of the influence within in it.

2.4. Vegetation Map

[12] The vegetation map we used in calculating the biome fractional influence is similar to that described in the work of *Schuh et al.* [2010]. We obtained biomes from the Terra MODIS 12 Landcover 1 km product and mapped them to SiB biome classes, with corrections for C4 grasses. We disaggregated corn, soy, and wheat biomes from the original grassland/agriculture biome using county-level estimates of land use from the USDA National Agriculture Statistics Service. The new grassland/agriculture (C3) category thus includes crops such as alfalfa hay and oats as well as the more predominant pastureland. Tallgrass (C4) prairie and wheat are not predominant in the MCI region, and are included in the "other" category. Forested biomes were combined. The final vegetation map includes the fractional coverage of the four most represented biomes in the MCI region with an additional category for all other biomes (forest, soy, grassland, corn, and other) at 1 km resolution. In section 3.1 this map is combined with 20 km resolution footprints to represent the fractional influence at the towers for each of the five categories.

2.5. NDVI Time Series Crop Phenology Curves

[13] The Normalized Difference Vegetative Index (NDVI) was estimated using 250 m spatial resolution, 8 day composite, collection-5 reflectance data (MOD09Q1) from NASA's Terra Moderate Resolution Imaging Spectroradiometer (MODIS) sensor. MODIS reflectance data is corrected for atmospheric gases and aerosols [*Vermote et al.*, 2002], and has high subpixel geolocation accuracy [*Wolfe et al.*, 2002]. MOD09Q1 reflectance data consists of observations that are selected on the basis of quality, view angle, and absence of clouds [*Vermote et al.*, 2011]. MOD09Q1 also includes binary quality control flags that provide information on pixel quality. We used the quality control information to select high-quality, cloud-free data from days

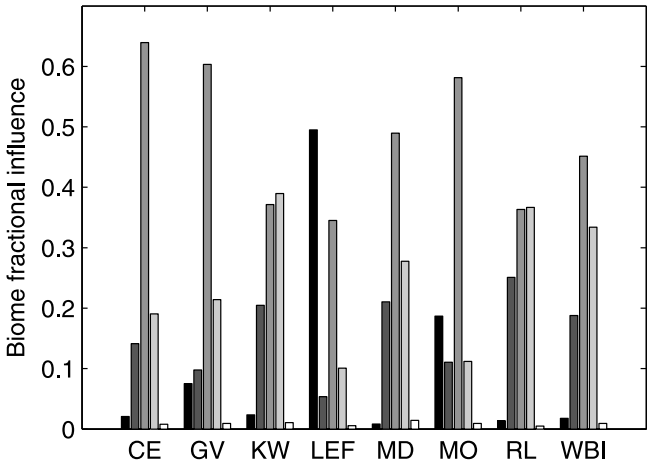

Figure 2. Biome fractional influence, averaged over July–August 2007, for the daytime only (not available for Rosemount). The biomes include, from left to right: forest, soy, grassland, corn, and other.

81–321 for years 2007–2009. The tiled reflectance data was mosaicked and then reprojected from Sinusoidal to Albers Equal-Area Conic Projection using the MODIS Reprojection Tool (MRT) [*Dwyer and Schmidt*, 2006]. The Cropland Data Layer (CDL), an annual crop-specific land cover data set based on satellite data [*Johnson and Mueller*, 2010], was used to retrieve reflectance data from MOD09Q1 for corn and soybean crops. NDVI was calculated for each composited day and for each crop, and then combined to generate time series crop phenology curves for years 2007–2009. Positive and negative changes in the slope of the phenology curves represent plant emergence and senescence, while plant maturity occurs at peak NDVI.

3. Results

3.1. Atmospheric- and Inventory-Based Detection of CO_2 Flux Spatial Variability

[14] Before examining the CO_2 mole fraction measured in the MCI, we first consider the spatial areas that contribute to the signal measured at each tower. Mole fraction footprints, when combined with the spatially varying flux, indicate the relative influence of a location at the surface to the mole fraction measured at a tower. July–August 2007 averaged, daytime-only footprints are shown in Figure 1 for the MCI towers. About 39% of the total signal (ΔCO_2/flux) originates with a 150 km radius of each tower. Conversely, 28% originates outside of the MCI domain. The signal per unit area decreases quickly with distance from the towers: pixels surrounding each of the towers each contribute 1–3% of the total signal, while pixels on the edge of the domain each contribute two orders of magnitude less per pixel to the total signal (Figure 1).

[15] We now couple the footprints with the vegetation map described in section 2.4 to determine the biome fractional influence (Figure 2), a measure of the fractional time that an air parcel arriving at each tower has spent influenced by each biome. The contribution of each biome varies considerably among the sites. Grassland, which includes alfalfa and oats as well as the more predominant pastureland, is the biome most influencing Centerville, Galesville, and Mead. Park Falls (LEF) and Missouri Ozarks are influenced primarily by forest and grassland biomes. Although corn influences each site, the contribution is largest at Kewanee, Round Lake, and West Branch. Soybeans, while common in the region, do not dominate the influence of any of the sites. Wheat and tallgrass prairie are not common in the MCI region.

[16] The variability in the predominant vegetation types of the region affects the regional patterns in CO_2 flux because of the variability of carbon uptake per unit area of each vegetation type. Shown in Figure 3 is the weekly averaged daytime (12:00–17:00 LST) net ecosystem exchange (NEE) measured at four corn (Rosemount-G19 in Minnesota; see *Griffis et al.* [2010] and Mead-rain, Mead-irrigated, and Mead-irrigated/rotated in Nebraska; see *Verma et al.* [2005]), two grassland (Brookings and Fermi prairie in Illinois; see *Matamala et al.* 2008]), two forest (LEF in Wisconsin; see *Davis et al.* [2003] and Missouri Ozarks in Missouri; see *Gu et al.* [2008]), and one soy (Fermi agriculture in Illinois; see *Matamala et al.* [2008]) eddy-covariance flux sites in the MCI region. The peak daytime NEE of corn during the growing season is significantly larger than that of each of the other vegetation types. The peak daytime NEE over the year for the corn sites occurs in mid-July, averaging -51 μmol m^{-2} s^{-1} for the four corn sites. The average of the Mead corn sites in 2001/2003 is -63 μmol m^{-2} s^{-1} [*Verma et al.*, 2005]. In 2002, two of the Mead sites were planted with soybean and their peak CO_2 uptake averages -37 μmol m^{-2} s^{-1} [*Verma et al.*, 2005]. In summary, using the peak daytime weekly averaged NEE for site-years shown in Figure 3 in addition to the results in the work of *Verma et al.* [2005], the corn/soy peak NEE ratio varies between 1.4 and 3.2, the corn/grassland peak NEE ratio varies between

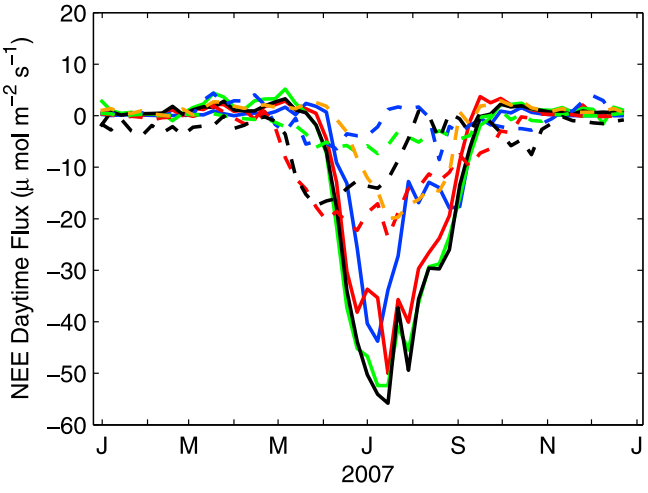

Figure 3. Weekly averaged daytime (12:00–17:00 LST) net ecosystem exchange measured at corn-dominated eddy flux sites Rosemount-G19 (blue solid line), Mead-rain (red solid line), Mead-irrigated (green solid line), and Mead-irrigated/rotated (black solid line); grassland-dominated sites Brookings (blue dotted line) and Fermi-prairie (red dotted line); forested sites LEF (green dotted line) and Missouri Ozarks (black dotted line); and soy site Fermi-agriculture (orange dotted line).

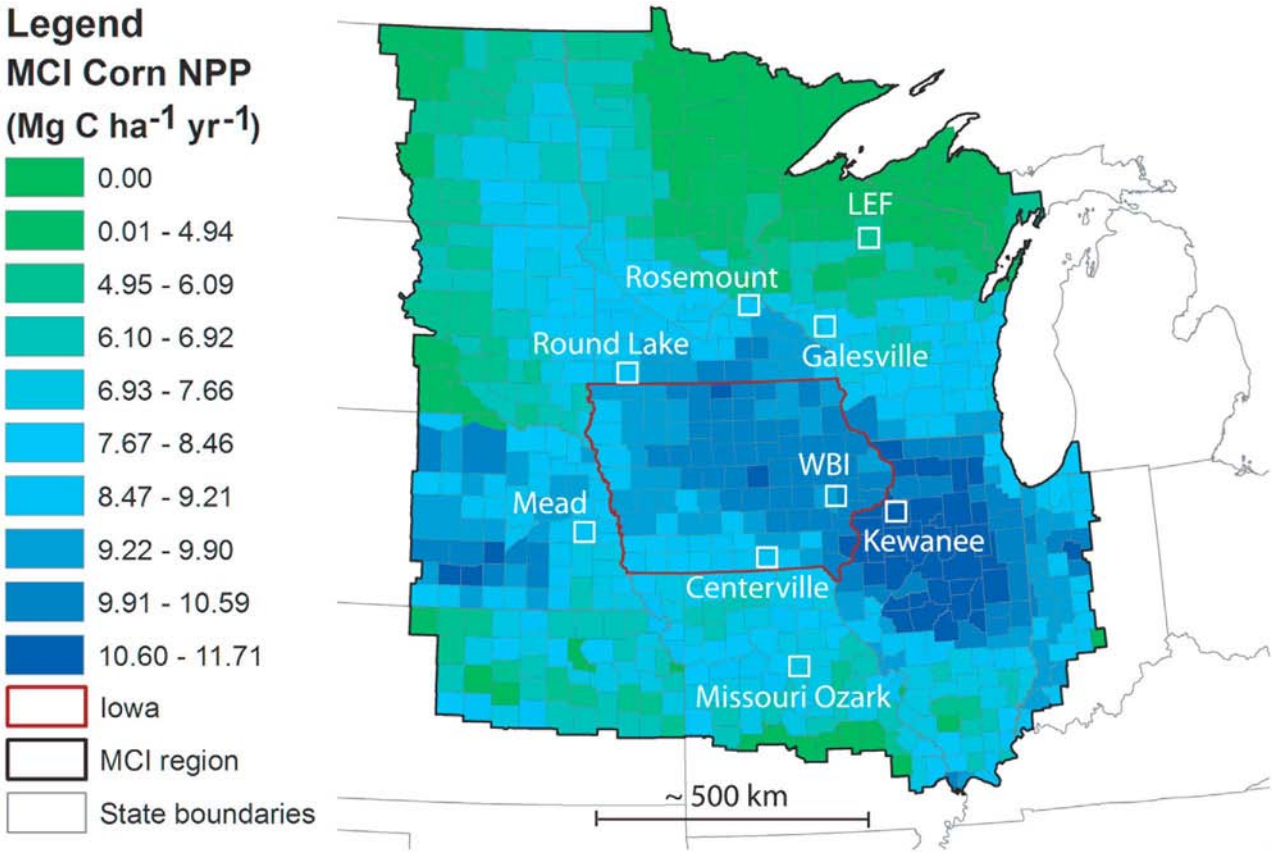

Figure 4. Inventory-based corn flux (corn NPP) in the MCI region for 2007, including corn grain and corn silage. Tower-based CO_2 mixing ratio measurement site locations in the MCI region are shown (open squares). Map resolution is the county geopolitical unit.

2.3 and 7.0, and the corn/forest peak NEE ratio varies between 3.0 and 9.0. The large difference in NEE between corn and noncorn sites when the plants are growing contributes to the important role that corn plays in the carbon budget of this largely agricultural region.

[17] We now consider the net primary production (NPP) for corn in the MCI region, derived from USDA National Agricultural Statistics Service inventory data based on methods described by *West et al.* [2010]. Areas of highest corn flux per unit area are in Nebraska, southern Minnesota, Iowa, and northern and central Illinois (Figure 4). The corn NPP within the MCI region varies from about 5 to 10 Mg C ha^{-1} yr^{-1}, nearly doubling carbon uptake when moving from southeast Iowa to northwest Iowa. We describe the three sites with corn fractional influence greater than 0.30 (Kewanee, Round Lake, and West Branch) as "corn dominated" and the remaining six as "non–corn dominated" to reflect the differences in corn fractional influence and corn NPP per unit area. The threshold of 0.30 was chosen to minimize the sum of the standard deviations of the corn fractional influence within the two groups, requiring each group to have at least three members.

[18] From the above results, we have inferred regional patterns in ecosystem NEE. We now determine whether these patterns are apparent in the CO_2 mole fractions measured at the towers, or if, instead, atmospheric mixing equilibrates the gradients. In the smoothed time series of CO_2 mole fraction (Figure 5), the corn-dominated sites in fact exhibit extremely low growing season minima, in the range of 358–364 ppm. These low values are near those last observed in the globally averaged marine surface annual CO_2 mole fractions 10–13 years prior to the beginning of this study (see http://www.esrl.noaa.gov/gmd/cgg/trends). The growing season minima are correlated with the relative influence of corn, with the corn-dominated minima average 6–8 ppm lower than the non-corn-dominated average (Table 3). Similarly, the seasonal drawdown (the difference between dormant season maxima and growing season minima for each year) also varies within the MCI region. The seasonal drawdown averages 35 ppm for corn-dominated sites (Table 3), which is significantly larger than that measured at non–corn belt sites (27 ppm), and is 5 times larger than the tropospheric "background" as represented by Mauna Loa (7 ppm). Aircraft-measured free tropospheric CO_2 mole fractions at WBI also exhibit a 7 ppm drawdown (see http://www.esrl.noaa.gov/gmd/cgg/trends). The corn-dominated seasonal drawdown is larger than that previously observed at continental boundary layer sites, for example, 26 ppm at Hegyhátsál [*Haszpra et al.*, 2008] and 23 ppm at LEF [*Davis et al.*, 2003]. Although Centerville, Galesville, Mead, and Rosemount have a large influence from crops, the CO_2 seasonal pattern of those sites is more similar to the forested sites LEF and Missouri Ozarks (Figure 5).

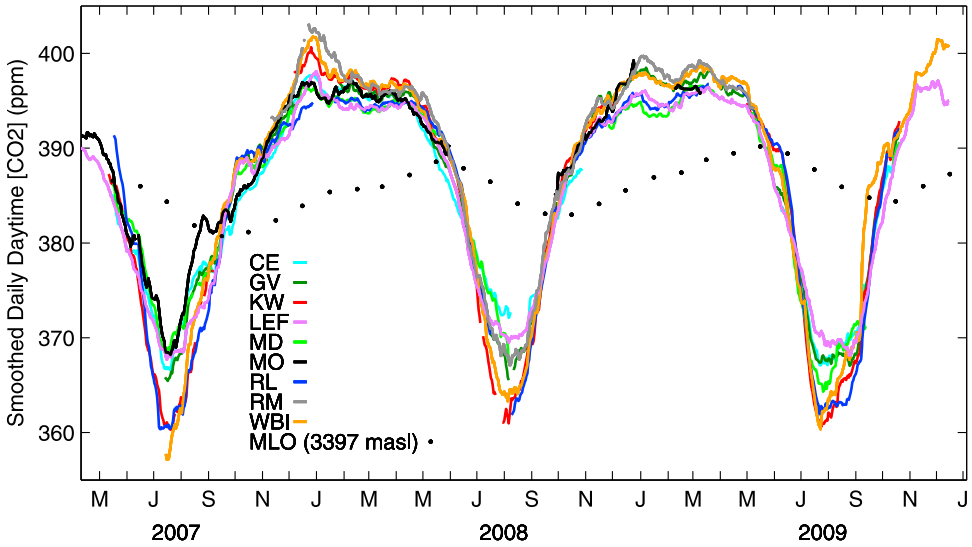

Figure 5. Smoothed CO_2 mole fraction for each site in the MCI region. Data for Mauna Loa (MLO), representing the tropospheric "background," are shown for reference (data courtesy of NOAA-ESRL; see http://www.esrl.noaa.gov/gmd/cgg/trends). Rosemount data are courtesy of T. Griffis (University of Minnesota).

[19] We now consider the magnitude of the seasonal drawdown expected because of the differing NEE from each biome. As a first-order estimate, the magnitude expected is proportional to the sum of the fractional influence of each biome multiplied by the average biome flux. The average corn, soy, grass, and forest fractional influence for corn-dominated sites is 0.36, 0.21, 0.39, and 0.02, respectively, whereas for non-corn-dominated sites the fractional influence is 0.18, 0.12, 0.53, and 0.16 (Figure 2). Using a range of values for each corn/noncorn biome NEE ratio (Figure 3), the expected ratio between the average seasonal drawdown of the corn-dominated versus the non-corn-dominated sites is 1.29–1.56. The actual ratio is 1.26 (Table 3). Since our estimate excludes the effects of atmospheric mixing, it is not surprising that the actual ratio is near the lower extreme of the estimate. A more precise analysis is prohibited by lack of knowledge of the exact corn/noncorn flux ratios.

[20] As is apparent in Figure 5, on a seasonal timescale, gradients observed across the region are strongly dependent on local vegetation type. We consider spatial differences and gradients of two different groups of site pairs: similar vegetation site pairs (either both corn dominated or both non–corn dominated), and cross-vegetation site pairs (one corn-dominated site paired with one non-corn-dominated site). Distributions of the differences and gradients for two similar vegetation site pairs and two cross-vegetation site pairs are shown in Figure 6. The magnitude of the median intersite difference for pairs including only similar vegetation types

Table 3. Dormant Season Maxima, Growing Season Minima, and Seasonal Drawdown of the Smoothed CO_2 Mole Fraction for Each Site Compared to Reference Values of 395 and 360 ppm[a]

		2007			2008			2009		
Site	Rank in Terms of Corn Biome Influence	Dormant Season Maxima	Growing Season Minima (ppm)	Seasonal Drawdown[b]	Dormant Season Maxima	Growing Season Minima (ppm)	Seasonal Drawdown[b]	Dormant Season Maxima	Growing Season Minima (ppm)	Seasonal Drawdown[b]
Park Falls	9	–	8	25[c]	−1	10	24	1	9	27
Missouri Ozarks	8	–	8	26[c]	0	–	–	1	–	–
Centerville	7	–	7	27[c]	0	13	22	–	7	29[c]
Galesville	6	–	6	29[c]	1	7	29	2	7	30
Rosemount	5	–	–	–	1	8	28	–	–	–
Mead	4	–	9	24[c]	−1	7	27	1	4	32
West Branch	3	–	−2	38[c]	2	4	33	3	0	38
Round Lake	2	–	1	32[c]	−1	3	31	1	3	33
Kewanee	1	–	1	34[c]	1	2	34	–	1	36[c]
Reference value		–	360	–	395	360	–	395	360	–

[a]For example, the actual dormant season maxima for Park Falls is 395 + (−1) = 394 ppm. The sites are ordered according to corn biome influence (Figure 2). Although the values are higher in January for 2007, we consistently use April values for the dormant season maxima for comparability.
[b]Seasonal drawdown is calculated by subtracting the growing season minima from each year's dormant season maxima.
[c]In site-years with missing dormant season maxima; the value was estimated by adding (subtracting) the difference between the 2008 and 2009 site-averaged dormant season maximum to (from) the site's 2008 dormant season maximum.

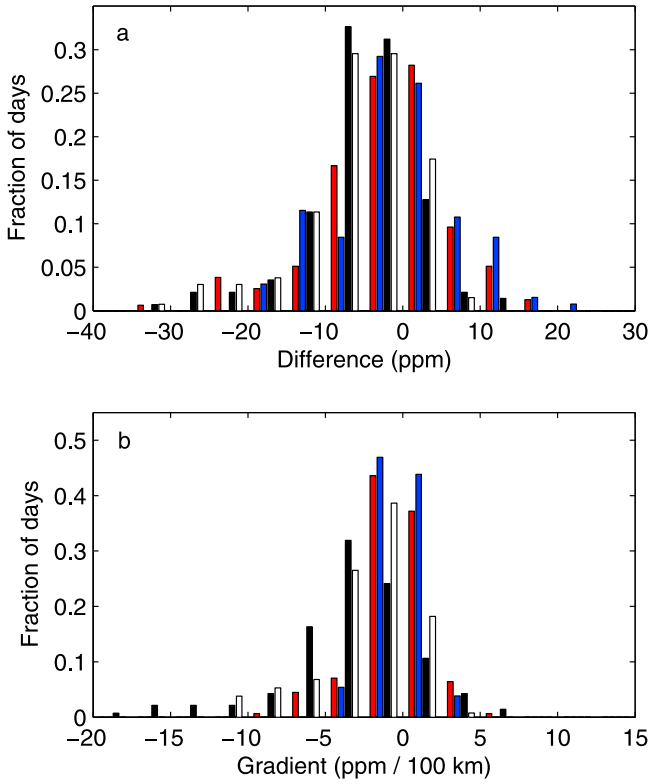

Figure 6. (a) The 2007–2009 averaged peak growing season (July–August) distribution of daily daytime average CO_2 mole fraction differences between Galesville and Centerville (red), Round Lake and Kewanee (blue), West Branch and Centerville (black), and Kewanee and Centerville (white). The bin size is 5 ppm. (b) As in Figure 6a but for gradients rather than differences. The bin size is 2.5 ppm/100 km. For both Figures 6a and 6b, colored bars represent distributions of similar vegetation site pairs, and black and white bars represent distributions of cross-vegetation site pairs.

is 0.9 ppm (see Figure 7a and Table 2) during the peak growing season (July–August), whereas the median of the intersite differences for cross-vegetation pairs is 5.2 ppm, with clear separation between the two groups. The pattern is similar for the gradients (see Figure 7b and Table 2) with the median magnitude of similar vegetation site pairs being 0.3 ppm/100 km, and that of cross-vegetation pairs being 1.5 ppm/100 km. West Branch (corn dominated) and Centerville (non–corn dominated), sites separated by only 164 km, exhibited the largest median intersite peak growing season gradient, 3.1 ppm/100 km, with a median intersite difference magnitude of 5.1 ppm (Table 2).

[21] Although the categorization of corn-dominated and non-corn-dominated groups simplifies the discussion, the relationship holds for the individual sites as well. The biome fractional influence for corn, or the average amount of time air parcels eventually arriving at each tower spent above land planted with corn, is shown as a function of the seasonal drawdown for each site in Figure 8. Sites most influenced by corn have larger seasonal drawdown, with a coefficient of determination (r^2) of 0.59.

[22] Another explanation for the observed differences in seasonal drawdown could be meteorological differences if corn were preferentially planted in areas with larger than average temperatures (enhancing plant growth and thus CO_2 uptake) or lower winds (thus lower mixing). However, analysis of July–August 2007 NCEP Reanalysis Products air temperature and wind speed (see http://www.esrl.noaa.gov/psd/data/reanalysis/) revealed no correlation of average temperature at each site with its seasonal drawdown (r^2 = 0.01) and only a slight correlation of the average wind speed (r^2 = 0.1).

3.2. Daily Scale Variability of CO_2 Fluxes

[23] In the previous discussion, we focused on the seasonal-scale patterns of CO_2 mole fraction in the MCI region. We now consider the large day-to-day weather-related variability (shown for WBI in Figure 9a). As an example of a corn-dominated and a non-corn-dominated site, we examine the histograms of CO_2 mole fraction for WBI and LEF for July–August 2007 (Figure 9b). While there is considerable overlap between the histograms, the median CO_2 mole fraction for WBI is 365.1 ppm, compared to 371.1 ppm for LEF. The standard deviation of the distribution is larger at WBI (11.7 ppm) compared to LEF (6.3 ppm), and there are several days during the growing seasons of 2007–2009 in which the daytime average CO_2 mole fraction measured at WBI is in the range 340–350 ppm.

[24] Both local weather and the overall weather patterns affect the daily CO_2 mole fraction measured at a tower. As local weather conditions change from one day to the next,

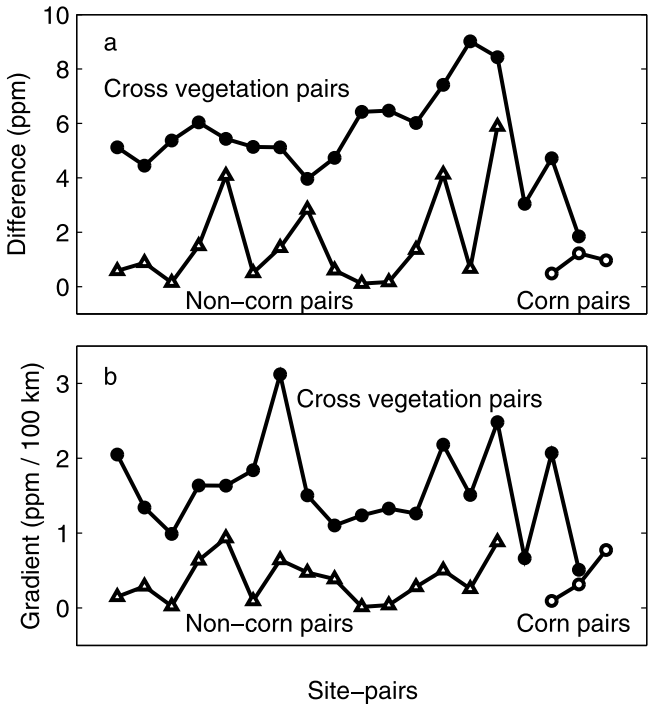

Figure 7. CO_2 mole fraction spatial differences and gradients. (a) Magnitude of the median intersite difference CO_2 mole fraction during the peak growing season (July–August 2007 to 2009) for pairs including only non-corn-dominated sites (triangles), pairs including only corn-dominated sites (open circles), and cross-vegetation pairs (solid circles). (b) Corresponding magnitude of the median intersite gradients.

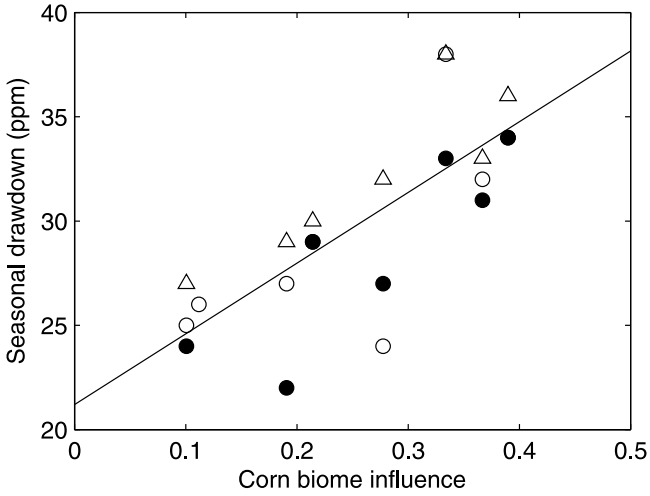

Figure 8. Fractional biome influence attributable to corn (as in Figure 2) as a function of seasonal drawdown (as in Table 3) in 2007 (open circles), 2008 (solid circles), and 2009 (triangles).

the fluxes are scaled accordingly, leading to daily changes in the CO_2 mole fractions. For example, *Chan et al.* [2004] showed that cloud cover in frontal regions reduces photosynthetic uptake, resulting in CO_2 mole fraction gradients across frontal regions. The CO_2 mole fractions of the air masses entering the region are dependent on their source region. A large-scale N–S gradient in near-surface CO_2 mole fractions exists between the largely agricultural MCI region and the relatively unproductive south-central United States (Texas/Louisiana/Oklahoma/Arkansas); the regional pattern of CO_2 mole fraction is thus dependent on large-scale wind direction [*Corbin et al.*, 2010].

[25] During the peak growing season (July–August), 5% of the day-to-day changes at individual sites are greater than 20 ppm and a few are greater than 30 ppm (Figure 10). While the day-to-day changes are large, they depend only weakly on local vegetation type: the mean magnitude is 7.3 ppm for corn-dominated sites, compared to 6.2 ppm for non-corn-dominated sites. Temporal changes and spatial gradients are inherently linked; the range of intersite gradients on a daily timescale is similarly only weakly dependent on local vegetation type. For similar vegetation site pairs, 9% of the gradients are larger than 5.5 ppm/100 km, and for cross-vegetation sites pairs 10% are. The contribution of the local flux to the CO_2 mole fraction spatial variability is thus dependent on timescale. While the daily scale CO_2 mole fraction depends most strongly on regional-scale weather conditions and air mass origin, when these daily values are averaged to a seasonal scale, we see the strong effects of the local flux as we showed in section 3.1.

3.3. Interannual Variability in CO_2 Fluxes

[26] The majority of sites exhibited relatively little change in their growing season minima from year to year. Some sites, however, showed interannual variability related to climate variability (Table 3). Flooding occurred in the midwestern United States during the first half of June 2008 (see http://www.ncdc.noaa.gov), although it was not uniform over the region. While Missouri Ozarks, Centerville, and West Branch recorded cumulative precipitation exceeding 30% above normal over the months of March–September, Round Lake, Rosemount, and Park Falls (LEF) experienced lower than normal precipitation during that time period. Two of the three sites experiencing the most flooding (Centerville and West Branch) exhibited decreased seasonal CO_2 drawdown (by 4–6 ppm) in 2008 as compared to 2007 and 2009. The vegetation of the flood-affected site that did not, Missouri Ozarks, includes a higher percentage of forest, which perhaps mitigated the flooding effects.

[27] Agriculture within the region was considerably affected by the 2008 flooding. Considering corn and soybeans together, the total harvested volume (grain production) of these crops decreased by 7% for the state of Iowa, compared to 2007 and 2009 [*USDA-NASS*, 2010]. The total estimated NPP of corn, using the method documented in the work of *West et al.* [2010], was 221.57, 207.33, and

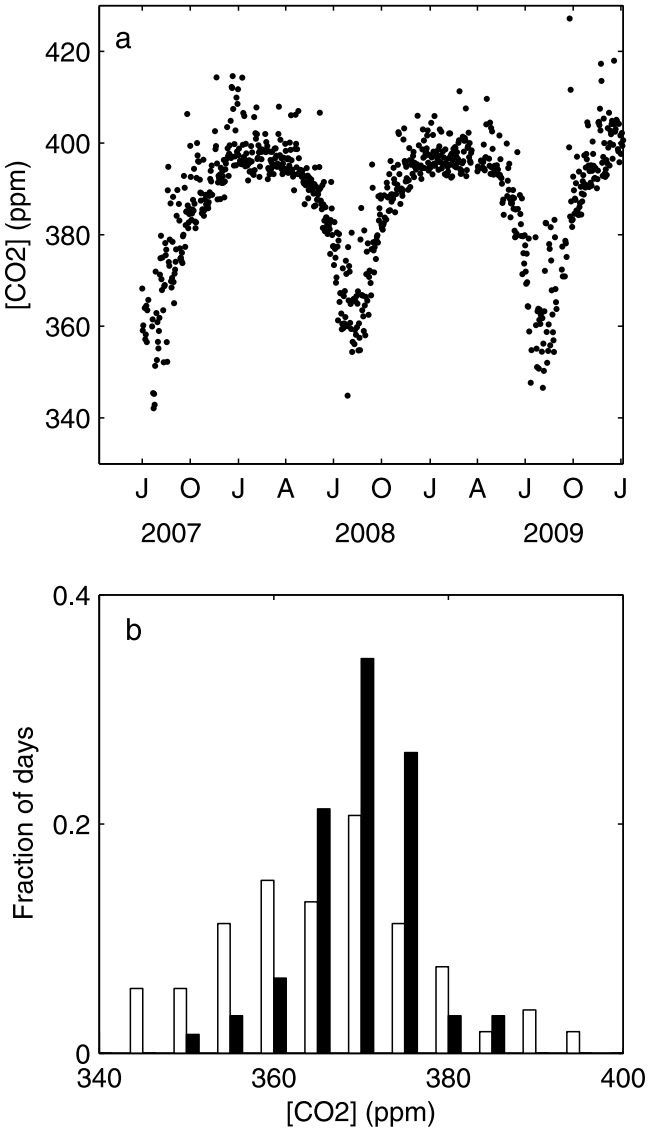

Figure 9. (a) Daily daytime CO_2 mole fraction for WBI. (b) Histogram of CO_2 mole fraction, for July–August 2007 only for WBI (white bars) and LEF (black bars). The bin size is 5 ppm.

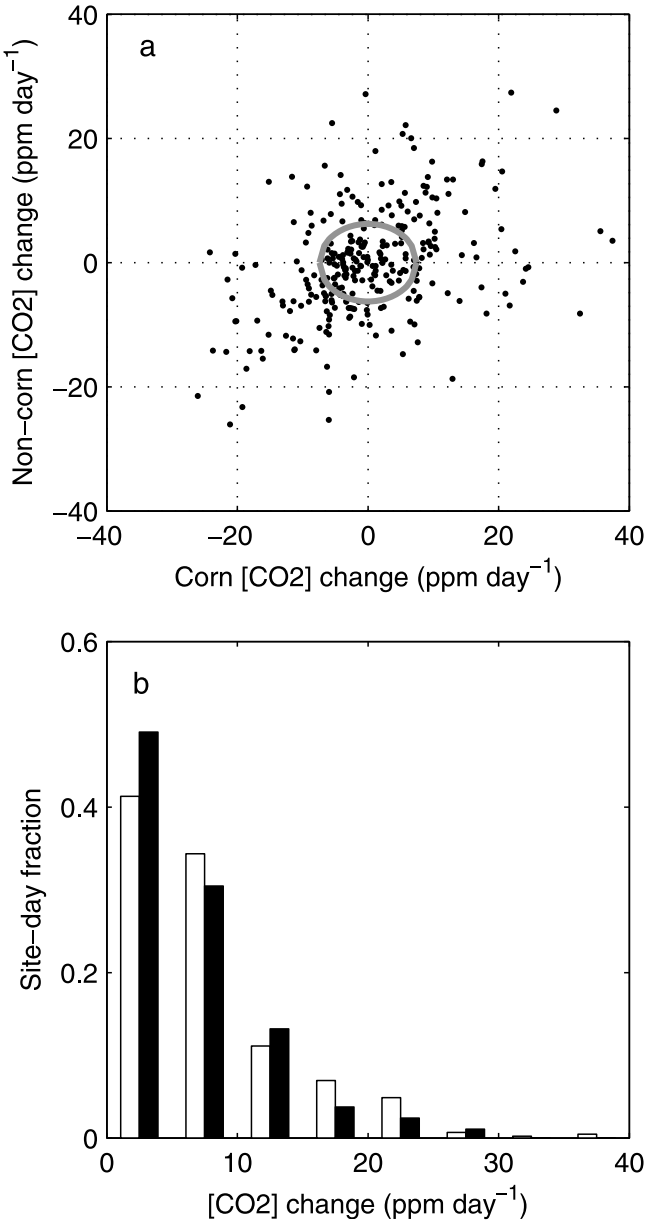

Figure 10. (a) The 2007–2009 peak growing season day-to-day change in daily daytime average CO_2 mole fraction observed at corn-dominated sites (WBI, KW, and RL) versus three of the non-corn-dominated sites (LEF, MO, and CE). Each point represents one day-to-day change for a cross-vegetation pair. The axes of the ellipse indicate the mean magnitude of the day-to-day change for the corn-dominated sites (7.3 ppm) and non-corn-dominated sites (6.2 ppm). (b) Histogram of the magnitude of the day-to-day changes in Figure 10a for corn-dominated sites (white bars) and non-corn-dominated sites (black bars).

222.52 Tg C in 2007, 2008, and 2009, respectively. Agricultural areas surrounding the Centerville site were most affected by the flooding of 2008, with corn harvested volume down by 18% compared to the 2007–2009 average, and soybean harvested volume down by 10% [*USDA-NASS*, 2010]. Other sites were affected by varying degrees. The total regional flux, of course includes contributions from natural ecosystems as well; they may be less affected by flooding.

[28] In addition to detecting effects of the 2008 flooding, we also see more subtle climate-based interannual variability, particularly in the timing of the crop growth. The onset of the growing season, as evidenced by the onset of the seasonal drawdown in CO_2, was 2–3 weeks early in 2007, compared to 2008 and 2009 (Figure 11a). Similarly, interannual differences are observed in the normalized difference vegetation index (NDVI) time series curves for corn and soybean fields in the State of Iowa. The emergence, maturity, and senescence of both corn and soy were late by 1–2 weeks in 2008 compared to 2007 (Figures 11b and 11c). Except for mid-June to mid-July, the 2009 corn NDVI followed that of 2008; soy NDVI for 2009 was similar to that of 2007 through August and then more similar to 2008. The coefficient of determination (r^2) between corn NDVI and smoothed atmospheric CO_2 mole fraction at Kewanee in 2007, 2008, and 2009 was 0.66, 0.85, and 0.75, respectively.

[29] Agricultural inventory statistics, based on farmer surveys [*USDA-NASS*, 2010], also indicate considerable interannual variability: corn in Iowa reached maturity about the same time in 2008 and 2009, but 3–4 weeks earlier in 2007. The spring of 2007 was particularly warm for the state

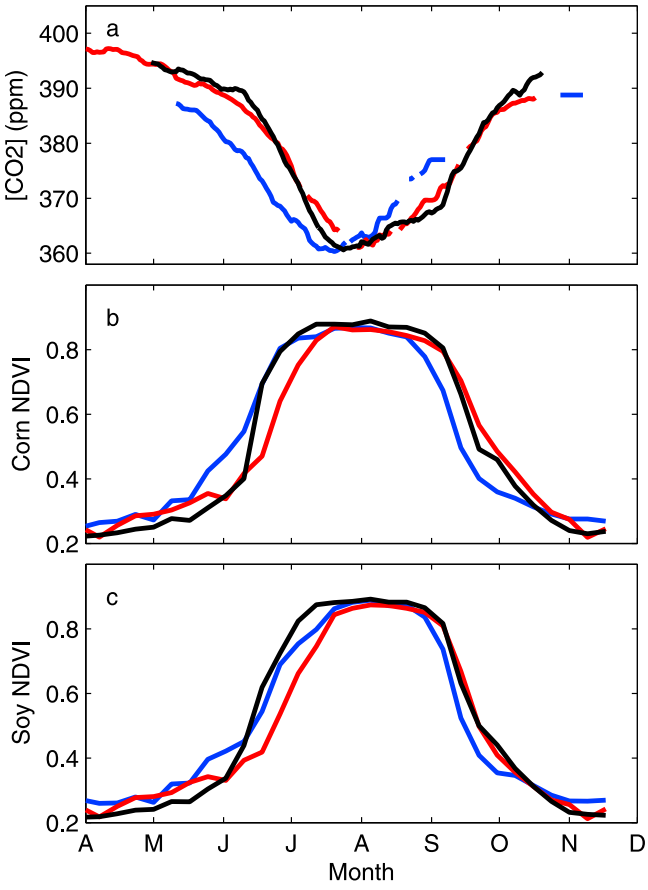

Figure 11. (a) Smoothed daily daytime average CO_2 mole fraction at Kewanee for 2007 (blue), 2008 (red), and 2009 (black). (b) Normalized difference vegetation index (NDVI) for corn averaged for the state of Iowa. (c) Same as Figure 11b but for soybeans.

of Iowa (above the 90th percentile for the period 1895–2009), whereas the springs of 2008 and 2009 were slightly below and near normal in temperature, respectively (see http://www.ncdc.noaa.gov). The summer of 2007 was near normal, 2008 was slightly below normal, and 2009 was below the 10th percentile in temperature. The warm spring of 2007, the flooding of 2008, and the cool summer of 2009 appear to have contributed to an early growing season with high NPP in 2007, a late growing season with low NPP in 2008, and a late growing season with high NPP in 2009, relative to each other. Thus, with a tower-based network of mole fraction measurements, we detect climate-driven interannual changes in crop growth timing that are confirmed via satellite and inventory methods.

[30] The separation between corn-dominated and non-corn-dominated sites in CO_2 mole fraction minima (Figure 5), while apparent in all three years, is most pronounced in 2007. This phenomenon, while possibly related to climate-induced variability, may also be related to crop management induced changes in the carbon flux. The acreage of corn planted in Iowa in 2007 increased in response to demand for ethanol production; the ratio of the area of corn planted to that of soy in 2007 was 1.61 compared to 1.33 and 1.46 in 2008 and 2009, respectively [*USDA-NASS*, 2010]. Additionally, *Griffis et al.* [2010] found a 10% increase in the contribution of corn to regional flux in the Rosemount area in 2007 compared to 2008. The increased separation between the CO_2 mole fraction minima could be explained if the footprints of the corn-dominated sites specifically included increased corn influence relative to the non-corn-dominated sites in 2007 compared to 2008 and 2009.

4. Implications for Atmospheric Verification of CO_2 Fluxes

[31] These observations show that, instead of being dominated by white noise, regional-scale CO_2 mole fraction networks obtain large, coherent signals. These signals are linked to both local vegetation and weather, and can be used in designing future observational networks. To put in perspective the magnitude of the spatial gradients observed in the MCI, we compare to ocean-continent values and to interhemispheric values, the mean annual spatial gradients that have been the traditional focus of atmospheric inversion studies. The ocean-continent gradient during the continental peak growing season [*GLOBALVIEW-CO2*, 2011] based on LEF is about 0.4 ppm/100 km. The annual interhemispheric mean difference for 2007–2009 is about 3.6 ppm [*GLOBALVIEW-CO2*, 2011]. The corresponding gradient is 0.036 ppm/100 km. The median gradient measured in the MCI region between cross-vegetation site pairs (1.5 ppm/100 km) is thus a factor of 4 times as large as the ocean-continent gradient and a factor of 40 times as large as the interhemispheric gradient. The atmosphere does not "mix out" these persistent and strong seasonal differences and gradients in the MCI region. It is therefore particularly important for regional, subseasonal inversion models to use accurate transport fields in areas like the MCI.

[32] The seasonal pattern in mole fractions across the region show persistent spatial structure that appears to be strongly dependent upon the dominance of corn, with implications for the footprint size, as well as for network design. The strong dependence of growing season median gradients on local vegetation type is consistent with the calculated footprint extents. Similarly, recent studies [*Lauvaux et al.*, 2008; *Gerbig et al.*, 2009] have documented the importance of the near field. Using synthetic data, *Lauvaux et al.* [2008] found significant error reduction in only about half of their 300 km × 300 km domain by including two towers. If the influence functions are integrated over the fluxes, the near-field effects can be stronger or weaker, depending on the surrounding vegetation. *Gerbig et al.* [2009], for August 2002 measurements at Harvard Forest, reported that the fluxes in the nearest 20–60 km contribute about half of the total, representing a larger near-field influence than shown in the current study. Centerville and West Branch, towers separated by only 164 km, differed in terms of seasonal-scale CO_2 patterns, with a median intersite peak growing season gradient of 3.1 ppm/100 km. These large gradients corroborate the importance of the near field. The implication of the two distinct groups (corn dominated and non–corn dominated) in the current study for network design is that tower locations should be distributed on the basis of prior ground-based fluxes, rather than homogenously distributed on the basis of statistical footprints.

[33] Links among observed CO_2 mole fraction, satellite-derived measures of plant growth, and agricultural inventory statistics corroborate the ability of the mole fraction to record crop management- and climate-induced changes in carbon flux. We are able to detect both regional-scale flooding effects and more subtle climate-induced changes in the timing of plant growth.

[34] From a monitoring perspective, it is the spatially and time-dependent regional flux determined from CO_2 mole fraction measurements and inversion models that is necessary to evaluate inventory methods. The uptake of CO_2 of corn and other crops compared to natural ecosystems during the growing season leads to a large-scale minimum of CO_2 mole fraction in the MCI region [*Corbin et al.*, 2010]. The NEE over the course of the year (on the larger, national scale) is almost zero, since crops are harvested, transported, and used for food and livestock feed, and the crop residues decompose during the dormant season [*West et al.*, 2011]. Assessing the ability of inversion models to determine the regional flux is the focus of current research [e.g., *Lauvaux et al.*, 2011].

[35] In summary, these results suggest that a limited number of samples across the corn belt of the U.S. upper Midwest captured the dominant spatial patterns in CO_2 mole fraction. In this region with extensively documented inventory data, spatial and temporal variability in CO_2 fluxes was concurrently recorded in tower, inventory, and satellite data. Similar regional networks, deployed in other parts of the globe, are therefore highly likely to capture strong regional signals characteristic of CO_2 fluxes. Relatively simple, moderate-cost, ground-based networks, combined with mesoscale inverse modeling systems, could be an effective means of providing atmospheric verification of regional CO_2 emissions inventories.

[36] **Acknowledgments.** The authors gratefully acknowledge the tower owners for allowing tower access and for on-site help; without their cooperation this work would not have been possible. We thank T. Griffis (University of Minnesota) for providing Rosemount CO_2 mole fraction and flux data. We recognize P. Tans (NOAA-ESRL) for providing globally

averaged data and C. Sweeney (NOAA-ESRL) for providing West Branch aircraft data. We thank A. Schuh (Colorado State University) for providing biome maps. For eddy-covariance flux data we acknowledge A. Suyker and S. Verma (University of Nebraska at Lincoln) for Mead, R. Matamala (Argonne National Laboratory) for Fermi and Brookings, and L. Gu (Oak Ridge National Laboratory) for Missouri Ozarks. This research was sponsored by the U.S. Department of Energy Office of Science TCP Program (DE-FG02-06ER64315) and by the U.S. Department of Commerce, NOAA Office of Global Programs (NA08OAR4310533). Processing of MODIS NDVI was sponsored by the NASA Earth Sciences Division. MCI tower data are available online at http://www.ring2.psu.edu.

References

Bakwin, P. S., P. P. Tans, C. Zhao, W. Ussler, and E. Quesnell (1995), Measurements of carbon dioxide on a very tall tower, *Tellus, Ser. B*, *47*, 535–549, doi:10.1034/j.1600-0889.47.issue5.2.x.

Bakwin, P. S., P. P. Tans, D. F. Hurst, and C. Zhao (1998), Measurements of carbon dioxide on very tall towers: Results of the NOAA/CMDL program, *Tellus, Ser. B*, *50*, 401–415, doi:10.1034/j.1600-0889.1998.t01-4-00001.x.

Butler, M. P., K. J. Davis, A. S. Denning, and S. R. Kawa (2010), Using continental observations in global atmospheric inversions of CO_2: North American carbon sources and sinks, *Tellus, Ser. B*, *62*, 550–572, doi:10.1111/j.1600-0889.2010.00501.x.

Chan, D., C. W. Yuen, K. Higuchi, A. Shashkov, J. Liu, J. Chen, and D. Worthy (2004), On the CO_2 exchange between the atmosphere and the biosphere: The role of synoptic and mesoscale processes, *Tellus, Ser. B*, *56*, 194–212, doi:10.1111/j.1600-0889.2004.00104.x.

Chen, H., et al. (2010), High-accuracy continuous airborne measurements of greenhouse gases (CO_2 and CH_4) using the cavity ring-down spectroscopy technique, *Atmos. Meas. Tech.*, *3*, 375–386, doi:10.5194/amt-3-375-2010.

Committee on Methods for Estimating Greenhouse Gas Emissions (2010), *Verifying Greenhouse Gas Emissions: Methods to Support International Climate Agreements*, Natl. Res. Counc., Natl. Acad. Press, Washington, D. C. [Available at http://www.nap.edu.]

Corbin, K. D., A. S. Denning, E. Y. Lokupitiya, A. E. Schuh, N. L. Miles, K. J. Davis, S. Richardson, and I. T. Baker (2010), Assessing the impact of crops on regional CO_2 fluxes and atmospheric concentrations, *Tellus, Ser. B*, *62*, 521–532, doi:10.1111/j.1600-0889.2010.00485.x.

Crevoisier, C., C. Sweeney, M. Gloor, J. L. Sarmiento, and P. P. Tans (2010), Regional U.S. carbon sinks from three-dimensional atmospheric CO_2 sampling, *Proc. Natl. Acad. Sci. U. S. A.*, *107*, 18,348–18,353, doi:10.1073/pnas.0900062107.

Crosson, E. R. (2008), A cavity ring-down analyzer for measuring atmospheric levels of methane, carbon dioxide, and water vapor, *Appl. Phys. B*, *92*, 403–408, doi:10.1007/s00340-008-3135-y.

Davis, K. J., P. S. Bakwin, C. Yi, B. W. Berger, C. Zhao, R. M. Teclaw, and J. G. Isebrands (2003), The annual cycles of CO_2 and H_2O exchange over a northern mixed forest as observed from a very tall tower, *Global Change Biol.*, *9*, 1278–1293, doi:10.1046/j.1365-2486.2003.00672.x.

Denning, A. S. (Ed.) (2005), Science implementation strategy for the North American carbon program: Report of the NACP Implementation Strategy Group of the U.S. Carbon Cycle Interagency, report, U.S. Carbon Cycle Sci. Program, Washington, D. C. [Available at http://www.carboncyclescience.gov/documents/nacp_sis_2005.pdf.]

Dolman, A. J., et al. (2006), The CarboEurope Regional Experiment Strategy, *Bull. Am. Meteorol. Soc.*, *87*, 1367–1379, doi:10.1175/BAMS-87-10-1367.

Dwyer, J., and G. Schmidt (2006), The MODIS reprojection tool, in *Earth Science Satellite Remote Sensing*, edited by J. J. Qu et al., pp. 162–177, Springer, Berlin.

Gerbig, C., J. C. Lin, S. C. Wofsy, B. C. Daube, A. E. Andrews, B. B. Stephens, P. S. Bakwin, and C. A. Grainger (2003), Toward constraining regional scale fluxes of CO_2 with atmospheric observations over a continent: 1. Observed spatial variability from airborne platforms, *J. Geophys. Res.*, *108*(D24), 4756, doi:10.1029/2002JD003018.

Gerbig, C., A. J. Dolman, and M. Heimann (2009), On observational and modeling strategies targeted at regional carbon exchange over continents, *Biogeosciences*, *6*, 1949–1959, doi:10.5194/bg-6-1949-2009.

GLOBALVIEW-CO_2 (2011), *Cooperative Atmospheric Data Integration Project–Carbon Dioxide* [CD-ROM], NOAA Earth Syst. Res. Lab., Boulder, Colo.

Griffis, T. J., J. M. Baker, S. D. Sargent, M. Erickson, J. Corocoan, M. Chen, and K. Billmark (2010), Influence of C_4 vegetation on $^{13}CO_2$ discrimination and isoforcing in the upper Midwest, United States, *Global Biogeochem. Cycles*, *24*, GB4006, doi:10.1029/2009GB003768.

Gu, L., P. J. Hanson, W. M. Post, D. P. Kaiser, B. Yang, R. Nemani, S. G. Pallardy, and T. Meyers (2008), The 2007 eastern U.S. spring freezes: Increased cold damage in a warming world?, *Biosciences*, *58*, 253–262, doi:10.1641/B580311.

Gurney, K. R., D. L. Mendoza, Y. Zhou, M. L. Fischer, C. C. Miller, S. Geethakumar, and S. De La Rue Du Can (2009), High resolution fossil fuel combustion CO_2 emissions fluxes for the United States, *Environ. Sci. Technol.*, *43*, 5535–5541, doi:10.1021/es900806c.

Haszpra, L., Z. Barcza, D. Hidy, I. Szilágyi, E. Dlugokencky, and P. Tans (2008), Trends and temporal variations of major greenhouse gases at a rural site in Central Europe, *Atmos. Environ.*, *42*, 8707–8716, doi:10.1016/j.atmosenv.2008.09.012.

Houweling, S., et al. (2010), The importance of transport model uncertainties for the estimation of CO_2 sources and sinks using satellite measurements, *Atmos. Chem. Phys.*, *10*, 9981–9992, doi:10.5194/acp-10-9981-2010.

Hurwitz, M. D., D. M. Ricciuto, P. S. Bakwin, K. J. Davis, W. Wang, C. Yi, and M. P. Butler (2004), Transport of carbon dioxide in the presence of storm systems over a northern Wisconsin forest, *J. Atmos. Sci.*, *61*, 607–618, doi:10.1175/1520-0469(2004)061<0607:TOCDIT>2.0.CO;2.

Johnson, D. M., and R. Mueller (2010), The 2009 cropland data layer, *Photogramm. Eng. Remote Sens.*, *76*, 1201–1205.

King, A. W., L. Dilling, G. P. Zimmerman, D. M. Fairman, R. A. Houghton, G. Marland, A. Z. Rose, and T. J. Wilbanks (Eds.) (2007), The first State of the Carbon Cycle Report (SOCCR): The North American carbon budget and implications for the global carbon cycle, report, 242 pp., NOAA Natl. Clim. Data Cent., Asheville, N. C. [Available at http://cdiac.ornl.gov/SOCCR/.]

Lauvaux, T., M. Uliasz, C. Sarrat, F. Chevallier, P. Bousquet, C. Lac, K. J. Davis, P. Ciais, A. S. Denning, and P. J. Rayner (2008), Mesoscale inversion: First results from the CERES campaign with synthetic data, *Atmos. Chem. Phys.*, *8*, 3459–3471, doi:10.5194/acp-8-3459-2008.

Lauvaux, T., et al. (2009), Bridging the gap between atmospheric concentrations and local ecosystem measurements, *Geophys. Res. Lett.*, *36*, L19809, doi:10.1029/2009GL039574.

Lauvaux, T., et al. (2011), Constraining the CO_2 budget of the corn belt: Exploring uncertainties from the assumptions in a mesoscale inverse system, *Atmos. Chem. Phys.*, *12*, 337–354, doi:10.5194/acp-12-337-2012.

Lin, J. C., C. Gerbig, B. C. Daube, S. C. Wofsy, A. E. Andrews, S. A. Vay, and B. E. Anderson (2004), An empirical analysis of the spatial variability of atmospheric CO_2: Implications for inverse analysis and space-borne sensors, *Geophys. Res. Lett.*, *31*, L23104, doi:10.1029/2004GL020957.

Lokupitiya, E., A. S. Denning, K. Paustian, I. Baker, K. Schaefer, S. Verma, T. Meyers, C. Bernacchi, A. Suyker, and M. Fischer (2009), Incorporation of crop phenology in Simple Biosphere Model (SiBcrop) to improve land-atmosphere carbon exchanges from croplands, *Biogeosciences*, *6*, 969–986, doi:10.5194/bg-6-969-2009.

Martins, D. K., C. Sweeney, B. H. Stirm, and P. B. Shepson (2009), Regional surface flux of CO_2 interred from changes in the advected CO_2 column density, *Agric. For. Meteorol.*, *149*, 1674–1685, doi:10.1016/j.agrformet.2009.05.005.

Matamala, R., D. J. Jastrow, R. M. Miller, and C. Garten (2008), Temporal changes in the distribution of C and N stocks in a restored tallgrass prairie in the U.S. Midwest, *Ecol. Appl.*, *18*, 1470–1488, doi:10.1890/07-1609.1.

Matross, D. M., et al. (2006), Estimating regional carbon exchange in New England and Quebec by combining atmospheric, ground-based and satellite data, *Tellus, Ser. B*, *58*, 344–358, doi:10.1111/j.1600-0889.2006.00206.x.

Nisbet, E., and R. Weiss (2010), Top-down versus bottom-up, *Science*, *328*, 1241–1243, doi:10.1126/science.1189936.

Ogle, S., K. Davis, A. Andrews, K. Gurney, T. West, R. Cook, R. Parkin, J. Morisette, S. Verma, and S. Wofsy (2006), Science Plan: Mid-Continent Intensive Campaign, report, U.S. Global Change Res. Program, North Am. Carbon Program, Greenbelt, Md. [Available at http://www.nacarbon.org/nacp/mci.html.]

Ogle, S., F. J. Breidt, M. Easter, S. Williams, K. Killian, and K. Paustian (2010), Scale and uncertainty in modeled soil organic carbon stock changes for U.S. croplands using a process-based model, *Global Change Biol.*, *16*, 810–822, doi:10.1111/j.1365-2486.2009.01951.x.

Peters, W., et al. (2007), An atmospheric perspective on North American carbon dioxide exchange: CarbonTracker, *Proc. Natl. Acad. Sci. U. S. A.*, *104*, 18,925–18,930, doi:10.1073/pnas.0708986104.

Peylin, P., P. J. Rayner, P. Bousquet, C. Carouge, F. Hourdin, P. Heinrich, P. Ciais, and AEROCARB contributors (2005), Daily CO_2 flux estimates over Europe from continuous atmospheric measurements: 1, Inverse methodology, *Atmos. Chem. Phys.*, *5*, 3173–3186, doi:10.5194/acp-5-3173-2005.

Richardson, S. J., N. L. Miles, K. J. Davis, E. R. Crosson, C. Rella, and A. E. Andrews (2012), Field testing of cavity ring-down spectroscopy

analyzers measuring carbon dioxide and water vapor, *J. Atmos. Oceanic Technol.*, doi:10.1175/jtech-d-11-00063.1, in press.

Schuh, A. E., A. S. Denning, K. D. Corbin, I. T. Baker, M. Uliasz, N. Parazoo, A. E. Andrews, and D. E. J. Worthy (2010), A regional high-resolution carbon flux inversion of North America for 2004, *Biogeosciences*, *7*, 1625–1644, doi:10.5194/bg-7-1625-2010.

Skamarock, W. C., J. B. Klemp, J. Dudhia, D. O. Gill, D. M. Barker, M. Duda, X.-Y. Huang, W. Wang, and J. G. Powers (2008), A description of the Advanced Research WRF version 3, *NCAR Tech. Note 475+STR*, Natl. Cent. for Atmos. Res., Boulder, Colo.

Stephens, B. B., N. L. Miles, S. J. Richardson, A. S. Watt, and K. J. Davis (2011), Atmospheric CO_2 monitoring with single-cell NDIR-based analyzers, *Atmos. Meas. Tech.*, *4*, 2737–2748, doi:10.5194/amt-4-2737-2011.

Tans, P. P., I. Y. Fung, and T. Takahashi (1990), Observational constraints on the global atmospheric CO_2 budget, *Science*, *247*, 1431–1438, doi:10.1126/science.247.4949.1431.

Tolk, L. F., W. Peters, A. G. C. A. Meesters, M. Groenendijk, A. T. Vermeulen, G. J. Steeneveld, and A. J. Dolman (2009), Modelling regional scale surface fluxes, meteorology and CO_2 mixing ratios for the Cabauw tower in the Netherlands, *Biogeosciences*, *6*, 2265–2280, doi:10.5194/bg-6-2265-2009.

Uliasz, M. (1994), *Lagrangian Particle Modeling in Mesoscale Applications, Environmental Modelling II*, edited by P. Zanetti, pp. 71–102, Comput. Mech. Publ., Southampton, U. K.

U.S. Department of Agriculture-National Agricultural Statistics Service (USDA-NASS) (2010), Quick Stats Database, http://www.nass.usda.gov/Data_and_Statistics/Quick_Stats/index.asp, Washington, D. C.

Verma, S. B., et al. (2005), Annual carbon dioxide exchange in irrigated and rainfed maize-based agroecosystems, *Agric. For. Meteorol.*, *131*, 77–96, doi:10.1016/j.agrformet.2005.05.003.

Vermote, E. F., N. Z. El Saluous, and C. O. Justice (2002), Atmospheric correction of MODIS data in the visible to near infrared: First results, *Remote Sens. Environ.*, *83*, 97–111, doi:10.1016/S0034-4257(02)00089-5.

Vermote, E. F., S. Y. Kotchenova, and J. P. Ray (2011), MODIS surface reflectance user's guide, v. 1.3, user's manual, MODIS Land Surface Reflectance Sci. Comput. Facil., NASA, Greenbelt, Md. [Available at http://modis-sr.ltdri.org/products/MOD09_UserGuide_v1_3.pdf.]

Wang, J.-W., A. S. Denning, L. Liu, I. T. Baker, K. D. Corbin, and K. J. Davis (2007), Observations and simulations of synoptic, regional and local variations in atmospheric CO_2, *J. Geophys. Res.*, *112*, D04108, doi:10.1029/2006JD007410.

West, T. O., C. C. Brandt, B. S. Wilson, C. M. Hellwinckel, D. D. Tyler, G. Marland, D. G. De La Torre Ugarte, J. A. Larson, and R. Nelson (2008), Estimating regional changes in soil carbon with high spatial resolution, *Soil Sci. Soc. Am. J.*, *72*, 285–294, doi:10.2136/sssaj2007.0113.

West, T. O., et al. (2010), Cropland carbon fluxes in the United States: Increasing resolution of inventory-based carbon accounting, *Ecol. Appl.*, *20*, 1074–1086, doi:10.1890/08-2352.1.

West, T. O., V. Bandaru, C. C. Brandt, A. E. Schuh, and S. M. Ogle (2011), Regional uptake and release of crop carbon in the United States, *Biogeosciences*, *8*, 2037–2046, doi:10.5194/bg-8-2037-2011.

Wofsy, S. C., and R. C. Harriss (2002), The North American Carbon Program (NACP), report, U.S. Global Change Res. Program, Washington, D. C.

Wolfe, R. E., M. Nishihama, A. J. Fleig, J. A. Kuyper, D. P. Roy, J. C. Storey, and F. S. Patt (2002), Achieving sub-pixel geolocation accuracy in support of MODIS land science, *Remote Sens. Environ.*, *83*, 31–49, doi:10.1016/S0034-4257(02)00085-8.

Xiao, J., et al. (2008), Estimation of net ecosystem carbon exchange for the conterminous United States by combining MODIS and AmeriFlux data, *Agric. For. Meteorol.*, *148*, 1827–1847, doi:10.1016/j.agrformet.2008.06.015.

Zhao, C., P. S. Bakwin, and P. P. Tans (1997), A design for unattended monitoring of trace gases on a tall tower, *J. Atmos. Oceanic Technol.*, *14*, 1139–1145, doi:10.1175/1520-0426(1997)014<1139:ADFUMO>2.0.CO;2.

A. E. Andrews, Earth System Research Laboratory, Global Monitoring Division, National Oceanic and Atmospheric Administration, 325 Broadway, R/GMD1, Boulder, CO 80305, USA.

V. Bandaru and T. O. West, Pacific Northwest National Laboratory, Joint Global Change Research Institute, University of Maryland, 5825 University Research Ct., Ste. 3500, College Park, MD 20740, USA.

E. R. Crosson, Picarro, Inc., 480 Oakmead Pkwy., Sunnyvale, CA 94085, USA.

K. J. Davis, T. Lauvaux, N. L. Miles, and S. J. Richardson, Department of Meteorology, Pennsylvania State University, 503 Walker Bldg., University Park, PA 16802, USA. (nmiles@met.psu.edu)

Tellus SERIES B CHEMICAL AND PHYSICAL METEOROLOGY
PUBLISHED BY THE INTERNATIONAL METEOROLOGICAL INSTITUTE IN STOCKHOLM

Network design for mesoscale inversions of CO_2 sources and sinks

By T. LAUVAUX[1]*, A. E. SCHUH[2,5], M. BOCQUET[3], L. WU[3,4], S. RICHARDSON[1], N. MILES[1] and K. J. DAVIS[1], [1]*Department of Meteorology, The Pennsylvania State University, University Park, TX, USA;* [2]*Natural Resource Ecology Laboratory, Colorado State University, Fort Collins, CO, USA;* [3]*CEREA, Joint Laboratory Ecole Nationale des Ponts et Chaussées/EDF R&D, Champs sur Marne, France;* [4]*Laboratoire des Sciences du Climat et de l'Environnement, IPSL-LS, CECEA-CNRS-UVSQ, UMR8212, Saclay, France;* [5]*Department of Atmospheric Science, Colorado State University, Fort Collins, CO, USA*

(Manuscript received 4 March 2012; in final form 26 April 2012)

ABSTRACT

Recent instrumental deployments of regional observation networks of atmospheric CO_2 mixing ratios have been used to constrain carbon sources and sinks using inversion methodologies. In this study, we performed sensitivity experiments using observation sites from the Mid Continent Intensive experiment to evaluate the required spatial density and locations of CO_2 concentration towers based on flux corrections and error reduction analysis. In addition, we investigated the impact of prior flux error structures with different correlation lengths and biome information. We show here that, while the regional carbon balance converged to similar annual estimates using only two concentration towers over the region, additional sites were necessary to retrieve the spatial flux distribution of our reference case (using the entire network of eight towers). Local flux corrections required the presence of observation sites in their vicinity, suggesting that each tower was only able to retrieve major corrections within a hundred of kilometres around, despite the introduction of spatial correlation lengths ($\sim$100 to 300 km) in the prior flux errors. We then quantified and evaluated the impact of the spatial correlations in the prior flux errors by estimating the improvement in the CO_2 model-data mismatch of the towers not included in the inversion. The overall gain across the domain increased with the correlation length, up to 300 km, including both biome-related and non-biome-related structures. However, the spatial variability at smaller scales was not improved. We conclude that the placement of observation towers around major sources and sinks is critical for regional-scale inversions in order to obtain reliable flux distributions in space. Sparser networks seem sufficient to assess the overall regional carbon budget with the support of flux error correlations, indicating that regional signals can be recovered using hourly mixing ratios. However, the smaller spatial structures in the posterior fluxes are highly constrained by assumed prior flux error correlation lengths, with no significant improvement at only a few hundreds of kilometres away from the observation sites.

Keywords: carbon dioxide, atmospheric inversion, air–land interaction, mesoscale modelling, carbon cycle, data assimilation

1. Introduction

The remaining fraction of atmospheric carbon from anthropogenic emissions corresponds to about 45% of the total emissions, due to absorption mechanisms on the continents and the oceans (Raupach et al., 2008; LeQuéré et al., 2009). Although anthropogenic emissions are reported with high accuracy at the national level (Gurney et al., 2009), the role of continental surfaces affected by a large interannual variability remains critical to better understand and predict the atmospheric accumulation (Canadell et al., 2007). Their contribution remains poorly constrained at the continental and regional levels using inverse approaches despite consistency at larger scales (Ciais et al., 2010). Process-based approaches and statistical regression methods for parameter optimisation have also been used to constrain the carbon pools and the net flux from the terrestrial vegetation (Ricciuto et al., 2011),

*Corresponding author.
email: lauvaux@meteo.psu.edu

Citation: Tellus B 2012, **64**, 17980, http://dx.doi.org/10.3402/tellusb.v64i0.17980

but large discrepancies remain on the annual and seasonal time scales (Keenan et al., 2012).

Because of the absence of direct measurements of regional carbon fluxes, the evaluation of the methods at policy relevant scales (few 10ths of kilometres) is limited to intermodel comparisons (Schwalm et al., 2010) and uncertainty analysis of parameters (Knorr and Heimann, 2001) or based on direct or indirect measurements (Wang et al., 2001). The Mid Continent Intensive (MCI) experiment focused on an intensively managed area for which agricultural inventories can provide reliable annual flux estimates (West et al., 2011), primarily driven by harvest production of crops. The inventory product can be used to evaluate other carbon flux estimates from biogeochemical terrestrial models, model-data fusion approaches, or atmospheric inversions. Despite the high precision obtained in the inventories from the collected crop harvest data (Ogle et al., 2010), the uncertainty over the entire region is increased by lower sampling frequency in the forest inventory, the parameterisations involved in the inventory models, the high variability from natural ecosystems and poorly documented semi-managed ecosystems such as pasture.

Mesoscale atmospheric inversions were used in several studies as a promising tool to monitor and estimate regional flux balances at high resolution (Lauvaux et al., 2009; Schuh et al., 2010; Göckede et al., 2010a). Though errors in the atmospheric transport model and at the boundaries limit the potential of the method (Göckede et al., 2010b; Lauvaux et al., 2012), mesoscale inverse systems have shown consistent improvements from prior fluxes over short periods of time (Lauvaux et al., 2009), and at the annual time scale over the region (Schuh et al., 2010). Over longer time scales, the assessment of the regional flux balance implies the capability of capturing the spatio-temporal variability in the atmospheric CO_2 mixing ratios and avoiding persistent errors from the atmospheric transport models (e.g. Gerbig et al. 2006). Although prior fluxes, uncertainty assessment and transport models are evaluative components of the system, the deployment strategy of observation sites affects the potential of the inversion indefinitely.

The design of regional atmospheric networks amounts to the optimisation of the observational constraint on the surface fluxes from the atmospheric concentrations. The atmospheric integrator effect is one part of the answer, and actual footprints of hourly tower concentration data were shown to constrain mainly the few hundreds of kilometres around each site (Lauvaux et al., 2008; Gerbig et al., 2009). Even though large-scale signals are present in the concentrations, their relative contribution being 20–40% (depending on the season) of the observed hourly variability (Miles et al., 2012), but the corresponding flux area is so large that very little information is carried by the data to constrain the flux per surface unit. In addition, CO_2 fluxes show large diurnal patterns varying from negative values during the day to positive during the night (photosynthesis and respiration), resulting in a substantial loss of information at the daily time scale (Gerbig et al., 2009). Still, regional-scale signals and redundant flux signatures in the atmospheric concentrations might inform us about larger flux balances, depending on the site location and the strength of the local fluxes.

Previous studies have demonstrated the relative contribution of the near-field fluxes in the hourly atmospheric observations using a limited number of observation sites deployed over short periods of time (Lauvaux et al., 2009). Other studies have used similar modelling tools at coarser resolution but for non-CO_2 trace gases, *i.e.* those not affected by diurnal cycles, and limited by the resolution to extract the high time frequency atmospheric information from the observations (Gloor et al., 2001). In addition to the use of high-frequency data, the a priori flux spatial distribution in the region of interest is the second major element. Once combined in the inverse system, both determine the potential of convergence to assess the regional carbon balance and the capability to retrieve the correct spatial flux distribution. The convergence of the system is directly related to the spatial and temporal resolutions of the aggregated fluxes. The aim is to constrain the surface fluxes which is different from observing signals from different scales in the observations. The relative contribution of one scale can limit the use of the others. A crucial element of the inverse system concerns the detection of major discrepancies in the prior fluxes. These are not detectable by any pseudo-data sensitivity study without prior knowledge of potential biases or errors in the prior fluxes. If towers are to be deployed, the design of the network is based on its ability to capture surface flux discrepancies at any place in the domain. Networks that are too sparse might have limited potential, whereas too dense networks are cost-prohibitive and harder to maintain on a long-term basis. Basically, the distance between observation sites and critical flux areas has to be determined within an inverse framework, such that atmospheric signals are strong enough to optimise the regional fluxes relatively to other contributors.

We propose here a set of tests based on previous results over the MCI area (Lauvaux et al., 2012) using different combinations of tower sites, considering their impacts on the regional flux balance and its spatial distribution. We focus on June to December 2007 which allows us to (1) evaluate the weight of the observations from each site to help constrain the regional carbon balance and its spatial distribution and (2) investigate the impact of different prior error statistics that may be used in network design studies

and evaluate our own assumptions. This step is critical before using the error reduction as a reliable estimate for network design purposes; furthermore, a large correlation length in the prior flux errors can lead to over-constrained systems (or under-estimated posterior uncertainties).

2. Methods

2.1. The campaign and the modelling tools

For this study, we used eight CO_2 mixing ratio tower sites that were deployed for the MCI experiment (Miles et al., 2012). Two towers are part of the permanent tall tower NOAA network, LEF and WBI; five sites were instrumented for the campaign, Kewanee, Round Lake, Mead, Galesville, Centerville; and the last site is the calibrated flux tower Missouri Ozarks [cf. Fig. 1(a)]. The inverse system, described in a previous study (Lauvaux et al., 2012), uses WRF-Chem meteorological fields at 10 km resolution to drive the Lagrangian Particle Dispersion Model (Uliasz, 1994) and generates the concentration footprints over the entire period of observations. The prior fluxes were simulated with the SiBcrop model, with an improved phenology for crops based on several eddy-flux sites over the MCI (Lokupitiya et al., 2009). The inverse CO_2 fluxes are at 20 km resolution over the domain at a weekly time step. We solve for two flux components (one for daytime and one for nighttime). We also solve for boundary condition concentrations from the CarbonTracker system corrected by aircraft data (Lauvaux et al., 2012). The boundary conditions are additional unknowns here but in practice act as an additional source of uncertainties, reducing the overall error reduction of the different cases equally.

2.2. Inverse methodology

The method used in the paper was described in the study of Lauvaux et al. (2012). The state vector ($\mathbf{x}$) that includes the three components described above (daytime fluxes, nighttime fluxes and boundary inflow) is obtained by the following equation:

$$\mathbf{x} = \mathbf{x}_0 + \mathbf{B}\mathbf{H}^T(\mathbf{H}\mathbf{B}\mathbf{H}^T + \mathbf{R})^{-1}(\mathbf{y} - \mathbf{H}\mathbf{x}_0) \quad (1)$$

where $\mathbf{x}$ are the unknown fluxes and the boundary conditions we invert for, $\mathbf{x}_0$ the a priori flux and boundary estimates, $\mathbf{y}$ the observations, $\mathbf{H}$ the linearised transport matrix and $\mathbf{R}$ and $\mathbf{B}$ the error covariance matrices of the observations and the a priori fluxes, respectively.

We can define the posterior error covariance matrix A for fluxes given by the following expression:

$$\mathbf{A}^{-1} = \mathbf{B}^{-1} + \mathbf{H}^T\mathbf{R}^{-1}\mathbf{H} \quad (2)$$

In the study, we perform error reduction analyses as if exploring optimal tower locations for a network design study. The error reduction is the ratio between flux error variances before and after inversion $[1 - (\sigma_A/\sigma_B)]$ with values ranging from 0 to 1, with σ_A the posterior flux root mean square error (RMSE) and σ_B the prior flux RMSE. A value of 0 indicates no improvement of the initial prior errors. Between 0 and 1, the value is interpreted as a ratio of error reduction, referred in percentage in this study.

In addition, we define prior flux error structures in two different ways: first by considering the ecosystem distribution in space and a correlation length L, and second only by the correlation length L (Lauvaux et al., 2012). The distance L remains difficult to rigorously estimate but its impact on the retrieved fluxes can be large (Wu et al., 2011). Additional tests will be performed based on our subsampled network inversions, to evaluate the impact of the flux corrections on the CO_2 concentration mismatch of the observation sites not used in the inversion.

2.3. Evaluation of the assumptions in spatial structures of the prior flux errors

2.3.1. Ratio between the observational constraint and prior flux errors. To evaluate the impact of the correlation structures on the solutions, we use the degree of freedom for the signal (DFS) from Rodgers (2000). A large (respectively, small) correlation length reduces (respectively, increases) the DFS. The DFS was defined following Bocquet (2009) as:

$$\mathrm{DFS} = \mathrm{Tr}(\mathbf{B}\mathbf{H}^T(\mathbf{H}\mathbf{B}\mathbf{H}^T + \mathbf{R})^{-1}\mathbf{H}) \quad (3)$$

The DFS is used in this study to investigate the impact of the correlation length on the solutions. Small DFS values compared to the number of observations indicates that the posterior fluxes are constrained mainly by the prior uncertainties. Large correlation lengths lead to less information brought by the observations. We discuss the DFS values in Section 4.

The variances in the prior flux errors vary slightly from one case to the next to conserve the same ratio between the observational constraint and the prior flux uncertainties. This balance was ensured by estimating the normalised distance λ of the χ^2 test as follows:

$$\lambda = \frac{1}{n}[(\mathbf{y} - \mathbf{H}\mathbf{x_0})^T(\mathbf{H}\mathbf{B}\mathbf{H}^T + \mathbf{R})^{-1}(\mathbf{y} - \mathbf{H}\mathbf{x_0})] \quad (4)$$

with n the degree of freedom of the state vector. A value close to one indicates reasonable estimates of prior errors in the inverse system, balancing the weight of the atmospheric observations and their related errors ($\mathbf{y}$ and $\mathbf{R}$) compared with the initial uncertainties in the fluxes ($\mathbf{x}_0$ and $\mathbf{B}$) and

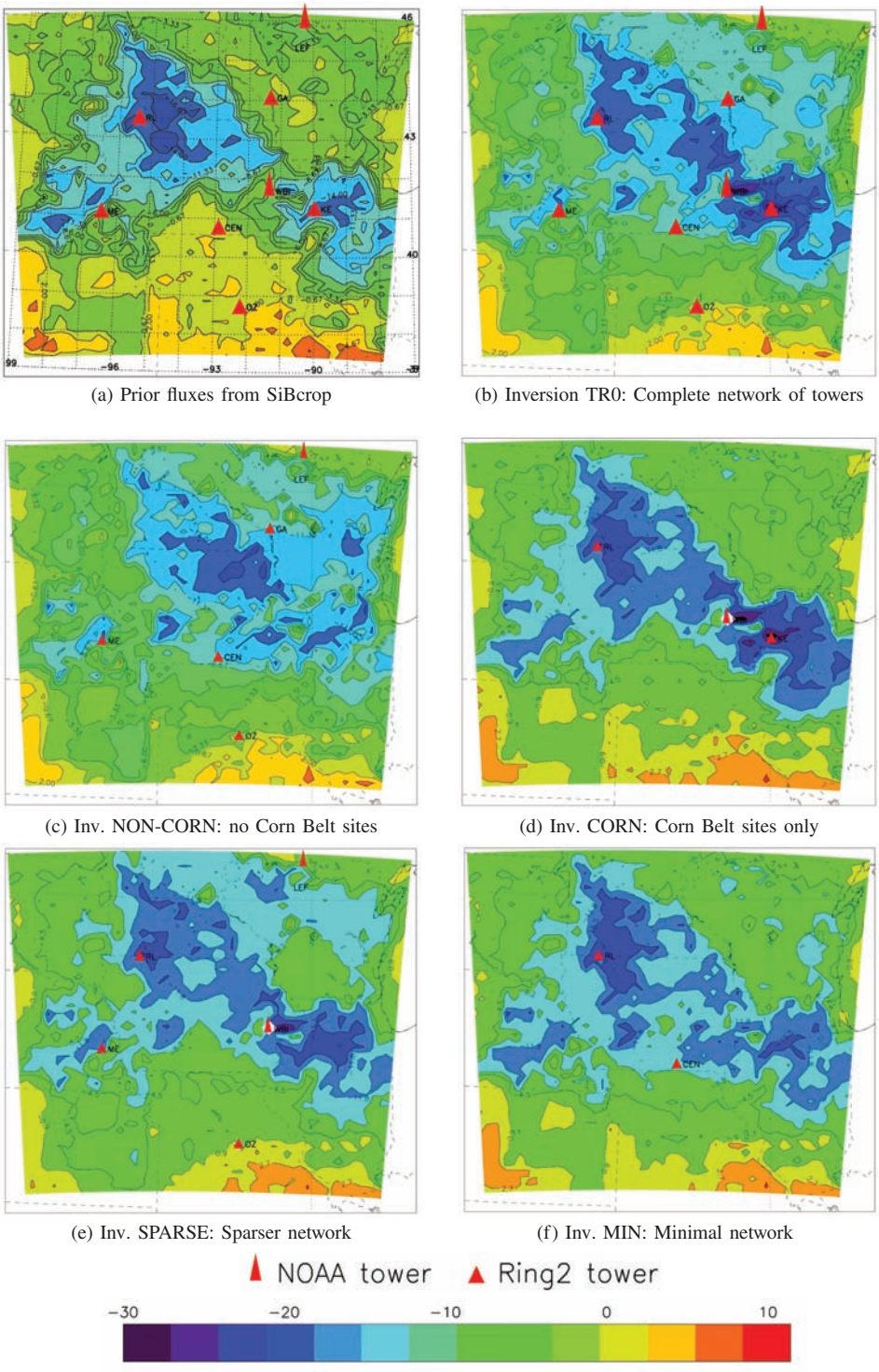

(a) Prior fluxes from SiBcrop

(b) Inversion TR0: Complete network of towers

(c) Inv. NON-CORN: no Corn Belt sites

(d) Inv. CORN: Corn Belt sites only

(e) Inv. SPARSE: Sparser network

(f) Inv. MIN: Minimal network

Fig. 1. CO_2 fluxes from June to December in TgC.degree^{-2} over the MCI from the SiBcrop vegetation model (a), our reference case TR0, i.e. the inverse system using the entire network of observation sites (b), using only the sites outside of the Corn Belt area (c), using the sites only within the Corn Belt area (d), using a sparser network (e) and using a minimal configuration of two sites (one in the Corn Belt and one out) (f).

the number of independent elements in the state vector. The values of λ range between 0.75 and 1.25 for all our tests, and the corresponding correlation lengths from 50 to 300 km, including both biome-dependent and non-biome-dependent structures. We increase (or decrease) the RMS (diagonal elements of **B**) to compensate for changes in the correlation length based on the values of lambda for each case.

2.3.2. Leave-One-Out Cross-Validation. We evaluated the gain from the inversion in terms of mixing ratio mismatch with Leave-One-Out Cross-Validation (LOOCV) tests. We performed eight consecutive inversions using seven of the eight available tower sites. The remaining site is used as a validation of the inverse fluxes. The simulated mixing ratios of the validation site are reconstructed using its influence functions and the fluxes from the corresponding 7-tower inversion. The mixing ratio mismatch at the validation site i ($\Delta_i = \mathbf{y} - \mathbf{H}\mathbf{x_j}$) is computed before ($\mathbf{x_j} = \mathbf{x_0}$) and after inversion ($\mathbf{x_j} = \mathbf{x}$). The mean of the mismatch represents the impact of the correction of weekly biases in the observation space (mixing ratios). The RMSE of hourly mismatches represents smaller-scale corrections (from hourly mixing ratios) produced by changing wind conditions at each site. These tests provide an assessment of the overall gain after inversion, gain from corrections on the weekly fluxes and in space around the validation site. Considering that most tower mixing ratio footprints do not overlap between sites, the LOOCV evaluates primarily the veracity of the spatial correlation in the prior flux errors.

3. Results

The amount of information from the observation network varies with two major elements: the spatial density of the network and the correlations of the prior flux errors. To explore these two components, first we define several subnetworks using only some of the eight available sites, and second, we assume different prior flux error structures with an evaluation of their impact.

3.1. Regional CO_2 flux balance

In this section, we diagnose the information content of the observations using different combinations of sites to constrain the regional balance. We defined four cases as follows: the first network excludes sites in the corn belt (Round Lake, West Branch and Kewanee) referred here as NON-CORN; the second case uses sites within the corn belt only (the ones precedently excluded) referred as CORN; a sparser network of observations but homogeneously distributed in space (excluding Centerville, Galesville and Kewanee) referred as SPARSE; and finally the minimum configuration with one site in the corn belt area and one for the mixed grassland-crop-forest area, Round Lake and Centerville, referred as MIN.

We present the inversion-based regional balances using the different network configurations as shown in Table 1. Table 1 underlies the capacity of the system to constrain the overall regional balance of the MCI domain and displays the averaged CO_2 fluxes over corn-dominated areas and non-corn-dominated areas to highlight the attribution of flux corrections over the domain in the two most distinct vegetated areas. Considering the MIN case, the density of the network is apparently not the main leverage to constrain the regional balance. Only two towers are used in this case, and the final balance and area averaged fluxes are close to the initial full network inversion result (about 30 TgC difference or less than 1-sigma from the posterior uncertainties). In the CORN case using three sites in the corn belt area, we observe that the correction is weaker (only -49 TgC instead of -84 TgC). The locations of the

Table 1. Regional CO_2 flux balance from June to December 2007 in TgC over the MCI (first line), and averaged fluxes over the corn-dominated area (which corresponds to 23% of the domain) and out of it in gC m^{-2}, for Sibcrop (prior fluxes), using the complete observation network (posterior or TR0), using towers around the corn belt (NON-CORN), using towers within the corn belt area (CORN), using a sparser network of towers (SPARSE), and using only two towers (MIN)

	Prior	Posterior (TR0)	NON-CORN (five sites)	CORN (three sites)	SPARSE (five sites)	MIN (two sites)
Regional carbon balance (TgC)	-110	-194	-179	-159	-185	-177
Total flux error (TgC)	35.5	32.1	32.7	33.1	32.5	33.6
Corn area averaged flux (gC m^{-2})	-335.7 ± 98.6	-343.84 ± 88.16	-280.62 ± 92.39	-372.38 ± 88.92	-328.9 ± 89.56	-336.85 ± 92.03
Out-of-corn averaged flux (gC m^{-2})	-27.3 ± 36.13	-110.71 ± 32.86	-114.49 ± 32.87	-69.56 ± 34.75	-108.23 ± 33.26	-97.75 ± 34.55

towers seem more important than the absolute number of sites. Considering the averaged fluxes over corn-dominated areas and grass-dominated areas, the complete network case (referred here as posterior) indicates a slight increase of the uptake in corn-dominated areas and an important increase elsewhere (cf. Table 1). The posterior uncertainties over the domain for the different cases vary from 5 to 10% error reduction compared to the initial uncertainties. A large fraction of the domain being unconstrained by the observations, the error reduction is relatively small for the different cases. Although most cases as can be seen in Table 1 show similar flux corrections for the corn area (between the prior and posterior values), the NON-CORN case shows here an opposite flux correction in the corn area due to the absence of observation sites. We investigate the spatial distribution of the corrections in the next section.

3.2. Spatial flux distributions

The spatial distribution of the corrections appears critical around the central Corn Belt, and the net fluxes averaged over the corn area remains similar (Table 1). The initial spatial distribution (prior flux) was centred and highly correlated with the corn-dominated area [Fig. 1(a)]. In the posterior fluxes, the sink area is extended to the South (northern Missouri) and to the North–West and North–East (South Dakota and Wisconsin) [cf. Fig. 1(b)].

With the inversion including only corn sites [Fig. 1(d)], the averaged fluxes in the non-corn-dominated areas show the smallest increase in uptake. The uptake in the north-eastern part of the domain remains low [case CORN and MIN, or (d) and (f) in Fig. 1]. In the other cases, both Galesville and LEF towers introduce an increase of the uptake [NON-CORN and SPARSE, or (c) and (e) in Fig. 1], *i.e.* extending the sink area to the North East. The most variable and important change compared to the initial setup occurs in northern Illinois where there is the largest uptake in the posterior fluxes [Fig. 1(b)]. Comparatively, the prior fluxes showed a maximum around Round Lake in northern Iowa and southern Minnesota [Fig. 1(a)]. The maximum in Illinois is present only if the Kewanee or West Branch sites are included [CORN and SPARSE, or (d) and (e) in Fig. 1]. Other cases produce the maximum of uptake in northern Iowa and southern Minnesota (MIN), or decrease the uptake but without detecting the northern Illinois area (NON-CORN). The tower sites at Centerville or Galesville are located about 300 km from northern Illinois but do not produce an increase in uptake.

3.3. Spatial distribution of flux corrections

We present the flux corrections shown in Fig. 2 to highlight the contribution of different combination of towers applied to the prior fluxes. Across the four cases, the main spatial patterns are conserved indicating consistent corrections across towers. The only case which indicates a disagreement between tower corrections is NON-CORN, with an important positive correction around Round Lake. The presence of Round Lake in the other cases induces little to no change around the tower location. Overall, the intensity of these changes is highly variable. In most cases, the large uptake around Round Lake is decreased, the NON-CORN case being the most positive correction in this area. Once again, the corrections appear only when towers are in the area of interests (*e.g.* the negative correction around Centerville in NON-CORN and MIN) or when two towers surround the area (Ozarks and WBI also decrease the Centerville area in SPARSE). The positive correction around Round Lake is produced in all cases. Otherwise, the corrections disappear if the closest tower is missing. As an illustration of the prior error correlation impact on the retrieved fluxes, the Fig. 2(b) shows the flux corrections if biome-related structures are removed from the prior errors. We will discuss this point in Section 4.

3.4. Theoretical error reduction and observed flux corrections

We now consider an experimental network design based on the error reduction only. We compare here the theoretical benefits from our system (without using observations) to the actual changes in the posterior fluxes (with observations). Because the two are basically related to the prior flux error structures, we investigate the impact of different correlation structures on the flux corrections and the error reduction. The impact of the prior fluxes themselves was investigated in the study of Lauvaux et al. (2012).

The reference setup TR0 includes all the towers in the region and flux error covariances based on ecosystems and distance ($L = 300$ km). The error covariances are based on model-data mismatch and correlation analysis using several eddy-flux sites over the domain (Lauvaux et al., 2012). As a comparison, for a similar correlation length but without considering ecosystems, the overall constraint in our system is equivalent to $L = 100$ km. The biome dependence, as defined here, reduces the initial correlation length (cf. Fig. 3). We then ran our 7-month inversion at the weekly time scale. The error reduction in Fig. 3(a) is about 30–40% in the vicinity of the towers and about 10–20% in the first 100–200 km. We then ran a second inversion (case TRD)

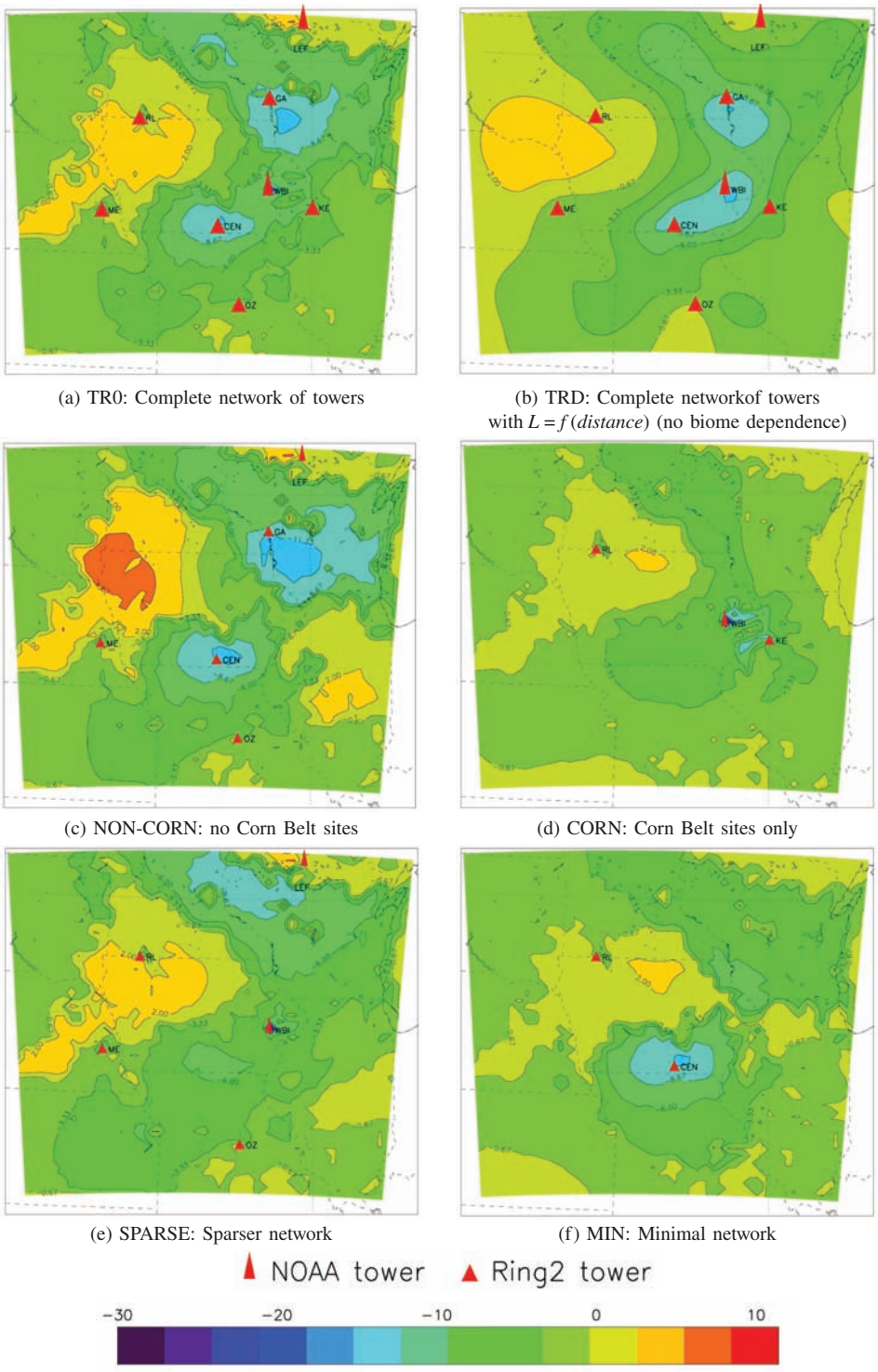

(a) TR0: Complete network of towers

(b) TRD: Complete networkof towers with $L = f(distance)$ (no biome dependence)

(c) NON-CORN: no Corn Belt sites

(d) CORN: Corn Belt sites only

(e) SPARSE: Sparser network

(f) MIN: Minimal network

Fig. 2. CO_2 flux correction from June to December in TgC.degree^{-2} over the MCI using the SiBcrop prior fluxes, with our reference case, i.e. the inverse system using the entire network of observation sites (a), with the entire network but the flux error correlation is built on an exponentially decreasing model only (b), using only the sites out of the Corn Belt area (c), using the sites only within the Corn Belt area (d), using a sparser network (e) and using a minimal configuration of two sites (one in the Corn Belt and one out) (f).

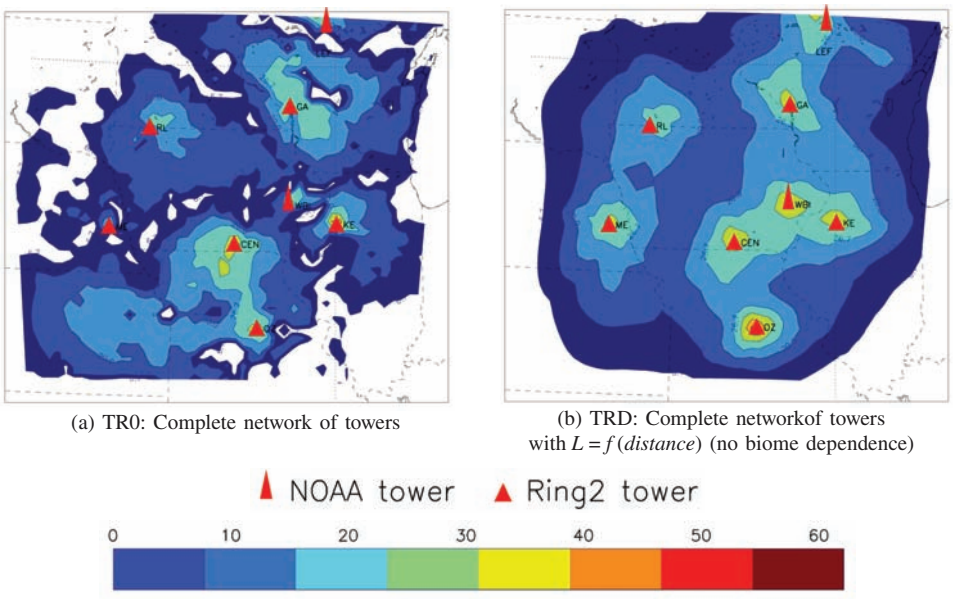

(a) TR0: Complete network of towers

(b) TRD: Complete networkof towers with $L = f(distance)$ (no biome dependence)

Fig. 3. Error reduction in % using all the towers and prior flux errors with ecosystem-based standard deviations (RMS) and spatial correlations based on ecosystems and distances between pixels (case TR0) (a) and the second case considering correlations with distance only (exponentially decaying model) (TRD) (b).

using the same standard deviations for every 20 km by 20 km pixels, but prior flux error correlations are based on the distance only, with an exponentially decaying model ($L = 300$ km). The simpler structure of the prior flux errors here induces the propagation of corrections in space from grass to corn dominated pixels for example. This assumption seems somewhat unrealistic as Net Ecosystem Exchange (NEE) for corn is driven by a different phenology and several human-driven processes such as irrigation or fertilisation. Corrections applied to corn-dominated pixels might not be applicable to grassland areas as vegetation responses and error sources might be highly variable across these ecosystems. The spatial distribution of the error reduction [Fig. 3(a) and (b)] for the two cases shows large differences. The second case (TRD) shows exponentially decreasing error reduction from the tower locations as prescribed by the error correlations.

The flux corrections from these two cases [cf. Fig. 2(a) and (b)] show clear differences even though their respective regional carbon balances remain close, with -194 TgC for the TR0 case and -179 TgC for the TRD case. Posterior uncertainties and fluxes are highly affected by the assumptions in the prior error statistics even if the main patterns remain somehow similar. The posterior flux errors for the TR0 case are about 32 TgC (with 35.5 TgC error in the prior fluxes), whereas the TRD case posterior errors are about 25.2 TgC (with an error of 30.5 TgC in the prior fluxes). The relationship between prior error structures and posterior errors and fluxes has a consequent impact on the flux errors, but little impact on the regional carbon balance (posterior fluxes). In Section 4, we investigate the observational constraint and the validity of the flux error correlation assumption by estimating the degree of freedom of the signals (DFS) (Rodgers, 2000; Bocquet, 2009) and by evaluating the flux corrections on towers that were not used in the inversion from our different cases (LOOCV).

4. Discussion

4.1. Optimal choice of prior error structures

The different inversions performed here and their interpretation are highly dependent on the prior error covariances. Wu et al. (2011) noted the impact of incorrect flux error correlations in the prior error covariance matrix. The definition of prior error structures in space remains difficult to estimate quantitatively, and several studies discussed the estimation of the potential correlations using different techniques. Although geostatistical approaches propose to diagnose these structures from different observational datasets (Michalak et al., 2005), other inverse studies have optimised these distances based on correlation analysis of biogeochemical models (Rödenbeck et al., 2003; Chevallier et al., 2006) or derived them from climatological and ecological considerations (Peters et al., 2007). At large scale, the ill-conditioning of the inverse problem leads to significantly long spatial flux error correlations in order to keep a sufficient observational constraint. Here, a large

number of observations and the relatively short distances between sites tend to rapidly reduce the DFS and lead to the convergence of the solutions. The estimation of flux error correlations, if they exist, is required to obtain precise estimates of the a posteriori flux errors. We performed several tests using only a subsample of the complete network, with several observation sites available for a cross-validation of the corrections. We considered here the case CORN, using only Round Lake, West Branch and Kewanee sites, the other five being used as independent observations to evaluate the flux corrections. We define three cases with different correlation structures, the first one using a correlation length of 300 km, exponentially decaying with the distance, and combined with the biome map of the region (Lauvaux et al., 2012) (referred here as TR0), then a second case using correlation length of 300 km only (TRD) and finally a third case with a correlation length of 50 km (L_{50}). We estimated the gain in terms of the final CO_2 concentration mismatch compared to the initial (a priori) model-data mismatch at the five remaining towers, in ppm. Over the 28 periods of inversions from June to December, the gain for the cases TR0 or TRD improves the initial mismatch by 0.823 and 0.861 ppm, respectively, compared to the case L_{50} with only 0.561 ppm. On average, the simpler exponentially decaying model (=TRD) shows a larger gain compared to the more complex vegetation-based description TR0, but 4 of the 28 periods show small net degradations of the initial mismatch, against two for the TR0 case. Similarly, the DFS drops from 284 for the case L_{50}, and 281 for the TR0 case, down to 59 for the case TRD, indicating an important increase of the apparent observational constraint due to the correlation length in the flux errors. This first analysis shows that the larger flux correlations of 300 km seems the most profitable assumption in terms of gain. But the presence of degradation of several periods (4 out of 28) indicates that more refinement is required, including temporal variability for example. The gain increasing with the correlation length might also correspond to the overall decrease of the regional flux bias. This overall gain remains valid at the regional scale, but the inherited structures in space in the posterior fluxes might be artificial, constrained by the assumed correlation length more than the data and their adjoint transport.

4.2. *Cross-validation of posterior fluxes*

We performed LOOCVs to evaluate the gain at each tower in terms of the CO_2 concentration mismatch. The principle of cross-validation relies on eight inversions using seven towers only out of the eight available concentration sites. The retrieved fluxes are then propagated through the influence function of the validation tower. The improvement in the concentration mismatch at the eliminated tower is a direct evaluation of the posterior fluxes. We computed both RMSEs and means for each of the inversions with a different validation tower. This analysis evaluates the assumptions made in the prior flux errors (spatial correlation) in terms of systematic error corrections and sub-weekly corrections (RMSE). The results are presented in Table 2. The means show that all the inversions, but one provides smaller mismatch at the validation tower. We conclude here that the inversion improved the fluxes in terms of systematic errors at the weekly timescale. In terms of RMSE, the results indicate no or little decrease in the concentration mismatch compared to the reference inversion (using the eight concentration towers), with an increase of the mismatch in three cases. The absence of

Table 2. Mixing ratio residuals in ppm for each tower, averaged over the 7 months (mean) and their related RMSE at the hourly time scale before and after inversion. The three lines correspond to the initial mismatch between modelled and observed mixing ratios (a priori), posterior residuals after inversion using the eight towers (a posteriori) and residuals from each inversion excluding the tower indicated in the first line, used for validation (LOOCV)

	Centerville	Kewanee	Round Lake	Mead	Galesville	Missouri	WBI	LEF
A priori								
Mean	−1.708	−1.248	−0.583	−1.025	−1.912	−0.578	−1.203	−0.167
RMSE	7.641	7.169	7.284	6.858	7.970	7.884	8.341	6.786
A posteriori								
Mean	−0.103	−0.028	−0.104	−0.074	−0.162	0.102	0.467	0.171
RMSE	3.711	3.757	3.638	3.511	4.244	4.067	4.269	3.837
LOOCV								
Mean	−1.045	−0.283	−0.613	−0.883	−1.371	−0.119	0.235	0.865
RMSE	7.003	7.564	7.479	6.794	7.602	7.727	7.656	7.848

Residuals in LOOCV correspond to cross-validation of the inverse fluxes retrieved from the Leave-One-Out experiments. Values closer to zero compared with the a priori mismatch indicate an improvement.

improvement in the RMSE shows that the subweekly variability due to smaller-scale flux signals is not captured correctly compared to the reference inversion. The spatial error correlation might be over-estimated in our setup, even though the regional balance with fewer towers is consistent with previous findings. The small structures in the flux corrections are not realistic at the validation tower. The extent of corrections in space is artificial and only helps to improve larger-scale systematic errors. However, the two inversions without WBI or Kewanee show almost identical improvements compared to the reference inversion in terms of means of the mismatch. The redundancy of the information from these two towers is in agreement with earlier findings, co-located in the corn belt area.

4.3. *Estimation of prior error structures*

From our analysis, we can disaggregate two correction terms from the flux correction, one due to local atmospheric signals, and one induced by the presence of spatial correlations in the prior flux errors. The second seems consistent following our previous tests. Even if not perfect, long correlation lengths ($L \sim 300$ km) showed an improvement compared to the initial CO_2 concentration mismatch, and better results than smaller correlation lengths ($L \sim 50$ km). For the first term, the simulated atmospheric mixing drives primarily the size of the main area of influence on the concentrations. The model resolution might affect the dimensions of the concentration footprints noting that horizontal diffusion is related to model parameterisation optimised at given resolutions. Comparisons are needed to explore the sensitivity of the footprint size to the model configuration. Although the two terms might seem contradictory, they reflect two different facts. The first term represents directly observed flux signals in the atmospheric concentrations. The second term represents the common sources of errors in the fluxes. This term is problematic in the sense that corrections are distributed spatially, even though the observations alone were not able to constrain these areas initially. Chevallier et al. (2006) investigated the presence of flux error correlations using eddy-flux sites, at a daily time scale. The temporal scale of this study was shorter than the present pixel-based inversion at the weekly time scale. They found no clear spatial structures in the prior flux errors. Hilton (2011) optimised parameters of a vegetation model with 100 eddy-covariance NEE measurement sites across North America and diagnosed the covariances in the residuals. The most likely correlation length was about 400 km at the monthly time scale and 200 km at the 10-day time scale. Before that, Rödenbeck et al. (2003) performed model sensitivity tests at the monthly time scale and diagnosed correlation lengths of about 1200 km. Michalak et al. (2005) proposed the use of the Maximum Likelihood algorithm to derive prior flux error correlations based upon observations which were a direct result of those fluxes. While the method is very informative for the modellers to evaluate the balance of the inverse system, the reality of flux error correlations has to be investigated, not only to fit the inverse setup because of other limiting factors (model resolution, number of observations, dimension of the matrices to invert), but also to represent the real structures of the prior flux errors.

5. Conclusions

We have evaluated here the CO_2 posterior fluxes over the corn belt of the US Midwest by subsampling the MCI tower network. Atmospheric inversions at 20-km resolution were performed for a 7-month period, with similar assumptions but variable observational constraints. These sensitivity tests correspond to different network configuration, including a sparser network of observations or ecosystem-specific networks. The four different subsampled networks showed consistent regional carbon balances despite tower removals (–178 TgC $\pm$ 13). The DFS showed that the posterior fluxes are constrained mainly by flux error correlation when the correlation length is larger than 150 km. The gain in the final concentration mismatch indicates an improvement of the overall regional fluxes with large correlation length (300 km or more) but might correspond to artificial extension of the regional bias correction rather than realistic spatial structures in the posterior fluxes. This preliminary study shows that the MCI campaign provides a sufficient number of observations to constrain the Corn Belt carbon balance over the 7-month period, but the spatial distribution of the inverse fluxes is still under-constrained with too little observational constraint compared to the assumed flux error structures.

6. Acknowledgements

We thank Arlyn Andrews from NOAA/ESRL for providing the data from the West Branch tall tower site (WBI) and the WLEF tower (LEF). We thank Peter J. Rayner for fruitful discussions. This work was supported by the Office of Science (BER) US Department of Energy, Terrestrial Carbon Program, the US National Aeronautics and Space Administration's Terrestrial Ecology Program, the US National Oceanographic and Atmospheric Administration, Office of Global Programs and Global Carbon Cycle Program.

References

Bocquet, M. 2009. Towards optimal choices of control space representation for geophysical data assimilation. *Mon. Weather Rev.* **137**, 2331–2348. Online at: http://journals.ametsoc.org/doi/abs/10.1175/2009MWR2789.1

Canadell, J. G., Le Quéré, C., Raupach, M. R., Field, C. B., Buitenhuis, E. T. and co-authors. 2007. Contributions to accelerating atmospheric CO_2 growth from economic activity, carbon intensity, and efficiency of natural sinks. *Proc. Natl Acad. Sci.* **104**(47), 18866–18870. DOI: 10.1073/pnas.0702737104. Online at: http://www.pnas.org/content/104/47/18866.abstract

Chevallier, F., Viovy, N., Reichstein, M. and Ciais, P. 2006. On the assignment of prior errors in Bayesian inversions of CO_2 surface fluxes. *Geophys. Res. Lett.* **33**, L13802. DOI: 10.1029/2006GL026496. Online at: http://www.agu.org/pubs/crossref/2006/2006GL026496.shtml

Ciais, P., Rayner, P., Chevallier, F., Bousquet, P., Logan, M. and co-authors. 2010. Atmospheric inversions for estimating CO_2 fluxes: methods and perspectives. *Clim. Change* **103**(1/2), 69–92. DOI: 10.1007/s10584-010-9909-3. Online at: http://www.springerlink.com/content/pnk685jh102375r0/

Gerbig, C., Dolman, A. J. and Heimann, M. 2009. On observational and modelling strategies targeted at regional carbon exchange over continents. *Biogeosciences* **6**(10), 1949–1956. DOI: 10.5194/bg-6-1949-2009. Online at: http://www.biogeosciences.net/6/1949/2009/

Gerbig, C., Lin, J. C., Munger, J. W. and Wofsy, S. C. 2006. What can tracer observations in the continental boundary layer tell us about surface-atmosphere fluxes? *Atmos. Chem. Phys.* **6**(2), 539–554. DOI: 10.5194/acp-6-539-2006. Online at: http://www.atmos-chem-phys.net/6/539/2006/acp-6-539-2006.html

Gloor, M., Bakwin, P., Hurst, D., Lock, L., Draxler, R. and co-authors. 2001. What is the concentration footprint of a tall tower? *J. Geophys. Res.* **106**, 17831–17840.

Göckede, M., Michalak, A. M., Vickers, D., Turner, D. P. and Law, B. E. 2010a. Atmospheric inverse modeling to constrain regional scale CO_2 budgets at high spatial and temporal resolution. *J. Geophys. Res.* **115**, D15113. DOI: 10.1029/2009JD012257. Online at: http://www.agu.org/pubs/crossref/2010/2009JD012257.shtml

Göckede, M., Turner, D. P., Michalak, A. M., Vickers, D. and Law, B. E. 2010b. Sensitivity of a subregional scale atmospheric inverse CO_2 modeling framework to boundary conditions. *J. Geophys. Res.* **115**, D24112. DOI: 10.1029/2010JD014443. Online at: http://www.agu.org/pubs/crossref/2010/2010JD014443.shtml

Gurney, K. R., Mendoza, D., Zhou, Y., Fischer, M., Miller, C. and co-authors. 2009. High resolution fossil fuel combustion CO_2 emission fluxes for the United States. *Environ. Sci. Technol.* **43**(14), 5535–5541. Online at: http://pubs.acs.org/doi/abs/10.1021/es900806c

Hilton, T. W. 2011. *Spatial Structure in North American Terrestrial Biological Carbon Fluxes and Model Errors Evaluated with a Simple Land Surface Model*. PhD Dissertation. The Pennsylvania State University. Online at: http://etda.libraries.psu.edu/

Keenan, T. F., Baker, I., Barr, A., Ciais, P., Davis, K. and co-authors. 2012. Terrestrial biosphere model performance for inter-annual variability of land-atmosphere CO_2 exchange. *Glob. Change Biol.* **18**(6), 1971–1987. DOI: 10.1111/j.1365-2486.2012.02678.x.

Knorr, W. and Heimann, M. 2001. Uncertainties in global terrestrial biosphere modeling, part II: global constraints for a process-based vegetation model. *Glob. Biogeochem. Cycl.* **15**, 227–246. Online at: http://www.agu.org/pubs/crossref/2001/1998GB001060.shtml

Lauvaux, T., Gioli, B., Sarrat, C., Rayner, P. J., Ciais, P. and co-authors. 2009. Bridging the gap between atmospheric concentrations and local ecosystem measurements. *Geophys. Res. Lett.* **36**, L19809. DOI: 10.1029/2009GL039574. Online at: http://www.agu.org/pubs/crossref/2009/2009GL039574.shtml

Lauvaux, T., Schuh, A. E., Uliasz, M., Richardson, S., Miles, N. and co-authors. 2012. Constraining the CO_2 budget balance of the corn belt: exploring uncertainties from the assumptions in a mesoscale inverse system. *Atmos. Chem. Phys.* **12**, 337–354. DOI: 10.5194/acp-12-337-2012. Online at: http://www.atmos-chem-phys.net/12/337/2012/acp-12-337-2012.html

Lauvaux, T., Uliasz, M., Sarrat, C., Chevallier, F., Bousquet, P. and co-authors. 2008. Mesoscale inversion: first results from the Ceres campaign with synthetic data. *Atmos. Chem. Phys.* **8**(13), 3459–3471. DOI: 10.5194/acp-8-3459-2008. Online at: http://www.atmos-chem-phys.net/8/3459/2008/

LeQuéré, C., Raupack, M. R., Canadell, J., Marland, G., Bopp, L. and co-authors. 2009. Trends in the sources and sinks of carbon dioxide. *Nat. Geosci.* **2**, 831–836. DOI: 10.1038/ngeo689. Online at: http://www.nature.com/ngeo/journal/v2/n12/abs/ngeo689.html

Lokupitiya, E., Denning, S., Paustian, K., Baker, I., Schaefer, K. and co-authors. 2009. Incorporation of crop phenology in Simple Biosphere Model (SiBcrop) to improve land-atmosphere carbon exchanges from croplands. *Biogeosciences* **6**, 969–986. DOI: 10.5194/bg-6-969-2009. Online at: http://www.biogeosciences.net/6/969/2009/

Michalak, A. M., Hirsch, A., Bruhwiler, L., Gurney, K. R., Peters, W. and co-authors. 2005. Maximum likelihood estimation of covariance parameters for Bayesian atmospheric trace gas surface flux inversions. *J. Geophys. Res.* **110**, D24107. DOI: 10.1029/2005JD005970. Online at: http://www.agu.org/pubs/crossref/2005/2005JD005970.shtml

Miles, N. L., Richardson, S. J., Davis, K. J., Lauvaux, T., Andrews, A. E. and co-authors. 2012. Large amplitude spatial and temporal gradients in atmospheric boundary layer CO_2 mole fractions detected with a tower-based network in the U.S. upper midwest. *J. Geophys. Res.* **117**(B), G01019. DOI: 10.1029/2011JG001781. Online at: http://www.agu.org/pubs/crossref/2012/2011JG001781.shtml

Ogle, S., Breidt, F., Easter, M., William, S., Killian, K. and Paustian, K. 2010. Scale and uncertainty in modeled soil organic carbon stock changes for us croplands using a process-based model. *Glob. Change Biol.* **16**, 810–822. DOI: 10.111/j.1365-2486.2009.01951.x. Online at: http://onlinelibrary.wiley.com/doi/10.1111/j.1365-2486.2009.01951.x/abstract

Peters, W., Jacobson, A. R., Sweeney, C., Andrews, A. E., Conway, T. J. and co-authors. 2007. An atmospheric perspective

on North American carbon dioxide exchange: CarbonTracker. *Proc. Natl Acad. Sci.* **104**(48), 18925–18930. DOI: 10.1073/pnas.0708986104. Online at: http://www.pnas.org/content/104/48/18925.abstract

Raupach, M. R., LeQuéré, C. and Heimann, M. 2008. Anthropogenic and biophysical contributions to increasing atmospheric co_2 growth rate and airborne fraction. *Biogeosciences* **5**, 1601–1613. DOI: 10.5194/bg-5-1601-2008. Online at: http://www.biogeosciences.net/5/1601/2008/bg-5-1601-2008.html

Ricciuto, D., King, A., Dragoni, D. and Post, W. 2011. Parameter and prediction uncertainty in an optimized terrestrial carbon cycle model: effects of constraining variables and data record length. *J. Geophys. Res.* **116**, G01033. Online at: http://www.agu.org/pubs/crossref/2011/2010JG001400.shtml

Rödenbeck, C., Houweling, S., Gloor, M. and Heimann, M. 2003. Time-dependent atmospheric CO_2 inversions based on interannually varying tracer transport. *Tellus B* **55**(2), 488–497.

Rodgers, C. D. 2000. *Inverse Methods for Atmospheric Sounding: Theory and Practice*. World Scientific, Singapore.

Schuh, A. E., Denning, A. S., Corbin, K. D., Baker, I. T., Uliasz, M. and co-authors. 2010. A regional high-resolution carbon flux inversion of North America for 2004. *Biogeosciences* **7**(5), 1625–1644. DOI: 10.5194/bg-7-1625-2010. Online at: http://www.biogeosciences.net/7/1625/2010/

Schwalm, C. R., Williams, W. A., Schaefer, K., Anderson, R., Arain, M. A. and co-authors. 2010. A model-data intercomparison of CO_2 exchange across North America: results from the North American carbon program site synthesis. *J. Geophys. Res.* **115**, G00H05. DOI: 10.1029/2009JG001229. Online at: http://www.agu.org/pubs/crossref/2010/2009JG001229.shtml

Uliasz, M. 1994. Lagrangian particle modeling in mesoscale applications. In: *Environmental Modelling II* (ed. P. Zanetti). Computational Mechanics Publications, Southampton, pp. 71–102.

Wang, Y. P., Leuning, R., Cleugh, H. and Coppin, P. A. 2001. Parameter estimation in surface exchange models using nonlinear inversion: how many parameters can we estimate and which measurements are most useful? *Glob. Change Biol.* **7**, 495–510. Online at: http://onlinelibrary.wiley.com/doi/10.1046/j.1365-2486.2001.00434.x/abstract

West, T. O., Bandaru, V., Brandt, C. C., Schuh, A. E. and Ogle, S. M. 2011. Regional uptake and release of crop carbon in the United States. *Biogeosciences* **8**, 631–654. Online at: http://www.biogeosciences.net/8/2037/2011/bg-8-2037-2011.html

Wu, L., Bocquet, M., Lauvaux, T., Chevallier, F., Rayner, P. and Davis, K. 2011. Optimal representation of source-sink fluxes for mesoscale carbon dioxide inversion with synthetic data. *J. Geophys. Res.* **116**, D21304. Online at: http://www.agu.org/pubs/crossref/2011/2011JD016198.shtml

Evaluating atmospheric CO_2 inversions at multiple scales over a highly-inventoried agricultural landscape.

Andrew E. Schuh
Dept of Atmospheric Sciences, Colorado State University, Fort Collins, CO, U.S.
Natural Resources Ecology Lab., Colorado State University, Fort Collins, CO, U.S.

Thomas Lauvaux
Dept of Meteorology, Pennsylvania State University, University Park, PA, U.S.

Tris West
Joint Global Change Research Institute, College Park, MD, U.S.

A. Scott Denning
Dept of Atmospheric Sciences, Colorado State University, Fort Collins, CO, U.S.

Kenneth J. Davis
Dept of Meteorology, Pennsylvania State University, University Park, PA, U.S.

Natasha Miles
Dept of Meteorology, Pennsylvania State University, University Park, PA, U.S.

Scott Richardson
Dept of Meteorology, Pennsylvania State University, University Park, PA, U.S.

Marek Uliasz
Dept of Atmospheric Sciences, Colorado State University, Fort Collins, CO, U.S.

Erandi Lokupitiya
Dept of Atmospheric Sciences, Colorado State University, Fort Collins, CO, U.S.

Daniel Cooley
Dept of Statistics, Colorado State University, Fort Collins, CO, U.S.

Arlyn Andrews
NOAA-ESRL, Boulder, CO, U.S.

Stephen Ogle
Natural Resources Ecology Lab., Colorado State University, Fort Collins, CO, U.S.

Short title: PREDICTING CO_2 FLUX OVER THE MIDWESTERN U.S.

Abstract. An intensive regional research campaign was conducted by the North American Carbon Program (NACP) in 2005 to study the carbon cycle of the highly productive agricultural regions of the Midwestern United States. Forty-five different associated projects were spawned across five U.S. agencies over the course of nearly a decade involving hundreds of researchers. The primary objective of the project was to investigate the ability of atmospheric inversion techniques to use highly calibrated CO_2 mixing ratio data to estimate CO_2 exchange over the major croplands of the U.S. Statistics from densely monitored crop production, consisting primarily corn and soybeans, provided the backbone of a well studied "bottom up" flux estimate that was used to evaluate the atmospheric inversion results. Three different inversion systems, representing spatial scales varying from high resolution mesoscale, to continental, to global, coupled to different transport models and optimization techniques were compared to the "bottom up" inventory estimates. The mean annual CO_2-C sink for 2007 from the inversion systems ranged from 120 TgC to 170 TgC, when viewed across a wide variety of inversion setups, with the "best" point estimates ranging from 145 TgC to 155 TgC. Inversion-based mean C sink estimates were generally slightly stronger, but statistically indistinguishable, from the inventory estimate whose mean C sink was 135 TgC. The inversion results showed temporal correlations at seasonal lengths while week to week correlations remained low. While the comparisons in this paper show that the MCI region-wide C sink is robust across inversion system and spatial scale, significant differences in inversion-based flux estimates remain at finer spatial scales of 100km - 200km. Furthermore, we present comparisons between atmospheric transport fields for the two regional inversions and show that it is critical that regional inversion systems must carefully account for biases in the boundary inflow of CO_2.

Introduction

For over half a century, the analysis of trace gases in the atmosphere has been a rich source of information about the contemporary global carbon cycle. Early studies of the secular trend and seasonal cycles of CO_2 mixing ratio revealed the accumulation of fossil carbon and the striking role of terrestrial ecosystems in planetary metabolism, and by the mid-1960s scientists had used spatial patterns in CO_2 and its isotopic composition to establish rates of atmospheric mixing [Bolin & Erickson, 1959; Bolin & Keeling, 1963], the penetration of anthropogenic CO_2 into the oceans, and the existence of a net sink in the terrestrial biosphere [Bolin & Keeling, 1963]. Beginning in the 1980s, the global network of sampling stations from which accurate CO_2 measurements were available expanded rapidly with accurate CO_2 measurements to support carbon cycle research. Denser data allowed formal estimation of the spatial patterns of sources and sinks at continental and ocean basin scale using inverse modeling, which also required quantitative accounting for atmospheric transport [Pearman & Hyson, 1981; Fung *et al.*, 1987; Heimann & Keeling, 1986; Tans *et al.*, 1990]. A community of global CO_2 inverse modelers emerged during the 1990s and performed a series of atmospheric transport intercomparison (TransCom) experiments. TransCom documented the sensitivity of estimated source/sink patterns to differences in advection, turbulence, and cloud transport among atmospheric models [Law & Simmonds, 1996; Denning *et al.*, 1999; Gurney *et al.*, 2002; Baker *et al.*, 2006].

Despite decades of measurements, modeling, and field experiments, future interactions between the carbon cycle, climate, and management now constitute a leading source of uncertainty in projections of 21st century climate change. Experiments with fully coupled carbon cycle-climate models show a range of over 250 ppm in CO2 by 2100 given identical fossil fuel emissions [Friedlingstein *et al.*, 2006; Solomon *et al.*, 2007]. Estimation of space/time variations of carbon sources and sinks by transport inversion provide an important constraint on coupled Earth system prediction. Tracking

interannual variations in carbon sources sinks using transport inversion of atmospheric observation has become nearly routine in the 21st Century [Peters *et al.*, 2007, 2010]. However, the relatively sparse data still requires aggressive regularization through the use of Bayesian priors [Baker *et al.*, 2006], geospatial smoothing [Michalak *et al.*, 2004], or pre-aggregation of sources and sinks into coarse basis functions within which space/time patterns of flux are assumed to be known [Peters *et al.*, 2007].

Although Bayesian inverse methods provide estimates of uncertainty, formal evaluation of the accuracy of regional sources and sinks has remained elusive, because we lack reliable independent measurements of these quantities. Surface exchanges of CO2 can be estimated locally by eddy covariance [Baldocchi *et al.*, 2012], but the area represented by these estimates is many orders of magnitude smaller than can be estimated from available concentration data. Field experiments during which greatly enhanced data collection is performed temporarily over a limited region and time period has provide opportunities to evaluate transport inversions (RECAB: [Filippi *et al.*, 2003], ChEAS: http://cheas.psu.edu/ [Chen *et al.*, 2008], LBA: http://daac.ornl.gov/LBA/lba.shtml, COBRA: [Gerbig *et al.*, 2003], CERES: [Dolman *et al.*, 2006], ORCA: [Goeckede *et al.*, 2010a]). Even for such limited regions, local bottom-up fluxes (estimated from surface data) must be interpolated across orders of magnitude of spatial scales to provide a quantitative constraint on top-down fluxes (estimated from atmosphere measurements). Evaluation of regional inversions using bottom-up interpolation can also be informed by studies using synthetic observations [Gerbig *et al.*, 2003; Lin *et al.*, 2003; Zupanski *et al.*, 2007; Schuh *et al.*, 2009; Lauvaux *et al.*, 2009]. These studies have shown that regional inversions always involve a trade-off between the stronger flux constraint due to dense atmospheric observations and the weaker constraint because of the influence of unknown tracer fluxes at the lateral boundaries. It is also possible to formally estimate lateral boundary fluxes as well as surface fluxes [Lauvaux *et al.*, 2008], but this necessarily dilutes the information

content of the observations. The influence of lateral boundary fluxes increases as fluxes are estimated over smaller domains. Even over small regional domains with dense measurements, the inverse problem must be regularized by applying aggregation of some kind to reduce the number of estimated fluxes. Advances have also been made in formally combining available estimates from both inventory and inversion studies into a single estimate of the kind often needed by policy makers [Cooley *et al.*, 2012].

As part of the North American Carbon Program [Wofsy & Harriss, 2002; Denning, 2005], a field experiment was designed to evaluate innovative methods for CO2 flux inversion and data assimilation by performing quantitative comparison of top-down and bottom-up estimates of a regional carbon budget. The experiment was performed over a relatively flat, heavily managed landscape in the mid-continent region of North America [Ogle *et al.*, 2006] Detailed information on surface carbon fluxes was analyzed to provide highly resolved maps of uptake and release of CO2 by agriculture, forests, fossil fuel combustion, and human respiration [West *et al.*, 2011]. Surface fluxes over croplands were estimated by eddy covariance [Verma *et al.*, 2005]. Atmospheric CO2 concentration was measured using in-situ analyzers installed on a ring of communication towers in the region [Miles *et al.*, 2012], and vertical profiles of CO2 were measured by a short dense aircraft sampling campaign [Martins *et al.*, 2009].

This paper presents an intercomparison of three estimates of regional carbon balance over the area of the NACP mid-continent intensive (MCI) experiment, and an evaluation of their respective accuracy relative to bottom-up flux maps. The three inverse analyses presented span a range of spatial domains from global to regional, and also a range of resolutions and different techniques for regularization. Comparing their results allows us to explore, for the first time, the strengths and weaknesses of many methodological choices in regional carbon analysis for a field experiment in which we have uniquely detailed independent data.

Figure 1.

Materials and Methods

Inversions

Most inversions use the same basic principles and structure that includes observations, a priori estimates for CO_2 fluxes, and a mapping from fluxes to observations based upon an atmospheric transport model. For those unfamiliar with the technique, it is best to initially think of the method as being built upon a standard regression problem with a vector $\mathbf{y}$ of observations, vector β of regression coefficients, and H matrix which presents the sensitivity of a particular observation to all possibly surface fluxes being considered. There is a rich literature on the subject and several applications to CO_2 fluxes [Tarantola, 1987; Evensen, 1994; Enting *et al.*, 1994; Bishop *et al.*, 2001; Whitaker & Hamill, 2002; Tippett *et al.*, 2003; Zupanski, 2005; Peters *et al.*, 2007; Lokupitiya *et al.*, 2008]. A simplified flowchart of the atmospheric inversion technique is provided in Figure 2. The goal of all three inversions is to provide time-varying mean and covariance estimates for a set of spatial carbon fluxes covering the MCI region. However, due to the scale differences among the inversions, the actual number of regions/parameters optimized by the inversions differs. Additionally, the finer resolution regional models require an estimate of the boundary CO_2 inflow into the region. Details are summarized in Table 1.

CarbonTracker The first inversion used comes from the operational NOAA data assimilation system CarbonTracker (CT)[Peters *et al.*, 2007]. This system is based on a sequential ensemble Kalman filter (EnKF) framework and provides global estimates of NEE from 2000 through 2009. The main contrast of the EnKF method with a standard regression is that the EnKF is performed in a Monte Carlo style, essentially running a regression in "sample" space. The most significant advantage to EnKF methods like those used for CT is that an explicit transport adjoint is not needed. This makes the system very well suited for operational style problems where the creation of new adjoint

models would be resource prohibitive. The CT inversion utilizes a 5 week lag filter [Bruhwiler *et al.*, 2005] to optimize weekly correction factors for NEE in a limited set of ecoregions [Olson *et al.*, 1985]. Biases at time t are related to the estimates at the previous two time steps as well as the original prior guess. Transport fields are provided by the TM5 model [Krol *et al.*, 2005], and those winds are derived from the ECMWF operational forecast model. CO_2 fluxes are transported for a maximum of 5 weeks which accommodates long-scale global transport effects. Of particular note, the optimization of NEE contrasts with the estimate of GPP and respiration fluxes (CSU) or nightly and daily fluxes (PSU).

Figure 2.

CSU inversion The "CSU" inversion technique is a weekly sequential Bayesian batch inversion, with occasional modifications to test the propagation of certain portions of the mean and/or covariance, similar to a Kalman filter but lacking a non-trivial dynamical forecast operator. The inversion domain consists of most of North America. An important contrast to the CT system is that total respiration (TRESP) and gross primary production (GPP) are simultaneously "corrected" via regression factors, β_{TRESP} and β_{GPP} applied to the a priori fluxes. The model and associated cost function, *F(x)*, for a particular week, or "cycle", are:

$$NEE(x,y,t) = \beta_{TRESP}(x,y)TRESP(x,y,t) - \beta_{GPP}(x,y)GPP_(x,y,t) \quad (1)$$

$$F(\beta) = \frac{1}{2}\left[(\beta-\beta_0)^T B^{-1}_{\beta-\beta_0}(\beta-\beta_0)+(H(\beta\cdot flux_{prior})-obs)^T R^{-1}(H(\beta\cdot flux_{prior})-obs)\right] \quad (2)$$

B and R are the associated error covariance matrices for the a priori flux corrective factors and the model/data mismatch, where β is the true but unknown correction factor on the fluxes and β_0 is the assumed correction factor, a priori. Results presented in this paper are calculated independently from cycle to cycle and thus β_0 is equal to

one and is not propagated through time like in Schuh *et al.* [2010]. H is the observation operator providing the mapping from the flux space to concentration space and *obs* is the observed CO_2 vector. The regression style approach prohibits an explicit dynamic model of the corrections because there is no dynamical model of the empirical regression coefficients, and thus any week to week propagation is performed ad-hoc.

The inversion is a "grid" based system where the a priori spatial covariance estimate plays the role of the pre-defined ecoregions used in the CT inversion. The inversion technique is very similar to that in [Schuh *et al.*, 2010] and is constructed to provide estimates over North America utilizing inflow estimates from a global inversion system (e.g. CT) as well as interpolated global CO_2 from NOAA's GlobalView (GV) product. Given that there are known seasonal and annual biases in the CarbonTracker optimized CO2 in the northern midlatitudes, we chose to run inversions with two different inflows. First we ran the inversion with both CarbonTracker optimized CO_2. Then we used an 2D (latitude and altitude) empirical CO2 product based upon the NOAA CO2 network and the GlobalView CO_2 product [GLOBALVIEW-CO2, 2010; Gourdji *et al.*, 2012] to bias correct the CarbonTracker optimized CO_2. This was done by calculating inflow estimates with both the CarbonTracker optimized CO_2 and the GlobalView 2D product and then calculating a 3-week moving average difference between the two. This moving average was then subtracted from the CarbonTracker optimized CO_2 product. The intent of this was to remove longer time scale biases while maintaining the synoptic variability which is implicitly in the CarbonTracker system.

The a priori assumptions of the inversion are based on the Simple Biosphere model (SiB), a land surface parameterization scheme originally used to compute biophysical exchanges in climate models [Sellers *et al.*, 1986],but later adapted to include ecosystem metabolism [Sellers *et al.*, 1996; Denning *et al.*, 1996]. SiB has been coupled to the Brazilian version of the Regional Atmospheric Modeling System (RAMS) [Pielke *et al.*, 1992] and used to study planetary boundary layer (PBL) scale interactions

among carbon fluxes, turbulence, and CO_2 mixing ratio [Denning *et al.*, 2003] and regional-scale controls on CO_2 variations [Nicholls *et al.*, 2004; Wang *et al.*, 2006; Corbin *et al.*, 2010; Schuh *et al.*, 2010]. Notable differences between the inversion framework here and that used in Schuh *et al.* [2010] was a stronger adherence to fully coupled atmosphere-biosphere model using 24 hour exponentially weighted nudging window for the horizontal mean winds U and V, humidity, temperature, and pressure, an update to the SiB3 biosphere model [Baker *et al.*, 2008], the use of the North American Regional Reanalysis (NARR) reanalysis products for the aforementioned nudging, and the incorporation of the SiBCROP module for estimation of corn, soy, and wheat fluxes [Lokupitiya *et al.*, 2009]. It is important to note that "interior nudging of prognostic fields" was used in contrast to a re-initialized forecast which was used in the next inversion framework (PSU). The spatial resolution of the transport (RAMS) and fluxes was 40 km by 40 km with 3 landcover patches per grid cell. The inversion domain consisted of a grid of 200 km by 200 km gridcells over most of North America with higher resolution grid of 40 km by 40 km grid cells over the MCI. A priori covariance assumptions were largely simplistic using isotropic exponential spatial covariance structures over North America with decorrelation length scales of 500 km and 1000 km.

PSU inversion The "PSU" inversion is also a sequential Bayesian batch inversion, such as the CSU inversion, but it is constructed on a 1000 km by 1000 km grid of 20 km by 20 km gridcells. Due to limitations of the rectangular model grids used in the system, "spatially summed" results will be calculated on the intersection of the PSU inversion domain and the MCI domain, which covers approximately 71% of the MCI domain. In contrast to the CSU inversion, where respiration and GPP are being estimated, daytime (06:00 LT - 18:00 LT) and nighttime fluxes (19:00 LT - 05:00 LT) are estimated in this inversion. For example, this means that the PSU inversion is estimating corrections to NEE during the day, while the CSU inversion is estimating corrections to both the respiration and GPP components of the NEE separately during

the day. The meteorology is derived from 10 km forecasts given by the WRF model with boundary conditions provided by the NARR fields. There are a few other significant differences between the CSU and PSU inversions. The first difference concerns the boundary inflow conditions for CO_2. The CSU inversion is driven by estimated marine boundary CO_2 inflow, while the PSU inversion is driven by CO_2 inflow that is estimated over the center of the North America continent. The variability in CO_2 mixing ratios over land is generally far larger than that over the ocean due to the strong diurnal and seasonal cycles of carbon exchange over the land, perturbed by synoptic actions of the atmosphere. In order to remove biases in the boundary inflow, which was estimated from CarbonTracker optimized CO_2 mixing ratio fields, aircraft data [Crevoisier *et al.*, 2010] was employed to provide weekly bias corrections to each of the four sides of the domain. The second significant difference is that the PSU inversion technique solves for "additive" corrections to the night/day fluxes as opposed to multiplicative corrections such as the CSU model. While these corrections incorporate more detail and have less dependence upon the a priori mean fluxes, they also require more ancillary information to determine accurate a priori variability that sets the bounds within which the additive corrections will be made. The model and associated cost function are:

$$NEE(x,y,t) = TRESP(x,y,t) - GPP(x,y,t) \tag{3}$$

$$F = \frac{1}{2}\left[(flux - flux_{prior})^T B^{-1}_{flux-flux_{prior}}(flux - flux_{prior}) + (H(flux) - obs)^T R^{-1}(H(flux) - obs)\right] \tag{4}$$

A priori covariance assumptions included smaller decorrelation length scales (exponential covariance) of approximately 300 km, compared to the CSU inversion which generally employed 500 km and 1000 km for results shown in this paper. The smaller decorrelation length scales of the PSU inversion were further decreased by

modeling the covariance length scale as a function of ecosystem type, resulting in equivalent isotropic decorrelation length scales of approximately 100 km. A last difference is the observational constraining of the meteorological forecast which was performed in the PSU inversion by running 4 day forecasts and utilizing the last three days which allows the first day to be utilized for PBL spinup. More details can be found in Lauvaux *et al.* [2012b].

Inventory Methods

A carbon inventory was compiled for the Midwestern region for the purpose of evaluating against the atmospheric inversion results. This assessment utilizes data on forest biomass, harvested woody products, and agricultural soil C from the US Greenhouse Gas Inventory [EPA, 2010; Ogle *et al.*, 2010], in addition to fine resolution data on fossil and biofuel CO2 emissions [Gurney *et al.*, 2009], CO2 uptake by agricultural crops and grain harvest [West *et al.*, 2011], and CO2 losses through livestock and human respiration associated with agricultural products [West *et al.*, 2011]. Uncertainties were derived from a Monte Carlo analysis of the variability of the original sources in the publications. Carbon emissions are dominated by combustion of fossil carbon, in addition to carbon uptake during crop production and export of grain from the region, and to a lesser extent from forest growth and incorporation of carbon into timber products.

Observational data

The CSU and PSU inversions both used data from a ring of 5 towers [Miles *et al.*, 2012]. These five sites were located in the MCI region of the North American Carbon Program [Ogle *et al.*, 2006] and were outfitted with Picarro cavity ring down analyzers [Crosson, 2008] that were calibrated daily and recorded mixing ratios of CO_2 every two minutes. The analyzers had related measurement errors that were approximately 0.2-0.3

ppm for the hourly average mixing ratio data used in the two inversions [Richardson *et al.*, 2012]. In addition to these data, both inversions used calibrated CO_2 data from the 40 meter Missouri Ozarks Ameriflux tower [Stephens *et al.*, 2011] at the southern edge of the domain as well as NOAA-ESRL data from the WLEF tall tower in Wisconsin at the northern end of the domain and the WBI tall tower in the center of the domain. The PSU inversion used data from 100 meters in order to be consistent with the other tower heights while the CSU inversion used the highest levels for WLEF and WBI which are 400 meters. Furthermore, the CSU inversion used data from continental *in situ* sites located in Canada (provided by Doug Worthy:EnviroCanada) and various locations around the United States (provided by Arlyn Andrews:NOAA/ESRL, Tim Griffis:UMN, and Beverly Law/Mathias Goeckede:Oregon State University). In total, the CSU inversion used 19 tower sites across North America while the PSU inversion used 8 across the MCI region.

The CT inversion is nearly real-time operational and uses global in-situ as well as flask-collected data in its flux optimization [Peters *et al.*, 2007]. An important note is that it does not use the ring of towers situated in the heart of the MCI region [Miles *et al.*, 2012]. Modified runs were performed with the data from the ring but did not significantly alter the flux estimates (personal communication Andy Jacobson) and therefore the original and publicly available flux estimates [Peters *et al.*, 2007] were used in this paper. The lack of any sensitivity of CarbonTracker to the ring data was one particular reason that mesoscale inversions were employed in this study.

Sensitivity of Flux Estimation Techniques to Transport Fields

The main sources of variations between the two mesoscale inversions should be due to (1) transport uncertainty (winds and PBL characteristics), (2) boundary CO_2 conditions, (3) inversion methodology and (4) observations (i.e. filtering). We investigated (1) and (2) in this research.

Lagrangian Transport The Lagrangian particle model LPDM[Uliasz & Pielke, 1991; Uliasz, 1993, 1994, 1996] is used by both PSU and CSU. It effectively acts as a transport adjoint by diagnosing turbulent motions in the atmosphere as a function of high time resolution fields of zonal and meridional winds, potential temperature, and turbulent kinetic energy (TKE) output from a parent mesoscale model. This allows for the creation of a Jacobian matrix representing the partial derivatives of CO_2 concentration (at a fixed location) with respect surrounding fluxes of CO_2. The details of the Lagrangian model that produces the particle movements from the parent mesoscale model can be found in Uliasz [1994] and there are many applications in the literature [Zupanski *et al.*, 2007; Lauvaux *et al.*, 2008; Schuh *et al.*, 2009, 2010; Lauvaux *et al.*, 2012b]. The time of release from the tower, backward in time, is notated the "sampling" time while the time associated with a particle's location over a flux producing location is referred to as "flux time". Particles can be integrated over the 'flux' time for fixed sampling times in order to produce a time series of expected concentration at the sampling location. The spatial map of integrated "flux" release associated with a sampling time is referred to as the influence function.

Sensitivity to variations in transport In order to investigate transport uncertainty, we constructed diagnostics of the influence functions for each tower, for each of the two mesoscale models (RAMS and WRF). The influence functions are radially integrated in order to show "influence" as a function of distance from the sampling location. In order to remove the effect of differing fluxes in the models, we run passive fluxes of 1 umol $m^{-2}sec^{-1}$ thereby normalizing the two influence functions. In order to investigate differences, we partitioned influence functions into (1) daytime and (2) nighttime. The CSU passive influence functions are partitioned using a daytime filter that consisted of excluding any particle which was over a grid cell with GPP $<$ 0.01 umol m^{-2} sec^{-1}, while the nighttime filter used particles in grid cells with GPP $>=$ 0.01 umol $m^{-2}sec^{-1}$. The PSU inversion used 06:00 LT to 18:00 LT to identify

"daytime" and 19:00 LT to 05:00 to identify "nighttime".

Climatic conditions

Our results are restricted to a single year in this paper (2007) and as a result it is important to characterize the weather in 2007 and how it may have differed from the longer term average climate. The year 2007 was the 10th warmest year for the contiguous U.S. since 1895 (NCDC). Two seasonal anomalies stand out. A record cold anomaly followed very warm early spring temperatures in the Great Plains and SouthEastern U.S. This caused extremely heavy losses to crops such as winter wheat and recently emerged corn. The record warmth earlier in the season had advanced the timing of leaf out and bloom for many fruits across the south leaving them more susceptible to damage from the cold outbreak. In addition, the severe drought and heat wave over the Southeastern U.S. was probably the most extreme U.S. weather event reported in 2007. The drought was particularly strong from mid summer through late fall over a large portion of the southeast and the associated heat wave peaked in August. Smaller more regional heat waves and droughts were also recorded in the upper midwest and Northeastern U.S. Large portions of the mountain west from California to Wyoming also recorded unusually dry conditions. In contrast to the drought in the Southeastern U.S., the MCI received above average precipitation as it often does during periods of drought in the Southeastern U.S. [Dirmeyer & Kinter, 2010].

Results

Annual Carbon Budget

The non-fossil fuel inventory data show a net carbon uptake of 135 TgC for 2007 and are shown in Figure 3 [West et al, 2010]. Sources of CO2 in the MCI domain are dominated by fossil fuel combustion (262 TgC source), in particular the city of Chicago, and sinks are dominated by harvest (and export) of grain (132 TgC sink).

Smaller sources and sinks due to feedlots, forests, other natural vegetation, and human respiration also contribute to the total. Uncertainty for the MCI as a whole is largely dominated by the harvest product while relative uncertainties, i.e. standard deviation in NEE as function of mean NEE, is largest for the FIA forest product. Using a Monte Carlo analysis based on uncertainties in each component flux, we constructed 95% confidence limits on the carbon balance (net fossil fuels) of the MCI domain which resulted in a sink of -104 to -204 TgC for 2007 (mean: -135 TgC). The results for all three inversions are statistically indistinguishable from the inventory results for the annual net carbon budget of the region (Figure 4). After correcting the regional inversions for boundary inflow, all three inversion estimates show a slightly stronger sink than the inventory (CT= -155 +/- 14 TgC, PSU= -140 +/- 16 TgC for reduced 'PSU domain', CSU= -145 +/- 29 TgC). This is remarkable considering the different modeling setups, domains, and observational constraints for each inversion. The variability in the inversion system results was influenced heavily by the a priori flux estimates, i.e. the initial range for the "best guess" NEE. The CSU inversion used independent +/- 20% standard deviations for GPP and TRESP fluxes which is equivalent to an enormous range of possible flux results. This introduces flux scenarios which seem to be well outside the range of reasonableness, for example a 20% increase in annual TRESP and 20% reduction in annual GPP, relative to a balanced biosphere would cause a C source on the order of 300 TgC, well outside of what we believe is possible in this area, a priori. In contrast, the PSU inversion used a more carefully constructed, well constrained, a priori flux covariance estimate based upon regional eddy covariance flux measurements [Lauvaux *et al.*, 2012b] which explains the large contrast in the posterior range of the estimated sink.

Figure 3.

Overall, the three different inversions produce similar spatial patterns in annual NEE compared to the inventory, with an important sink in the center of the domain corresponding roughly to the agricultural area. However, at finer scales, the location

Figure 4.

Figure 5.

of the maximum of uptake and the shape of the sink area varies substantially among the different inversions. Much of the spatial structure in the estimated maps of net annual flux is driven by the structure of the Bayesian priors and the optimization method in each inversion model. The CSU inversion shows a strong correlation to the a priori June/July/August uptake in the region, but with a weaker C sink in Illinois and a stronger C sink in western Iowa. The spatial resemblance to the inventory is likely due to the strong 500 km to 1000 km a priori decorrelation lengths used in the inversion and the strong summer time CO_2 deficit. Using a 500 km decorrelation length as an example, and noting that the width of Iowa is about 500 km, the inversion would assume that a weekly multiplicative error in GPP on one end of Iowa is correlated to an error in GPP on the other end of Iowa at a level of 0.37, a priori. Posterior correlations were reduced by about half although the reduction was different for GPP and TRESP and not isotropic, instead following the sampling gradient. There did not appear to be significant differences between using 500 km and 1000 km on the regional NEE (Table 2). The smaller a priori decorrelation length scales used in the PSU inversion, approximately five times less that those used in the CSU inversion , allowed much finer spatial corrections in the region. The PSU inversion shows a very large sink in the eastern part of the domain (northern Illinois), 20% to 30% larger than the inventory estimate in the area, as well as a stronger more diffuse sink to the northeast of the domain, an area of larger uncertainty in the inventory. In contrast, the strongest sink for the CarbonTracker inversion is located in the extreme northwest portion of the MCI. This is likely due to a strong flux in the prior for this particular area of the MCI and may be a result of inadequate crop modeling in CASA, which does not explicitly account for agricultural crops. Northern portions of the MCI have strong influences from soybeans and spring wheat but these crops don't assimilate as much carbon during the peak of summer and inventory and eddy covariance studies [Lokupitiya *et al.*, 2009] suggest that these crops contribute a weaker NEE signal than soybeans and corn.

Scatterplots of annual NEE values for the inversions versus the inventory are shown in Figure 6. Consistent with the previous comments, correlations with the inventory are higher for the CSU and PSU inversion results than the CarbonTracker results and this very likely is a function of the quality of the prior fluxes used. While the accuracy of the a priori flux estimate may reduce the amount of data needed in the inversion, it is the lack of knowledge of the prior fluxes which demonstrates the importance of densely collected CO_2 data [Lauvaux *et al.*, 2012b, a]. Although the influence of the different transport models is uncertain, it certainly appears that the different inversion results are very sensitive to the a priori flux patterns and accurate a priori flux estimates play a large role in determining correlations between posterior flux estimates and inventory results.

Figure 6.

Although not included in Figure 4, we also assessed the variability in CO_2 inflow and its effect on the PSU and CSU inversions. For the CSU inversion, this sensitivity can be viewed in Table 2 while a general discussion of the inflow uncertainty for both regional inversions is provided later.

Inversion results in time

Inventory data are available only at the annual scale and thus they can't be compared to inversion results on sub-annual scales. Nevertheless, it would seem prudent to provide a quick comparison on how the inversions differed. The time series of results for 2007 are shown in Figure 7. In the spring of 2007, the CarbonTracker estimates rarely deviate from their prior, which arises from a Carnegie-Ames-Stanford Approach (CASA) based model run with annual NEE close to zero. At locations of strong deviation, the posterior generally reduces the efflux from the prior, pushing the estimate to be in closer agreement with the results from the CSU and PSU inversions. One might hypothesize that the CT inversion does not have sufficient data to allow deviation from its prior, and when it does it effectively increases the annual sink (in the early spring).

412 One also notices much weaker temporal correlation on the scale of weeks in the CT
413 inversion compared to the CSU inversion. The PSU inversion posterior is simply the
414 prior over this period of time because data was not available from the ring of towers
415 until May 2007. The timing of the peak summer drawdown for the area seems to be
416 the same for all models, around the middle of July. The CT, PSU and CSU inversions
417 agree reasonably well on the magnitude of this drawdown. Nevertheless, there is strong
418 variability on the scale of weeks. A noticeable deviation in the CSU inversion appears
419 in mid-August and corresponds to the renewal of precipitation over portions of the MCI
420 after an extended dry spell. It is likely that the weekly a priori flux estimates from CT
421 are more variable than the rest due to somewhat crude flux downscaling from monthly
422 CASA data. **Figure 7.**

423 Results from all three estimates provide posterior NEE estimates less than (i.e.
424 stronger sink) their a priori NEE estimates for midsummer when crops are sequestering
425 the most carbon. A trend emerges during the late summer where there is a local
426 reduction in most of the sinks between mid-July and early August. The summer was
427 relatively dry over large portions of the MCI and in particular in northern Iowa and
428 southern Minnesota in which a localized drought existed from mid-July until early
429 August. These dry conditions likely caused the dramatic decrease in the C sink seen
430 in the inversions. It is possible that the corn could have been approaching maturity,
431 however, corn is usually still absorbing significant amounts of C at the start of August
432 if conditions are favorable. This theory is corroborated by a combination of CO_2 flux
433 data and soil moisture data (Figure 2, Corbin et al. 2010) as well as Long Term Palmer
434 Drought indices. The inversions agree reasonably well in the fall and winter seasons of
435 2007, although weekly differences exist particularly in the early fall.

Transport Considerations: Variations between mesoscale inversions (CSU and PSU).

Figure 8 shows the contribution from daytime passive flux releases to daytime observations for the two different models. In order to keep comparisons consistent, we subset the influence footprints to the smaller PSU transport domain. Additionally, the LEF and WBI towers were sampled at different levels (PSU: 122 meters and CSU: 400 meters) leading to inherent differences for these two towers. Despite these differences, the general strength of influence from each model was similar indicating PBL/wind speed regimes that are roughly the same. There is a noticeably stronger local influence in the near field in the PSU influence functions and somewhat stronger far-field effect in the CSU model as can be seen in the figure. It is possible that variations in the modeling of convective processes has some influence on the differences seen in Figure 8 but this will require further research to evaluate.

Figure 8.

Figure 9 shows the contribution from nighttime passive flux releases to daytime observations for the two different models. There is a noticeably stronger influence from the nocturnal fluxes in the PSU model. The PSU inversion uses data from the 99 meter level of WBI tower while the CSU inversion uses data from the 379 meter level. The stronger influence in the PSU model from particles released at a lower level, which are more likely to be trapped in the nocturnal boundary layer than those released at higher levels, likely explains the difference in the influence plots for this tower. However, other towers show similarly significant differences. The source of the differences is uncertain although likely causes are differences in surface layer mixing schemes in the two models as well as the higher near-surface vertical resolution in the PSU WRF runs. The use of lower level tower data and the associated stronger nocturnal signal in the PSU model may play a part in the stronger C drawdown estimated by the PSU inversions near tower locations seen in Figure 5. Further research into the underlying model differences and corresponding impact on near surface transport will be needed to fully explain the

differences. **Figure 9.**

Boundary Inflow Considerations.

Regional inversion results can be very sensitive to boundary conditions [Goeckede *et al.*, 2010b; Gourdji *et al.*, 2012] and thus this sensitivity was investigated in both regional inversions. Inflow boundary conditions for CO_2 for the PSU inversion were created by using flask data from routine NOAA-ESRL aircraft flights (locations shown in Figure 1) to bias correct optimized CarbonTracker CO_2. An a priori flux bias with an upper limit of around +24 TgC was possible as a result of 0.55 ppm average inflow bias, which was the average error over the optimization period of the PSU inversion [Lauvaux *et al.*, 2012b]. However, it is likely that inflow corrections using weekly vertical profile data [Crevoisier *et al.*, 2010] substantially reduced this bias. Boundary inflow sensitivity for the CSU continental inversions was tested by comparing inflows derived from CarbonTracker optimized CO_2 and the GlobalView CO_2 product. The GlobalView CO_2 product is built from the modeling and interpolation of routine NOAA flask and aircraft samples in the marine boundary layer. Globalview-based inflow conditions for the CSU inversion were then created by subtracting a 3-week moving average of the difference between CarbonTracker optimized CO_2 and Globalview CO_2, from the CarbonTracker optimized CO_2. In this fashion, the CarbonTracker synoptic variability is preserved while being "bias-corrected" by the observed data over longer time scales. The use of this bias-correction reduced the CSU sink in the MCI by approximately 33%, from 174 TgC to 117 TgC in the "online" case, while reducing the continental sink by 62% (1.6 PgC to 0.6 PgC). This is consistent with the findings of others using similar methodologies (Gourdji et al. 2011), although the posterior continental sink estimates appeared to match bottom-up inventory results more [King *et al.*, 2007].

Discussion

The MCI study region was chosen in order to take advantage of high quality a priori knowledge of crop production in the Midwest as well as large amounts of independently collected data on crop yields, and other data, by the United States Department of Agriculture [NASS, 2011; West *et al.*, 2010, 2011]. A significant advantage of the study region was the fact that this area was relatively flat and devoid of complex topography. Complex topography or landcover can make the meteorology, which is essential for inversion studies, difficult to model. In this sense, the project probably represents the best possible scenario for a CO_2 inversion study; strong, reasonably well-known CO_2 fluxes and somewhat simple meteorology.

We constructed mesoscale inversions for 2007 and compared a well-known global inversion framework as well (e.g. CarbonTracker). NEE flux estimates appear somewhat similar among inversions and are reasonable for 2007 in the sense that they are statistically consistent with the inventory. These results are promising because they show that CO_2 inversion methods can be robust, in the sense that they deliver similar inverse flux solutions which also are consistent with C inventory results, despite being constructed across very different frameworks, e.g. global to continental to regional, with very different assumptions. Nevertheless, comparisons at spatial scales finer than 100 km to 200 km and finer temporal scales on the order of weeks, illuminate that differences still exist between the various inversion systems.

The transport fields produced from the mesoscale models displayed a surprising amount of similarity. Given the very distinct ways in which the transport was created, i.e. different mesoscale models, PBL schemes, land surface models, and external forcing scales in time and space, there were relatively small differences in time-space integrated footprints for the towers in the "ring". The scope of the project only allowed for exploratory comparisons on wind speeds, PBL heights, and high time-resolution footprints. Among the differences between the transport fields that could not be

514 immediately explained, was the sensitivity to surface fluxes as a function of distance
515 from tower. The RAMS model (CSU) appeared to show weaker sensitivity in the local
516 vicinity of the tower and a stronger long-distance sensitivity than the corresponding
517 WRF model (PSU). The difference could be a byproduct of the difference between
518 the external forcings or possibly a more subtle theoretical difference between the two
519 models.

520 A significant amount of uncertainty in the inversion results appears due to
521 variability in boundary inflow of CO_2 and to a lesser degree prior flux signals. Inflow
522 corrections were performed using the GlobalView NOAA product and the NOAA weekly
523 aircraft samples as the basis of the bias correction scheme to the optimized global
524 CarbonTracker CO_2 product and significantly improved the accuracy of the inversion
525 results. This demonstrates the importance of maintaining well calibrated global CO_2
526 networks and in particular aircraft profile programs with respect to estimating regional
527 carbon budgets with CO_2 data.

528 Posterior variance estimates of CO_2 exchange continue to be one of the most
529 difficult estimates to make for inversion modelers. Variance estimates from these
530 CO_2 inversion systems are sensitive to both inversion method and a priori covariance
531 specifications. For example, posterior covariance from EnKF methods such as used for
532 CarbonTracker are strongly dependent upon the particular EnKF algorithm [Tippett
533 *et al.*, 2003]. Shortages of ancillary information on NEE, such as spatially dense eddy
534 covariance observations or temporally and spatially rich biomass accumulation statistics
535 often necessitate "broad" a priori covariance structures be used in inversion systems.
536 While inversion modelers can attempt to control for portions of this uncertainty, i.e.
537 model methodology, other portions such as ancillary data to constrain the fluxes a priori
538 are generally outside of their control. Nevertheless, results from this paper showed that
539 quite good agreement can result from two inversions (CSU and PSU) where significantly
540 difference a priori flux uncertainties, as well as system and method, were used.

In summary, we have brought together three different inversion techniques, driven by different meteorology and somewhat different a priori assumptions, available at three commonly employed scales (global, continental and regional). Regional flux estimates from each of the three frameworks agreed well with the estimates provided by the inventory data. We consider this a first step towards ascertaining feasibility of the CO_2 inversion method to produce regional carbon flux estimates as would be done under a monitoring program. Moreover, this study shows that atmospheric inversions are capable of capturing regional CO_2 flux estimates at sub-national scales, scales which will be useful for future carbon-cycle research and regional greenhouse gas initiatives. The most critical next steps are to further refine the inversion frameworks to better quantify boundary inflow uncertainty, sensitivity to a prior flux estimates, and provide explicit characterizations of transport variability as well as leverage the most recent and comprehensive sources of data on CO_2.

Acknowledgments. Andrew Schuh and Thomas Lauvaux performed the biospheric model runs, atmospheric transport runs, and new atmospheric inversions included in this manuscript. Tristram West and Stephen Ogle provided most of the inventory data used for the 'bottom up' portion of the comparison with the exception of fossil fuel inventory data for the MCI region, which was provided by Kevin Gurney (Arizona State). Natasha Miles and Scott Richardson instrumented, maintained and analyzed the PSU "ring of towers" CO2 data for the MCI campaign (and the Missouri Ozarks tower) while Arlyn Andrews did the same for the WBI and WLEF towers within the MCI domain, in addition to the remainder of NOAA's tall tower sites across the U.S.. Marek Uliasz provided assistance with the LPDM model used by both the PSU and CSU inversions. Dan Cooley and F. Jay Breidt provided advice and discussion on inversions and state-space modeling. Scott Denning provided the introduction and Scott Denning, Ken Davis and Stephen Ogle helped initiate the original campaign and provide overall guidance to the project. The authors would like to thank a great many

Table 1. Inversion Comparison

	CarbonTracker	SiB-RAMS-LPDM	WRF-LPDM
Inversion Method	Ensemble Kalman Filter	Synthesis Bayesian	Synthesis Bayesian
Transport	TM5	BRAMS 3.2[a]	WRF-Chem
Land Surface Model	TESSEL	SiB3-(CROP)	NOAH
A prior CO_2 fluxes	CASA	SiB3-(CROP)	SiB3-(CROP) [b]
Domain	global	continental (North America)	regional
Transport Resolution	3x2deg (1x1 deg nest)	40km	10km
Inversion Resolution	Ecoregions (Olsen)	40km/200km nest[c]	20km
Boundary CO_2	none (global)	CarbonTracker and GlobalView	aircraft-corrected CarbonTracker

[a]BRAMS 3.2 was used as the basis for the transport model but the code has undergone numerous changes, fixes, and improvements over the last decade at Colorado State University

[b]CarbonTracker posterior CO2 fluxes were also used in Lauvaux et al. 2012 but not shown here.

[c]see notes in Inversion section

Table 2. MCI Source/Sink Results (due to Model Variations)

Inversion Method	Inflow	Prior Description	Prior NEE (MCI)	Post NEE (MCI)	Prior NEE (PSU Dom.)	Post NEE (PSU Dom.)
CarbonTracker	N/A	CASA-GFED	-40 TgC	-155 TgC		
PSU	Aircraft-corrected CT	SiB3-offline	N/A	N/A	-65 TgC	-140 TgC
PSU	Aircraft-corrected CT	CarbonTracker optimized	N/A	N/A	-154 TgC	-127 TgC
CSU	CarbonTracker opt.	SiB3-offline	-82 TgC	-235 TgC	-75 TgC	-200 TgC
CSU	GV-corrected CT opt.	SiB3-offline (forced annual balance)	0 TgC	-145 TgC	-75 TgC	-127 TgC
CSU	GV-corrected CT opt.	SiB3-offline (dec length: 1000KM)	-82 TgC	-162 TgC	-75 TgC	-144 TgC
CSU	GV-corrected CT opt.	SiB3-offline (dec length: 500KM)	-82 TgC	-160 TgC	-75 TgC	-143 TgC
CSU	CarbonTracker opt.	SiB3-RAMS coupled	0 TgC	-174 TgC	0 TgC	-154 TgC
CSU	GV-corrected CT opt.	SiB3-RAMS coupled	0 TgC	-117 TgC	0 TgC	-107 TgC
Inventory	N/A	N/A	N/A	*-135 TgC*	N/A	*-117 TgC*

Negative NEE indicates carbon moving from atmosphere to the biosphere. These SiB3-offline fluxes were driven from offline run of the model driven by NARR data, which was used as the driving external forcing necessary for both WRF and RAMS. Inversion results for PSU inversion are put on a full annual 2007 basis by adding a priori fluxes from SiB3-CROP for Jan - May 2007 (before MCI towers were instrumented) to both a priori and a posterior flux estimates for June 2007 through Dec 2007. PSU inversion results for the "optimized CarbonTracker flux" case are on the native PSU grid which is slightly larger than the "PSU grid" which is used throughout this paper which represents the intersection of the native PSU grid and the MCI domain. A priori fluxes from SiB3-offline are characterized by a "realistic" annual harvest sink while the "forced annual balance" case forces NEE to zero over all gridcells by balancing total respiration with gross primary production. Typically, the a priori fluxes and transport are derived in a de-coupled environment. However, the "SiB3-RAMS" a priori fluxes are those produced as a result of the parent SiB3-RAMS simulation which produced the transport used in the CSU inversion, i.e coupled. "Dec length" indicates the a priori decorrelation length scale , or e-folding length, used for the exponential spatial correlation in the a priori fluxes. This value is generally less than 300KM for PSU inversions and 1000KM for CSU, unless otherwise noted.

567 people who were involved with this project as well as generous support from the National
568 Aeronautics and Space Administration (NASA #NNX08AK08G), National Oceanic and
569 Atmospheric Administration (NOAA #NA08OAR4320893) and the Department of Energy
570 (DOE #DE-FG02-06ER64317). Thanks for NOAA-ESRL for many useful discussions on these
571 inversions as well as the CarbonTracker results which were used in this paper. Tower data was
572 graciously provided, and commented on, by Bev Law and Matthias Goeckede (Oregon State
573 University), NOAA-ESRL (Arlyn Andrews), Environment Canada (Doug Worthy), and Penn
574 State University (Natasha Miles and Scott Richardson).

References

Baker DF, Doney SC, Schimel DS (2006) Variational data assimilation for atmospheric co2. *Tellus*, **58B**, 359–365.

Baker IT, Prihodko L, Denning AS, *et al.* (2008) Seasonal drought stress in the amazon: Reconciling 3 models and observations. *Journal of Geophysical Research*, **113**.

Baldocchi D, Reichstein M, Papale D, *et al.* (2012) The role of trace gas flux networks in the biogeosciences. *EOS Trasacations, American Geophysical Union*, **Vol. 93 No. 23**, 217–224.

Bishop CH, Etherton BJ, Majumjar S (2001) Adaptive sampling with the ensemble transform kalman filter: Part 1: Theoretical aspects. *Mon. Wea. Rev.*, **129**, 420–436.

Bolin B, Erickson E (1959) *Changes in the Carbon Dioxide Content of the Atmosphere and Sea due to Fossil Fuel Combustion*. The Rockefeller Int. Press, New York.

Bolin B, Keeling CD (1963) Large-scale atmospheric mixing as deduced from the seasonal and meridional variations of carbon dioxide. *Journal of Geophysical Research*, **68**, 3899–3920.

Bruhwiler LMP, Michalak AM, W Peters DFB, *et al.* (2005) An improved kalman smoother for atmospheric inversions. *Atmos. Chem. Phys.*, **5**, 2691–2702.

Chen J, Davis KJ, Meyers TP (2008) Ecosystem-atmosphere carbon and water cycling in the upper great lakes region. *Agricultural and Forest Meteorology*, **148**, 155–157.

Cooley D, Breidt F, Ogle S, *et al.* (2012) A constrained least-squares approach to combine bottom-up and top-down co₂ flux estimates. *Environmental and Ecological Statistics*, pp. 1–18. URL `http://dx.doi.org/10.1007/s10651-012-0211-6`. 10.1007/s10651-012-0211-6.

Corbin KD, Denning AS, Lokupitiya EY, *et al.* (2010) Assessing the im-

pact of crops on regional co2 fluxes and atmospheric concentrations. *Tellus B*, **62**, 521–532. doi:10.1111/j.1600-0889.2010.00485.x. URL http://dx.doi.org/10.1111/j.1600-0889.2010.00485.x.

Crevoisier C, Sweeney C, Gloor M, *et al.* (2010) Regional us carbon sinks from three-dimensional atmospheric co2 sampling. *PNAS*, **107**, 18348–18353.

Crosson E (2008) A cavity ring-down analyzer for measuring atmospheric levels of methane, carbon dioxide, and water vapor. *Applied Physics B: Lasers and Optics*, **92**, 403–408. URL http://dx.doi.org/10.1007/s00340-008-3135-y. 10.1007/s00340-008-3135-y.

Denning AS (2005) Science implementation strategy for the north american carbon program. Prepared for the U.S. Carbon Cycle Scientific Steering Group and Interagency Working Group by the North American Carbon Program Implementation Strategy Group.

Denning AS, Holzer M, Gurney KR, *et al.* (1999) Three-dimensional transpot and concentration of sf6: A model intercomparison study (transcom 2). *Tellus*, **51B**, 266–297.

Denning AS, Nicholls M, Prihodko L, *et al.* (2003) Simulated variations in atmospheric co2 over a wisconsin forest using a couple ecosystem-atmosphere model. *Global Change Biology*, **9**, 1241–1250.

Denning AS, Randall DA, Collatz GJ, *et al.* (1996) Simulations of terrestrial carbon metabolism and atmospheric co2 in a general circulation model. part 2: Spatial and temporal variations of atmospheric co2. *Tellus*, **48B**, 543–567.

Dirmeyer PA, Kinter JL (2010) Floods over the u.s. midwest: A regional water cycle perspective. *J. Hydrometeor*, **11**, 1172–1181.

Dolman AJ, Noilhan J, Durand P, *et al.* (2006) Ceres, the carboeurope regional

experiment strategy in les landes, south west france, mayjune 2005. *Bull. Am. Meteorol. Soc.*, **87(10)**, 1367–1379.

Enting I, Trudinger C, Francey R (1994) A synthesis inversion of the concentration and d13c of atmospheric co2. *Tellus*, **47B**, 35–52.

EPA (2010) Inventory of u.s. greenhouse gas emissions and sinks: 1990-2008. u.s. environmental protection agency, washington, d.c.

Evensen G (1994) Sequential data assimilation with a nonlinear quasi-geostrophic model using monte carlo methods to forecast error statistics. *Journal of Geophysical Research*, **99**, 143–162.

Filippi D, Ramonet M, Ciais P, *et al.* (2003) Greenhouse airborne measurements over europe. *Geophys. Res. Abstracts*, **5**.

Friedlingstein P, Cox P, Coauthors (2006) Climatecarbon cycle feedback analysis: Results from the c4mip model intercomparison. *J. Climate*, **19**, 33373353.

Fung I, Tucker C, Prentice K (1987) Application of advanced very high resolution radiometer vegetation index to study atmosphere-biosphere exchange of co2. *J. Geophys. Res.*, **92**, 2999–3015.

Gerbig C, Lin JC, Wofsy SC, *et al.* (2003) Toward constraining regional-scale fluxes of co2 with atmospheric observations over a continent: 2. analysis of cobra data using a receptor-oriented framework. *Journal of Geophysical Research*, **108**, ACH 6 1–19.

GLOBALVIEW-CO2 (2010) Cooperative atmospheric data integration project - carbon dioxide. URL `ftp.cmdl.noaa.gov:/ccg/co2/GLOBALVIEW`.

Goeckede M, Michalak AM, Vickers D, *et al.* (2010a) Atmospheric inverse modeling to constrain regional scale co2 budgets at high spatial and temporal resolution. *Journal of Geophysical Research*, **115**.

650 Goeckede M, Turner DP, Michalak AM, *et al.* (2010b) Sensitivity of a subregional scale
651 atmospheric inverse co2 modeling framework to boundary conditions. *Journal of*
652 *Geophysical Research*, **115**.

653 Gourdji SM, Mueller KL, Yadav V, *et al.* (2012) North american co2 exchange:
654 intercomparison of modeled estimates with results from a fine-scale atmospheric
655 inversion. *Biogeosciences Discussions*, **9**, 457–475.

656 Gurney K, Mendoza D, Zhou Y, *et al.* (2009) High resolution fossil fuel combustion co2
657 emissions fluxes for the united states. *Environmental Science and Technology*,
658 **43**, 5535–5541.

659 Gurney KR, Law RM, Denning AS, *et al.* (2002) Towards robust regional estimates of
660 co2 sources and sinks using atmospheric transport models. *Nature*, **415**, 626–630.

661 Heimann M, Keeling CD (1986) Meridional eddy diffusion model of the transport of
662 atmospheric carbon dioxide 1. the seasonal carbon cycle over the tropical pacific
663 ocean. *Journal of Geophysical Research*, **91**, 7765–7781.

664 King AW, Dilling L, Zimmerman G, *et al.* (2007) Ccsp: The first state of the carbon
665 cycle report (soccr): The north american carbon budget and implications for the
666 global carbon cycle, a report by the u.s. climate change science program and the
667 subcommittee on global change research. National Oceanic and Atmospheric
668 Administration, National Climatic Data Center, Ashville, NC USA.

669 Krol M, Houweling S, Bregman B, *et al.* (2005) The two-way nested global chemistry-
670 transport zoom model tm5: algorithm and applications. *Atmos. Chem. Phys.*,
671 **5(2)**, 417–432.

672 Lauvaux T, Pannekoucke O, Sarrat C, *et al.* (2009) Structure of the transport
673 uncertainty in mesoscale inversions of co2 sources and sinks using ensemble model
674 simulations. *Biogeosciences*, **6**, 1089–1102.

675 Lauvaux T, Schuh AE, Richardson S, *et al.* (2012a) Network design for mesoscale
676 inversions of co2 sources and sinks. *Tellus B (accepted with minor revisions).*

677 Lauvaux T, Schuh AE, Uliasz M, *et al.* (2012b) Constraining the co_2 budget of the corn
678 belt: exploring uncertainties from the assumptions in a mesoscale inverse system.
679 *Atmospheric Chemistry and Physics*, **12**, 337–354. doi:10.5194/acpd-12-337-2012.

680 Lauvaux T, Uliasz M, Sarrat C, *et al.* (2008) Mesoscale inversion: first results from the
681 ceres campaign with synthetic data. *Atmos. Chem. Phys.*, **8**, 3459–3471.

682 Law R, Simmonds I (1996) The sensitivity of deduced co2 sources and sinks to variations
683 in transport and imposed surface concentrations. *Tellus B*, **48**, 613625.

684 Lin J, Gerbig C, Wofsy S, *et al.* (2003) A near-field tool for simulating the upstream
685 influence of atmospheric observations: The stochastic time-inverted lagrangian
686 transport (stilt) model. *Journal of Geophysical Research*, **108**, ACH 2 1–17.

687 Lokupitiya E, Denning S, Paustian K, *et al.* (2009) Incorporation of crop phe-
688 nology in simple biosphere model (sibcrop) to improve land-atmosphere
689 carbon exchanges from croplands. *Biogeosciences*, **6**, 969–986. URL
690 `http://www.biogeosciences.net/6/969/2009/`.

691 Lokupitiya R, Zupanski D, Denning AS, *et al.* (2008) Estimation of global co2 fluxes
692 at regional scale using the maximum likelihood ensemble filter. *Journal of*
693 *Geophysical Research*, **113**.

694 Martins DK, Sweeney C, Stirm BH, *et al.* (2009) Regional surface flux of co2 inferred
695 from changes in the advected co2 column density. *Agric. For. Meteor.*, **149**,
696 16741685.

697 Michalak AM, Bruhwiler L, Tans PP (2004) A geostatistical approach to surface flux
698 estimation of atmospheric trace gases. *Journal of Geophysical Research*, **109**,
699 1–19.

Miles NL, Richardson SJ, Davis KJ, *et al.* (2012) Large amplitude spatial and temporal gradients in atmospheric boundary layer co2 mole fractions detected with a tower-based network in the u.s. upper midwest. *Journal of Geophysical Research Biogeosciences*, **117**, G01019.

NASS (2011) Agricultural statistics data base. Electronic Database. URL `http://www.nass.usda.gov`.

Nicholls ME, Denning AS, Prihodko L, *et al.* (2004) A multiple-scale simulation of variations in atmospheric carbon dioxide using a coupled biosphere-atmospheric model. *Journal of Geophysical Research*, **109**.

Ogle S, Breidt F, Easter M, *et al.* (2010) Scale and uncertainty in modeled soil organic carbon stock changes for us croplands using a process-based model. *Global Change Biology*, **16**, 810–820.

Ogle S, Davis K, Andrews A, *et al.* (2006) Science plan: Mid-continent intensive campaign of the north american carbon program. north american carbon program, maryland, usa.

Olson JS, Watts JA, Allsion LJ (1985) Major world ecosystem complexes ranked by carbon in live vegetation: A database. *ORNL/CDIAC-134, NDP-017. Carbon Dioxide Information Analysis Center, U.S. Department of Energy, Oak Ridge National Laboratory, Oak Ridge, Tennessee, U.S.A. (Revised 2001).*

Pearman G, Hyson P (1981) The annual variation of atmospheric co2 concentration observed in the northern hemisphere. *Journal of Geophysical Research*, **86**, 9839–9843.

Peters W, Jacobson AR, Sweeney C, *et al.* (2007) An atmospheric perspective on north american carbon dioxide exchange: Carbontracker. *Proceedings of the National Academy of Sciences of the United States of America*, **104**, 18925–18930.

725 Peters W, Krol M, Coauthors (2010) Seven years of recent european net terrestrial
726 carbon dioxide exchange constrained by atmospheric observations. *Global Change*
727 *Biology*, **16**, 13171337.

728 Pielke RA, Cotton W, Walko R, *et al.* (1992) A comprehensive meteorological modeling
729 system – rams. *Meteorology and Atmospheric Physics*, **46**, 69–91.

730 Richardson SJ, Miles NL, Davis KJ, *et al.* (2012) Field testing of cavity ring-down
731 spectroscopy analyzers measuring carbon dioxide and water vapor. *Journal of*
732 *Atmospheric and Oceanic Technology*, **29**, 397–406.

733 Schuh AE, Denning AS, Corbin KD, *et al.* (2010) A regional high-resolution carbon flux
734 inversion of north america for 2004. *Biogeosciences*, **8**, 1625–1644.

735 Schuh AE, Denning AS, Uliasz M, *et al.* (2009) Seeing the forest through the trees:
736 Recovering largescale carbon flux biases in the midst of smallscale variability.
737 *Journal of Geophysical Research*, **114**.

738 Sellers PJ, Mintz Y, Sud YC, *et al.* (1986) A simple biosphere model (sib) for use within
739 general circulation models. *Journal of Atmospheric Sciences*, **43**, 505–531.

740 Sellers PJ, Randall DA, Collatz GJ, *et al.* (1996) A revised land surface parameterization
741 (sib2) for atmospheric gcms. part i: Model formulation. *Journal of Climate*, **9**,
742 676–705.

743 Solomon S, Qin D, Manning M, *et al.*, eds. (2007) *IPCC, 2007: Climate Change*
744 *2007: The Physical Science Basis. Contribution of Working Group I to the*
745 *Fourth Assessment Report of the Intergovernmental Panel on Climate Change*.
746 Cambridge University Press, Cambridge, United Kingdom and New York, NY,
747 USA.

748 Stephens BB, Miles NL, Richardson SJ, *et al.* (2011) Atmospheric co2 monitoring with

single-cell ndir-based analyzers. *Atmospheric Measurement Techniques*, **4**, pp 2737–2748.

Tans PP, Fung IY, Takahashi T (1990) Observational constraints on the global atmospheric co2 budget. *Science*, **247**, 1431–1438.

Tarantola A (1987) *Inverse Problem Theory: Methods for Data Fitting and Parameter Estimation*. Elsevier Science, New York.

Tippett M, Anderson JL, Bishop CH, *et al.* (2003) Ensemble square-root filters. *Mon. Wea. Rev.*, **131**, 1485–1490.

Uliasz M (1993) The atmospheric mesoscale dispersion modeling system (mdms). *Journal of Applied Meteorology*, **32**, 139–149.

Uliasz M (1994) Lagrangian particle modeling in mesoscale applications. In: *Environmental Modeling II* (ed. Zannetti P), pp. 71–102. Computational Mechanics Publications.

Uliasz M (1996) Lagrangian particle modeling in mesoscale applications. In: *Environmental Modeling III* (ed. Zannetti P), pp. 145–182. Computational Mechanics Publications.

Uliasz M, Pielke RA (1991) Application of the receptor oriented approach in mesoscale dispersion modeling. In: *Air Pollution Modeling and its Applications VIII* (eds. Dop HV, Steyn DG), pp. 399–408. Plenum Press, New York.

Verma S, Dobermann A, Cassman K, *et al.* (2005) Annual carbon dioxide exchange in irrigated and rainfed maize-based agroecosystems. *Agricultural and Forest Meteorology*, **131**, 77–96.

Wang JW, Denning AS, Lu L, *et al.* (2006) Observations and simulations of synoptic, regional, and local variations in atmospheric co2. *Journal of Geophysical Research*, **112**.

774 West TO, Bandaru V, Brandt CC, *et al.* (2011) Regional uptake and release of crop
775 carbon in the united states. *Biogeosciences*, **8**, 2037–2046.

776 West TO, Brandt CC, Baskaran LM, *et al.* (2010) Cropland carbon uxes in the united
777 states: increasing geospatial resolution of inventory-based carbon accounting.
778 *Ecological Applications*, **20**, 1074–1086.

779 Whitaker JS, Hamill TM (2002) Ensemble data assimilation without perturbed
780 observations. *Mon. Wea. Rev.*, **130**, 1913–1924.

781 Wofsy SC, Harriss RC (2002) The north american carbon program plan (nacp) a report
782 of the committee of the u.s. carbon cycle science steering group. Prepared at the
783 Request of the Agencies of the U.S. Global Change Research Program.

784 Zupanski D, Denning AS, Uliasz M, *et al.* (2007) Carbon flux bias estimation employing
785 maximum likelihood ensemble filter (mlef). *Journal of Geophysical Research*,
786 **112**.

787 Zupanski M (2005) Maximum likelihood ensemble filter: Theoretical aspects. *Mon.*
788 *Wea. Rev.*, **133**, 1710–1726.

---

789 E-mail: Corresponding aschuh@atmos.colostate.edu

790 Received _____

---

791 This manuscript was prepared with AGU's LaTeX macros v4, with the extension package 'AGU++' by P. W. Daly,
792 version 1.6b from 1999/08/19.

Figure Captions

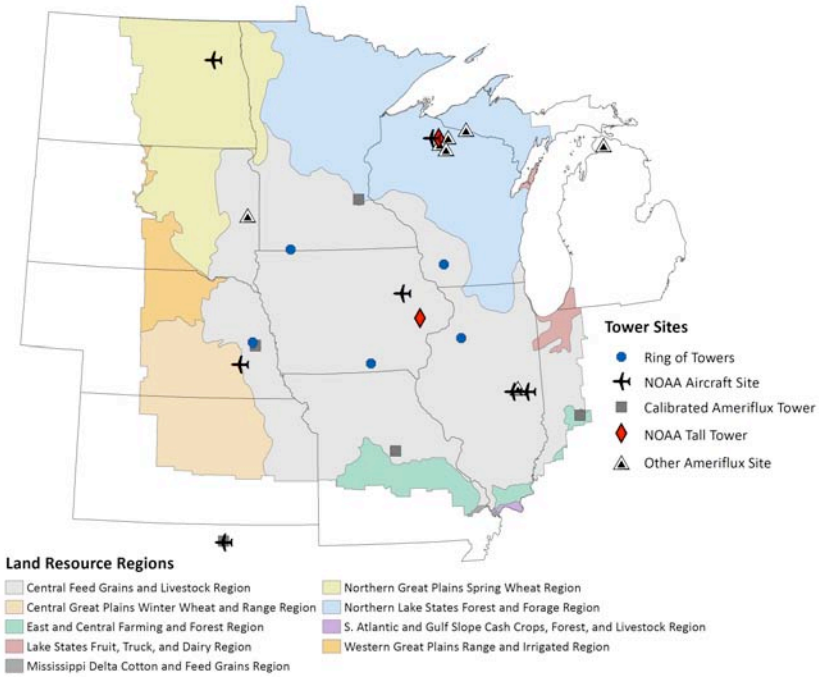

Figure 1. Map of MCI domain.

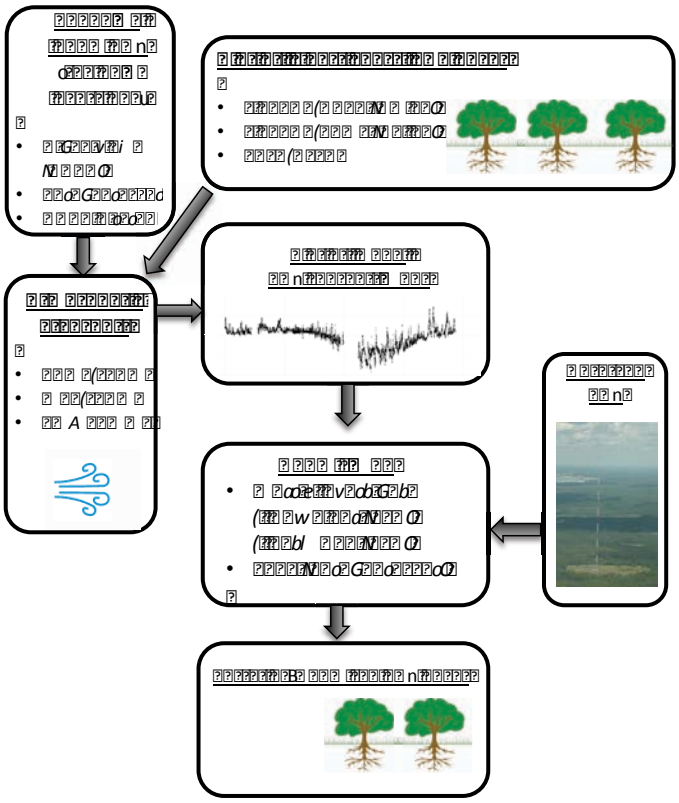

Figure 2. Flowchart of atmospheric inversion process.

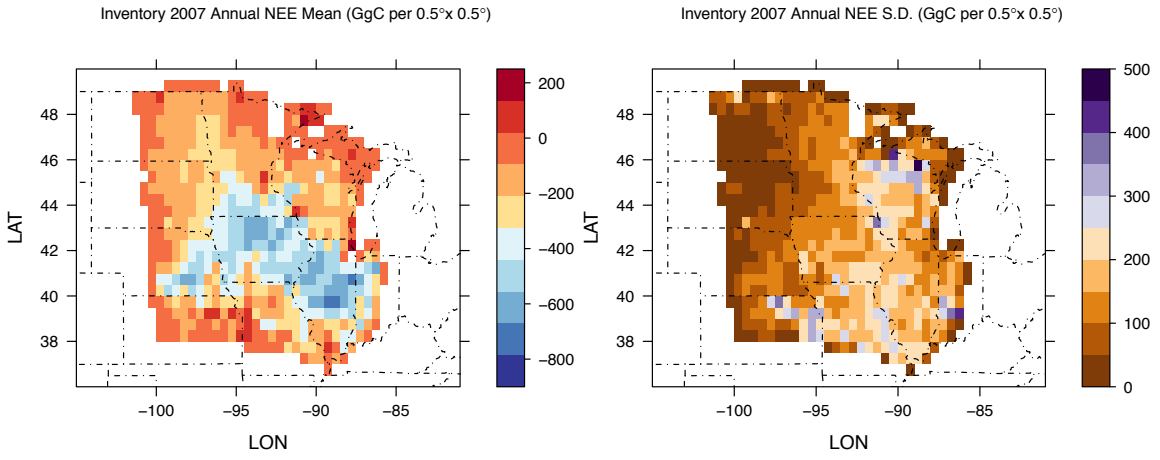

Figure 3. Annual NEE estimate by the inventory components. Mean estimates are shown in left panel and standard deviations are shown on right side. Note that the distribution of the inventory is not necessarily Gaussian and therefore, in a rigorous sense, the standard deviation is simply a measure of uncertainty.

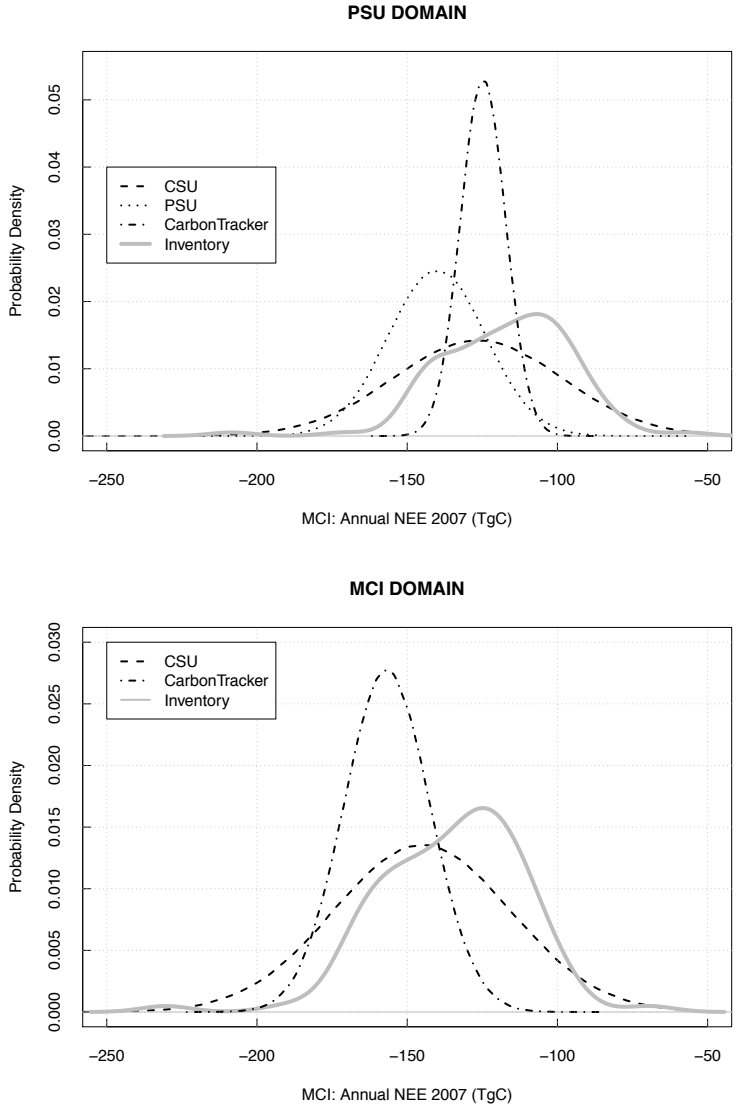

Figure 4. Densities for annual NEE for inversion results and inventory (2007). Top panel shows results for entire MCI region while bottom panel shows results for the intersection of the PSU inversion model domain and MCI domain. PSU inversion is based on SiB3-CROP offline prior. CSU inversion is also based on SiB3-CROP offline prior with GV-bias corrected CT inflow. These results include explicit variability estimates that were constructed for the inventory using a Monte Carlo anlysis and variability estimates that arise naturally from the matrix-based atmospheric inversion procedure. Due to difficulty in obtaining covariances for the CarbonTracker ecoregion estimates, only marginal ecoregion specific variances were used in the figure for NEE. The variability induced by varying inflow CO_2 or underlying transport model characteristics is not implicitly included here but can be seen in Table 2.

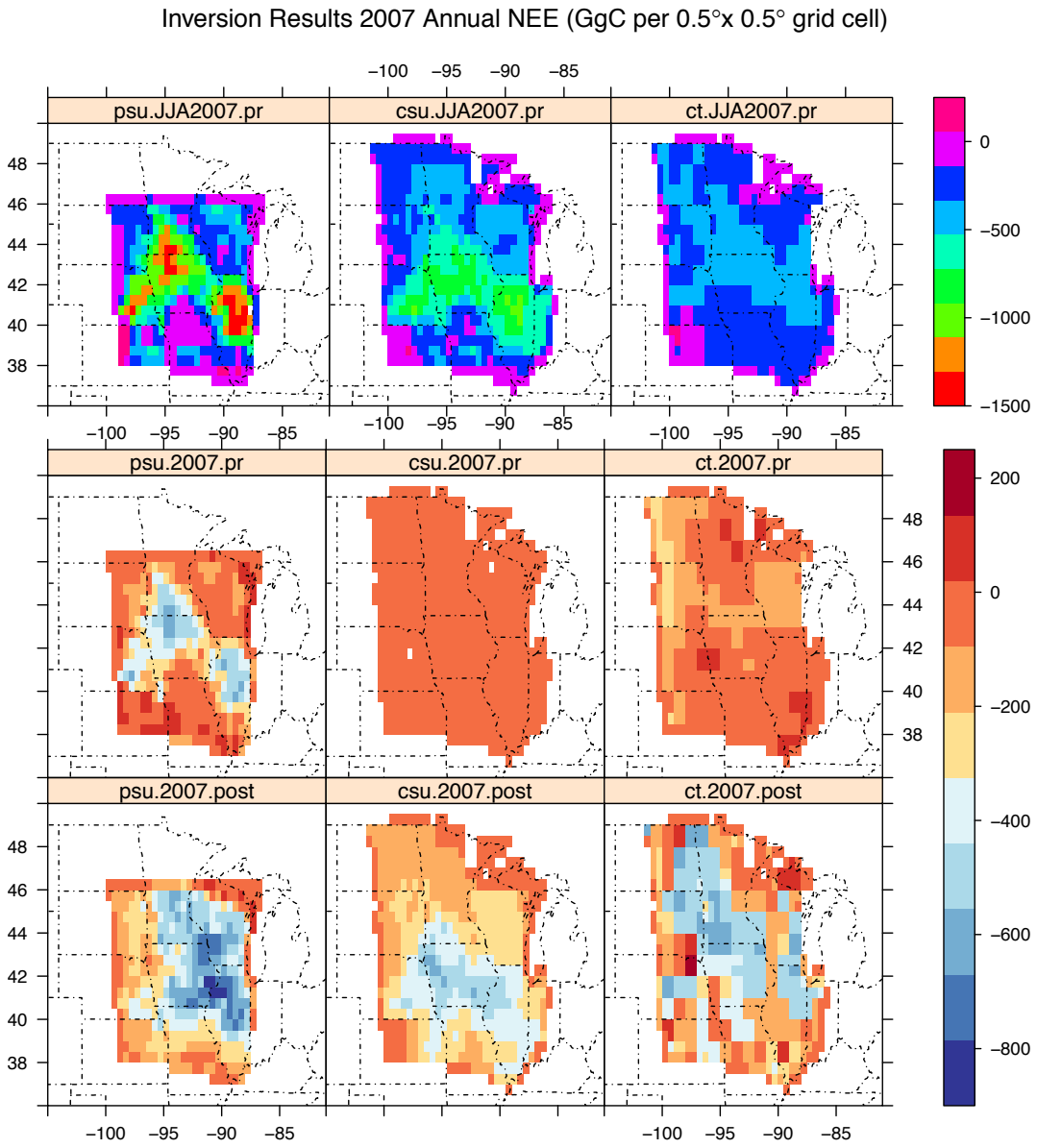

Figure 5. Each panel name is composed of (1) inversion model, (2) 2007 for annual total or JJA2007 for June/July/August sum, and (3) "pr" for a priori and "post" for posterior flux. A priori annual 2007 NEE estimates are shown in middle row with posterior annual 2007 NEE estimates shown in the bottom row. PSU inversion is based on SiB3-CROP offline prior with residual 109 TgC harvest sink. CSU inversion is also based on same prior (and underlying seasonality) but with residual harvest sink balanced by respiration annually to induce net zero NEE and uses GlobalView bias-corrected CT inflow. The top row shows the June/July/August total NEE for each prior flux which is indicative of the spatial signal of strong summer crop carbon drawdown.

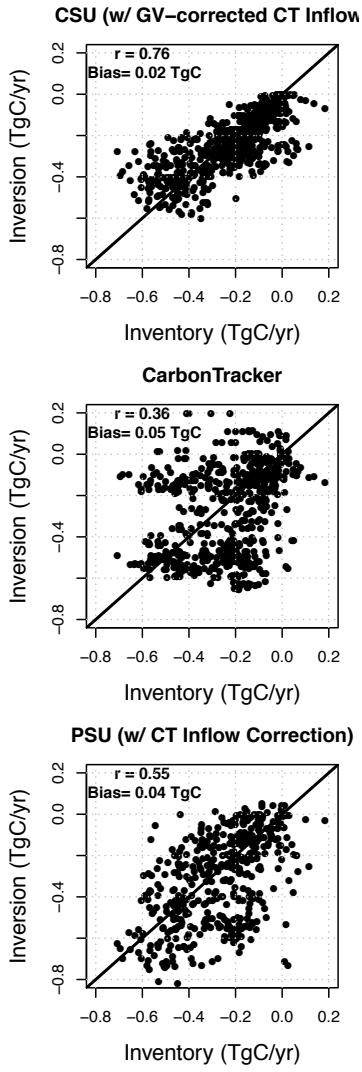

Figure 6. Plots of inventory estimates vs inversion for annual 2007 NEE. Each pixel of Figure 5 is represented as a datum in the figure. PSU inversion is based on SiB3-CROP offline prior. CSU inversion is also based on SiB3-CROP offline prior with GV-bias corrected CT inflow

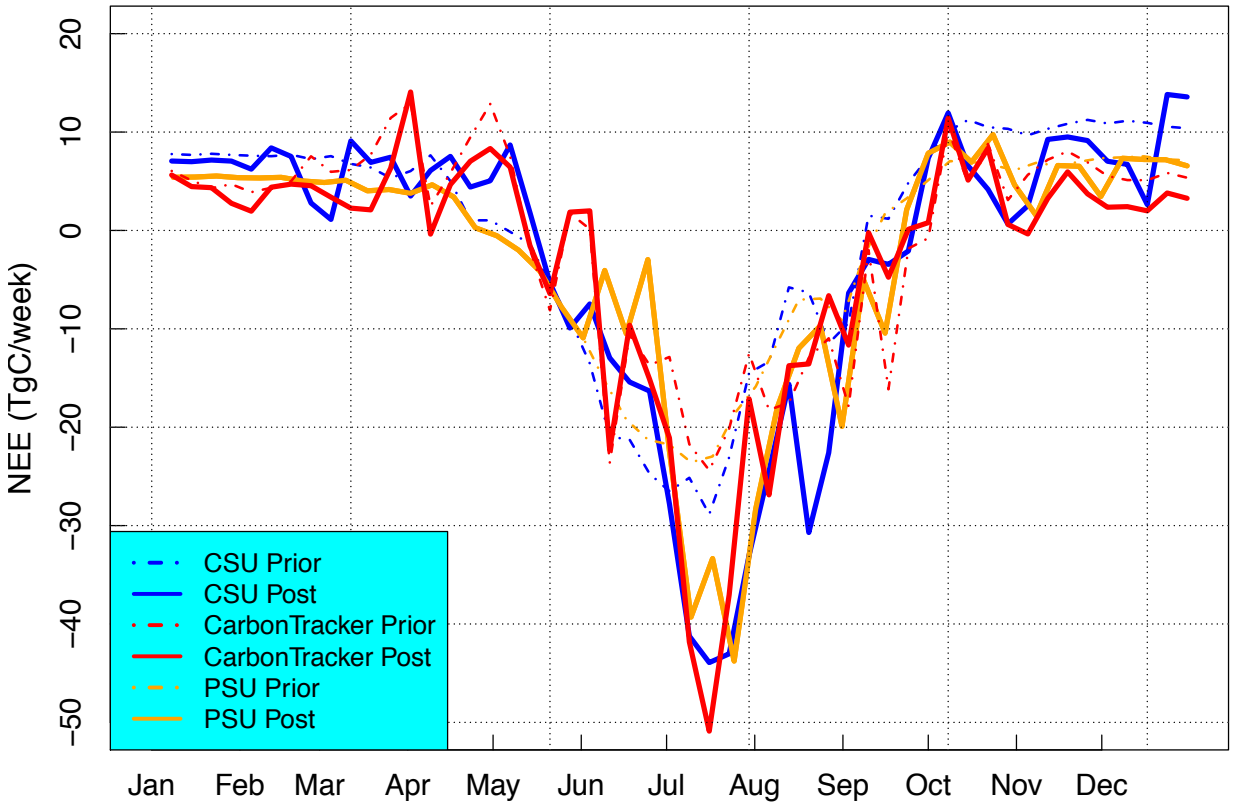

Figure 7. Time series of net ecosystem exchange (NEE) estimates from a variety of inversion models for 2007. PSU inversion is based on SiB3-CROP offline prior. CSU inversion is also based on SiB3-CROP offline prior with GlobalView-bias corrected CT inflow. Results from PSU inversion are from the intersection of PSU inversion domain and MCI domain while the results for the CarbonTracker and CSU inversions are on the MCI domain.

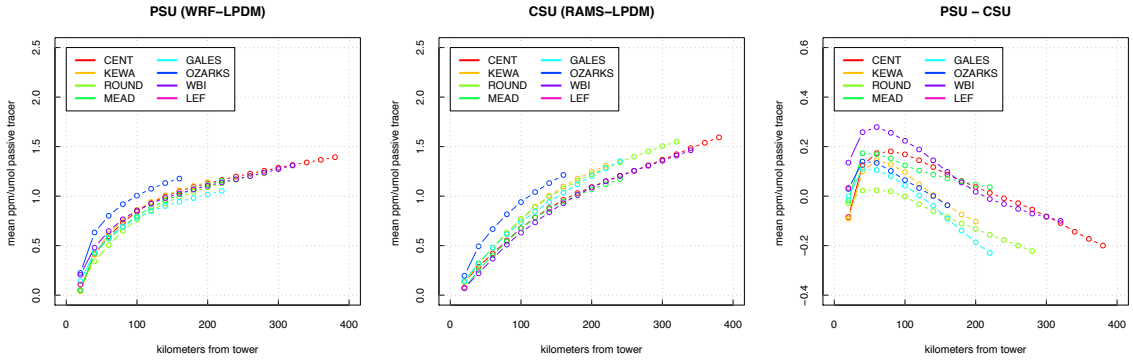

Figure 8. Sensitivity of daytime observations of passive surface flux to daytime passive flux releases. Left panel shows results for PSU transport with WRF and LPDM and right panel shows results for CSU transport with RAMS and LPDM.

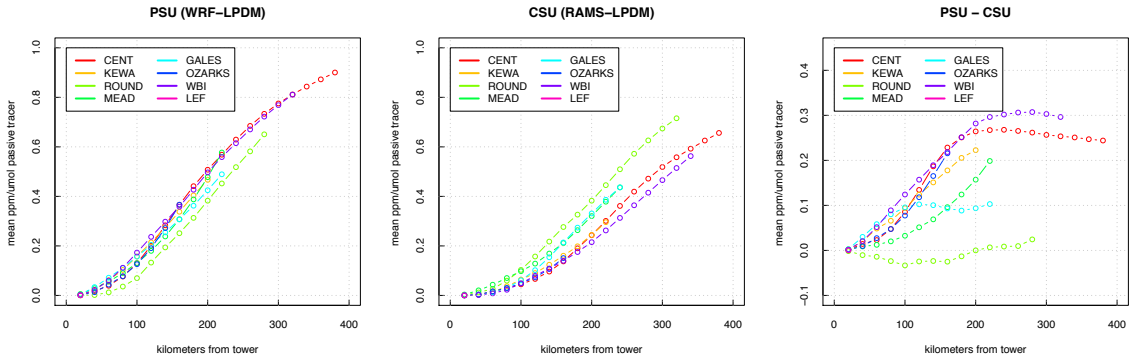

Figure 9. Sensitivity of daytime observations of passive surface flux to nighttime passive flux releases. Left panel shows results for PSU transport with WRF and LPDM and right panel shows results for CSU transport with RAMS and LPDM.

Atmos. Chem. Phys., 12, 337–354, 2012
www.atmos-chem-phys.net/12/337/2012/
doi:10.5194/acp-12-337-2012

Atmospheric Chemistry and Physics

Constraining the CO_2 budget of the corn belt: exploring uncertainties from the assumptions in a mesoscale inverse system

T. Lauvaux[1], A. E. Schuh[2,5], M. Uliasz[5], S. Richardson[1], N. Miles[1], A. E. Andrews[4], C. Sweeney[4], L. I. Diaz[1], D. Martins[1], P. B. Shepson[3], and K. J. Davis[1]

[1]Department of Meteorology, The Pennsylvania State University, Inversity Park, Pennsylvania, USA
[2]NREL, Fort Collins, Colorado, USA
[3]Purdue University, W. Lafayette, Indiana, USA
[4]National Oceanic and Atmospheric Association, ESRL/GMD, Boulder, Colorado, USA
[5]Department of Atmospheric Science, Colorado State University, Fort Collins, Colorado, USA

Correspondence to: T. Lauvaux (lauvaux@meteo.psu.edu)

Received: 27 June 2011 – Published in Atmos. Chem. Phys. Discuss.: 22 July 2011
Revised: 8 November 2011 – Accepted: 13 December 2011 – Published: 5 January 2012

Abstract. We performed an atmospheric inversion of the CO_2 fluxes over Iowa and the surrounding states, from June to December 2007, at 20 km resolution and weekly timescale. Eight concentration towers were used to constrain the carbon balance in a $1000 \times 1000\,km^2$ domain in this agricultural region of the US upper midwest. The CO_2 concentrations of the boundaries derived from CarbonTracker were adjusted to match direct observations from aircraft profiles around the domain. The regional carbon balance ends up with a sink of 183 Tg C±35 Tg C over the area for the period June–December, 2007. Potential bias from incorrect boundary conditions of about 0.55 ppm over the 7 months was corrected using mixing ratios from four different aircraft profile sites operated at a weekly time scale, acting as an additional source of uncertainty of 24 Tg C. We used two different prior flux estimates, the SiBCrop model and the inverse flux product from the CarbonTracker system. We show that inverse flux estimates using both priors converge to similar posterior estimates (20 Tg C difference), in our reference inversion, but some spatial structures from the prior fluxes remain in the posterior fluxes, revealing the importance of the prior flux resolution and distribution despite the large amount of atmospheric data available. The retrieved fluxes were compared to eddy flux towers in the corn and grassland areas, revealing an improvement in the seasonal cycles between the two compared to the prior fluxes, despite large absolute differences due to representation errors. The uncertainty of 34 Tg C (or 34 g C m^2) was derived from the posterior uncertainty obtained with our reference inversion of about 25 to 30 Tg C and from sensitivity tests of the assumptions made in the inverse system, for a mean carbon balance over the region of −183 Tg C, slightly weaker than the reference. Because of the potential large bias (∼24 Tg C in this case) due to choice of background conditions, proportional to the surface but not to the regional flux, this methodology seems limited to regions with a large signal (sink or source), unless additional observations can be used to constrain the boundary inflow.

1 Introduction

Atmospheric inversions have been used to quantify the exchanges of CO_2 between the atmosphere and the continents, and the atmosphere and the oceans, each of them contributing to a significant part of the global carbon cycle (Tans et al., 1990; Francey et al., 1995; Bousquet et al., 2000; Chevallier et al., 2010). Uncertainties and variability amongst studies remain large (Gurney et al., 2002), especially for the continental surface exchanges that are highly variable in time and space and closely related to land use change, climate variability and ecosystem responses to environmental changes (Canadell et al., 2007). The misrepresentation of atmospheric processes in the transport models (Baker et al., 2007; Stephens et al., 2007), the lack of available measurements

around the globe responsible for the ill-conditionning of the problem at large scales (Enting, 2002), and the errors of representation at the scales they have been performed (Geels et al., 2007), limit the potential of the method.

Several studies attempted to reduce these major sources of uncertainties by improving temporal and spatial resolutions, from global to continental scales solving for homogeneous flux areas called ecoregions (Peters et al., 2007; Butler et al., 2010), or pixel-based fluxes (Carouge et al., 2010; Gourdji et al., 2010; Schuh et al., 2010), and from continental to regional domains (Lauvaux et al., 2009a; Göckede et al., 2010a).

Refinement of the resolution requires the deployement of high density measurement networks in order to solve for the increasing number of unknowns in the state vector. Past campaigns were limited to a few surface tower sites or flights for a short period of time as CERES (CarboEurope Regional Experiment Strategy) (Dolman et al., 2006) or for very limited areas as in the bay of Valencia, (i.e. during the RECAB campaign, Pérez-Landa et al., 2007). Second, the bounded simulation domain becomes an important limitation if not well-informed of the CO_2 inflow and requires the accurate knowledge of concentrations representing the far field influence (Rödenbeck et al., 2009). The boundaries require then additional observation datasets to inform the system about potential biases due to incorrect carbon mass in the air flow. Third, as inverse methods rely on a sufficiently good prior flux estimate, the performances of terrestrial ecology models need to be enhanced by finer vegetation description, especially its phenology, and a good description of the diurnal variability (Corbin et al., 2008; Gourdji et al., 2010). Finally, the mesoscale atmospheric transport models, even if better able to simulate the atmospheric dynamics driving hourly concentrations compared to general circulation models (Ahmadov et al., 2007), are still affected by transport errors from parametrizations of the Planetary Boundary Layer dynamics in particular (Gerbig et al., 2005; Sarrat et al., 2007a).

More recent studies have shown the potential of the atmospheric inversion methodology at the mesoscale (Lauvaux et al., 2009a). The evaluation of the inverse fluxes was limited to 18 days at 8km resolution, but this study demonstrated for the first time the improvement of the fluxes in time and space against direct flux measurements from aircraft (Gioli et al., 2004). Over longer timescales, relatively small biases at short time scales become increasingly important leading to large final uncertainties at the annual time scale (Schuh et al., 2010). Even if the use of high temporal frequency data increases the amount of information in the system (Law et al., 2003), the flow-dependence of the error structures in the observation space increases with data density too, shown through model error propagation (Lauvaux et al., 2009b) or variograms of model-data mismatch (Gerbig et al., 2003b). Finally, flux errors from ecosystem models used to generate prior fluxes can be correlated, but studies at different time scales and using different models revealed a variety of spatial error correlation structures from large (Peylin et al., 2005) to very small (Chevallier et al., 2006) length scales.

In this study, we developed a mesoscale inversion at 20 km resolution generating inverse fluxes from June (start of the measurement campaign) to December 2007, at a weekly time scale (7.5 days), over the Mid Continent Intensive (MCI) domain, including Iowa and the surrounding states, known as the "Corn Belt" area. This unique instrumental deployement of concentration towers (Miles et al., 2010) and the presence of the National Oceanic and Atmospheric Administration (NOAA) aircraft profile sites (Sweeney et al. (2011), http://www.esrl.noaa.gov/gmd/ccgg/aircraft/index.html) enable the most data-constrained regional inversion. The abundance of crops in the area (corn, soybean, wheat) includes C_4 and C_3 vegetation types, with a contribution of 20 to 40 % by C_4 crops on the growing season gross photosynthetic CO_2 exchange (Griffis et al., 2010). The apparent atmospheric sink, due to the prevention of the decomposition of crop material after harvest, is one of the largest contributions to the overall US carbon budget annually (West et al., 2011), even though this carbon is released by livestock and humans elsewhere in the country during the following year. The strength of the atmospheric signals and the observation network are optimal conditions to test the potential of an atmospheric inversion at the regional scale.

We first describe the system and the different models used to generate the transport fields used to link concentrations to fluxes and their related uncertainties (cf. Sect. 2). Then we estimate the inverse fluxes using two different prior fluxes over the area, one being the direct results of the vegetation model SiBcrop (Lokupitiya et al., 2009) and second the product from the CarbonTracker inverse system (Peters et al., 2007), that we compared to several eddy flux sites over corn and grass ecosystems (cf. Sect. 3). We ran several sensitivity tests and demonstrate the importance of the different components of the system, especially the assumptions made in the error covariance matrices, the potential errors due to boundary conditions, and tested the potential of the system in a more general case. Finally, the remaining uncertainties and the potential of the inverse system are discussed in Sect. 4.

2 The inverse system

2.1 Analytical inversion framework

The inverse system used in this study is an analytical inversion framework (Tarantola, 2004) correcting for temporally averaged fluxes over 7.5 day periods, separated into the averaged daytime (6 a.m. to 6 p.m.) and nighttime (7 p.m. to 5 a.m.) components at 20 km resolution, and boundary mixing ratios. We solved the inverse problem using the classical matrix solution by minimizing the cost function F defined as follows:

$$F = \frac{1}{2}[(\boldsymbol{x}-\boldsymbol{x}_0)^T B^{-1}(\boldsymbol{x}-\boldsymbol{x}_0) + (H\boldsymbol{x}-\boldsymbol{y})^T R^{-1}(H\boldsymbol{x}-\boldsymbol{y})] \quad (1)$$

where $\boldsymbol{x}$ are the unknown flux vector we invert for, $\boldsymbol{x}_0$ the a priori flux estimate, $\boldsymbol{y}$ the observations, H the influence functions, and R and B the uncertainty covariance matrices of the observations and the fluxes respectively. The control vector $\boldsymbol{x}$ includes the surface fluxes and the pre-processed boundary mixing ratios, and the influence function H describes the relationship between the observed mixing ratios, the surface fluxes, and the pre-processed boundary mixing ratios. Minimizing the equation with respect to $\boldsymbol{x}$ yields:

$$\boldsymbol{x} = \boldsymbol{x}_0 + BH^T(HBH^T + R)^{-1}(\boldsymbol{y} - H\boldsymbol{x}_0) \quad (2)$$

We can define the posterior error covariance $\boldsymbol{A}$ for sources given by the following expression:

$$A^{-1} = B^{-1} + H^T R^{-1} H \quad (3)$$

For the boundaries, we defined two different time frequencies that are applied to the different boundary condition time series for each tower: hourly, and every 90 h, as explained in Sect. 2.5.3. In our inversion, the contributions of the boundary conditions to the modeled concentrations (referred as boundary conditions) are defined for each tower separately and only vary in time (i.e. no spatial description of the inflow in the inversion). The initial boundary condition is computed in the direct simulation and corresponds to the influence of the boundaries at the observation location. The spatial component is also considered during the pre-processing using the aircraft data and the influence functions (one for each boundary) to correct for biases. In the inversion, we adjust the overall inflow for each tower and at each time step using the surface tower mixing ratios but no explicit adjoint model. The final state vector dimension, on a grid of 980×980 km at 20 km resolution (49 grid points in each direction) and for two components (nighttime and daytime), ranges from $49\times49\times2+2\times8=4818$ (90 hour frequency at the boundaries, or 2 unknowns per observation sites over 180 h) to $49\times49\times2+180\times8=6242$ (hourly frequency at the boundaries, or 180 unknowns per tower). The observations are at the hourly frequency ($180\times8=1440$ observations per 7.5 days). One of our inversion setups includes observation error correlations depending on the time of the day, but not our reference setup. The transport error correlations were defined at similar scales but not for the transport model used in this study. As a conservative choice, error correlations were used only in the sensitivity experiments (cf. Sect. 3.6). The system is more constrained than past studies thanks to the large amount of data over the domain (1440 atmospheric observations versus 4818 to 6242 unknowns). Inverse fluxes over 7.5 day periods are decorrelated from one period to the next, considering the low temporal correlations in daily averaged flux errors over few days (Chevallier et al., 2006).

2.2 Mixing ratio towers over the MCI

We used hourly CO_2 mixing ratios from seven towers all located in the Mid Continent Intensive Experiment area (Miles et al., 2010), part of the North American Carbon Program (Ogle et al., 2006) (cf. Fig. 1). Five of them were deployed from 2007 to 2009 as additional sites for inversion purposes, on ∼100m high towers, located in and out of the corn belt area: Centerville, Mead, Round Lake, Galesville, and Kewanee (Fig. 1). These five sites were equiped with cavity ring-down analyzers (Crosson, 2008), calibrated daily, and related measurement errors are 0.2–0.3 ppm for the hourly averages (Richardson et al., 2011). One Ameriflux site, Missouri Ozarks (Gu et al., 2006), on a 40 m tower was calibrated during the period to provide an additional observation site during our study period. Finally, two NOAA tall tower sites were also available in the area: Park Falls (LEF), and West Branch (WBI). We used 100m sampling heights from all the sites to remain consistent. Compared to previous regional campaigns, the large number of observation sites offers the unique opportunity to constrain the regional carbon balance and assess the full potential of such methodology. Mixing ratio data were recorded every two minutes, and averaged to hourly resolution for this study.

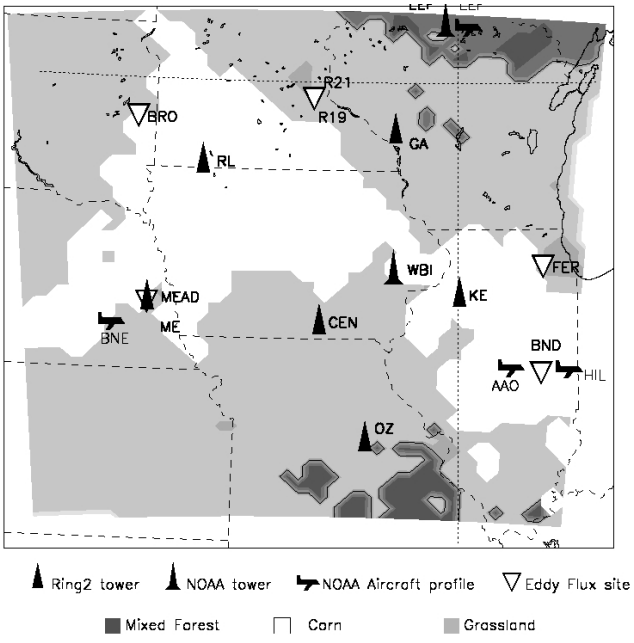

Fig. 1. The Mid Continent Intensive domain with the dominant plant functional types and the observation locations including the concentration tower sites used in the inversion (Ring2 and NOAA towers), the boundary conditions (NOAA aircraft profiles), and the eddy-flux sites used to evaluate the posterior fluxes.

2.3 The prior fluxes and their associated errors

Two prior flux estimates are used in this study: the first is the direct simulation of CO_2 Net Ecosystem Exchange (NEE) with the SiBcrop vegetation model (Lokupitiya et al., 2009), and the second is the optimized flux estimate from the

CarbonTracker inverse system (Peters et al., 2007). The CO_2 fluxes of the first prior were simulated using the Simple Biosphere model including the recent developments of crop phenology and physiology (SiBcrop) at 10 km resolution and at hourly time step, forced by the NARR meteorological renalysis product (North American Regional Reanalysis). This version of SiB (Lokupitiya et al., 2009) includes a parametrization of the Leaf Area Index (LAI) and the fraction of Photosynthetically Active Radiation (fPAR) for crops that showed better agreement in comparison to eddy flux sites than previous NDVI-derived phenology. The allocation of carbon to the different pools (leaves, roots, stems, flowers,...) is estimated on a daily basis, the leaf pool being used to estimate the LAI, and the crop harvest takes place after maturity of the plants. In each pixel, three fluxes corresponding to the three dominant vegetation types are computed. The total flux corresponds to the sum of the three fluxes weighed by their relative vegetation fraction. The second prior fluxes used in this study are the inverse flux estimates from CarbonTracker 2009 system (CT_{v09}) for the year 2007, computed at a 1° by 1° resolution, and a 3 hourly time step over North America (Peters et al., 2007). The CarbonTracker inverse system uses atmospheric mixing ratios from the NOAA global network of surface stations to optimize surface fluxes over large ecoregions. Compared to the present inversion system, the spatial patterns in the inverse fluxes are prescribed for these ecoregions to compensate for the lack of observational constraint. The initial fluxes used in the CarbonTracker inverse system comes from the Carnegie-Ames Stanford Approach (CASA) biogeochemical model[1], which lacks a description of applied phenology that is specific to crops. A linear interpolation was applied to generate hourly fluxes. Most of the towers used in our inversion are not currently used in CT_{v09}, only WBI and LEF. These two prior fluxes were used to investigate the importance of the spatial and temporal distribution of the prior fluxes on the final retrieved estimates. We also assess the degree to which the regional cumulative flux will converge given very different priors (Sibcrop with a June-December balance of 109 Tg C sink, and CT_{v09} final product with 198 Tg C sink) over the region. We also investigated the robustness of the system by adding substantial biases in the prior fluxes in summer and winter (cf. Sect. 4).

We quantified prior flux uncertainties based on the weekly flux model-data mismatch at several locations within the domain (cf. Sect. 2.6). We first defined the standard deviations as the maximum difference observed during the year between the weekly averaged modelled and observed NEE for the three most represented vegetation types of the region (corn, soybean, and grassland). This maximum model-data mismatch is then normalized for every week following the seasonal variability of the absolute fluxes (from 1 to 0.2), to define a weekly standard deviation. The combination of the observed seasonal cycle and the maximum model-data mismatch limits representation errors between site-level observations and grid point modeled fluxes. The final standard deviations represent 30 to 50 % of the weekly net fluxes, and 40 to 70 % of the total mismatch once projected in the observation space. The uncertainty assessment was finally controlled by computing the reduced χ^2 value. Depending on the plant functional type (PFT), the maximum values for the standard deviations range in the growing season from 5 μmol m^{-2} s^{-1} for grassland to 10 μmol m^{-2} s^{-1} for corn, and 1 to 5 μmol m^{-2} s^{-1} during fall and winter. Error flux correlations are based on the vegetation cover map combined with an averaged correlation length. We defined the ecosystem spatial error correlation as the minimum of the vegetation fraction for one given ecosystem in the two pixels (following the SiBcrop ecosystem classification, from Lokupitiya et al., 2009), usually from 0.4 to 0.8, as follows:

$$C_{m,n}^{\mathrm{eco}_1} = \min(f_m^{\mathrm{eco}_1}, f_n^{\mathrm{eco}_1}) \quad (4)$$

with $C_{m,n}^{\mathrm{eco}_1}$ the correlation coefficient between the pixel m and the pixel n for the ecosystem type eco_1, and f^{eco_1} the fraction of vegetation for eco_1 in one given pixel. We considered only the three major ecosystem types of each pixel. For example, two pixels including respectively 25 % and 60 % of corn will end up with .25 correlation coefficient. We combined this ecosystem-based error correlation with a distance-based error correlation (exponentially decaying correlation in space with a correlation length L) to create the final prior error correlation tensor as in Lauvaux et al. (2009b) by:

$$\boldsymbol{C'} = (\boldsymbol{C}_{\mathrm{eco}}^{1/2}\boldsymbol{C}_{\mathrm{dist}}^{1/2})(\boldsymbol{C}_{\mathrm{eco}}^{1/2}\boldsymbol{C}_{\mathrm{dist}}^{1/2})^T \quad (5)$$

with the associated correlation tensors, $\boldsymbol{C}_{\mathrm{eco}}$ for the ecosystem component and $\boldsymbol{C}_{\mathrm{dist}}$ for the distance component, and $\boldsymbol{C'}$ the correlation matrix in the control variable space. The definition of the correlation length L in $\boldsymbol{C}_{\mathrm{dist}}$, based on previous studies, is highly uncertain. For example, at the monthly timescale, Chevallier et al. (2006) showed no significant spatial correlations in the model-data mismatch. Other studies have used large error correlation lengths (Peylin et al., 2005; Schuh et al., 2010), with an isotropic distance-based distribution (Carouge et al., 2010). In the current inverse system, several tests showed that correlation lengths of more than 50 km showed very similar results in terms of inverse fluxes, primarily due to the large observational constraint on the fluxes. Past studies estimated clear spatial structures for crops at short distances ($\leq$100 km) (Lauvaux et al., 2009a). We decide here to use $L = 300$ km as correlation length, decreased by the combination of ecosystem-based correlations. As a comparison, the overall uncertainty on the prior is similar to $L = 100$ km without considering the ecosystem influence. The choice of the error correlation length does impact the posterior uncertainties and further investigations will be performed in forthcoming studies. The prior error variances were finally slightly modified to adjust the ratio between the observational constraint and the prior errors. We used the

[1] http://geo.arc.nasa.gov/sge/casa/

reduced χ^2 value to adjust the flux error variances (Kaminski et al., 2001). However, the adjustment of the flux errors remains lower than 10 % compared to the initial estimates.

2.4 Influence functions and atmospheric transport model errors

2.4.1 Atmospheric transport model WRF-CHEM

The atmospheric transport model used in this study is the Weather Research Forecast model (Skamarock et al., 2005), including the chemistry module slightly modified here for CO_2 (referred to as WRF-ChemCO_2). The simulation domain is centered on Iowa, covering 1000 km by 1000 km at a 10 km resolution (Fig. 1). The atmospheric boundary layer scheme used is the Mellor-Yamada-Nakanishi-Niino (MYNN) 2.5 scheme (Nakanishi and Niino, 2004) coupled to the Monin-Obukhov (Jancic Eta) scheme for the surface physics. The atmospheric vertical column was described by 60 levels, with 40 levels in the lower 2 km, the first level being at about 20 m above ground. The NOAH land surface model (Chen and Dudhia, 2001) was used to simulate the surface energy balance, and the National Centers for Environmental Prediction (NCEP) Eta/NAM model analysis product at 40 km resolution was used for the initial and boundary meteorological and surface conditions.

2.4.2 Lagrangian particle dispersion modeling

The influence functions, representing the relationship between concentrations at the tower locations and their related flux footprints at the surface, were simulated with the Lagrangian Particle Dispersion Model from Uliasz (1994). The mean winds (u,v,w), potential temperature, and turbulent kinetic energy from the WRF-Chem CO_2 simulations are used as input variables each 30 min to drive the particle motions from the receptor locations (receptor oriented framework), as described in Lauvaux et al. (2008). 1800 particles are released incrementally at equal intervals over one hour periods to describe the influence functions for every hourly observations. We also ran an additional Lagrangian simulation with a limited number of particles (180 per hour) to describe the boundary influence. In this study, we used the boundary influence functions to relate every observations with one of the four cardinal directions, in and above the planetary boundary layer (PBL). The method is described in Sect. 2.5. The final resolution of the inversion was degraded to 20 km at the surface for computational efficiency of the system, which remains adequate considering the spatial dimensions of the flux patterns in the area.

2.4.3 The MCI 2007 aircraft campaign

For the quantification of vertical transport errors, we used aircraft observations, mainly vertical profiles of CO_2 concentrations, that were measured using a twin-engine Beechcraft Duchess (Garman et al., 2006) during summer 2007 over Iowa (Martins et al., 2009). The vertical profiles ranged from the surface to the lower free troposphere ($\sim$3 km a.g.l.) with an approximate ascent/descent rate of 2.5 m s^{-1}. A non-dispersive infrared differential absorption spectrophotometer was used to detect dry mole fractions of CO_2 every second, with an uncertainty of the measurements of $\pm$0.3 ppm (Martins et al., 2009). In-flight calibrations were conducted every 3 min using a reference gas standard (386.12 ppm) prepared at the NOAA Earth Systems Research Laboratory and traceable to the World Meteorological Organization Central Calibration Laboratory for CO_2 (Zhao et al., 1997). Between 15 June to 25 June 2007, nine flights were performed in central Iowa, which corresponds to one to three flights every two days on average. Six flights including long transects and vertical profiles were used in this study to evaluate the atmospheric model performances.

2.4.4 Atmospheric transport model errors

We estimated the transport model errors in four different steps: (1) we evaluated the WRF modeling performance by comparing the simulated concentrations to observations from nine aircraft transects between June 17 and 25 June 2007 (with six flights presented here); (2) we avoided inconsistencies in the Lagrangian model simulation by removing observations showing large differences between the direct CO_2 concentrations from WRF-ChemCO_2 and the backward concentrations from the LPDM; (3) we computed the aggregation errors and adjoint model errors using the standard deviation of the difference between the direct WRF mixing ratios and the backward LPDM mixing ratios over each week; and (4) we defined for one setup of our sensitivity experiment the error correlations in the observation error covariance matrix from previous studies based on ensemble simulations (Lauvaux et al., 2009b).

We describe here the four steps in more detail. First, we evaluated the simulated PBL heights by comparing the CO_2 vertical distributions to observed CO_2 concentations from nine aircraft flights that occured between the 17 to 25 June 2007 (Martins et al., 2009). The aircraft campaign consisted of several transects located in central Iowa and encompassed variable altitudes, ranging from a few hundreds of meters above ground level (in the convective PBL) to a few thousand (in the free troposphere). We present results for six flights of the campaign with long transects and repeated vertical profiles. The PBL height errors are diagnosed from these flights for transition periods (morning to early afternoon) and well-mixed conditions (midday to late afternoon), and converted into mixing ratio uncertainties. Results are presented in Sect. 3.

Second, we compared the CO_2 concentrations from the direct simulation (WRF-ChemCO_2) to the backward generated concentrations from LPDM for the 8 towers over the 7 months. Both simulations are coupled to the Sibcrop fluxes at

10 km resolution. When the difference is larger than 2σ, the standard deviation in the observation error covariance matrix is increased such that the concentration is ignored.

Third, we estimated the potential biases between the two simulated concentrations. The standard deviation is added to the initial one (from the previous step). This part includes the errors in the adjoint and due to aggregation of the fluxes from 10 km to 20 km. The results and the impacts are presented in Sect. 3.

Finally, we compared two estimates of temporal error correlations in the observation error covariance matrix. Because of the continuous flow of the atmosphere, errors affecting hourly observations are propagated through time and space. Lauvaux et al. (2009b) showed that spatial correlations are significant below a distance of 150 km between observation locations when using hourly observations, corresponding to a correlation length of 30 to 40 km. Similarly, Gerbig et al. (2003a) found an exponentially decreasing correlation length of about 40 km from variograms of aircraft measurements. So we have not included any spatial correlation in the observation errors in regard of distances between towers in the present network (>150 km). But hourly observation errors are affected by temporal correlations. We used a description of the temporal error correlations for each hour of the day based on a previous ensemble of perturbed model simulations (Lauvaux et al., 2009b). For each hourly observation time step, the correlation coefficients with the following hours are prescribed. These correlation functions correspond to the propagation of errors from any hour of the day to the following hours. For example, large correlation coefficients relate one hour in the afternoon to the next ones (up to 0.6 for the first following hours) to lower values during the night (less than 0.4 for the first following hours). Lauvaux et al. (2009b) showed the conservation of the transport model error structures during the afternoons, whereas transitions to different stability conditions (mornings and late afternoons) tend to dissipate these structures. In our case, the error correlation functions are defined over 12 h (linking for example errors at 2 p.m. with the 12 following hours), or less if the correlation coefficient becomes negative (e.g., 8 p.m. error correlation function equals zero at 10 p.m.), meaning that the error structures disappear rapidly when the stability conditions are changing. Here, we defined our reference case with no temporal correlation because the correlation functions were computed with a different mesoscale model (MesoNH in this case), and over a different region. Though, we compare the impact of these error correlations in Sect. 3.6 to our reference inversion that assumes no temporal correlation to quantify their relative importance compared to other components of the system.

2.5 Boundary conditions and aircraft observations

The modeled CO_2 mixing ratios can be decomposed in two seperate contributions: the local surface fluxes within the modeling domain, and the boundary conditions corresponding to the far field influence, i.e. the contribution of the CO_2 inflow from the outer domain to the observed concentrations. We describe in this section the aircraft measurements used to correct initial model outputs, the pre-processing of the boundary mixing ratios to reduce the potential biases, and finally the estimation of their associated uncertainties. This pre-processing of the boundary conditions using aircraft flask data is done independently, before the inversion. The final corrected boundary conditions will be used as prior inflow in the flux inversion. Previous studies at the regional scale showed limited impact from the boundaries because of the oceanic influence and the orography, forcing the scale of the atmospheric processes to mesoscale circulation patterns. These campaigns were in summer, over short time periods (a few weeks), with little changes in the far-field influence compared to large local vegetation signals (Pérez-Landa et al., 2007; Sarrat et al., 2007b). Over longer time scales, systematic errors become increasingly important and need to be corrected (Göckede et al., 2010b).

2.5.1 Weekly aircraft data from NOAA

In this study, the flat terrain and the absence of orography around our domain allow large circulation patterns to affect the background air concentration through seasonal circulation patterns, longitudinal continental jets, and latitudinal conveyor systems as fronts pass (Wang et al., 2007). Here, aircraft data, and more specifically vertical profiles, were used to correct for biases and misrepresentation of the inflow. We used weekly flights operated by the Carbon Cycle Greenhouse Gases Aircraft Project (Sweeney et al., 2011) run by the NOAA's Earth System Research Laboratory (NOAA/ESRL). Four sites were selected to represent our four simulation boundaries: the Airborne Aerosol Observing near Bondville, Illinois (AAO), Beaver crossing in Nebraska (BNE), Homer in Illinois (HIL), and Park Falls in Wisconsin (LEF) (cf. Fig. 1). We compare flask data to modelled mixing ratios at the boundaries, for each week of the 7 months, and compute a correction which we apply to the inflow boundaries to remove or at least decrease biases by pre-processing of the boundary concentrations.

2.5.2 Pre-processing of the boundary CO_2 concentrations

The boundary conditions are defined in two steps: first, we compute time series at each tower location. Second, these time series are used in the inversion system. But before adding these time series to the state vector in the inversion, we removed systematic errors with the help of aircraft measurements, and computed their associated uncertainties. The pre-processing of the boundaries helps to limit potential biases affecting boundary conditions.

Four aircraft profile sites were selected to correct for potential biases in the CT_{v09} mixing ratios. We attributed each of the four aircraft profile sites to one or two of the four cardinal boundaries. The choice of four cardinal boundaries is due to the lack of extensive datasets in space. We limit our correction here to the mean wind direction represented by the four boundaries of our domain. Two of the sites (AAO and HIL, cf. Fig. 1) located in the South East of the domain were both used to assess the South and East boundary corrections, LEF for the North boundary, and BNE for the West. The framework is presented in Fig. 2. First, we compared the aircraft profile mixing ratios to the modeled CT_{v09} mole fractions integrated over two layers: one PBL contribution and one free tropospheric contribution. The PBL height is determined with the LPDM particle distribution over the column, defined by higher densities of particles within the PBL, directly related to the TKE profile from WRF. Second, we computed the model-data mismatches (North, South, East, West, with one PBL and one free tropospheric values) at the exact time of the flights, and averaged them if several flights were performed during the week. These weekly model-data mismatches represent the systematic errors, and are used to correct the initial boundary conditions from CT_{v09}. Finally, we have to apply the corrections at the boundaries on the time series computed at the tower locations. At each time step, a correction is applied on the value of the time series depending on the origin of the inflow. Over a week, hourly obervations are influenced by one or more boundaries (following the main wind direction changes). We identified the inflow origin with the particle distribution at the boundaries of the domain. The particles are counted over each week on the two levels and for each boundary. The selected mismatches were then removed from the initial CT_{v09} inflow time series depending on the boundaries influencing the tower mixing ratios. These corrected values were then included in the inversion system as additional unknowns, described hereafter (cf. Sect. 2.5.3). The results are presented in Sect. 3.3.

2.5.3 Optimization of the boundary CO_2 concentrations in the inversion system

The processed boundary conditions are now treated as additional unknowns in the inverse system, decreasing slightly the observational constraint by increasing the number of elements in the state vector (representing both the fluxes and the boundaries). In the system, we attribute part of the atmospheric signals to the boundaries following the uncertainties, i.e. no transport model is used to attribute atmospheric signals to the inflow at this step. A transport model was used previously to estimate systematic errors and relate the observations with the boundaries. Here, we only consider the inflow as an uncertainty instead of trying to optimize it without the help of additional observations.

The temporal window for the correction of the boundary conditions corresponds to the temporal variability of the

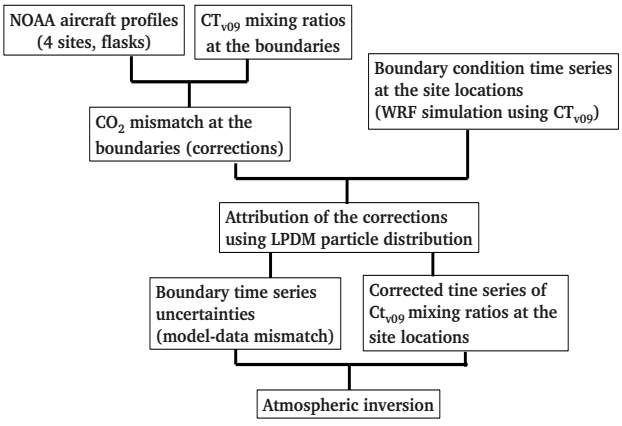

Fig. 2. Schematic framework of the boundary conditions including the mixing ratio pre-processing and the estimation of the uncertainties.

CO_2 inflow. We chose two different temporal windows to invert for the boundaries at each tower: one hour, and 90 hours. The dimensions increase with $2 \times 8 = 16$ additional unknowns when using 90-h averaged boundary mixing ratios or $180 \times 8 = 1440$ additional unknowns with hourly boundary mixing ratios. Hourly changes correspond to large gradients, whereas several days represent only synoptic changes. Theoretically, longer time windows imply longer temporal correlations in the boundary conditions. The implicit definition of the correlations in the state vector errors implies more than the physical duration of events but also the capacity of the system to invert for biased concentrations. 90 h (about four days) corresponds to the length of synoptic events affecting the inflow concentrations. In our study, we estimated the boundary condition uncertainties based on the standard deviations of the model-aircraft data mismatch, ranging from 2 to 4 ppm at the hourly time step, and from 0.5 to 1 ppm on 90 h-averages.

Depending on the time of the day, the combination of the performance of the mesoscale model, the reproductability of the concentrations by the Lagrangian model, and the boundary condition uncertainties, the inverse system will distribute the atmospheric signals amongst the different components (nighttime and daytime surface fluxes, and boundary concentrations). We discuss in Sect. 4 the impact of these components and their related uncertainties associated on our final CO_2 balance.

2.6 Evaluation of the inverse fluxes: Eddy-flux sites over the MCI

We used observed Net Ecosystem Exchange (NEE) measurements from six different eddy-covariance flux sites to evaluate the temporal patterns of the inverse analysis. Four are located in the corn area: Bondville (Meyers and Hollinger, 2004), Rosemount 21 and 19 (Baker and Griffis, 2004), and

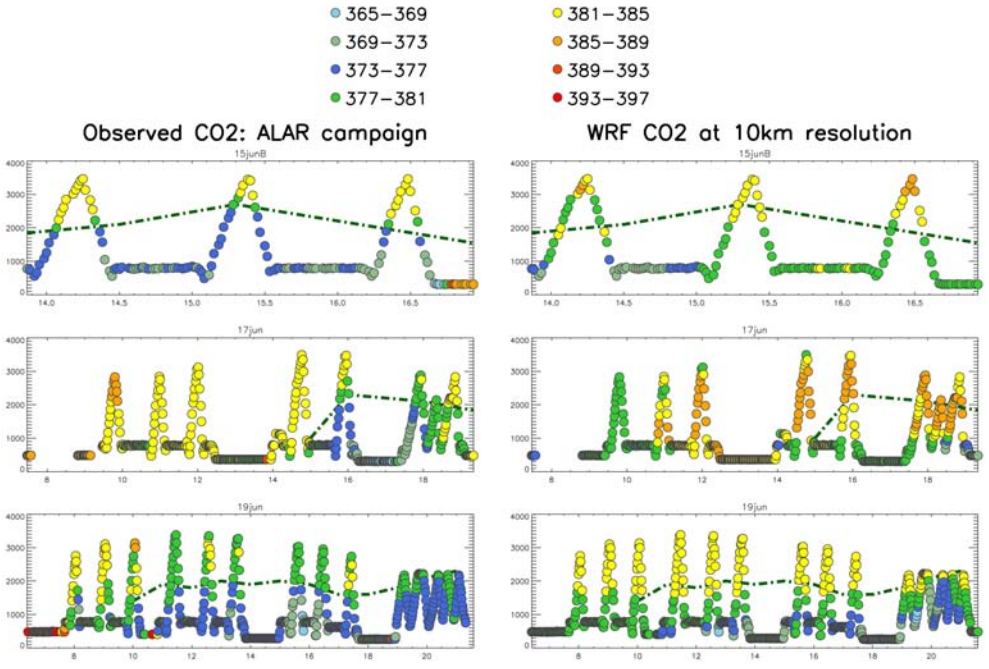

Fig. 3. CO_2 concentrations observed during several flights of the ALAR campaign for 15, 17 and 19 June (on the left) compared to WRF-ChemCO_2 concentrations using SiBcrop fluxes (=before flux optimization) (on the right). Colors indicate the mixing ratio range in ppm. The top of the PBL is indicated by the large vertical gradients from low to high mixing ratios in the free troposphere (green dashed line). The differences between observed and simulated PBL heights are large during transition periods (mornings), overwhelming signals during nighttime, but are low during daytime (afternoons), ranging from 10 to 15 % of the PBL height.

Mead (with three sites on irrigated, rainfed, and irrigated with crop rotation ecosystems) (Verma et al., 2005), and two in grassland areas: Brookings and Fermi prairie sites (Matamala et al., 2008), all part of the Ameriflux network [1] (Fig. 1). We focused our evaluation on the flux sites whose dominant landcover was corn or grassland in order to gauge the success of the inverse fluxes over the most represented ecosystems. The four eddy flux sites over corn are reliable indicators of the temporal variability but representation errors remain large when compared to our 20 km resolution inverse product. The ecosystem variability in one given grid point at 20 km resolution is far from negligeable. The fraction of corn in one pixel is between 40 to 60 % in the corn belt area (referred here as corn-dominated pixels). Eddy flux measurements indicate larger uptake during the growing season, corn being the most active plant in term of photosynthetic activity at this time of the year (Verma et al., 2005). The uptake is larger by at least a factor of two during the maximum growth period (July) compared to other plant types. We used the seasonal cycle and the week-to-week variations to evaluate the temporal corrections in the inverse fluxes. We assume that the observed variability in the eddy-flux measurements is robust and well-correlated with larger scale variability, but too limited to be extrapolated to a region (Wang et al., 2006). We focus on temporal behaviour observed during the season and droughts occuring later in summer of the year 2007. We represented eddy flux site errors by the variations across sites, assuming that representation errors are dominant in our context.

3 Results

3.1 Aircraft data and transport errors due to vertical mixing

We analyze here model-data mismatch using prior fluxes and pre-processed boundary conditions to characterize the vertical structures of the lower troposphere and assign realistic uncertainties representing transport errors due to incorrect vertical mixing. The absolute concentration mismatch is not considered as an indication of transport errors as the CO_2 flux errors represent the majority of the final mismatch. In Figs. 3 and 4, we show the simulated CO_2 concentrations within 4ppm-intervals represented by colored circles against aircraft observed concentrations during 6 different aircraft flights. The PBL heights defined by the vertical gradient in CO_2 show relatively good agreement during the afternoon with differences of about 10 to 15 %, in the range of the observed variability of the entrainment zone depth between the convective boundary layer and the free troposphere (Grabon

[1] http://public.ornl.gov/ameriflux/

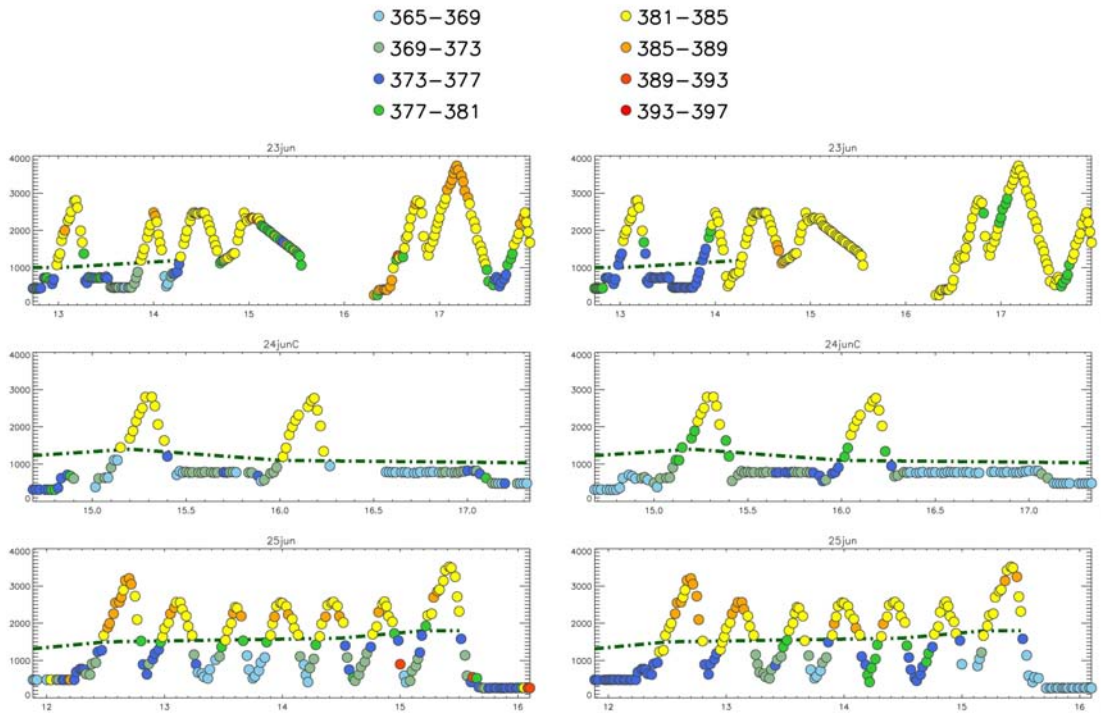

Fig. 4. Same figure for 23, 24 and 25 June flights.

et al., 2010), whereas transition periods are not well captured by the model. In the early morning (19 June, 7 a.m. to 10 a.m.), the PBL is well-developed in the model whereas no vertical gradient between the PBL and the free troposphere is observed during the flight. In the late afternoon (17 and 19 June, from 7 p.m. to 9 p.m.), the vertical distributions of CO_2 are simulated well by the model. We defined the standard deviations (diagonal terms of the R matrix) based on this comparison by assigning large errors during the late morning (10 a.m.–12 p.m.) of 30 to 50 % of the total model-data mismatch, then smaller errors of 10 to 15 % of the signal as transport errors (2 to 3 ppm in summer on average) during the well-mixed conditions, and finally very large errors for nighttime concentrations (after 8pm) that almost remove entirely the observational constraint during these hours ($\sigma_{\text{night}} = 100$ ppm).

3.2 Backward/Forward transport comparison

We evaluate the internal consistency of our forward and inverse modeling systems which represents the adjoint and the aggregation errors. We also eliminate time periods when there are significant discrepancies between forward and backward simulated mixing ratios. We do this by computing the CO_2 mixing ratios predicted at the tower sites using the same prior fluxes with both WRF-chem and LPDM, and compare these hourly estimates over the entire 7-month period of study.

The initial mismatch between the Eulerian model (WRF-chem) and the Lagrangian model (LPDM) is affected by large differences in the concentration time series during a few days per month (one isolated day or few hours). These larges biases are correlated with more stable conditions in the lower atmosphere and indicates clear disagreements between the Lagrangian model and the Eulerian simulations. We applied a filter to remove these periods in our inverse system by increasing observation errors to 100 ppm for these observations. The assigned weights are equivalent to neglect these observations. The threshold that we chose as indicative of inconsistent dynamics, is 2σ of the residual distribution (defined as the square root of the mean square of the half-hourly model-model difference), where σ is computed on a weekly basis for each tower. This threshold ranges from 2 to 7 ppm depending on the season and the tower. We re-compute the daytime biases after removing the large mismatch periods. In summer, when the CO_2 surface flux is large (implying large atmospheric signals), the standard deviation of the residuals are now lower than ± 2.2 ppm, and show an averaged summer bias of 0.12 ppm.

We then added an uncertainty corresponding to the standard deviation for each week of 1 to 2 ppm to the initial WRF errors (diagonal terms in R) for the misrepresentation of the Eulerian dynamics by the Lagrangian model based on these results. During winter, weekly and seasonal biases are much lower, respectively less than 1.9 ppm at the hourly time scale and equal to 0.1 ppm on average. But

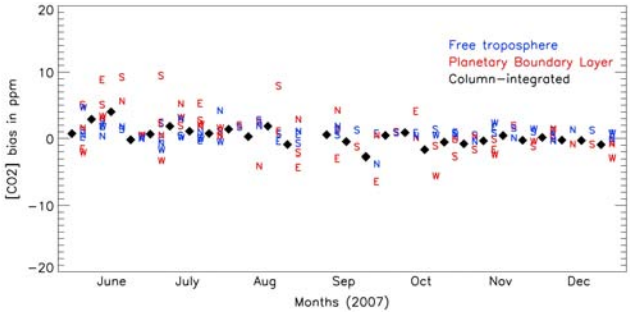

Fig. 5. CO_2 concentration differences between the observed CO_2 concentrations by the aircraft and simulated by CT_{v09} at the four aircraft sites (indicated by the cardinal directions) in the Planetary Boundary Layer (in red), the free troposphere (in blue), and column-averaged PBL (black diamonds).

the surface flux contribution to the atmospheric variability is lower, which explains the apparent smaller mismatch. We defined the additional uncertainties using the same methodology as for summer, from 0.2 to 0.9 ppm for the variances of the observation errors. The forward/backward revealed occasional large disagreements due to the Lagrangian model. Seasonal biases that will influence our final balance are small after removal of these periods (0.12 ppm over summer, and 0.1 ppm over winter), limiting the impact on the inverse CO_2 flux balance.

3.3 Pre processing for boundary conditions

The potential boundary inflow corresponds to the mole fraction from the CT_{v09} inverse system using the TM5 transport model at 1° resolution. We directly compared the mole fractions to observed mixing ratios from aircraft profiles at four different sites, each site being attributed to the closest boundary (or two for AAO and HIL sites) of the domain (cf. Sect. 2.5.2). In Fig. 5, we present the model-data mismatch in the PBL (blue letters), in the free troposphere (red letters), and the difference of the averaged model-data mismatch over the PBL (black diamonds), computed at the exact flight times and locations. If several profiles were available over a week, we show here the averaged differences. In the figure, the letters correspond to the boundaries of the domain (East, West, North, South) for each week. The very large residuals in June (more than 20 ppm) are observable within the two lower levels of the PBL, where the TM5 model is usually underestimating the vertical mixing (vertical profiles show clear unexpected gradients during convective days). We used the differences of the averaged mixing ratios over the higher levels of the PBL (black diamonds) to avoid these large differences in the lower levels of CT_{v09}.

In Fig. 6 (a), we present the histogram of the residuals between the aircraft data and the CT_{v09} mixing ratios. The averaged model-data mismatch (or bias) is about 1.17 ppm over summer (week 1 to 12) and 0.55 ppm over the 7 months. We investigate the impact of the 7-month bias on the final inverse flux balance over the region in Sect. 4.1. In Fig. 6 (b), no bias toward higher or lower mixing ratios is observed. We conclude here that, without the aircraft data correction, the weekly boundary conditions may contain large errors during critical periods, but on average over the 7 months, the bias remains modest (0.55 ppm).

3.4 CO_2 flux time series

The temporal variability observed at the local level using eddy-flux tower measurements is used to evaluate the posterior fluxes over two different ecosystem types. While this comparison is limited by representation errors, we believe that it is valid to compare the temporal patterns in both flux estimates. We compared our results by selecting the posterior fluxes in pixels where one ecosystem type covers more than 40 % of the landscape. In Fig. 7a, we present daily-daytime averages of the prior fluxes from Sibcrop compared to the observed fluxes (averages of the two sites) from two eddy-flux tower measurements, with their standard deviations, representing the grassland ecosystems in the region (Brookings and Fermi). The two sites are significantly different in 2007 resulting in a large representation error (in green in Fig. 7a). The maximum of uptake in June indicates that the growing season peak for grassland ecosystems is outside our study period. The seasonality of this ecosystem is accentuated by the atmospheric observations (larger uptake in July compared to the prior flux) but the uptake in June remains too low, underestimated after inversion. The large boundary condition differences observed in Fig. 5, despite the corrections applied, might still affect the inverse fluxes during this period. After June, the inverse flux variablity is well correlated with the observed eddy-flux variability with a peak of uptake in mid-July and a decrease of the uptake in mid-August due to a drought in the North West of the domain.

Concerning the corn dominated area (cf. Fig. 8), the seasonal variability is well-correlated with the observations but varies depending on the location. The correlations over the 7 months with the 4 different sites are respectively 0.832, 0.948, 0.964, and 0.950 with the prior compared to 0.91, 0.955, 0.965, and 0.953 with the posterior fluxes. The correlation with the mean (average of the time series from the four sites) is about 0.94 with the prior fluxes, and 0.96 with the posterior. The mismatch (square root of the squared differences) is decreasing from $1.949\,\mu\,\mathrm{mol\,m^{-2}\,s^{-1}}$ to $1.915\,\mu\,\mathrm{mol\,m^{-2}\,s^{-1}}$ on average. We see here that the initial fluxes were highly correlated with the observations, with consistent but relatively small corrections after inversions on a weekly basis. In northern Illinois (East of the domain), the inverse fluxes show a late start to the growing season (end of June). The posterior fluxes show distinct temporal patterns for the West and the East of the domain. The observations indicate a large standard deviation across eddy-flux sites (as

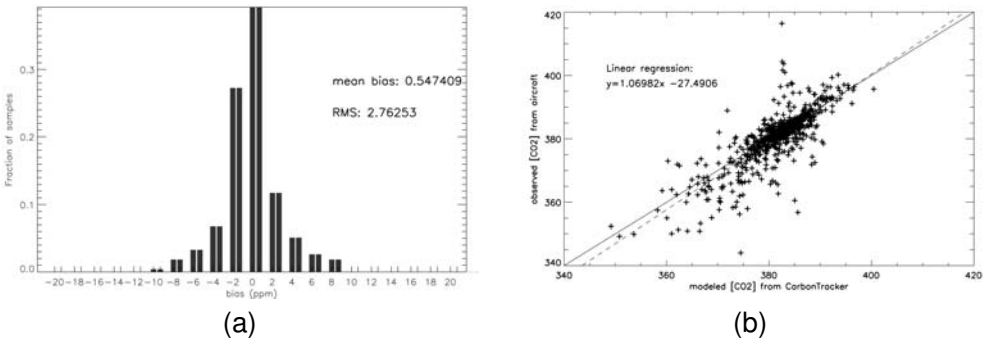

Fig. 6. Histogram of the model-data mismatch at the boundaries with the mean and standard deviation used to correct for the mean bias and to define uncertainties related to the boundaries in the inversion (on the left) and the linear regression between observed aircraft and CT_{v09} modeled CO_2 mixing ratios (on the right).

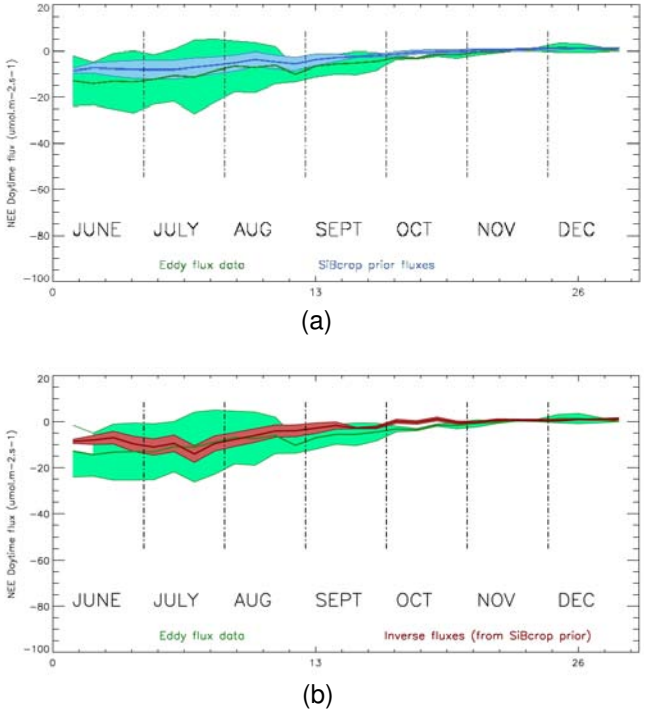

Fig. 7. Net Ecosystem Exchange comparison between Sibcrop grass-dominated pixels and eddy flux towers over grassland (Fermi prairie and Brookings) for the 7 months in umol.m^2.s^{-1} (in green): (a) SiBcrop prior (in blue) and (b) inverse fluxes (in red). The improvement after inversion remains limited in June but posterior fluxes (in red) are in better agreement with the observed fluxes on average over the period.

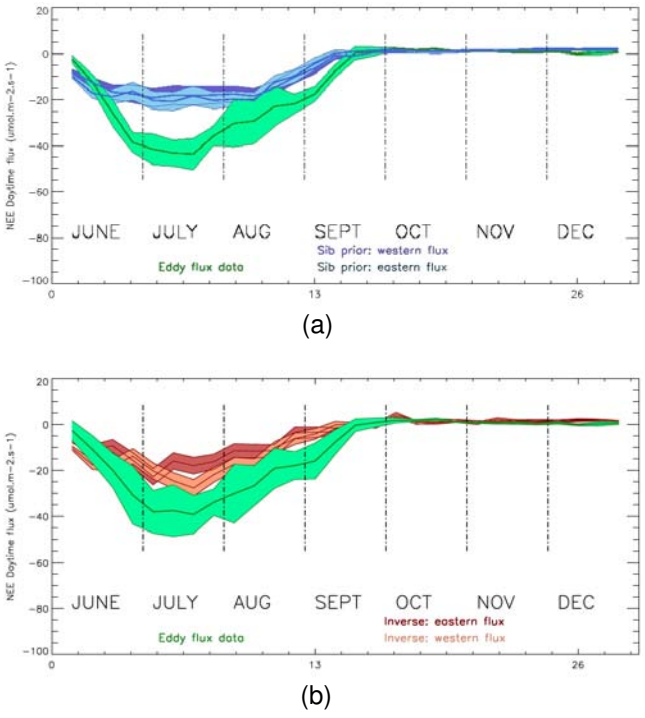

Fig. 8. Net Ecosystem Exchange comparison between Sibcrop corn-dominated pixels for the western (affected by droughts in July and August, in purple)) and the eastern part of the domain (in light blue), and eddy flux towers over corn fields (in green), irrigated or rainfed (Bondville, Rosemount G19 and G21, and Mead) in umol.m^2.s^{-1}: (a) SiBcrop prior (in blue) and (b) inverse fluxes (in red). Posterior fluxes are lower on average due to mixed vegetation types over the pixels.

seen for grass), two of them being irrigated (less affected by the sporadic dry periods) increasing the overall flux uptake over summer in the Western Corn Belt. The absolute values of the posterior fluxes remain smaller than the observed fluxes, as corn occupies only about 40 to 60 % of the pixel surface, mixed with soybean and other crop types. In the model, the presence of soybean with a lower uptake compensates for the large corn uptake. For grassland, the vegetation fraction in the grass-dominated pixels is usually larger (up to 80 %) explaining the better agreement between the modeled fluxes and the observed eddy-flux data. Despite the smaller

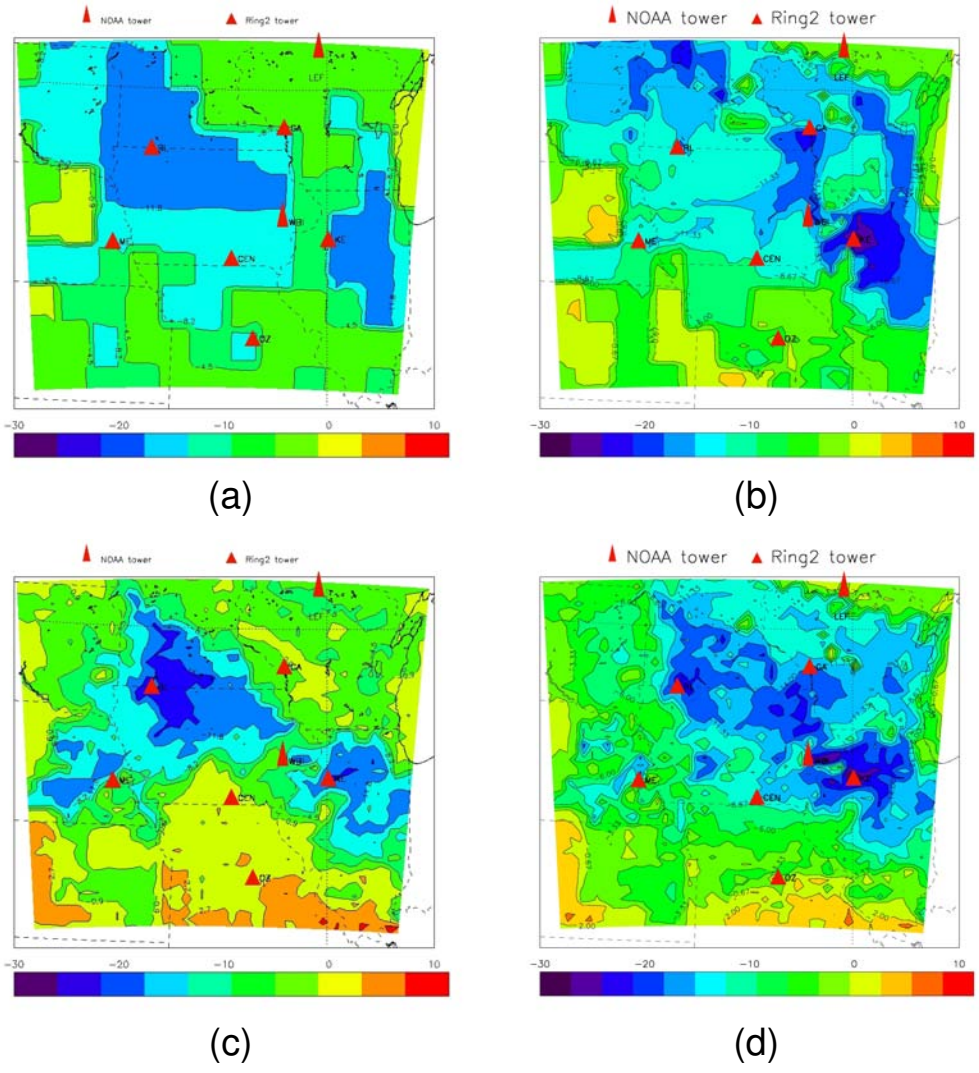

Fig. 9. Map of the CO_2 fluxes accumulated from June to December in TgC.degree^{-2} over the MCI using CarbonTracker2009 inverse fluxes as prior: (a) prior and (b) posterior fluxes; and direct flux estimates from SiBcrop as prior fluxes: (c) prior fluxes and (d) posterior fluxes.

surface flux corrections in wintertime (i.e. limited improvement, discussed in Sect. 4.3), the posterior fluxes show a better correlation with the observed fluxes over the 7 months (cf. Fig. 7b), and no clear bias was introduced by the system. We discuss in Sect. 4.3 the capacity of the system to correct for wintertime flux biases.

3.5 Convergence of the prior fluxes and impact on the posterior distribution

We present in this section the spatial distribution of the prior and posterior fluxes, using sibcrop (Fig. 9c) and CT_{v09} (Fig. 9a) as two distinct priors. First, both posteriors show similar features in space, as a maximum of uptake in northern Illinois, and a stronger sink in Wisconsin, suggesting that the observational constraint is sufficient in both cases to detect the main spatial characteristics of the fluxes. But several areas remain correlated to the initial prior flux distribution, such as in Kansas and Nebraska, west of Mead (cf. Fig. 9b). Other areas show clear posterior flux structures that are not present in any prior. In northern Illinois for example (around Kewanee), the strong sink indicated by the posterior is well defined in both cases. This correction is consistent with high corn productivity with +10 % for the year 2007 compared to the past years as indicated by the annual USDA-NASS report [1]. Northern Iowa, usually very productive in terms of corn Net Primary Production, was affected by severe droughts during August 2007, whereas southern regions recorded averaged precipitations.

[1] www.nass.usda.gov/il

In general, areas between tower sites show similar posterior flux distributions and magnitudes, resulting from the large constraint brought by the superimposed observation influence functions. The corn belt area, clearly defined in space in both priors, becomes wider with smaller spatial gradients.

3.6 CO_2 flux balance: final balance and uncertainties

In this section, we investigate the sensitivity of the integral of the inverse fluxes across the region, and its sensitivity to the assumptions. These uncertainties come from the different choices one could make, all being realistic, with different degrees of complexity. Other tests are performed in Sect. 4 for additional errors or biases that may affect the inverse estimate but are not part of the present system, as e.g. the impact of remaining biases in boundary conditions that may not have been removed. These second tests help quantify the sensitivity of the system to the different components for future inverse systems, in other areas or using different prior fluxes. Using two different prior fluxes (CT_{v09} and SiBcrop), we obtain similar posterior fluxes (cf. Table 1) though the prior fluxes were significantly different. We defined next several cases in which we dramatically increased or decreased uncertainties (prior flux errors, nighttime and daytime observation errors), inserted transport error correlations in time, modifying prior flux error correlations in space, and increased the time window over which the boundary conditions were optimized from one hour to four days. We increased our initial prior variances by 20 % for the first case. For transport errors, we decreased the daytime standard deviations σ_B to 2 ppm, about a factor two lower than our initial summertime standard deviations. We also considered the use of nighttime observations by decreasing the uncertainties to 10 ppm. The different cases are summarized in Table 1.

Increasing prior flux variance (larger σ_B) has little impacts on the posterior flux, similar to decreasing the observation error variances during the day (lower σ_R^{day}). This result, when compared to the large impact of temporal correlations in the observation errors ($\rho_{(X_t,X_{t+n})}\neq 0$), reinforces the importance of the covariances in our system (the structure of the errors), here having more impact on the regional fluxes than the daytime variances. Higher confidence in nighttime data ($\sigma_R^{\text{night}} = 10$ ppm) shows the largest decrease of NEE on the final flux balance. This impact is consistent with the consistently lower nighttime mixing ratios simulated by WRF-Chem. Fitting the nighttime observations is translated into an increase of the positive nighttime flux, decreasing the net sink over the region. Considering the impact of observation error correlations in time when using CT_{v09} as prior fluxes ($\rho_{(X_t,X_{t+n})}\neq 0$), the impact is lower (only 33 Tg C change compared to 41 Tg C change when using SiBcrop). We also examined the impact of using different time windows for the boundary conditions ($T_{bc} = 90$ h) and noticed a change of 16 Tg C on the 7-month regional balance. Finally, we simplified the prior error correlation by using a simple correlation length ($L = 300$ km), without considering ecosystem types ($\rho_B = f(\text{dist})$).

The posterior uncertainties from our system are, over the 7-month period, about 30 Tg C (depending on the selected case). Considering the different setups we defined, the uncertainty in the regional balance due to assumptions in the inverse system is about 15 Tg C, with a mean slightly weaker than the reference setup (mean balance of -183 Tg C$\pm$16 Tg C). This quantity is a range of solutions but is not following a Gaussian distribution. We excluded here the low nighttime transport error case, this one being fundamentally incorrect. For example, the choice of temporal correlations in the observation errors or the structure of the prior errors are motivated by previous studies and one may argue about their relevance. We consider here that any assumption made in the system, if not well established, has to be tested and considered as an additional source of uncertainty. In Sect. 4.1, we present the different sources of uncertainties and combine these to our posterior uncertainties.

4 Discussions

4.1 Boundary conditions and remaining uncertainties

We applied a pre-treatment of the boundary concentrations by correcting model-data mismatch at the boundaries before inversion instead of adding aircraft data to the inverse system to correct for the CO_2 inflow. The comparison between the observed and the simulated CT_{v09} concentrations could lead to an incorrect quantification of the boundary inflow errors for two main reasons: first, the aircraft profiles, punctual observations over the column, are not representative of the entire boundary of 1000 km long and the entire week; and second, the PBL mixing ratios affected by vertical mixing errors in CT_{v09} transport model (currently the TM5 model Krol et al., 2005) could be different in WRF-ChemCO_2 when remixed by our PBL scheme. We computed boundary mixing ratios at the tower locations. Along their path within the simulation domain from the boundary to the tower location, CT_{v09} mole fractions are redistributed on the vertical. The differences between CT_{v09} and aircraft data at the boundaries might not be valid at the tower locations, because the vertical mixing in WRF-ChemCO_2 modified the original vertical distribution of the CT_{v09} mole fractions. Because TM5 model is affected by low vertical mixing in the lower atmospheric levels (levels one and two mainly), we only used differences integrated over the PBL.

In the inversion, we defined the inflow as time series, instead of influence functions and gridded boundaries, to limit the increase of the dimension of the state vector. The CO_2 vertical distribution at the boundaries is also very sensitive to PBL dynamics and may contain large uncertainties at the pixel level if we grid the boundaries of our domain. Previous studies have also shown that the error reduction using

Table 1. Regional CO_2 flux balance from June to December 2007 in TgC over the MCI using Sibcrop and CarbonTracker2009 as prior fluxes in the reference setup (prior and posterior), then assuming larger uncertainties in the prior (= larger σ_B), more confidence in nighttime data i.e. 10 ppm instead of 100 ppm (=lower σ_R^{night}), more confidence in daytime data i.e. 2 ppm instead of 3 ppm for the lower limit (=lower σ_R^{day}),temporal correlations in hourly observation errors between the hour t with the following n hours (= $\rho_{(X_t, X_{t+n})} \neq 0$ or $\rho(t) \neq 0$), a longer time period to correct for boundary influence (= T_{bc} =90h), and prior error correlations based on distance only ($\rho_B = f(L)$).

	prior	post	large σ_B	low σ_R^{night}	low σ_R^{day}	$\rho(t)\neq 0$	$T_{bc} = 90$ h	$\rho_B = f(L)$
SiBcrop	−109	−194	−190	−149	-195	−153	−178	−179
CT_{v09}	−198	−215	/	/	/	−182	/	/

aircraft data is limited by the shorter time window of available observations (Lauvaux et al., 2008). We decided here to use the aircraft observations in a pre-processing of the boundaries and not directly as observations in the inverse system. The aircraft profiles available once a week on average over few hours contain little information to optimize the weekly fluxes biases and the boundaries. Using our approach in the future, more sophisticated methods could be applied as data nudging including additional dataset from commercial flight CO_2 profiles or satellite products where available.

Here, we investigate the impact of potential biases in the boundary concentrations by adding a constant change of +1 ppm. On the 7 month regional balance, this bias leads to a change of +45 Tg C. As explained in Sect. 3.3, the vertical mixing errors in TM5 (CT_{v09}) have a limited impact at the observation locations thanks to the remix of the lower part of the column along its path in the WRF simulation domain. This element is of major importance to avoid large differences as observed in the lower troposphere in the CT_{v09} residuals (cf. Fig. 5 in red). The potential bias due to incorrect boundary conditions can be estimated at half a ppm (defined as 1σ of the error distribution) based on the initial model-data mismatch using the NOAA aircraft vertical profiles. This bias is translated in terms of potential errors on the final balance into a ±24 Tg C. Because we are not considering the improvement of the boundary conditions thanks to the use of aircraft data, this error represents an upper limit on the 7-month balance. This value seems reasonable compared to the large sink of our region. But, because of the unique strength of the atmospheric sink due to the high corn productivity entirely harvested (responsible for the apparently large atmospheric sink), our region is not common and many other areas may suffer from this large potential bias compared to their relatively low annual flux (e.g. Göckede et al., 2010a). Further measurements will be needed to better constrain the error in the boundary conditions.

4.2 Temporal window for the boundaries – what is the impact?

The time length for the boundary conditions in our system, from hourly to a few days, has additional impacts on the correction of biases in the inflow. The surface fluxes are corrected on a weekly time scale. If the time resolution of the boundaries in the state vector is closer to one week, some signals originally attributed to the surface are transferred to the boundaries. But this assumption can be justified by the fact that inflow errors occur at the time scale of synoptic changes rather than the scale of the local dynamics. We investigated the two assumptions (one assuming rapid changes at the boundaries and the second slow changes driven by synoptic conditions) by changing the time period of the boundaries in the state vector as explained in Sect. 2.5.3. Table 1 shows that a change of the order of 16 Tg C was removed from the surface fluxes and transposed to the inflow. In order to compare the boundary condition corrections in both cases, we estimated the boundary condition impact on the optimized atmospheric concentrations. The first case, using hourly concentrations at each tower, shows large hour-to-hour variations. We then averaged over the longer period of time (90 h) and noticed that the contribution from the boundaries can change by several ppm when using hourly concentrations at the boundaries or averages over several days. Weekly surface fluxes changed depending on the inflow averaging period. But the final surface flux balance remains similar in both cases, with only 0.3 to 0.8 ppm (standard deviations of the corrections) reattributed to the boundary corrections, and similar mean corrections (about 0.4 ppm in both cases). Over the 7 months, less than 0.5 ppm of the 90h-averaged hourly boundary correction is due to the transfer of information from the surface to the boundary concentrations, implying an additional standard deviation of about 7 to 10 Tg C in the final regional carbon balance. At this point, the time window for boundary conditions will remain an underconstrained parameter in our system, considering the related uncertainty as additional errors in the final balance. Further study will focus on the autocorrelation of the residuals to define the time scale of the inflow errors.

4.3 What is the real potential of convergence of the system?

The impact of the prior flux spatial distribution affects several areas despite the large amount of atmospheric observations used to constrain the surface fluxes. For the 7-month balance, both priors end up at relatively similar values around

-205 Tg C$\pm$10 Tg C. Two additional cases were designed to evaluate the potential of convergence of the system. The first case assumes an additional flux bias in summer and in winter, by multiplying the SiBcrop prior fluxes by 1.5, i.e. increasing the seasonal signals considerably. This biased prior presents a larger 7-month sink (-164 Tg C instead of -109 Tg C) because of the large increase of the summer uptake compared to the relatively lower increase of the wintertime net positive flux. The results show that the summer bias is almost entirely removed (95 % retrieved), but the winter time bias after inversion is partially retrieved, with a difference with the reference inversion of 0.95 Tg C per week on average, corresponding to a posterior 7-month balance of -185 Tg C. It clearly indicates that the inverse system is limited in winter because of the larger boundary condition contribution compared to the surface flux signal. We computed the ratio of the boundary contribution to the surface flux contribution on hourly concentrations. In July, about 10 to 20 % is due to boundary contribution versus 30 to 40 % during winter. However, by including an additional 4.1 Tg C per week in winter, the inversion corrected for 77 % of this bias.

The second case uses a SiBcrop simulation affected by unrealistic water stress in summer. The 7-month balance of this prior is close to zero (-1.9 Tg C). Starting with this erroneous prior flux, the posterior flux balance ends up at -147 Tg C. The inverse system, even if not able to retrieve or converge to previous inverse estimates in this case, showed a large correction of the initial balance retrieving 80 % of the reference posterior flux balance. It suggests that the observational constraint is large enough to reach a reasonable estimate despite the distant initial carbon balance. As shown in Sect. 3.6, the spatial structure may be affected by the initial flux distribution. But the regional balance itself is highly constrained by the observations. Further investigations will consider the impact of observations on the inverse fluxes for concentration tower network design.

The transport model errors were evaluated using aircraft data vertical profiles. Additional errors from the Lagrangian model were also quantified by a forward-backward comparison and reasonable biases were included in our final flux uncertainty assessment. Part of the errors were not considered due to the lack of data to evaluate the atmosphere dynamics, as the advection of air or the convection scheme. We tested the potential impact of the daytime observation errors (variances) in the system by decreasing uncertainties to 2 ppm, and little impact affected our results (less than 1 Tg C change). Only uncertainties decreased in this case, with an underestimation of the posterior variances. Nighttime prior errors appeared more critical in our system. This result is consistent with past studies (e.g. Lauvaux et al., 2008) that showed the importance of the nighttime flux signals in the daytime observations to constrain the overall flux balance, affected by incorrect nighttime transport. Even though we almost removed the nighttime observations in our system ($\sigma_R = 100$ ppm), transport model errors during nighttime affect the daytime observation signals. This result explains also the strong impact of temporal error correlations reinforcing the impact of transition period observations (morning and evening). The performances of actual mesoscale models during nighttime (or more generally during stable conditions) have to be improved in the future to reduce actual uncertainties, despite the absence of nighttime data use in the inverse system.

Finally, the posterior uncertainties of the inverse fluxes at about 30 Tg C and the different sensitivity tests (16 Tg C), including potential biases from the boundaries of about 24 Tg C, gives a combined uncertainty of 34 Tg C, excluding the additional 24 Tg C of potential additional biases for a regional sink of about 183 Tg C. The present calculation is not a posterior uncertainty following a Gaussian distribution but an interval of confidence with an undefined distribution. Remaining errors are hard to quantify precisely (e.g. prior flux error correlations, complete transport model errors), and additional biases are likely to arise in future model intercomparisons. Further investigations will include transport evaluation and comparisons to independent estimates from inventory data at the regional level. High quality agricultural inventories made in the area (West et al., 2011) will allow the comparison to independent annual estimates of the regional carbon balance.

5 Conclusions

We presented here an inverse flux estimate at high resolution over the corn belt area for 2007 using eight CO_2 concentration towers and two different prior fluxes. The sensitivity to the different assumptions was used to evaluate a more complete final uncertainty for our inverse flux balance. Boundary conditions were corrected with aircraft data profiles, potentially leading to an error (or a potential bias) of about 24 Tg C over the 7 months. But more critical is the impact of nighttime transport model errors and temporal error correlations in the simulated concentrations. Total uncertainties are about 34 Tg C including 16 Tg C from the assumptions made in the system, 30 Tg C from the prior and the transport model, and 24 Tg C of potential bias from the boundary conditions. The impact of boundary conditions is independent of the regional balance but only of the domain size, limiting the actual method to regions presenting large annual flux balances (more than 20 Tg C year^{-1} for a 10^6 km^2 domain). The degree of convergence indicates a robust signal for a sink of about 180 Tg C for the June to December period. Spatial patterns inherited from the prior fluxes were still detectable in the posterior fluxes especially on the sides of the domain, despite the large observational constraint. The atmospheric signal remains large enough to constrain the regional flux balance but spatial distribution required that influence functions from different towers were super-imposed. Clear spatial patterns in the posterior fluxes were identified (as the

strong uptake in northern Illinois for the present year) despite the use of different priors.

Acknowledgements. We thank Andy Jacobson from NOAA/ESRL division for discussions and support with CarbonTracker products, Arlyn Andrews from NOAA/ESRL division for data support and management for the West Branch tall tower, Colm Sweeney and Gabrielle Petron from NOAA/ESRL division for data from the aircraft program, Tim Griffis from University of Minnesota for his comments and the eddy-covariance flux data from Rosemount, Shashi Verma and Andrew Suyker from University of Nebraska-Lincoln for eddy-covariance flux data from Mead, Tilden Meyers from NOAA/ARL division for eddy-covariance flux data from Brookings and Bondville, and Roser Matamala from Argonne National Laboratory for eddy-covariance flux data from Fermi. This research was supported by the Office of Science (BER) US Department of Energy, Terrestrial Carbon Program, the US National Aeronautics and Space Administration's Terrestrial Ecology Program, and the US National Oceanographic and Atmospheric Administration, Office of Global Programs, Global Carbon Cycle program.

Edited by: C. Gerbig

References

Ahmadov, R., Gerbig, C., Kretschmer, R., Koerner, S., Neininger, B., Dolman, A. J., and Sarrat, C.: Mesoscale covariance of transport and CO_2 fluxes: Evidence from observations and simulations using the WRF-VPRM coupled atmosphere-biosphere model, J. Geophys. Res., 112, D22107, doi:10.1029/2007JD008552, 2007.

Baker, D. F., Law, R. M., Gurney, K. R., Rayner, P., Peylin, P., Denning, A. S., Bousquet, P., Bruhwiler, L., Chen, Y.-H., Ciais, P., Fung, I. Y., Heimann, M., John, J., Maki, T., Maksyutov, S., Masarie, K., Prather, M., Pak, B., Taguchi, S., , and Zhu, Z.: TransCom 3 inversion intercomparison: Impact of transport model errors on the interannual variability of regional CO_2 fluxes, 1988–2003, Global Biogeochem. Cy., 20, 439, doi:10.1029/2004GB002, 2007.

Baker, J. and Griffis, T.: Examining strategies to improve the carbon balance of corn/soybean agriculture using eddy covariance and mass balance techniques, Agri. Forest Meteorol., 128, 163–177, doi:10.1016/j.agrformet.2004.11.005, 2004.

Bousquet, P., Peylin, P., Ciais, P., Quéré, C. L., Friedlingstein, P., and Tans, P. P.: Regional changes in carbon dioxide fluxes of land and oceans since 1980, Science, 290, 1342–1346, 2000.

Butler, M. P., Davis, K. J., Denning, A. S., and Kawa, S. R.: Using continental observations in global atmospheric inversions of CO_2: North American carbon sources and sinks, Tellus B, 62, 550–572, doi:10.1111/j.1600-0889.2010.00501.x, 2010.

Canadell, J. G., Le Qur, C., Raupach, M. R., Field, C. B., Buitenhuis, E. T., Ciais, P., Conway, T. J., Gillett, N. P., Houghton, R. A., and Marland, G.: Contributions to accelerating atmospheric CO_2 growth from economic activity, carbon intensity, and efficiency of natural sinks, Proc. Natl. Acad. Sci., 104, 18866–18870, doi:10.1073/pnas.0702737104, 2007.

Carouge, C., Rayner, P. J., Peylin, P., Bousquet, P., Chevallier, F., and Ciais, P.: What can we learn from European continuous atmospheric CO_2 measurements to quantify regional fluxes Part 2: Sensitivity of flux accuracy to inverse setup, Atmos. Chem. Phys., 10, 3119–3129, doi:10.5194/acp-10-3119-2010, 2010.

Chen, F. and Dudhia, J.: Coupling an advanced land surface-hydrology model with the PennState-NCAR MM5 modelling system. Part1: model implementation and sensitivity, Mon. Weather Rev., 129, 569–585, 2001.

Chevallier, F., Viovy, N., Reichstein, M., and Ciais, P.: On the assignment of prior errors in Bayesian inversions of CO_2 surface fluxes, Geophys. Res. Let., 33, L13802, doi:10.1029/2006GL026496, 2006.

Chevallier, F., Ciais, P., Conway, T. J., Aalto, T., Anderson, B. E., Bousquet, P., Brunke, E. G., Ciattaglia, L., Esaki, Y., Frohlich, M., Gomez, A., Gomez-Palaez, A. J., Haszpra, L., Krummel, P. B., Langenfelds, R., Leuenberger, M., Machida, T., Maignan, F., Matsueda, H., Morgui, J. A., Mukai, H., Nakazawa, T., Peylin, P., Ramonet, M., Rivier, L., Sawa, Y., Schmidt, M., Steele, P., Vay, S. A., Vermeulen, A. T., Wofsy, S. C., and Worthy, D.: CO_2 surface fluxes at grid point scale estimated from a global 21-year reanalysis of atmospheric measurements, J. Geophys. Res., doi:10.1029/2010JD013887, in press, 2010.

Corbin, K. D., Denning, A. S., Lokupitiya, E. Y., Schuh, A. E., Miles, N. L., , Davis, K. J., Richardson, S., and Baker, I. T.: Assessing the impact of crops on regional CO_2 fluxes and atmospheric concentrations, Tellus B, 62, 521–532, doi:10.1111/j.1600-0889.2010.00485.x, 2008.

Crosson, E. R.: A cavity ring-down analyzer for measuring atmospheric levels of methane, carbon dioxide, and water vapor, Appl. Phys. B, 92, 403–408, 2008.

Dolman, A. J., Noilhan, J., Durand, P., Sarrat, C., Brut, A., Piguet, B., Butet, A., Jarosz, N., Brunet, Y., Loustau, D., Lamaud, E., Tolk, L., Miglietta, R. R. F., Gioli, B., Magliulo, V., Esposito, M., Gerbig, C., Krner, S., Galdemard, P., Ramonet, M., Ciais, P., Neininger, B., Hutjes, R. W. A., Macatangay, J. A. E. R., Schrems, O., Pérez-Landa, G., Sanz, M. J., Scholz, Y., Facon, G., Ceschia, E., and Beziat, P.: CERES, the CarboEurope Regional Experiment Strategy in Les Landes, South West France, May–June 2005, Bull. Am. Meteorol. Soc., 87, 1367–1379, doi:10.1175/BAMS-87-10-1367, 2006.

Enting, I. G.: Inverse Problems in Atmospheric Constituent Transport, Cambridge University Press, Cambridge, UK, 412 pp., 2002.

Francey, R. J., Tans, P. P., Allison, C. E., Enting, I. G., White, J. W. C., and Trolier, M.: Changes in oceanic and terrestrial carbon uptake since 1982, Nature, 373, 326–330, 1995.

Garman, K., Hill, K. A., Wyss, P., Carlsen, M., Zimmerman, J. R., Stirm, B. H., Carney, T. Q., Santini, R., and Shepson, P. B.: An airborne and wind tunnel evaluation of a wind turbulence measurement system for aircraft-based flux measurements, J. Atmos. Ocean. Technol., 23, 1696–1708, 2006.

Geels, C., Gloor, M., Ciais, P., Bousquet, P., Peylin, P., Vermeulen, A. T., Dargaville, R., Aalto, T., Brandt, J., Christensen, J. H., Frohn, L. M., Haszpra, L., Karstens, U., Rdenbeck, C., Ramonet, M., Carboni, G., and Santaguida, R.: Comparing atmospheric transport models for future regional inversions over Europe; Part 1: mapping the atmospheric CO_2 signals, Atmos. Chem. Phys., 7, 3461–3479, 2007, http://www.atmos-chem-phys.net/7/3461/2007/.

Gerbig, C., Lin, J. C., Wofsy, S. C., Daube, B. C., Andrews,

A. E., Stephens, B. B., Bakwin, P. S., and Grainger, C. A.: Toward constraining regional-scale fluxes of CO_2 with atmospheric observations over a continent: 1. Observed spatial variability from airborne platforms, J. Geophys. Res., 108, 4756, doi:10.1029/2002JD003018, 2003a.

Gerbig, C., Lin, J. C., Wofsy, S. C., Daube, B. C., Andrews, A. E., Stephens, B. B., Bakwin, P. S., and Grainger, C. A.: Toward constraining regional-scale fluxes of CO_2 with atmospheric observations over a continent: 2. Analysis of COBRA data using a receptor-oriented framework, J. Geophys. Res., 108, 4757, doi:10.1029/2003JD003770, 2003b.

Gerbig, C., Lin, J. C., Munger, J. W., and Wofsy, S. C.: What can tracer observations in the continental boundary layer tell us about surface-atmosphere fluxes?, Atmos. Chem. Phys., 6, 539–554, doi:10.5194/acp-6-539-2006, 2006.

Gioli, B., Miglietta, F., Martino, B. D., Hutjes, R., Dolman, H., Lindroth, A., Schumacher, M., Sanz, M. J., Manca, G., Peressotti, A., and Dumas, E. J.: Comparison between tower and aircraft-based eddy covariance fluxes in five European regions, Agr. Forest Meteorol., 127, 1–16, 2004.

Göckede, M., Michalak, A. M., Vickers, D., Turner, D. P., and Law, B. E.: Atmospheric inverse modeling to constrain regional scale CO_2 budgets at high spatial and temporal resolution, J. Geophys. Res., 115, D15113, doi:10.1029/2009JD012257, 2010a.

Göckede, M., Turner, D. P., Michalak, A. M., Vickers, D., and Law, B. E.: Sensitivity of a subregional scale atmospheric inverse CO_2 modeling framework to boundary conditions, J. Geophys. Res., 115, D24112, doi:10.1029/2010JD014443, 2010b.

Gourdji, S. M., Hirsch, A. I., Mueller, K. L., Yadav, V., Andrews, A. E., and Michalak, A. M.: Regional-scale geostatistical inverse modeling of North American CO_2 fluxes: a synthetic data study, Atmos. Chem. Phys., 10, 6151–6167, doi:10.5194/acp-10-6151-2010, 2010.

Grabon, J. S., Davis, K. J., Kiemle, C., and Ehret, G.: Airborne Lidar observations of the transition zone between the convective boundary layer and free atmosphere during the international H_2O Project (IHOP) in 2002, Bound.-Layer Meteorol., 134, 61–83, 2010.

Griffis, T. J., Baker, J. M., Sargent, S. D., Erickson, M., Corcoran, J., Chen, M., and Billmark, K.: Influence of C_4 vegetation on $^{13}CO_2$ discrimination and isoforcing in the upper Midwest, United State, Global Biogeochem. Cy., 24, GB4006, doi:10.1029/2009GB003768, 2010.

Gu, L., Meyers, T., Pallardy, S. G., Hanson, P., Yang, B., Heuer, M., Hosman, K. P., Riggs, J. S., Sluss, D., and Wullschleger, S.D.: Direct and indirect effects of atmospheric conditions and soil moistre on surface energy partitioning revealed by a prolonged drought at a temperate forest site, J. Geophys. Res., 111, D16102, doi:10.1029/2006JD007161, 2006.

Gurney, K. R., Law, R. M., Denning, A. S., Rayner, P. J., Baker, D., Bousquet, P., Bruhwiler, L., Chen, Y.-H., Ciais, P., Fan, S., Fung, I. Y., Gloor, M., Heimann, M., Higuchi, K., John, J., Maki, T., Maksyutov, S., Masarie, K., Peylin, P., Prather, M., Pak, B. C., Randerson, J., Sarmiento, J., Taguchi, S., Takahashi, T., and Yuen, C.-W.: Towards robust regional estimates of CO_2 sources and sinks using atmospheric transport models, Nature, 415, 626–630, 2002.

Kaminski, T., Rayner, P. J., Heimann, M., and Enting, I. G.: On Aggregation Errors in Atmospheric Transport Inversions, J. Geophys. Res., 106, 4703–4715, 2001.

Krol, M., Houweling, S., Bregman, B., van den Broek, M., Segers, A., van Velthoven, P., Peters, W., Dentener, F., and Bergamaschi, P.: The two-way nested global chemistry-transport zoom model TM5: algorithm and applications, Atmos. Chem. Phys., 5, 417–432, doi:10.5194/acp-5-417-2005, 2005.

Lauvaux, T., Uliasz, M., Sarrat, C., Chevallier, F., Bousquet, P., Lac, C., Davis, K. J., Ciais, P., Denning, A. S., and Rayner, P. J.: Mesoscale inversion: first results from the CERES campaign with synthetic data, Atmos. Chem. Phys., 8, 3459–3471, doi:10.5194/acp-8-3459-2008, 2008.

Lauvaux, T., Gioli, B., Sarrat, C., Rayner, P. J., Ciais, P., Chevallier, F., Noilhan, J., Miglietta, F., Brunet, Y., Ceschia, E., Dolman, H., Elbers, J. A., Gerbig, C., Hutjes, R., Jarosz, N., Legain, D., and Uliasz, M.: Bridging the gap between atmospheric concentrations and local ecosystem measurements, Geophys. Res. Lett., 36, L19809, doi:10.1029/2009GL039574, 2009a.

Lauvaux, T., Pannekoucke, O., Sarrat, C., Chevallier, F., Ciais, P., Noilhan, J., and Rayner, P. J.: Structure of the transport uncertainty in mesoscale inversions of CO_2 sources and sinks using ensemble model simulations, Biogeosciences, 6, 1089–1102, doi:10.5194/bg-6-1089-2009, 2009b.

Law, R. M., Rayner, P. J., Steele, L. P., and Enting, I. G.: Data and modelling requirements for CO_2 inversions using high frequency data, Tellus, 55B, 512–521, doi:10.1034/j.1600-0560.2003.0029.x, 2003.

Lokupitiya, E., Denning, S., Paustian, K., Baker, I., Schaefer, K., Verma, S., Meyers, T., Bernacchi, C. J., Suyker, A., and Fischer, M.: Incorporation of crop phenology in Simple Biosphere Model (SiBcrop) to improve land-atmosphere carbon exchanges from croplands, Biogeosciences, 6, 969–986, doi:10.5194/bg-6-969-2009, 2009.

Martins, D. K., Sweeney, C., Stirm, B. H., and Shepson, P. B.: Regional surface flux of CO_2 inferred from changes in the advected CO_2 column density, Agric. For. Meteorol., 149, 1674–1685, doi:10.1016/j.agrformet.2009.05.005, 2009.

Matamala, R., Jastrow, D., Miller, R., and Garten, C.: Temporal changes in the distribution of C and N stocks in a restored tallgrass prairie in the U.S. Midwest, Ecol. Appl., 18, 1470–1488, 2008.

Meyers, T. and Hollinger, S.: An assessment of storage terms in the surface energy balance of maize and soybean, Agr. Forest Meteorol., 125, 105–115, 2004.

Miles, N. L., Richardson, S. J., Davis, K. J., Lauvaux, T., Andrews, A. E., West, T. O., Bandaru, V., and Crosson, E. R.: Large amplitude spatial and temporal gradients in atmospheric boundary layer CO2 mole fractions detected with a tower-based network in the U.S. Upper Midwest, J. Geophys. Res., accepted, 2011.

Nakanishi, M. and Niino, H.: An improved Mellor-Yamada level 3 model with condensation physics, Bound. Layer Meteorol., 111, 1–31, 2004.

Ogle, S., Davis, K., Andrews, A., Gurney, K., West, T., Cook, R., Parkin, R., Morisette, J., Verma, S., and Wofsy, S.: Science plan: Mid-Continent Intensive campaign of the North American Carbon Program, US Global Change Carbon Program – North American Carbon Program, available online at: http://www.nacarbon.org/nacp/mci.html, 2006.

Pérez-Landa, G., Ciais, P., Sanz, M. J., Gioli, B., Miglietta, F., Palau, J. L., Gangoiti, G., and Millán, M. M.: Mesoscale circula-

tions over complex terrain in the Valencia coastal region, Spain – Part 1: Simulation of diurnal circulation regimes, Atmos. Chem. Phys., 7, 1835–1849, doi:10.5194/acp-7-1835-2007, 2007.

Peters, W., Jacobson, A. R., Sweeney, C., Andrews, A. E., Conway, T. J., Masarie, K., Miller, J. B., Bruhwiler, L. M. P., Ptron, G., Hirsch, A. I., Worthy, D. E. J., van der Werf, G. R., Randerson, J. T., Wennberg, P. O., Krol, M. C., and Tans, P. P.: An atmospheric perspective on North American carbon dioxide exchange: CarbonTracker, Proc. Natl. Acad. Sci., 104, 18925–18930, doi:10.1073/pnas.0708986104, 2007.

Peylin, P., Rayner, P. J., Bousquet, P., Carouge, C., Hourdin, F., Ciais, P., Heinrich, P., and AeroCarb Contributors: Daily CO_2 flux estimate over Europe from continuous atmospheric measurements – Part 1 inverse methodology, Atmos. Chem. Phys., 5, 3173–3186, doi:10.5194/acp-5-3173-2005, 2005.

Richardson, S. J., Miles, N. L., Davis, K. J., Crosson, E. R., Rella, C., and Andrews, A. E.: Field testing of cavity ring-down spectroscopy analyzers measuring carbon dioxide and water vapor, J. Atmos. Oceanic Technol., 0739–0572, doi:10.1175/JTECH-D-11-00063.1, 2011.

Rödenbeck, C., Gerbig, C., Trusilova, K., and Heimann, M.: A two-step scheme for high-resolution regional atmospheric trace gas inversions based on independent models, Atmos. Chem. Phys., 9, 5331–5342, doi:10.5194/acp-9-5331-2009, 2009.

Sarrat, C., Noilhan, J., Dolman, A. J., Gerbig, C., Ahmadov, R., Tolk, L. F., Meesters, A. G. C. A., Hutjes, R. W. A., Ter Maat, H. W., Pérez-Landa, G., and Donier, S.: Atmospheric CO_2 modeling at the regional scale: an intercomparison of 5 meso-scale atmospheric models, Biogeosciences, 4, 1115–1126, doi:10.5194/bg-4-1115-2007, 2007a.

Sarrat, C., Noilhan, J., Lacarrère, P., Donier, S., Lac, C., Calvet, J. C., Dolman, A. J., Gerbig, C., Neininger, B., Ciais, P., Paris, J. D., Boumard, F., Ramonet, M., and Butet, A.: Atmospheric CO_2 modeling at the regional scale: Application to the CarboEurope Regional Experiment, J. Geophys. Res., 112, D12105, doi:10.1029/2006JD008107, 2007b.

Schuh, A. E., Denning, A. S., Corbin, K. D., Baker, I. T., Uliasz, M., Parazoo, N., Andrews, A. E., and Worthy, D. E. J.: A regional high-resolution carbon flux inversion of North America for 2004, Biogeosciences, 7, 1625–1644, doi:10.5194/bg-7-1625-2010, 2010.

Skamarock, W. C., Klemp, J. B., Dudhia, J., Gill, D. O., Barker, D. M., Wang, W., and Powers, J. G.: A Description of the Advanced Research WRF Version 2, National Center of Atmospheric Research, Boulder, CO, USA, 100 pp., 2005.

Stephens, B. B., Gurney, K. R., Tans, P. P., Sweeney, C., Peters, W., Bruhwiler, L., Ciais, P., Ramonet, M., Bousquet, P., Nakazawa, T., Aoki, S., Machida, T., Inoue, G., Vinnichenko, N., Lloyd, J., Jordan, A., Heimann, M., Shibistova, O., Langenfelds, R. L., Steele, L. P., Francey, R. J., and Denning, A. S.: Weak Northern and Strong Tropical Land Carbon Uptake from Vertical Profiles of Atmospheric CO_2, Science, 316, 1732–1735, doi:10.1126/science.1137004, 2007.

Sweeney, C., Karion, A., Wolter, S., Neff, D., Higgs, J. A., Heller, M., Guenther, D., Miller, B., Montzka, S., Miller, J., Conway, T., Dlugokencky, E., Novelli, P., Masarie, K., Oltman, S., and Tans, P.: Carbon dioxide climatology of the NOAA/ESRL Greenhouse Gas Aircraft Network, Journal of Geophysical Research, in prep., 2011.

Tans, P. P., Fung, I. Y., and Takahashi, T.: Observational constraints on the global atmospheric CO_2 budget, Science, 247, 1431–1438, 1990.

Tarantola, A.: Inverse Problem Theory and Methods for Model Parameter Estimation, SIAM, (ISBN 0-89871-572-5), 2004.

Uliasz, M.: Lagrangian particle modeling in mesoscale applications, in: Environmental Modelling II, edited by: Zanetti, P., Computational Mechanics Publications, 71–102, 1994.

Verma, S. B., Dobermann, A., Cassman, K. G., Walters, D. T., Knops, J. M., Arkebauer, T. J., Suyker, A. E., Burba, G. G., Amos, B., Yang, H., Ginting, D., Hubbard, K. G., Gitelson, A. A., and Walter-Shea, E. A.: Annual carbon dioxide exchange in irrigated and rainfed maize-based agroecosystems, Agr. Forest Meteorol., 131, 77–96, doi:10.1016/j.agrformet.2005.05.003, 2005.

Wang, J.-W., Denning, A. S., Lu, L., Baker, I. T., Corbin, K. D., and Davis, K. J.: Observations and simulations of synoptic, regional, and local variations in atmospheric CO_2, J. Geophys. Res., 112, D04108, doi:10.1029/2006JD007410, 2007.

Wang, W., Davis, K. J., Cook, B. D., Butler, M. P., and Ricciuto, D. M.: Decomposing CO_2 fluxes measured over a mixed ecosystem at a tall tower and extending to a region: A case study, J. Geophys. Res., 111, G02005, doi:10.1029/2005JG000093, 2006.

West, T. O., Bandaru, V., Brandt, C. C., Schuh, A. E., and Ogle, S. M.: Regional uptake and release of crop carbon in the United States, Biogeosciences, 8, 631–654, doi:10.5194/bg-8-631-2011, 2011.

Zhao, C. L., Tans, P. P., and Thoning, K. W.: A high precision manometric system for absolute calibrations of CO_2 in dry air, J. Geophys. Res., 102, 5885–5894, 1997.